VISUALIZING INORGANICS IN WOOD AND WOOD COMPOSITES USING X-RAY MICRO-CT

by

Dengcheng Feng

B.Sc., The University of British Columbia, 2018

B.Eng., Beijing Forestry University, 2018

A THESIS SUBMITTED IN PARTIAL FULFILLMENT
OF THE REQUIREMENTS FOR THE DEGREE OF

MASTER OF SCIENCE

in

THE FACULTY OF GRADUATE AND POSTDOCTORAL STUDIES

(Forestry)

THE UNIVERSITY OF BRITISH COLUMBIA

(Vancouver)

April 2022

The following individuals certify that they have read, and recommend to the Faculty of Graduate and Postdoctoral Studies for acceptance, a thesis entitled:

Visualizing Inorganics in Wood and Wood Composites Using X-ray Micro-CT

submitted by Dengcheng Feng in partial fulfillment of the requirements for the degree of Master of Science in Forestry

Examining Committee:

Dr. Philip D. Evans, Department of Wood Science, UBC
Supervisor

Dr. Chunping Dai, Department of Wood Science, UBC
Supervisory Committee Member

Dr. Gregory D. Smith, Department of Wood Science, UBC
Supervisory Committee Member

Dr. Nicolas Francois, The Australian National University
Additional Examiner

Abstract

Inorganic materials are a natural component of wood and can also be added to lumber and wood composites to improve their durability. Traditional methods of visualizing the distribution of inorganics in wood are limited to a two-dimensional space and thus are not ideal for studying the 3D distribution of inorganics. I hypothesize that X-ray micro-CT will be able to visualize and reveal novel information about spatial distribution of inorganics in wood. I first test this hypothesis by visualizing the distribution of silica particles in four siliceous Australian hardwood species. A number of novel findings arose from this research. I found that silica particles were associated with rays in the four hardwoods, but their distribution within rays varied. Silica particles were evenly distributed in rays in most species except in *Endiandra palmerstonii* where they were mainly found in the upright and square cells of rays. Silica particles were associated with growth rings in *Lophostemon confertus.* Dense materials other than silica particles were found in the vessels of *Syncarpia glomulifera* and *Syncarpia hillii*. X-ray fluorescence microscopy confirmed that these materials were inorganic silica and metal elements. Secondly, I tested my hypothesis by visualizing the distribution of zinc borate (ZB) in a wood-plastic-composite (WPC) and examined if a sodium iodide label could improve the contrast between wood and plastic in CT images of WPC. I found that ZB occurred mainly as discrete particles between wood flakes. Interfacial voids formed a network of cracks within the WPC. Impregnation with NaI improved visualization of wood and plastic and made it possible to quantify the levels of wood, plastic, void and zinc borate in the WPC and the geometry of wood particles. However, NaI impregnation swelled wood, closed interfacial voids, and partially dissolved ZB particles. In conclusion, X-ray micro-CT is an effective method for visualizing the spatial distribution of inorganics in solid wood and wood composites, but the intimate association of inorganics with the cell wall in solid wood, and the poor X-ray contrast between wood and polymers complicates the visualization of inorganics in wood and wood composites. Further research is required to address these issues.

Lay Summary

Inorganic materials such as silica are commonly found in timber and wood composites. In this thesis, I used X-ray micro-CT to visualize silica in wood, and zinc borate (ZB) in a wood-plastic-composite (WPC). Silica particles were associated with rays, and their distribution varied with ray-cell type and within annual rings. Inorganic elements were also found in vessels in some species and closely associated with cell walls. ZB particles mainly occurred as discrete entities in WPC. Iodine labeling of the WPC helped visualize and quantify components of the WPC, but it swelled wood, and partially dissolved ZB particles. In summary, X-ray micro-CT is capable of revealing new information about the microstructure of wood and wood composites, but better labeling techniques are needed (as in medical CT) to improve the X-ray contrast of the different components of wood composites.

Preface

This thesis represents original research conducted by Dengcheng Feng under the dedicated and helpful supervision of Professor Philip D. Evans. Parts of this thesis have been published in the listed referred papers below:

Parts of Chapter 3 have been published in Evans PD, Matsunaga H, **Feng D**, Turner M, Henley RW, Kewish CM (2021) Inorganic compounds in the marine borer resistant timber turpentine (*Syncarpia glomulifera*). Journal of Wood Chemistry and Technology 41(4), 185-197. doi: 10.1080/02773813.2021.1954952. I visualized X-ray micro-CT data of turpentine for this paper.

Some results in Chapter 3 have also been published in **Feng D**, Liu Y, Mazloomi MS, Limaye A, Turner M, Evans PD (2020) A virtual reality system to augment teaching of wood structure and protection. International Wood Products Journal 11(2), 46-56. doi: 10.1080/20426445.2020.1737773. I visualized the X-ray micro-CT data of satinay, made the CT data suitable for use by a virtual reality (VR) program, set up the VR system, and helped conduct a student survey.

A version of Chapter 4 has been published in **Feng D**, Turner M, Evans PD (2022) Sodium iodide as a contrast agent for X-ray micro-CT of a wood plastic composite. Applied Sciences 12(1), 208. doi: 10.3390/app12010208. I visualized the X-ray micro-CT data of a wood plastic composite (WPC), performed numerical analyses, and wrote the manuscript.

Table of Contents

List of Tables

List of Figures

Acknowledgements

I am extremely grateful to Professor Philip D. Evans for his mentoring and supervision throughout my graduate study. Thank you for your great patience and dedication to my research, writing, and presentations. Your professionality, passion, and attitude toward career and life has not only made me a better researcher, but also a better person too. Being a member of the Evans group is one of the most important decisions I made in my life, and I am absolutely proud to be one of your graduate students.

I also extend my gratitude to Dr. Chunping Dai and Dr. Gregory D. Smith for being on my supervisory committee. Thank you for your support throughout my graduate study.

This thesis project would not have been possible without the support of the Department of Applied Mathematics, Research School of Physics, The Australian National University (ANU). I am especially thankful to Dr. Michael Turner for X-ray micro-CT scans for my visualization work. I would also like to express my sincere gratitude to the ANU Supercomputer Facility for reconstructing X-ray micro-CT data sets, and Dr. Cameron M. Kewish and the Australian Synchrotron Facility for access to their X-ray fluorescence beamline.

I would like to express my gratitude to Dr. Ajay Limaye in the National Computational Infrastructure, ANU for his amazing work developing the tomographic data visualization software Drishti, and for his prompt replies to my requests for guidance on the visualization of X-ray micro-CT data sets. Thank you for your great generosity in making this incredible software open-source, and your enthusiasm in updating Drishti with latest computer technologies and maintaining the users' discussion group.

I thank the Canadian Wood Preservation Association (CWPA) for the award of the Robert W. Stephens Memorial Award and allowing me to freely participate in the 39th and 40th Annual Meeting of CWPA.

I thank the Faculty of Graduate and Postdoctoral Studies and the Faculty of Forestry at UBC for offering me the following awards: International Tuition Award, Faculty of Forestry Graduate Award, Donald S. McPhee Fellowship, and Mary and David Macaree Fellowship. I am grateful to Gayle Kosh, Robin Poirier-Vasic, and Julie Morey for their help throughout my graduate study.

I would like to thank every one of my colleagues in the Evans group for their friendship and assistance: Kenneth Cheng, Sina Heshmati, Joseph Kim, Lukie Leung, Sadegh Mazloomi, Farbod Moheb, Xuehua Wang (in alphabetical order).

I would like to express my warm gratitude to my parents Dr. Feng and Dr. Wang for being the best parents in the world. Thank you for the care, encouragement, emotional and financial support that helped me achieve milestone after milestone in my life, including this significant milestone of accomplishing my masters degree. You are also my greatest teachers that guide me during my academic career.

Special thanks to my wife Jialin Zhang for the endless love and support. You are the inspiration of my life.

Chapter 1: Introduction

1.1 Inorganic components of wood and wood composites

Inorganics in wood are mineral elements usually comprising less than 1% of the total weight of wood (Ivaska and Harju 1999). Despite their small quantities, inorganics are vital for the growth of trees since they are involved in the formation of tissues, enzymes, and buffer systems, and the regulation of osmotic pressure and membrane permeability (Kramer and Kozlowski 1979). Inorganics and other nutrients from the soil are dissolved in water and absorbed by the roots directly or via interactions with microorganisms (Morgan and Connolly 2013). Then, the mineral-rich solution is transported through the woody stem by the negative pressure caused by transpiration of water in leaves (McElrone et al. 2013). The solution travels longitudinally in the xylem (wood) along the conducting channels, which are vessels in hardwood or tracheids in softwood, and finally enters the leaves from the petioles (McElrone et al. 2013). The inorganics also move radially and tangentially in the trunk via the three-dimensional (3D) network of rays and axial parenchyma cells. Parenchyma cells store nutrients and minerals and act as interfaces between living cells and treachery elements (vessels or tracheids) (Kedrov 2012). Inorganic elements, particularly silica (Figure 1.1) can accelerate the wearing of cutting tools (Ching et al. 2011, Darmawan et al. 2011). Silica may also increase the resistance wood to teredinidae marine borers (Amos and Dadswell 1948). Inorganic elements in wood particularly crystals are important taxonomically for the identification of wood. For example, Eom et al. (2006) stated that crystals are the most important characteristics for identifying North American fir (*Abies* spp.) species.

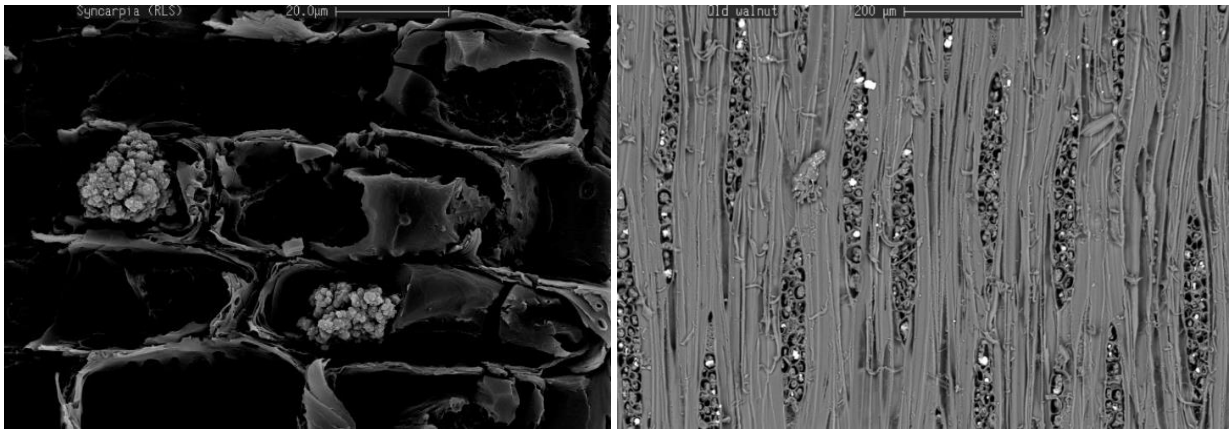

Figure 1.1 Scanning electron microscopy images of silica in wood. Left: a radial-longitudinal section of turpentine (*Syncarpia glomulifera* [Sm.] Nied.) showing silica aggregates in ray cells. Right: a tangential-longitudinal section of Walnut bean (*Endiandra palmerstonii* [F.M. Bailey] C.T. White & W.D. Francis) showing silica particles (white) in ray cells (photo, c/o Dr. Roger D. Heady)

Inorganics are also added to solid wood or wood products artificially to increase their durability. Lumber is commonly pressure-treated with dilute solutions containing metal salts or oxides in a pressure chamber which forces the solution into the wood (MacLean 1952). Following, evaporation of water the inorganic salts, oxides or their reaction products are deposited in the cell walls of wood or void spaces. Preservatives are also used to protect wood composites. For this application they can be mixed with adhesive (resin) or sprayed onto the wood composite when it is made (Gardner et al. 2003). Wood composites can also be pressure-treated with wood preservatives (Gardner et al. 2003). Preservatives can be completely inorganic such as chromated copper arsenate, or partially inorganic like alkaline copper quaternary (Rahman et al. 2004). Powdered zinc borate (ZB) is commonly added to oriented strand board, medium density fibreboard, and wood plastic composites (WPC) during their manufacture and acts as a fungicide, insecticide, and fire retardant (Sean et al. 1999, Tsunoda et al. 2002, Stark et al. 2010).

1.2 General hypothesis and objectives

The levels of inorganics in wood and wood composites are usually determined using spectroscopy or chromatographic methods (Ivaska and Harju 1999). The distribution of inorganic inclusions such as crystals, silica particles and preservative particles in wood and wood composites can be visualized using light or electron microscopy (Wheeler et al. 1989, Dong and Baas 1993, Evans et al. 2008). The inorganic elements in wood's cellular structures can be mapped in two-dimensions (2D) by combining electron microscopy with energy dispersive analysis of X-rays (Yata and Nishimoto 1983, Matsunaga et al. 2009, Evans et al. 2014). These approaches have a common limitation that they are limited to a 2D space. Thus, they are not good at revealing the distribution of inorganics in three dimensions (Evans et al. 2012), and particularly networks of inorganics formed by transpiration or fluid flow in the radial and longitudinal directions in wood via rays and tracheids or vessels, respectively. X-ray micro-computed tomography (micro-CT), which is based on X-ray absorption by materials with different density (Phelps et al. 1975, Elliott and Dover 1982), can overcome this limitation. Furthermore, inorganics in wood are usually denser than the wood cell wall. For example, the density of calcium oxalate crystal, silica, and zinc borate are 2.20 g/cm^3 (Deganello 1980), 2.20 g/cm^3 (Barsan 2007), and 3.64 g/cm^3 (Lewis 2007), respectively, which are all higher than that of wood cell wall (1.497-1.517 g/cm^3, Kellogg and Wangaard 1969). X-ray micro-CT has been successfully used for studying the spatial

distribution of inorganics in wood, such as silica (Koddenberg et al. 2019a) and copper (Feng et al. 2019) in solid wood, and zinc borate in wood composites (Evans et al. 2015).

I hypothesize that X-ray micro-CT will be able to visualize inorganic materials in 3D in silica rich Australian hardwoods and a wood plastic composite treated with zinc borate. The hardwood species analyzed were turpentine (*S. glomulifera*), satinay (*Syncarpia hillii* F.M. Bailey), brush box (*Lophostemon confertus* [R.Br.] Peter G.Wilson & J.T.Waterh.), walnut bean (*E. palmerstonii*), and also a non-siliceous species white beech (*Gmelina leichhardtii* [F. Muell.] Benth). The wood plastic composite I examined is a commercial product composed of wood particles, high-density polyethylene, air (voids), and zinc borate. I seek to produce images that show the 3D spatial distribution of inorganics in the silica-rich hardwoods thereby revealing new information about microstructure of siliceous species. Similarly, I image a WPC containing zinc borate and try to overcome limitations during X-ray imagining of WPCs resulting from the similarity in density of wood and plastic.

1.3 Outline of thesis

Chapter 1 provides background information on inorganic materials in solid wood and wood composites and briefly describes methods for detecting them. Chapter 1 also provides a general hypothesis for this thesis and its objectives. Chapter 2 reviews literature on X-ray imaging with a focus on the theory, instrumentation, and uses of X-ray micro-CT for imaging of solid wood and wood composites. Chapter 3 describes a qualitative study of the distribution of silica in silicious Australian wood species. Chapter 4 examines the distribution of zinc borate in a wood plastic composite and tries to overcome the problem of visualizing wood and plastic in a WPC. Chapter 5 discusses any novel findings and the extent to which results support my general hypothesis. Chapter 5 also suggests directions for future research, and draws general conclusions from the thesis.

Chapter 2: Literature Review

2.1 Introduction

Wood has been an important material for construction and furniture manufacture since the early stages of human history. But over the last two centuries it has been replaced in many end uses by metals, plastic, concrete, and composites. Recently, with increasing concern for the environment, wood is recapturing some of the markets it has lost. More people now recognize that wood is a naturally grown material which is both renewable and biodegradable. Wood is composed of various types of cells aggregated into complex macro- and microstructures. Wood components can also be bonded together to form engineered wood composites. These composites offer improved characteristics for some end uses. However, a greater understanding of the microstructures of wood composites would help to improve their performance and increase opportunities for wood as a structural and decorative material.

The microstructures of solid wood and wood composites are complex especially in three-dimensions (3D), where they present unique images in every viewing angle. For this reason, traditional two-dimensional (2D) microscopy methods, including both optical and electron microscopy, have limited ability to explore the microstructure of wood. For example, as pointed out by Evans et al. (2012), they are not good at visualizing the spatial distribution of inorganic preservatives in treated wood. Another relevant example is that 2D image analysis cannot accurately quantify the structure of wood-plastic composites (Bacaicoa et al. 2017).

In contrast to 2D microscopy, X-ray micro-computed tomography (CT) produces 3D images via a continuous series of cross-sectional images. The outcomes from X-ray micro-CT allow visualization through 3D rendered images, as well as quantitative analyses based on 3D geometries. Brodersen (2013) comprehensively reviewed the use of X-ray micro-CT for the study of the anatomical characteristics of solid wood. Jacquin et al. (2017) briefly reviewed its use as a tool for profiling density in wood, and Jakes et al. (2018) in their review mentioned the use of X-ray micro-CT to examine adhesive penetration in wood composites. Up to now, there has been no comprehensive review that covers the use of X-ray micro-CT for visualization and quantification of both solid wood and wood composites. X-ray CT requires significant graphical power from a computer workstation, but fortunately, rapid developments in personal computer (PC) technology in recent years has ameliorated this limitation. For example, the processing power of the top-tier PC graphic cards now is more than seven times (from 5 teraflops to

35.7 teraflops) that of cards available in 2013 (Véstias and Neto 2014, Kondo et al. 2021). Thanks in part to this improvement, CT analysis has become more accessible to researchers in recent years. In this chapter, I comprehensively review the literature on visualization and quantification of the microstructure of solid wood and wood composite using X-ray imaging technology. I also cover other wood-related X-ray micro-CT studies including those in archaeology and dendrochronology.

2.2 Historical information on X-ray analysis of wood

2.2.1 X-ray densitometry

Density is positively related to X-ray attenuation, i.e. denser material absorbs more X-rays (Phelps et al. 1975). Hence, X-ray instruments are the tool of choice for wood density measurements (Jacquin et al. 2017). The earliest use of X-rays to measure the density of wood dates back to the 1960's. The early use of radiation such as X-rays and gamma rays to measure wood density was reviewed by Polge (1978). His review describes the two stages involved in measuring density; data collected (density ranges, maximum and minimum density, latewood and earlywood widths, etc.); acquisition systems and instruments; and applications of radiation densitometry (Table 2.1). Polge (1966, 1970) measured wood density based on microdensitometry of images from X-ray radiographic films using a device similar to that in Figure 2.1. The steps involved in using this device to obtain wood density can be found in Appendix 7. Cown and Clement (1983) described an X-ray densitometer in which the X-ray detector was directly connected to a computer, thus eliminating the step involving photographic film. A schematic diagram of typical wood densitometers is shown in Figure 2.2. A cone-beam densitometer has magnification effects, but induces blurs. In contrast, a parallel beam densitometer has no blurring effect, but the field of view is smaller (Jacquin et al. 2017). Jacquin et al. (2017) reviewed the existing wood densitometers based on X-ray films, as well as the newer generation of X-ray wood densitometers, including the Itrax scanner which combines X-ray microdensitometry with X-ray fluorescence analysis; the QTRS scanner which can output density profiles as well as coloured images; and the SilviScan system which integrates X-ray densitometry, X-ray diffraction, and optical microscopy. They also mentioned X-ray macro and micro-CT scanners for wood densitometry. The newer generation of X-ray densitometers have extended the reach of X-ray densitometry for wood to include new areas as shown in Table 2.2.

Table 2.1 Applications of radiation densitometry for wood (Polge 1978)

Type	Area of application	Scope of study	References
Direct utilization of density	Wood anatomy and physiology	Cell wall thickness	Diaz Val Olmedo (1974), Harris (1969)
		Ray parenchyma	Keller and Thiercelin (1975)
		Localization of water; delimitation of heartwood and dry sapwood	Polge (1964)
		Localization of resin	Harris (1969), Polge (1966)
		Localization of lignan	Parker et al. (1974)
	Wood physical properties	Wood shrinkage, collapse, reconditioning	Polge (1966)
Density as dependent variable	Tree biology	Heredity	Nicholls and Brown (1971), Thoby (1975), Keller (1973), Nepveu (1973)
		Fertilization	McKinnel and Rudman (1973), Megraw and Nearn (1972), Nicholls (1971b), Polge (1969), Rudman and McKinnell (1970)
		Growth rate	Echols (1972), Nicholls (1971b), Sutton and Harris (1974), Polge and Keller (1973)
		Entomological defoliation	Polge and Garros (1971)
		Irrigation	Nicholls (1971a), Polge and Keller (1968)
		Effect of industrial smoke and green pruning	Polge and Keller (1969) Polge et al. (1973)
		Phenology	Polge (1968), Thiercelin (1970)
	Climate factors	Dendrochronology and dendroclimatology	Polge (1966), Bazerque (1974), Keller and Millier (1970), McNeely et al. (1973), Polge (1970), Polge (1971), Rothlisberger (1976)
Density as explanatory variable	Wood mechanical strength	Non-destructive prediction of mechanical properties	Keller (1968, 1971), Polge (1966)
		Windbreaks in living trees	Anonymous cited in Polge (1978)
	Wood machining	Methodology for testing sawtooth performance	Anonymous cited in Polge (1978)

Table 2.2 Newer areas of the application of X-ray densitometry for wood

Category	Sub-category	Area	References
Wood features	Juvenile and mature wood	X-ray densitometry to help calibrate near infrared imaging;	Ruano et al. (2019)
		Mapping of specific gravity	Eberhardt et al. (2019)
		Microfibril angle and fibre length and density as properly indicators	Rahayu et al. (2014)
		Growth ring boundaries	Alteyrac et al. (2006)
		Transition from juvenile to mature wood	Clark et al. (2006a), Gapare et al. (2006), Koubaa et al. (2005), Sauter et al. (1999)
		Patterns of density profile	Abdel-Gadir and Krahmer (1993a)
		Density in transition zones	Abdel-Gadir and Krahmer (1993b)
	Tracheids	Correlation between density and tracheid length	Klisz (2011)
	Knots in wood	Density of knots compared to stem wood	Caceres et al. (2018)
	Extractives	Radial variation of extractives mapped using X-ray densitometry	Helama et al. (2010)
		Effect of hot water extraction on density	Grabner et al. (2005)
Wood modification	Resin impregnation	Melamine formaldehyde impregnation and wood density	Lykidis et al. (2020)
		Thermoset resin distribution in wood	Klüppel and Mai (2013)
		Phenol resin distribution	Wu et al. (2003)

Table 2.2 Continued

Category	Sub-category	Area	References
Wood protection	Biodeterioration of wood	Barrier zones in decayed wood	Satini et al. (2019)
		Mass and strength losses	Maeda et al. (2015)
		Density decreases during decay	Bucur et al. (1997), Bouslimi et al. (2014), Brazolin et al. (2014)
	Preservative treatment of wood	Chromated copper arsenate treatment and wood density	Chagas et al. (2015)
	Oil impregnation	Distribution of linseed oil	Olsson et al. (2001)
Wood products	Oriented strand board	Density and composite properties	Surdi et al. (2014), Grandmont et al. (2010)
		Specific gravity and a decay model	Kent et al. (2006)
	Medium density fibreboard	Maximum, minimum, and mean densities	Belini et al. (2009)
	Particleboard	Correlation between X-ray density and gravimetry density	Tinti et al. (2018), Gonçalves et al. (2018)
	Sustainable biomass to replace wood for particleboards	Density measurements	Fiorelli et al. (2019)
	Adhesive bondlines in laminated wood	Effect of electrostatic field treatment on density at bonding interface	He et al. (2018)
	Densified wood composites	Vertical density profile	Rautkari et al. (2011)
	Wood pellets	Density variation	Gaitán-Alvarez et al. (2017)
Tree growth	Soil frost	Effect of frost on density	Jyske et al. (2012)
	Vegetation management	Effect of vegetation management on yield and wood properties	Aernouts et al. (2018), Clark et al. (2006b)
	Drought	Wood density and drought	George et al. (2015), Jyske et al. (2010), Wilkinson et al. (2015)
Fossilized wood	Subfossils of wood	Effect of cold rinsing on density	Kłusek et al. (2016)
		Variation in tree ring density over time	Helama et al. (2008)

Figure 2.1 A Joyce-Loebl micro-densitometer (autodensidater) at The Australian National University Department of Forestry used to measure the optical density of X-ray negatives of wood cores (photo, c/o Dr. Philip D. Evans)

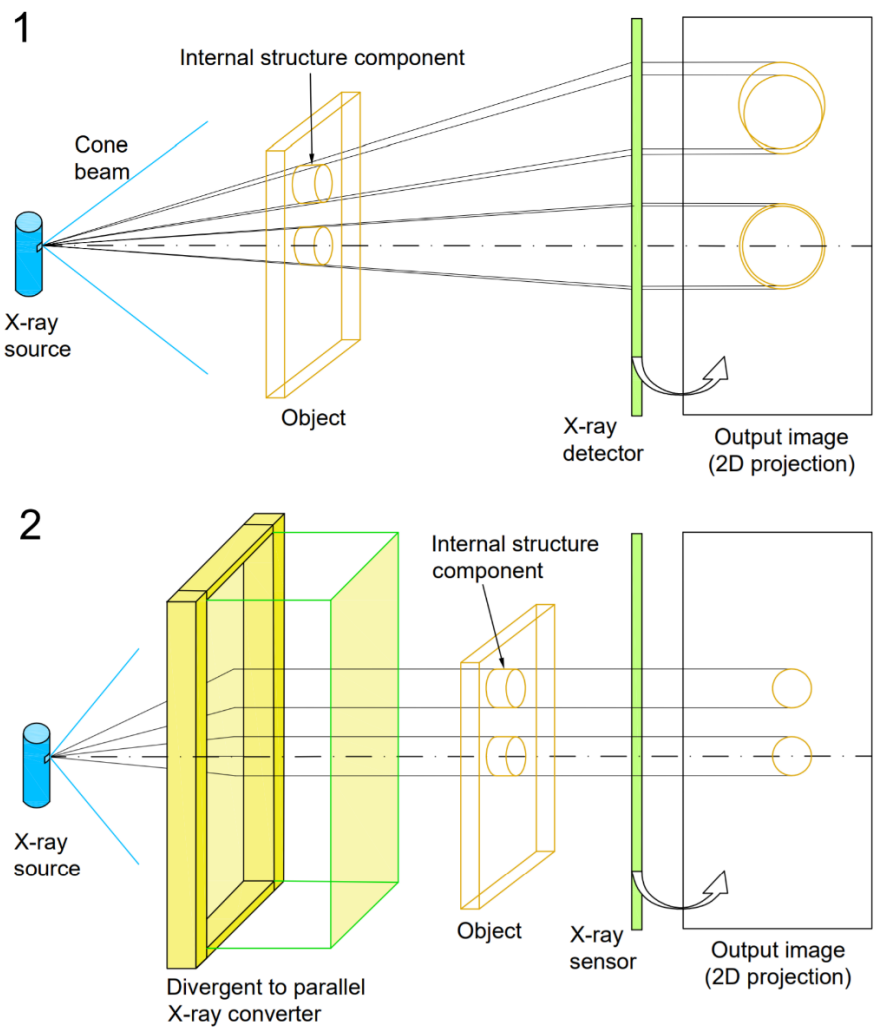

Figure 2.2 Schematic diagram of (1) a cone-beam densitometer and (2) a parallel beam densitometer (redrawn from Jacquin et al. 2017)

X-ray densitometry is a widely used non-destructive technique, but it does not easily lend itself to the study of the spatial distribution of density in wood, unlike X-ray CT. X-ray CT devices, like densitometers, are based on X-ray attenuation. Similarly, X-ray CT devices can profile density because the attenuation values from CT images can be transformed into physical density (Mull 1984). X-ray CT can also measure the density of small and large wood samples (Van den Bulcke et al. 2014). Another advantage is that the sample preparation for X-ray CT is easier than that involved in X-ray densitometry (Van den Bulcke et al. 2019). X-ray macro CT was used to measure the density of wood long before the wide-spread use of X-ray micro-CT. The macro scanners used for this purpose were usually medical CT

scanners (Mull 1984, Lindgren 1991a, Lindgren et al. 1992, Sugimori and Lam 1999). Another type of "macro" scanner was a portable device that could be used to measure the density of standing trees (Kim et al. 2014). In addition, X-ray CT log scanners can be used for densitometry of wood with large cross-sections (Giudiceandrea et al. 2011). X-ray micro-CT scanners are also able to profile wood density. Their applications will be discussed below.

2.2.2 X-ray detection of voids, moisture and foreign objects in wood using radiographical methods

2.2.2.1 X-ray detection of voids and cracks

Voids in wood are easy to detect in X-ray images because the densities of wood and air are very different. Thus, there is a large difference in X-ray attenuation and a high contrast between wood and voids in X-ray images. Wood scientists have long been interested in detecting voids and cracks in wood, and those present in manufactured wood products. A great variety of methods and machines have been used to detect voids and cracks in wood. This section focusses on radiography rather than medical (macro) CT or X-ray micro-CT.

X-ray radiography has been used to investigate voids in wood caused by wood-boring insects, particularly the larvae of house longhorn beetle (*Hylotrupes bajulus* L.). X-ray radiography detection of voids caused by insects was pioneered by Jacquiot (1961) who examined voids in wooden blocks caused by house longhorn beetle as well as the brown powderpost beetle (*Lyctus brunneus* Stephens). He found that X-ray radiography could visualize and detect voids non-destructively without harming the insects. Similarly, Schmidt (1962) used X-ray radiography to examine voids in wood caused by the house longhorn beetle. He found that wood samples thinner than 5 cm could yield photos with ideal clarity while those thinner than 10 cm and thicker than 5 cm could still produce acceptable photos. Baker (1965) developed a regression model to estimate the weight of the common furniture beetle (*Anobium punctatum* De Geer) based on X-ray radiography. Yates (1968) used X-ray radiography to detect house longhorn beetle in I-joists in houses. Jacquiot and Serment (1971) used X-ray radiography to examine the effect of preservative treatment on brown powderpost beetle larvae. They found that the penetration depth of larvae was not related to the mortality rate of larvae. In addition, most larvae

penetrated beyond the outer impregnated zone of the samples. Kerner et al. (1980) used an X-ray technique to detect the larvae of brown powderpost beetle and common household beetle in wood. Their method was 100% accurate in detecting the larvae and always effective at evaluating their mortality rate. In a more recent study, Krajewski et al. (2012) used X-ray radiography to validate their electro-acoustic method for the detection of house longhorn beetle in wood. They found that the electro-acoustic method was 70-80% accurate. Nowakowska et al. (2017) used X-ray radiography to examine the relationship between the weight and length of house longhorn beetle larvae in wood. They found that X-ray densitometry was not always accurate at measuring the length of larvae. Despite this, they managed to develop a regression model to estimate the weight of larvae based on their length. X-ray densitometry has become a standard method for evaluating the effect of preservatives against larvae of house longhorn beetle (British Standards Institution 2016).

Another example of the use of X-ray radiography to detect voids in wood are those created by marine borers. Oliver (1959) was the first to use X-ray radiography to detect shipworms (*Teredo* spp.) in wood. Fougerousse and Gueneau (1971) used X-ray radiography to evaluate the shipworm resistance of various wood species by quantifying the length of tunnels and their density. Tsunoda and Nishimoto (1978) measured the length of shipworms in wood blocks using X-ray radiography and found that the optimal temperature for the growth of shipworms was 15-25 °C. Junqueira et al. (1991) used X-ray radiography to examine the effect of a baiting method on the activity of shipworms (Figure 2.3). They found that X-ray radiography could estimate the density of tunnels, but it could not identify the shipworm species while the other method could. Edwin and Pillai (2004) studied the shipworm resistance of rubber wood (*Hevea brasiliensis* Müll.Arg.) treated with various preservatives. The X-ray radiography images indicated that the preservatives were effective because treated samples showed no internal damage. Appelqvist et al. (2015) used X-ray radiography to investigate the activity of shipworms in wood in the sea at sites along the Swedish coast. They found shipworm activity did not vary at the different sites.

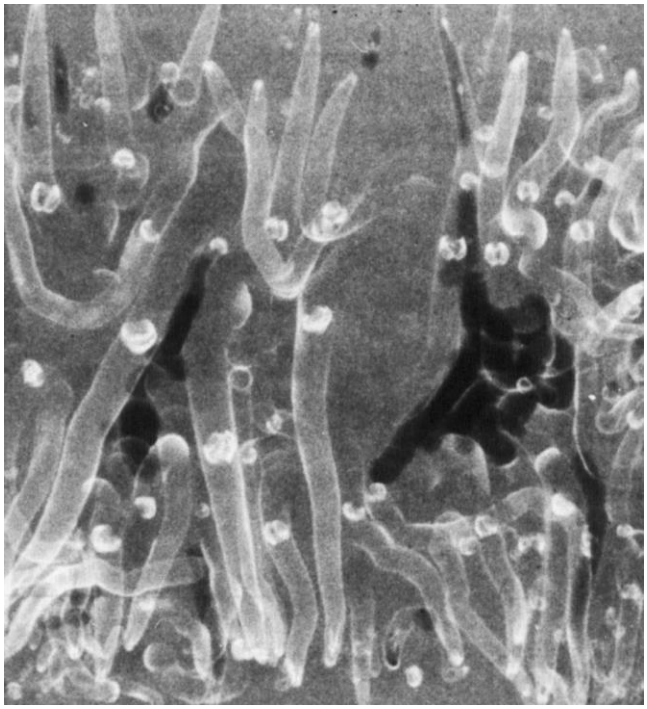

Figure 2.3 X-ray radiography image showing shipworms and their tunnels in wood (Junqueira et al. 1991, adapted with publisher's permission)

X-ray radiographic imaging has also been used to examine cracks in large timber structures. Jerzy et al. (2013) used X-ray radiography to detect cracks in historical wooden buildings. Kasal and Blass (2013) used a similar method to investigate crack development in a building arch made from glue laminated wood.

2.2.2.2 X-ray detection of foreign objects

X-ray radiography has been used to detect foreign objects such as bullets and shell fragments in wood. Koene and Broekhuis (2017) studied bullet penetration in seven different wood species. They used X-ray radiography to measure projectile penetration depth and found that the penetration could be described using the Robins-Euler and the Poncelet models. They also found that knots in wood affected penetration depth. Koene and Broekhuis (2019) subsequently used X-ray radiography to study the penetration of bullets into medium density fibreboard (MDF) targets. They found that the Poncelet model was better than the Robins-Euler model at describing bullet penetration in MDF.

2.2.2.3 X-ray detection of moisture

The detection of moisture in wood using X-rays uses the same principle as X-ray densitometry, by establishing a relationship between density and X-ray attenuation. The densities of an area of wood in its native state and its oven-dried state can be predicted by measuring its X-ray attenuation. Then, the density of moisture in the area can be calculated by subtracting the oven-dried wood density from the native density. The moisture content (MC) in the area is expressed as the ratio of the moisture density versus the oven-dried density in percentage terms (Watanabe et al. 2012). MC in a cross-section can be mapped if several areas in the section are selected. Caution should be exercised when using this method because wood shrinks when it dries, and this causes misalignments of X-ray images. The shrinkage value can be determined by comparing the number of pixels in the pre- and post-drying X-ray images. MC can then be adjusted based on the shrinkage value (Hattori and Kanagawa 1985, cited in Watanabe et al. 2012).

X-ray densitometry has also been used to examine moisture distribution in wood. For example, Yamamoto et al. (1983) used a soft X-ray densitometer to study water uptake by Hinoki (*Chamaecyparis obtusa* [Siebold & Zucc.] Endl.) wood. They found that moisture penetration was related to the anatomical characteristics of Hinoki. Sano et al. (1995) used X-ray images to visualize moisture distribution in wet-wood formed in Mongolian oak (*Quercus mongolica* Fisch. ex Turcz. var. *grosseserrata* [Bl.] Rehd. et Wils.), but they used a gravimetric method rather than the aformentioned X-ray method to determine MC. Liu et al. (1996) used an X-ray densitometer to map the MC distribution in growth rings in air-dried wood. They further improved their method by establishing an interpolation algorithm which accounted for shrinkage caused by drying (Liu et al. 1998). Nakada et al. (1999) and Nakada (2006) studied water distribution in conifers. They used X-ray photography to visualize water within the stem of Japanese cedar (*Cryptomeria japonica* D. Don) (Nakada et al. 1999) and 15 other coniferous species (Nakada 2006), but they did not use an X-ray method to quantify MC. Watanabe et al. (2008) used an X-ray microscope to measure the MC distribution in Japanese cedar wood during drying. They divided the X-ray images into multiple subsampling zones and studied the MC within each zone. Tanaka et al. (2009) also studied MC distribution in Japanese cedar using the same apparatus as Watanabe et al. (2008) but took a different approach: they did not subsample the images, instead they used a moving stage to image individual small zones in the sample, and then proceeded to the adjacent zone. Skuratov et al. (2015) determined the diffusion coefficients of wood during drying. The use of X-

ray densitometry to determine MC of wood is gradually declining and is being replaced by CT methods, which will be described below. Nevertheless, X-ray densitometry was recently used to examine MC and surface checking of wood (Tomoko et al. 2019).

In addition to densitometry, X-ray density profile analysis, which is commonly used to determine the vertical density profile of wood panels, has been used to examine moisture distribution in wood. This method is very similar to X-ray densitometry, but it is a one-dimensional method. Yu et al. (2012, 2013, 2014) and Hao et al. (2014) used X-ray density profile analysis to examine the moisture profile of Chinese fir (*Cunninghamia lanceolata* [Lamb.] Hook.). They found that their results accorded with those acquired from gravimetric measurement of density (Yu et al. 2012, 2013). They also developed a mathematical model for predicting the MC in wood (Yu et al. 2014). Hao et al. (2014) developed a calculation method for processing the results from X-ray density profile analysis. They compared their method with that developed by Cai (2008). They concluded that their method was equally as accurate as Cai's (2008) when the MC was below the fibre saturation point (FSP) and was more accurate at moisture contents above FSP.

2.2.3 Macroscale computed tomography of wood

2.2.3.1 Macro-CT for density measurements of wood

Images from X-ray CT devices are also based on X-ray attenuation like those from a densitometer. The unit of attenuation in CT images is called the CT number or Hounsfield unit. An X-ray CT device can profile density because the attenuation values from CT images can be transformed into physical density (Mull 1984). X-ray CT devices can measure the density of small and large wood samples. They have other advantages over X-ray radiography. For example, 3D densitometry of wood is possible (Van den Bulcke et al. 2014), unlike radiographical methods. Another advantage is that sample preparation for X-ray CT is easier than that involved in densitometry (Van den Bulcke et al. 2019 and see Appendix 7). X-ray CT is also a non-destructive method of measuring wood density (Lindgren 1991b).

Benson-Cooper et al. (1982) were the first to apply CT densitometry to wood. They used a medical CT device to measure the stem characteristics and density of greenwood from five different wood species, and developed a correlation between wood density and intensity for their CT images.

Mull (1984) used a medical CT scanner to estimate density and mass of wood blocks and compared his results with those acquired by gravimetric methods. However, the aim of his study was to calibrate the scanner for estimating mass of human organs, rather than to use it to estimate wood density. Lindgren (1985) tried to correlate X-ray attenuation values in CT images with wood density. Subsequently, he described the use of medical CT scanners to measure wood density and estimated their accuracy experimentally using wooden test samples (Lindgren 1991a, 1991b). Macedo et al. (2002) compared wood density values obtained using three different CT devices: a portable CT scanner, a millimetric CT scanner, and a micro-CT scanner. They found that density values obtained from CT devices were strongly correlated with those obtained from gravimetric methods. Espinoza et al. (2005) found a linear relationship between density and grayscale CT values of sugar maple (*Acer saccarum* Marsh) obtained using a medical CT device. Henze (2006) studied within-stem density variation in western hemlock (*Tsuga heterophylla* [Raf.] Sarg.) using X-ray CT. She found that the dense wood in stems were disconnected longitudinally and radially forming discrete areas, while the juvenile wood was more homogenous in the core of the stems. Taylor (2006) used a medical CT scanner to measure density in Sitka spruce (*Picea sitchensis* [Bong.] Carr.) and compared his results with those acquired gravimetrically or using a Pilodyn pin penetration device. He concluded that CT was more accurate because its results were more similar to gravimetric density than those obtained using the Pilodyn device. Freyburger et al. (2009) used a medical CT scanner to measure wood density across a wide density range. They found a very strong linear relationship between density and Hounsfield unit: the coefficient of the regression (R^2) was greater than 0.999. Similarly, He and Qi (2013) also found a strong linear correlation ($R^2 > 0.94$) between density and CT number. Steffenrem et al. (2014) used medical CT to measure density in increment cores from Norway spruce (*Picea abies* [L.] H. Karst.). They found their device had limited resolution when scanning cores that had diameters smaller than 5 mm, but this limitation could be circumvented by scanning a large number of samples at low resolution and then sub-sampling and re-scanning them at higher resolution. Jacquin et al. (2019) developed a computer program for quick measurement of density on wooden increment cores scanned using a CT device. Their program was accurate when the diameter of the cores was 5 mm, but its accuracy declined when the core diameter was 4 mm. Wang et al. (2019) developed models for estimating density and MC obtained using a medical CT scanner, and obtained R^2 values higher than 95% for all their models. In later related research they obtained R^2 values of greater than 97% (Wang et al. 2020).

CT has also been used to measure the density of a variety of wood products and also to assess changes in wood density due to biodeterioration within trees. Blomberg and Persson (2005) used a medical CT device to compare the density of Scots pine (*Pinus sylvestris* L.) boards before and after they were compressed. They found that heartwood, highly resinous wood, and wood that had high initial density were less easily compressed. Hervé et al. (2014) used a medical CT device to track the density changes in a piece of European beech (*Fagus sylvatica* L.) wood colonized by a white-rot fungus. They found that low density earlywood was more prone to fungal decay than latewood. Salim et al. (2014) used a medical CT device to measure the variation in density within Algerian oak (*Quercus canariensis* Willd.) and Afares oak (*Quercus afares* Pomel) trees. They found that there was a stronger correlation between density and distance from the pith in Afares oak compared to Algerian oak. More recently, Morgado-González et al. (2019) used a medical CT scanner to examine the relationship between altitude, orientation of sunlight exposure, and the density of Hartweg's pine (*Pinus hartwegii* Lind.). They found that wood density was affected by altitude when the trees had sunlight exposure in northwest orientation, but this was not the case for trees oriented to the southwest.

2.2.3.2 Macro-CT to detect water in wood

The approach to detecting moisture in wood using X-ray CT is the same as that described above for radiography. X-ray CT has a number of advantages for the determination of MC compared to radiography, including ease and non-destructive nature of sample preparation, and ability to obtain information on spatial distribution of MC. Hattori and Kanagawa (1985) were the first to use CT to examine wood MC. Subsequently, Kanagawa et al. (1992) published the first paper in English on the use of CT to measure the MC of wood during drying. Wilberg (1995) conducted a similar study, but he did not specify the type of CT scanner used to detect water in wood. Fromm et al. (2001) used a medical CT device to examine the distribution of water in Norway spruce and European oak (*Quercus robur* L.). They found a large difference in MC between latewood and earlywood in both species. They also found similar MC's in growth rings in oak sapwood. Eriksson et al. (2006) calculated the diffusion coefficients in wood drying using data from a medical CT scanner. Their results were in accord with those from previous studies, and measurement errors had little effect on their results. Alkan et al. (2007) used an industrial CT scanner to investigate wet-wood in subalpine fir (*Abies lasiocarpa* [Hook.] Nutt.). They found that the wet-wood dried much more slower than normal wood. Watanabe et al. (2012) used an industrial CT scanner to map MC in wood during drying, as an alternative to the X-ray microscope they

used previously (Watanabe et al. 2008). Their CT method was accurate when MC was between 19.2% and 47.3%. Hansson and Fjellner (2013) found that CT images could be used to calculate dry weight MC and shrinkage coefficient of wood. Li et al. (2013b) used a CT scanner to measure MC in wood. They compared their CT results with those obtained gravimetrically, and found that the results were similar. Osborne et al. (2016) developed a model for predicting MC in Douglas fir (*Pseudotsuga menziesii* [Mirbel] Franco) with an R^2 higher than 96% using data from a medical CT device. Li et al. (2018a) used a medical CT device to investigate the relationship between moisture and stress formation in a hexagonal glulam beam. They found that MC at the edges of the beam was lower than in other areas, which led to formation of stress and surface cracking. Couceiro et al. (2019) hypothesized that a dual-energy CT device could measure MC in real-time, but their results did not support their hypothesis. More recently, Wang et al. (2020) used a medical CT device to develop a linear model for predicting MC in *Populus xiangchengensis* C. Wang et Tung and moso bamboo (*Phyllostachys edulis* [Carrière] J.Houz). They found their model could accurately predict the MC of both wood and bamboo.

CT scanners can be modified into an "in-situ" device to track MC changes during drying without having to move samples. Couceiro and Elustondo (2015) and Couceiro et al. (2020) modified a medical CT scanner by placing a mini drying chamber in the gantry of the scanner. They concluded that the conditioning time for wood samples with a MC lower than 8% should be less than three hours, while samples with a MC higher than 18% required longer conditioning times. Scheepers et al. (2007) stated that they could capture changes in density of radiata pine (*Pinus radiata* D. Don) during drying. They also found that the loss of MC in the core and the decrease in cross-sectional area fluctuated when the MC was at 100%.

Medical and industrial CT devices are commonly used to examine moisture in wood, rather than micro-CT instruments. This preference is mainly because the sizes of samples for MC-related studies are usually too large to be accommodated within a micro-CT device. Another reason is that fast scanning times are needed to minimize moisture loss and movement during scanning. Here medical and industrial scanners have an advantage over micro-CT scanners. There are, however, some exceptions. For example, Li et al. (2018b) used an X-ray micro-CT device to study MC in plywood, oriented strand board (OSB), and medium density fibreboard (MDF). They reduced the scanning time to less than 2 minutes and concluded that their device was capable of studying moisture distribution in wood composites.

2.2.3.3 Macro-CT of voids and cracks in wood

Medical CT has also been used to scan larger composite samples. Sugimori and Lam (1999) used it to examine the distribution of macrovoids in parallel strand lumber (PSL) and created a database on the distribution of the microvoids. They concluded that their database could help people who were not familiar with image processing techniques to better understand CT data. Sackey and Smith (2010) used a similar device to characterize macrovoids in the core of particleboards and unpressed particleboard mats. They found that an increase in the content of fine particles in the core of particleboard and mats decreased the volume of macrovoids. Conversely, an increase in coarse particle content increased the volume of macrovoids in mats. Li et al. (2018a), as mentioned in section 2.2.3.2, scanned a large cross-sectional hexagonal glulam beam. They found that drying cracks were mostly located at the edges of the beam. Vaziri et al. (2012, 2020) studied crack formation in timber welded by linear friction. They determined the optimal setting for welding which minimized subsequent cracking of joined wood samples (Vaziri et al. 2012). They found that the formation of cracks was slower and water resistance was higher in samples with a wollastonite additive than in controls (Vaziri et al. 2020). They also used micro-CT to visualize the distribution of wollastonite in microcracks (Vaziri et al. 2020). Other than medical CT scanners, lab-based macro-CT scanners have also been used to study voids and cracks in wood. For example, Li et al. (2013a, 2016a) used CT data acquired from a lab-based CT device to perform fractal dimension analyses of voids in oriented strand boards. Ge et al. (2018) and Qi et al. (2018) used a custom-built CT scanner to look for macrocracks and other gross anatomical features in laminated lumber and tree trunks.

2.2.3.4 Macro-CT of features in logs

There are many features in logs that can degrade the value of sawn lumber, such as knots, pith, decay, etc. X-ray CT scanning is able to detect such features non-destructively and provide guidance for decision making during sawing (and optimize the value of sawn-products). Research in this area was pioneered by Benson-Cooper et al. (1982) who used CT to detect rot, defective core, insect attack, resin pockets, and bark in logs. Hailey and Morris (1987) scanned wood segments using a medical CT device and detected decay, knots, moisture pockets, compression wood, juvenile wood, wetwood, and boundaries of heartwood and sapwood in the segments. Marčok et al. (1996) used a medical CT scanner to look for reaction wood in logs. They found that reaction wood was more easily detected when MC was above fibre saturation point. Schad et al. (1996) compared X-ray CT with sound wave transmission

and impulse radar as means of detecting defects in logs. They found that X-ray CT had the best resolution for detecting knots, voids, and high MC areas, but it could not detect small areas of decay. Oja (1997) compared X-ray CT with two destructive methods for measuring size and position of knots in Norway spruce. He found that CT was a faster method with acceptable precision, and its non-destructive nature was another benefit. However, his device encountered difficulties in detecting small knots, which are abundant in Norway spruce. Guddanti and Chang (1998) scanned logs using an industrial X-ray CT scanner. They simulated the sawing of the logs based on CT data and compared the simulation results with results from real sawing of the same logs. They found that the estimated value of the simulated sawn lumber was 97% of that for actual sawn lumber. Grundberg and Grönlund (1997), Oja et al. (1998, 2000, 2001), Sepúlveda et al. (2002), and Nordmark and Oja (2004) conducted a series of studies involving X-ray CT scanning of logs. Seger and Danielsson (2003) also conducted a similar study. However, their studies were focused on using X-ray CT data for simulation of a 2D X-ray radiographical scanner, rather than simply using X-ray CT data to detect features in logs. An X-ray CT log scanner was commercialized by Giudiceandrea et al. (2011). This development led to the award of the 2016 Marcus Wallenberg Prize (the “Nobel Prize” for wood research) to Giudiceandrea and Alexander Katsevich for their contribution to the sawmill industry. Their CT device employed helical trajectory and fan beam which ensured higher scanning speed without significant loss of image quality compared to cone-beam CT. The literature on CT scanning of log features in the past two decades is summarized in Table 2.3.

Table 2.3 Progresses in the use of X-ray CT for detecting features in logs

Reference	Goal of study	Features studied	Device used	Species	Yield increased
Aguilera et al. (2002)	3D visualization of features	Knots	Medical CT scanner	Radiata pine	
Rinnhofer et al. (2003)	Sawing optimization	Knots	Airport CT scanner	Spruce, larch (*Larix* sp.)	
Espinoza et al. (2005)	CT image intensity of features	Knots, heartwood, sapwood, decay	Medical CT scanner	Sugar maple	
Yu and Qi (2008, 2011)	Image recognition of features	Decay (2008, 2011), knots (2011)	Unspecified	Unspecified (2008), Manchurian ash (*Fraxinus mandshurica* Rupr.) (2011)	
Chang and Gazo (2009)	Sawing optimization	Internal defects (unspecified)	Medical CT scanner	Black cherry (*Prunus serotine* Ehrh.), sugar maple, tulipwood (*Liriodendron tulipifera* L.), red oak (*Quercus rubra* L.), white oak (*Quercus alba* L.)	46%
Espinoza and Iribarren (2009)	Image recognition of features	Defective core	Medical CT scanner	Radiata pine	
Giudiceandrea et al. (2011)	Commercialization of log scanner		Industrial CT scanner	Radiata pine	
Boukadida et al. (2012)	Algorithm for detection of features	Pith	Medical CT scanner	Total 17 species (see Boukadida et al. 2012)	
Espinoza and Iribarren (2012)	Algorithm for detection of features	Knotty core	Medical CT scanner	Radiata pine	
Breinig et al. (2013)	Effect of errors in sawing	Knots	Industrial CT scanner	Norway spruce	
Fredriksson et al. (2014)	2D projection of knots	Knots	Medical CT scanner	Scots pine	2.2%
Stängle et al. (2015)	Sawing optimization	Knots	Industrial CT scanner	European beech	Up to 24%
Stängle et al. (2016)	Bark thickness prediction	Bark	Industrial CT scanner	Norway spruce	
Fredriksson (2016)	Sawing optimization	Knots	Industrial CT scanner	Norway spruce, Scots pine	4-11%
Rais et al. (2017)	Sawing optimization	Knots	Industrial CT scanner	Douglas fir	4-20%
Fredriksson et al. (2017)	Algorithm for detection of features	Knots, heartwood-sapwood border	Medical CT scanner	White spruce (*Picea glauca* (Moench) Voss), Jack pine (*Pinus banksiana* Lamb.)	
Belley et al. (2019)	Sawing optimization	Knots	Medical CT scanner	White spruce [1], Jack pine [2]	23% [1], 15% [2]
Brüchert et al. (2019)	Visual inspection of features, algorithm for detection of features	Knots, pith, heartwood, crack	Industrial CT scanner	Teak (*Tectona grandis* L. f.)	
Longo et al. (2019)	Algorithm for detection of features	Knots	Industrial CT scanner	Douglas fir	
Fredriksson et al. (2019)	Algorithm for detection of features	Knots	Lab-built CT scanner	Western redcedar (*Thuja plicata* Donn ex D. Don), white spruce, Douglas fir	

2.3 X-ray micro-computed tomography: principles and instrumentation

2.3.1 Principles of X-ray micro-CT

The principle of a micro-CT scanner is the same as that of the first clinical CT scanner invented by Hounsfield (1973). Like X-ray radiography, the general principle of X-ray CT involves the attenuation of X-rays, but CT acquires a series of X-ray images around the scanned object, rather than the single image obtained for X-ray radiography. Hounsfield (1973) placed an X-ray tube and two detectors at opposite positions on a rotating gantry (Figure 2.4). The X-ray tube and the detectors had synchronized movements on the gantry. The scanner finished scanning one position after the X-ray tube and detectors moved from their starting points to the endpoints. Then, the gantry moved to the next position by rotating one degree (1°), and the X-ray tube and detectors repeated their movements. When the gantry had rotated 180°, each detector gathered the necessary projection data to reconstruct an image of a slice. Scanning the other 180° was unnecessary because the scanned object (patient) was "transparent" to X-rays, so the scanner would only produce the same projection data as the first 180°. Because there were two detectors in Hounsfield's scanner, the scan of two slices was done simultaneously after a 180° rotation of the gantry. Then, the patient moved along the rotation axis of the gantry for scanning the next two slices. Reconstruction and analysis of CT data then occurred, which will be covered in the Section 2.4.

Using the same principle, Elliott and Dover (1982) invented the first X-ray micro-CT scanner. The X-ray source and the detector in their CT scanner were fixed. Elliott and Dover (1982) used a different approach to Hounsfield (1973): they rotated their specimen rather than the X-ray source. They loaded their specimen on a spur gear which was manually turned 3⅓ degrees after each scan. As its name suggests, X-ray micro-CT scanners, in contrast to conventional X-ray CT scanners, are capable of obtaining microscopic detail. The resolution of Elliott and Dover's scanner was 15 μm, which was much higher than the 2 mm resolution of medical CT scanners at that time (Elliott and Dover 1982).

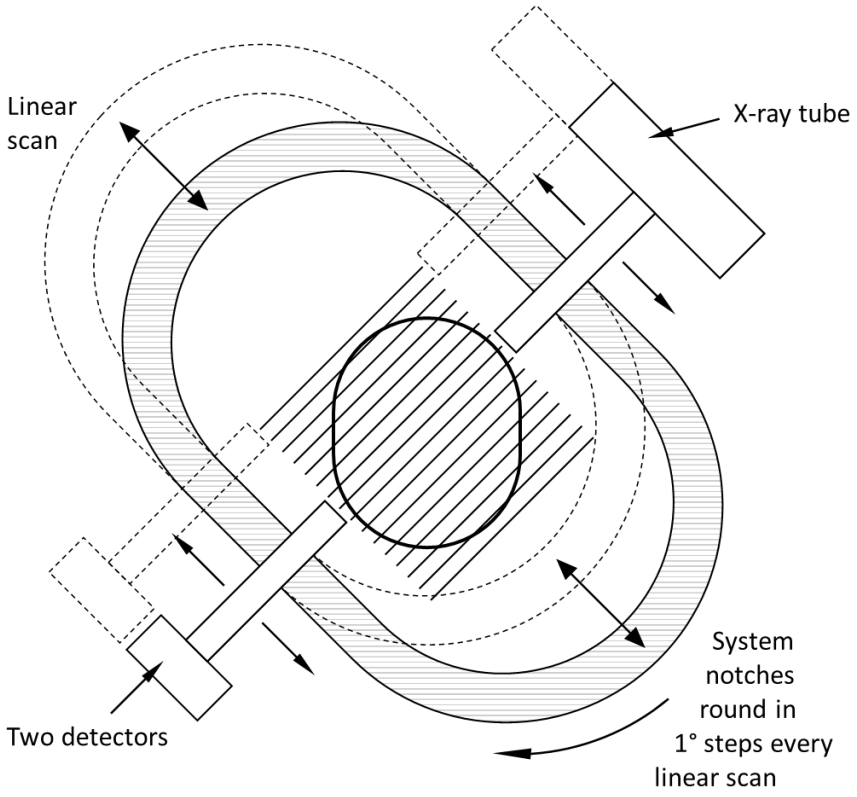

Figure 2.4 A schematic of Hounsfield's X-ray CT scanner (redrawn from Hounsfield 1973)

2.3.2 Instrumentation of X-ray micro-CT

2.3.2.1 Types of X-ray micro-CT scanners

There are two types of X-ray micro-CT scanners based on scanning mode: rotating object scanners and rotating gantry scanners (Kachelrieß 2008). The scanner built by Elliott and Dover (1982) is an example of a rotating object scanner. Figure 2.5 shows a newer rotating object scanner with an electric-powered rotation stage instead of the manually operated spur gear used by Elliott and Dover (1982). Kachelrieß (2008) described the benefits and drawbacks of the rotating object design. The design is cost-effective and reliable because there is only one moving component during scanning, which is the rotation stage. It is also more compact than a scanner with a rotating X-ray source and detector. The main drawback is that specimens are subject to centrifugal force, which can cause problems when scanning fluids or flexible objects.

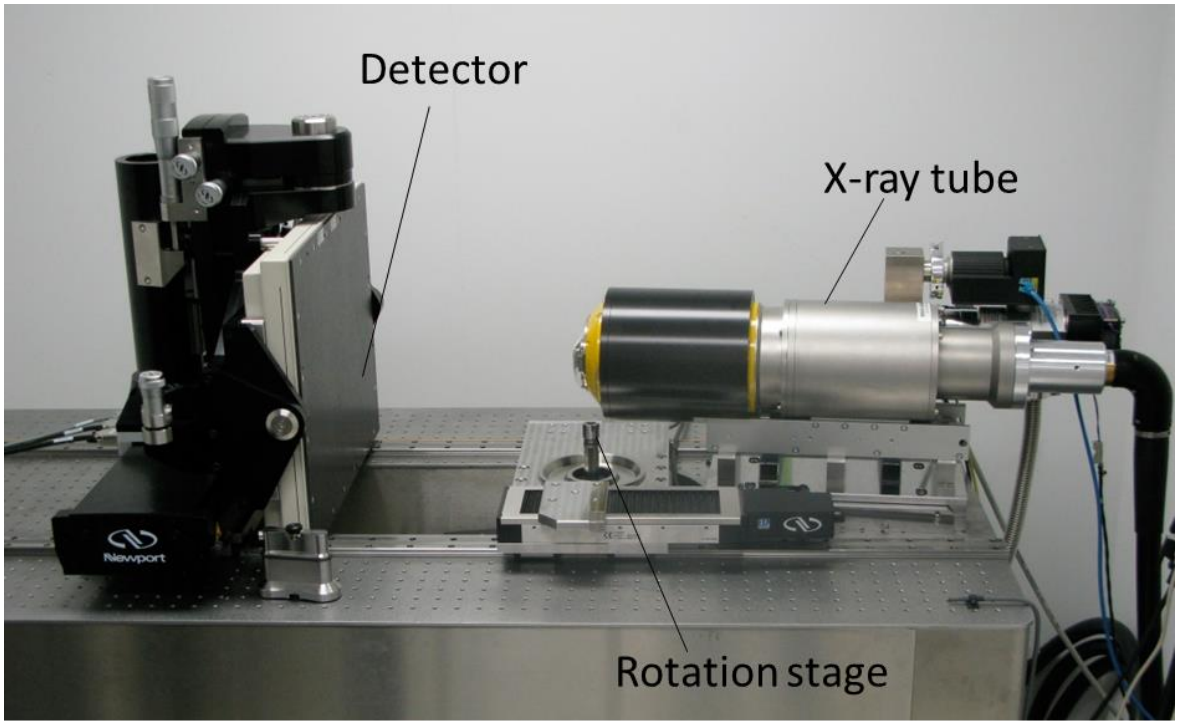

Figure 2.5 A rotating object X-ray micro-CT scanner designed and built by the Research School of Physics at The Australian National University (ANU). The sample holder is not shown in this image (photo, c/o Department of Applied Mathematics, ANU)

Like Hounsfield's (1973) scanner, rotating gantry scanners are commonly found in medical facilities. This design is also employed by some micro-CT devices because of the stability provided for specimens. However, the design is uncommon because it is more complex and expensive compared to instruments that rotate specimens (Kachelrieß 2008).

X-ray micro-CT scanners can also be classified into *ex-situ* scanners and *in-situ* scanners. The word *ex-situ* in this context means "off site" whereas *in-situ* means "on site". For *ex-situ* scanners, the experiment is carried out outside the scanner and the specimen is scanned before or after the experiment; while for *in-situ* scanners, the experiment occurs within the scanner (Leißner 2020). An *ex-situ* scanner could be converted into an *in-situ* scanner if the rotation stage is large enough to accommodate the experimental apparatus (Sakellariou et al. 2004).

Unless specified, the term "X-ray micro-CT scanner" in this thesis refers to an *ex-situ* X-ray micro-CT scanner with rotating object design and a conventional X-ray source.

2.3.2.2 X-ray sources in an X-ray micro-CT scanner

2.3.2.2(a) Types of X-ray sources

An X-ray micro-CT scanner uses either a conventional X-ray tube or a synchrotron as its X-ray source. Conventional X-ray tubes generate X-rays by accelerating highly energetic electrons in a metal anode, and then converting the kinetic energy from the electrons to electromagnetic radiation. A synchrotron generates radiation by changing the direction of electrons at a relativistic speed (Pacilè and Tromba 2018). Conventional X-ray micro-CT scanners have advantages such as large field of view and scanning volume, ease of use, and low cost. They can also have high throughput and penetration power if equipped with a high-power X-ray tube (Brunke et al. 2008). However, they suffer from beam hardening artifacts in the images as a result of their use of polychromatic X-ray beams (Chappard et al. 2006). Synchrotron X-ray micro-CT scanners avoid this problem because they employ monochromatic X-ray beams. They have other advantages over conventional devices such as lower acquisition time at high resolution, ease of reconstruction, and high signal-to-noise-ratio (Chappard et al. 2006). The main reasons that limit the more widespread use of synchrotron X-ray CT scanners by scientists is that they their high cost and limited availability of beam-lines (Goyens et al. 2017).

2.3.2.2(b) X-ray beam geometry

Hounsfield (1973) used a simple line geometry for the X-ray beam in his device. Modern X-ray micro-CT scanners can employ more complicated X-ray beam geometries including fan-beam, cone-beam, and parallel-beam geometries. These beam geometries are shown in Figure 2.6.

Sasov (2002) described how fan-beam and cone-beam geometries affect X-ray micro-CT images. He noted that a fan-beam geometry is good at rapidly acquiring a cross-sectional image near the center of a specimen. Cone-beam geometry is capable of obtaining geometrically correct cross-sectional images from any part of the specimen, but it requires more computational power and time to reconstruct images. A parallel-beam geometry is usually used in synchrotron X-ray micro-CT devices (Pacilè and Tromba 2018). Unlike fan-beam and cone-beam geometries, parallel-beam geometry does not have magnification effect, thus the resolution of the detector determines the resolution of the CT image (Chappard et al. 2006). Because the beam is parallel, the filtered back-projection method can be used directly to reconstruct CT images (Salomé et al. 1999).

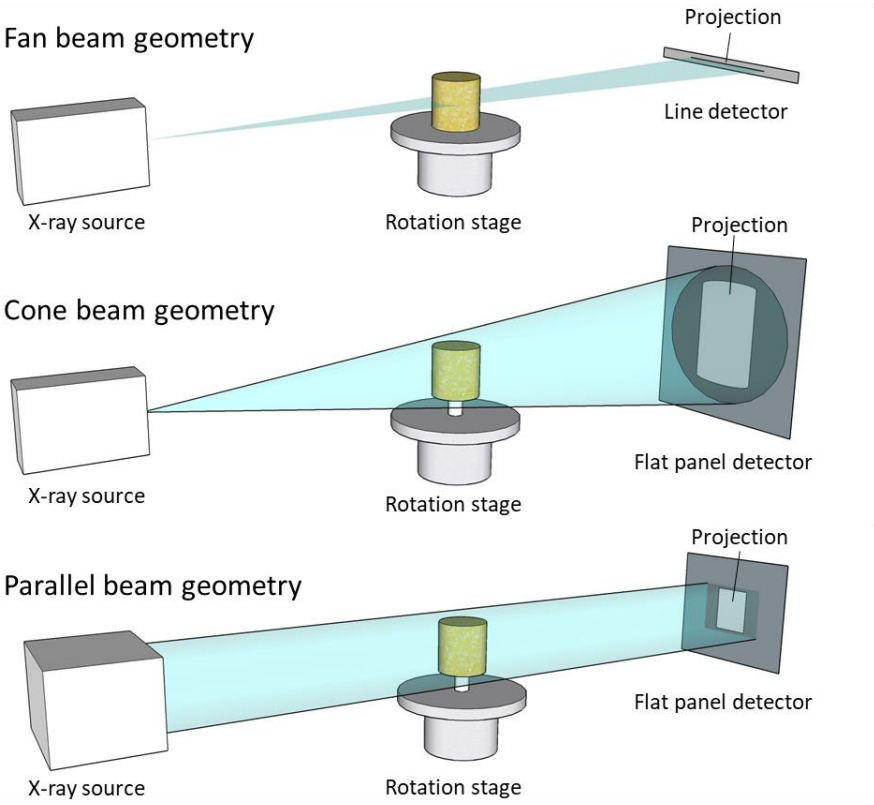

Figure 2.6 Schematic diagram of different beam geometries employed by X-ray micro-CT devices (modified from Ketcham 2017)

2.3.2.2(c) X-ray beam trajectory

Hounsfield's (1973) scanner, together with other first-generation CT scanners, have to move the patient every time the gantry rotates through 180°. The trajectory of their thin-line X-ray beam is not continuous. This type of beam trajectory is called "conventional trajectory". Scanners using this trajectory have declined in popularity due to drawbacks such as long scanning time, inability to perform dynamic contrast studies, difficulties in reformatting in different planes, and the possibility of missing small detail between slices (Garvey and Hanlon 2002).

There are two types of X-ray beam trajectories used in modern X-ray micro-CT scanners: (1) circular trajectory and; (2) helical (spiral) trajectory. A micro-CT scanner with a circular X-ray trajectory uses either a cone beam or a parallel beam to scan samples. The sample rotates on the rotation stage with no movement along the rotation axis. This type of trajectory is commonly used in micro-CT scanners because it is simple and easy to achieve good precision (Varslot et al. 2010). Caution should be

taken when using a cone-beam X-ray source and circular trajectory because it causes noticeable artifacts in images when the cone angle is above 5° (Sheppard et al. 2014). A way to mitigate this problem is to use small cone angles and perform a series of circular scans next to each other, but this approach leads to longer scanning times (Katsevich and Frenkel 2016). Another problem of using a cone-beam X-ray with a circular trajectory is that it does not provide enough information to reconstruct the exact image. Hence, images produced are only approximations (Varslot et al. 2011a). A helical trajectory overcomes this problem. A helical trajectory combines rotation and linear movement along the axis of rotation. In theory, it can provide all the information necessary to reconstruct the exact image of specimens (free of artifact) if an autofocus correction method is applied (Varslot et al. 2010, 2011b).

2.3.2.3 Operating an X-ray micro-CT device

Du Pless et al. (2017b) provided guidelines for scanning biological samples using X-ray micro-CT scanners. The first step is sample preparation and mounting. The sample needs to be mounted on a low-density holder and remain fixed to the rotating stage. Then, scanning parameters need to be selected. A balance needs to be found between the resolution of the scanner and the size of the sample. The size of a focused X-ray spot should not exceed the size of a voxel (a three-dimensional pixel). The spatial resolution of the scanner should be confirmed to ensure scan quality, and the full dynamic range of the X-ray detector should be tested to determine the best image acquisition time. The number of images should also be determined because it is related to magnification and sample size. The correct voltage and X-ray filter should be used to minimize image artifacts. After these parameters are set, the background should be normalized by using the X-ray beam to correct intensity variations of the detector. Then, the X-ray beam should be centred. Once all the previous steps are done, the scanner can be run automatically. After scanning, the data acquired from the device can be reconstructed and visualized. These steps are described in the next section.

2.4 X-ray micro-computed tomography data reconstruction, visualization, and analysis

2.4.1 Data reconstruction

Tomographic images are not acquired from a CT device directly. Instead, they are generated by a process called "reconstruction" in which the projection data obtained from the CT device are processed using mathematical algorithms (Varslot et al. 2011b). There are two commonly used methods for reconstruction of tomographic data: filtered back-projection and iterative reconstruction.

2.4.1.1 Filtered back-projection

Filtered back-projection (FBP) is the most widely used method for CT data reconstruction due to features such as speed, ruggedness, and modest computational power requirements (Stiller 2018). Because the mathematical expressions of FBP can be difficult to understand for most readers, Currie et al. (2015) wrote a non-mathematical explanation of FBP, which is summarized below:

"In the scanning process, the X-ray beam penetrates the scanned object and then creates a projection on the other end which is the X-ray detector. This projection is called forward projection (Figure 2.7a). After a scan circle, a number of individual projections are collected to produce X-ray intensity profiles. To generate tomography images, the steps involved in producing projections can be reversed – which means "X-ray beams" with the collected intensity profiles are virtually 'projected' back to the positions where the X-ray source were. This process is called back-projection. The intensity data are spread across the entire scanned region. When a single back-projection is done, the process can be repeated from another angle (for example, 45° and 90° to the first one), and a focal point can be found at where the back-projections meet (Figure 2.7b). When the number of repetitions increases, the focal point gives better depth information (Figure 2.7c, d). However, the image looks blurry because back-projection creates noise. To reduce the noise and improve the clarity of images, the back-projections should be filtered."

The process of FBP is the same as non-filtered back-projection, except that the former uses Fourier transformation to create "wings" with negative intensity values next to the positive peaks in the intensity profile (Figure 2.8a). Curie et al. (2015) used the phrase "*two erasers attached to the sides of a crayon*" to describe the positive and negative peaks in the intensity profiles of FBP. With an increase in the number of back-projections, the negative "wings" cancel the noise produced by back-projection

(Figure 2.8b, c). The result from FBP (Figure 2.8d) is much clearer than that from non-filtered back-projection (Figure 2.7d).

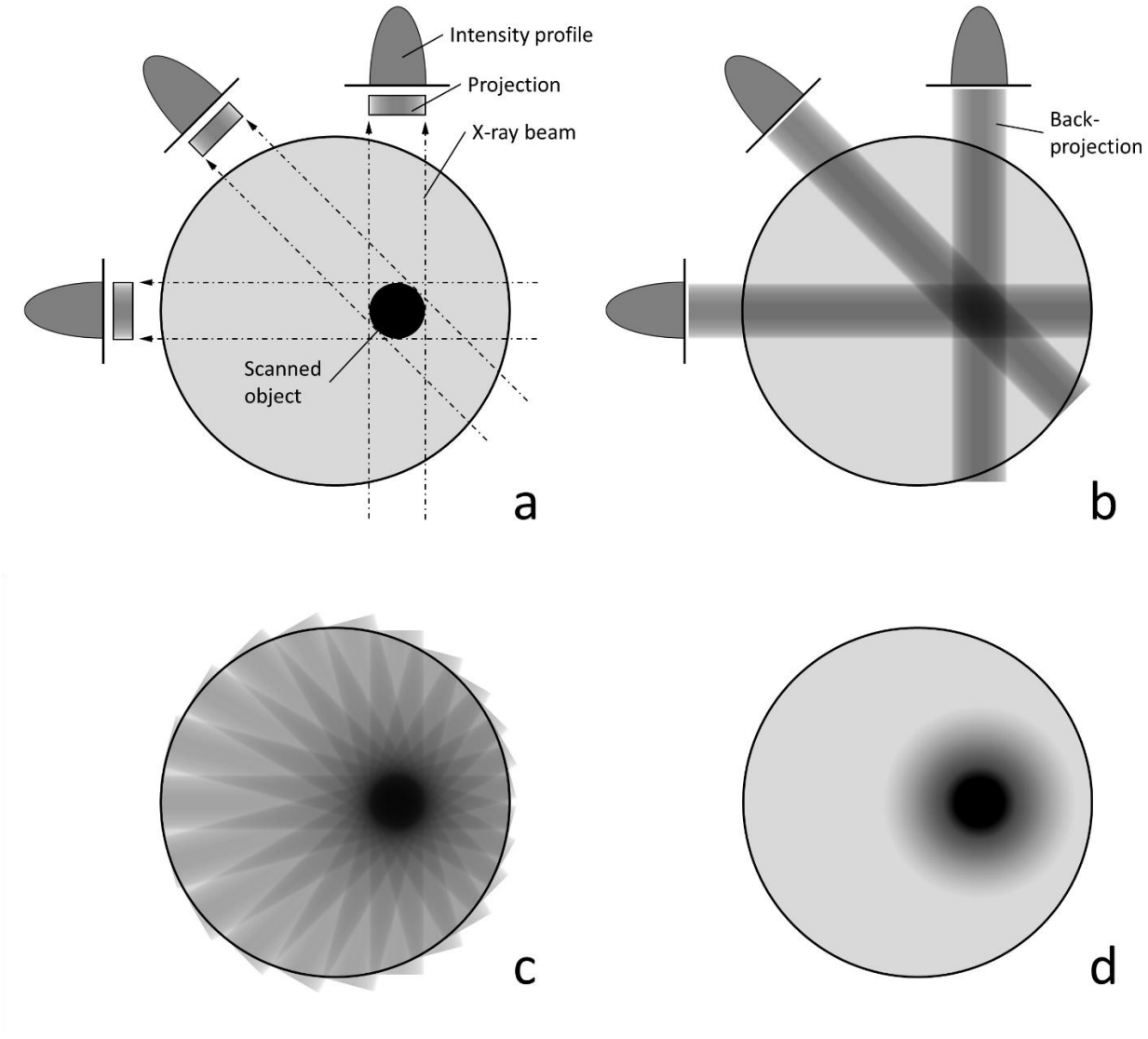

Figure 2.7 Schematic diagram of non-filtered back-projection: a) forward projection to produce projection images and intensity profile around the scanned object; b) three back-projections (0°, 45°, and 90°); c) 12 back-projections; d) a large number of back-projections (modified from Peters 2002)

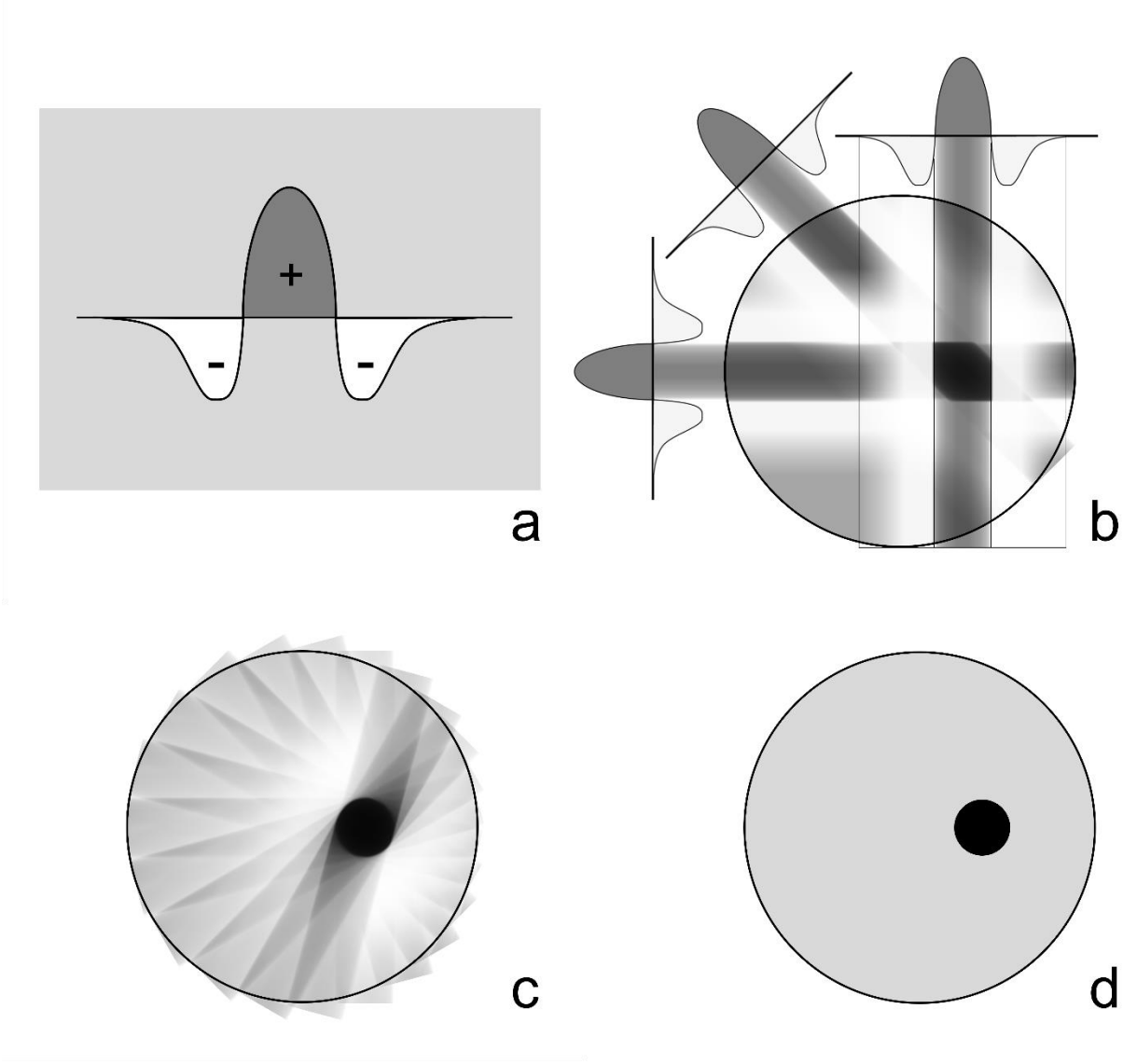

Figure 2.8 Schematic diagram of filtered back-projection (FBP): a) Fourier-transformed intensity profile containing the original positive peak (dark grey) and two negative peaks (white). The background is painted light grey to represent zero intensity value; b) three back-projections (0°, 45°, and 90°); c) 12 back-projections; d) a large number of back-projections (modified from Peters 2002)

The previously described FBP method is in 2D planes with 2D parallel X-ray beams. As mentioned in Section 2.3, most X-ray micro-CT scanners utilize 3D cone-beam X-ray sources. Additional algorithms are applied to FBP in 3D. The most common algorithms are: Feldkamp-Davis-Kress (FDK) algorithm for circular beam trajectory (Feldkamp et al. 1984), and Katsevich (2002) algorithm for helical beam trajectory. FDK algorithm is a modified fan-beam FBP algorithm (Zeng 2010). It is commonly used

for cone-beam reconstruction, but it only produces approximate reconstructions rather than exact reconstructions (Zeng 2010). This is because the circular trajectory it employs does not satisfy Tuy's (1983) data sufficiency condition in which any plane through any point in the scanned object should intersect with the X-ray source trajectory. The insufficiency of data causes the FDK algorithm to be unreliable when the cone angle exceeds ±5° (Varslot et al. 2011b). In contrast, the Katsevich algorithm produces theoretically exact reconstructions because it uses a helical trajectory that satisfies Tuy's condition, since the helical trajectory always intersects with any planes across the scanned object (Varslot et al. 2011b). Zeng (2010) stated that the Katsevich algorithm is the best for 3D cone-beam reconstruction.

2.4.1.2 Iterative reconstruction

Iterative reconstruction produces higher quality images with less noise compared to FBP (Stiller 2018). It is a promising technique, but it is not commonly used because it has several limitations: (1) it is much slower and requires much more computational power compared to FBP; (2) it requires a complete set of data to start the iterations; (3) it needs to determine the optimal number of iterations, otherwise the image quality is reduced due to overfitting; (4) lastly, it relies on assumptions and models to produce high-quality data (Fleischmann and Boas 2011). Figure 2.9 shows Fleischmann and Boas's (2011) explanation for iterative reconstruction. Figure 2.9a shows a 4×4 grid with intensity values. Forward projections are created by summing up the grids in all directions (from left to right, from top to bottom, and diagonally). The reconstruction starts with all grids set to zero. The first step in reconstruction starts in the vertical direction (Figure 2.9b). The measured values are 11 and 9, but the estimated values in the grids are all zero, so the "errors" of estimations are 11-0=11 and 9-0=9. The errors are equally divided, resulting in 5.5 in the left two grids and 4.5 in the right two grids. Afterwards, the values in the horizontal direction are compared with measured values, and the errors (+2 and -2) are evenly spread along the horizontal direction (Figure 2.9c). The process of comparing and spreading the errors continues in two diagonal directions (Figure 2.9d, e), and finally finishes one iteration of the data set. Because this data set is very small, it only takes one iteration to reconstruct the correct data. More complicated data sets require many more iterations.

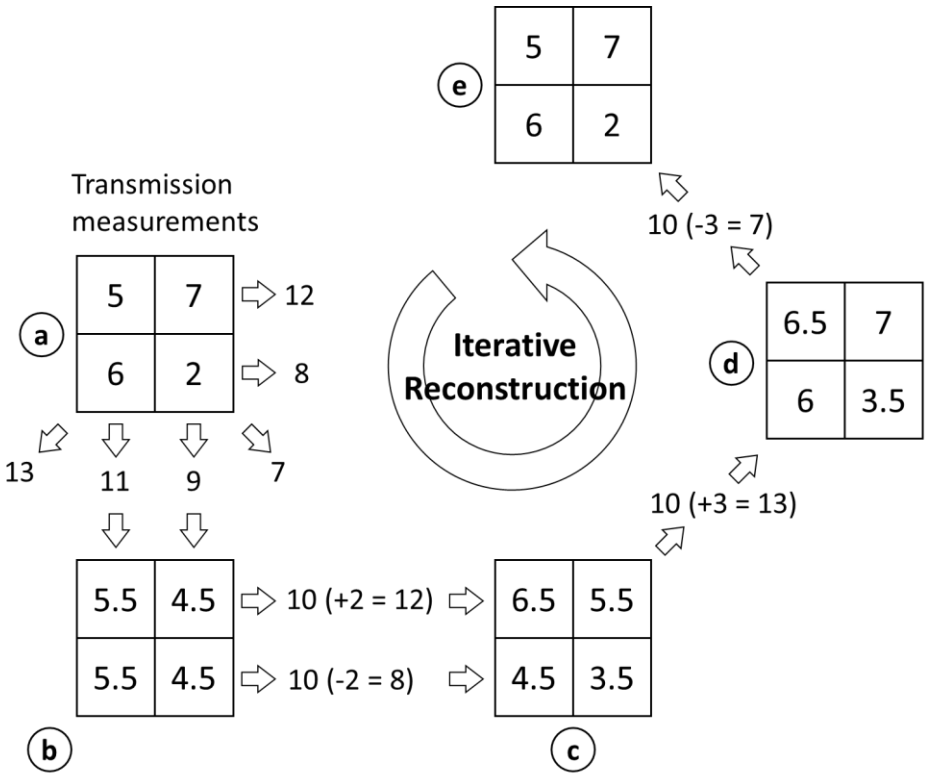

Figure 2.9 Iterative reconstruction of a 4×4 image (redrawn from Fleischmann and Boas 2011)

2.4.2 Data visualization

2.4.2.1 Voxels

Because voxels are the fundamental elements in a CT data set, I provide a definition of a voxel before proceeding to review data visualization techniques. Voxel stands for “volume element”. Unlike pixels which are flat squares in a 2D matrix, voxels are cubed and have a third dimension (Özer 2011). As volumetric data, voxels have four parameters (*x, y, z, v*), in which (*x, y, z*) is the 3D location of voxels, and *v* represents the intensity of a specific property (Kaufman 1994). In a CT data set, voxels form a 3D array, and the property they represent are X-ray attenuation coefficient values (Knackstedt et al. 2006). The coefficients are often expressed in the form of CT numbers, using a unit called the Hounsfield Unit (HU) (Bryant et al. 2012).

2.4.2.2 Shaded surface display and maximum intensity projection

Shaded surface display (SSD) and maximum intensity projection (MIP) were two of the earliest methods for 3D visualization of CT data. Their use has declined and now volume rendering is the method of choice for 3D visualization of CT data. Calhoun et al. (1999) explained how the techniques work and why volume rendering is superior to SSD and MIP, which are summarized below:

"SSD renders 3D images by displaying polygonal surfaces that represent the geometry of the data set. The surface is usually determined by thresholding the voxel intensities. Figure 2.10 gives an example of thresholding. The intensity values in the diagram range from 0 to 9. Then, a threshold is applied to select voxels with intensities ranging from 6 to 9, and voxels that are not in this range are left out. The boundary of the thresholded voxels is 6-6-6 in this case. Afterwards, an algorithm is applied to generate a polygonal surface, which consists of small triangles, along the located boundary. The advantages of SSD are its high speed and flexibility, and clear depth cue of the rendered images. However, it has a major problem in data utilization because it only uses a small percentage of the data set (less than 10%). It also has problems in visualizing data sets that do not have well distinguished surfaces.

MIP selects the voxel with the highest intensity along a line that is projected from the viewer's eye, and uses the selected intensity value as the displayed value. For example, in Figure 2.10, a row of voxels is evaluated. The algorithm found that 8 is the maximum intensity and chooses to display the voxel with that value. In some medical cases, MIP is very capable in rendering images and has better precision than SSD, but it has some disadvantages when applied to other fields: (1) high density material may obscure information from low-density material; (2) it usually does not generate any shading or depth cues, which makes assessing 3D relationships difficult; (3) also, it has a lot of artifacts caused by the algorithm."

In general, Calhoun et al. (1999) stated that volume rendering is superior to SSD and MIP in terms of flexibility and image fidelity.

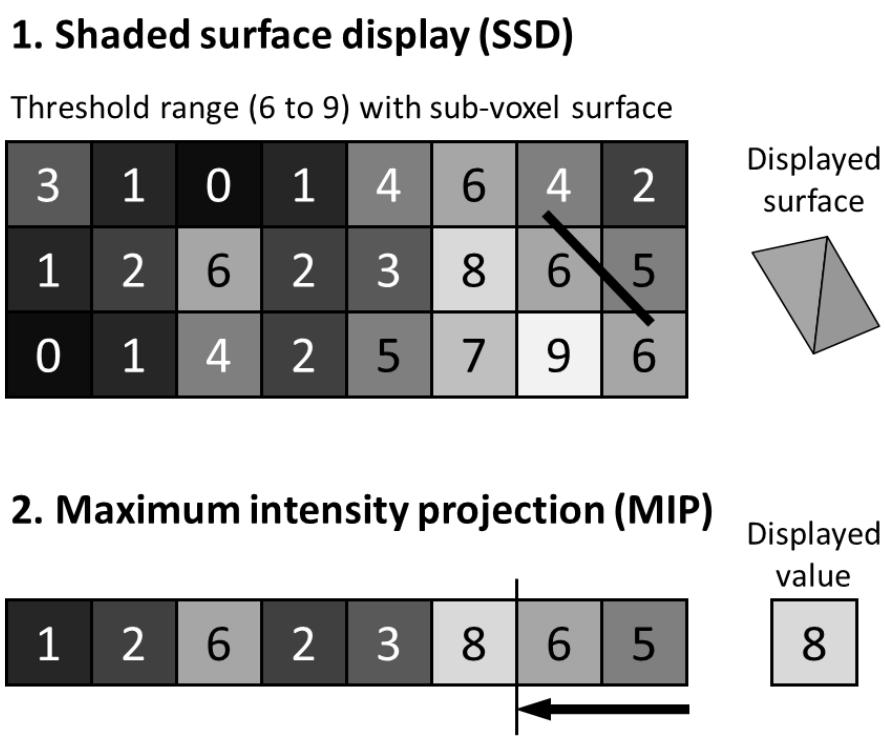

Figure 2.10 Schematic diagram of shaded surface display and maximum intensity projection for X-ray CT data visualization (redrawn from Calhoun et al. 1999)

2.4.2.3 Volume rendering

The volume rendering technique for CT data visualization was developed by Drebin et al. (1988). I summarize their description of the technique as follows:

"A CT data set contains a mixture of voxels with different intensities. Because the intensity of a voxel corresponds to material density, the first step of volume rendering is to categorize the mixture of voxels according to the materials they represent. To achieve this, a histogram can be generated to map the intensities of voxels. Figure 2.11 shows an example of an intensity histogram and the results of material assignments based on a maximum-likelihood classifier. Then, a matting procedure is used to remove some parts of the data that are not of interest, for example, air. The second step is to extract a surface where two materials meet. This is achieved by using the density of each assigned material to calculate the surface normal ($\vec{N}$). The third step is to add lighting, colour, and shading effects to the voxels (Figure 2.12). If a ray of light is beamed towards the observer's eyes and penetrates a voxel with transparency, its intensity will change from I to I'. If the voxel is coloured and has an extracted surface within it, the colour of I' will be decided by the colour of the material in front of the surface (C_F) and

behind the surface (C_B), and the reflected colour of the surface (C_S). C_s is related to the diffuse colour of the extracted surface (C_D), the colour (C_L) and direction ($\vec{L}$) of the light source, $\vec{N}$, and the direction of eyesight ($\vec{E}$). C_D is calculated by summing up C_F and C_B. After all these calculations, the colour and brightness of I' for each voxel are projected to a viewing plane, and that completes the rendering of a 3D image of a CT data set."

In more contemporary volume rendering techniques, algorithms called "transfer functions" are used to assign colour, brightness, and opacity to voxels with certain ranges of intensity values (Calhoun et al. 1999), rather than the complicated procedures described by Drebin et al. (1988).

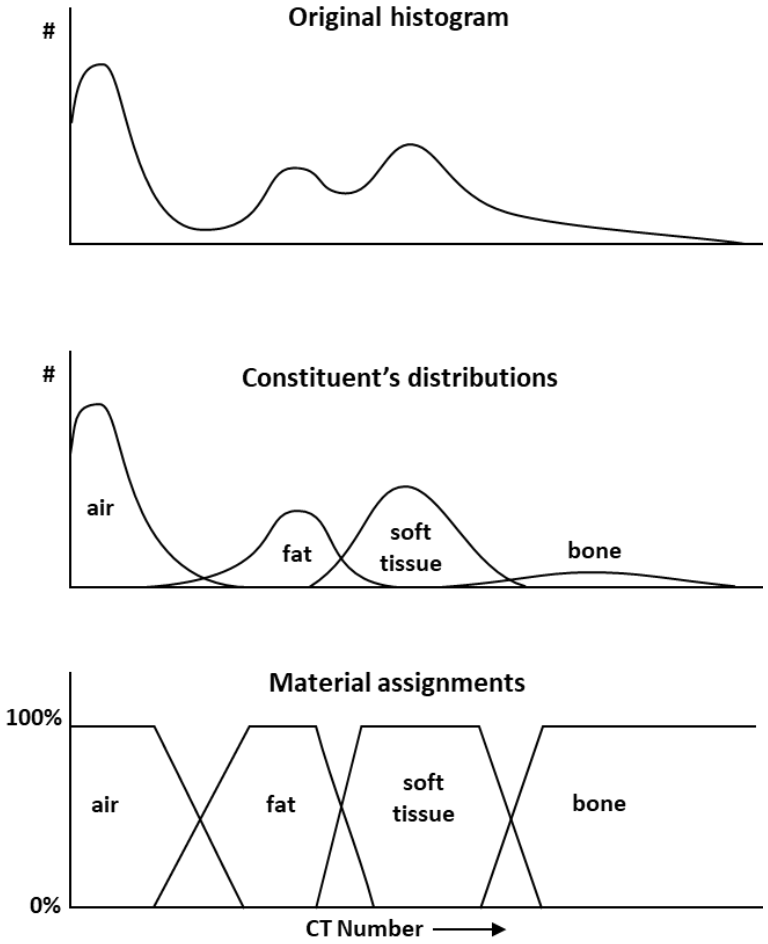

Figure 2.11 Material classification (redrawn from Drebin et al. 1988)

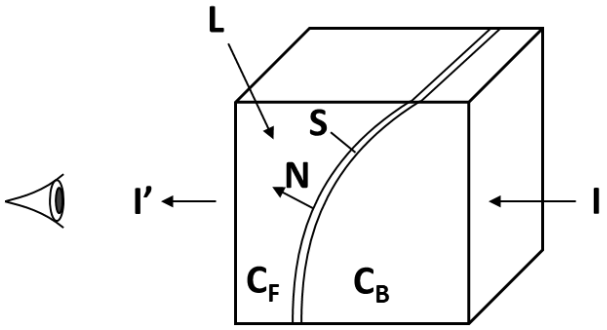

Figure 2.12 Voxel lighting and shading model, in which I is the intensity of a light ray entering the voxel; I' is the intensity of the same light ray exiting the voxel; S is the magnitude of the gradient; N is the surface normal; L is the direction of the light source; C_F is the colour of the material in front of the extracted surface; C_B is the colour of the material behind the extracted surface (redrawn from Drebin et al. 1988).

2.4.2.4 Data analysis

Quantitative analyses can also be performed on CT data sets. Schladitz (2011) summarized the use of quantitative analyses of X-ray micro-CT data into three categories: geometric characterization, analysis of material properties, and microstructural optimization.

As its name suggests, the goal of geometric characterization is to determine the geometric-related parameters of objective microstructures in a CT data set. Schladitz (2011) characterized the geometry of pores in a concrete sample (Figure 2.13). The CT images were firstly binarized to display pores in black and unimportant parts in white. Then, each pore was labelled, and all the voxels that belonged to the same pore were assigned the same label as the pore they belonged to. Subsequently, the dimension and shape of each pore were measured, and the best-fitting cuboids and ellipsoids were applied to the pores.

Figure 2.13 Example of geometric characterization. Left: original grayscale image. Centre: binarized image showing pores. Right: labeled pores, colours representing different labels (Schladitz 2011, adapted with publisher's permission)

Properties such as elasticity or thermal conductivity are influenced by the microstructure of a material. Therefore, CT can obtain information on properties by quantifying microstructure. For example, du Pless et al. (2017) used micro-CT to investigate the relationship between the microstructure of titanium alloy and its material properties. They found that ductility was associated with pore size and stress distribution. They also performed simulations based on micro-CT data and developed a model to predict ductility. As pointed out by Schladitz (2011), developing a model to predict mechanical properties based on microstructural features is the ultimate goal for the micro-CT analysis of materials. However, it is difficult to achieve this goal for some materials due to their complexity.

Schladitz (2011) described how analysis of CT data could be used to optimize the microstructure of a material. First, the microstructural information from a CT data set is fitted to a stochastic model, which is based on properties measured in the data set. Secondly, the microstructure is altered by changing the parameters in the model. This step simulates how the properties of this material will change when microstructure is altered. Then, the second step is repeated to find an optimal microstructure with the best material properties. Research on modeling foam structures by Redenbach (2009) is an example of microstructural optimization. She used synchrotron X-ray micro-CT to extract geometric data from foam samples. Then, she simulated the properties of the foam based on random tessellations models fitted to the geometric data. The generation of simulation data was then used to optimize the microstructure of foams.

2.5 X-ray micro-computed tomography of solid wood

2.5.1 Anatomical features in wood

2.5.1.1 Pioneers of X-ray micro-CT of wood

Davis et al. (1991) pioneered the use of X-ray micro-CT for wood science. They scanned a softwood sample, Scots pine, and a hardwood sample, alpine ash (*Eucalyptus delegatensis* R.T. Baker) at voxel sizes of 20 µm and 5 µm. They found that a resolution of 20 µm was adequate for displaying growth rings in Scots pine. Resin canals, rays, and tracheids in Scots pine could be detected in 20 µm images, but they were clearer in 5 µm images. Their 20 µm images of alpine ash showed a collapse check adjacent to a vessel. Their 5 µm images showed a clear distinction between the collapsed and uncollapsed areas. They estimated that their CT device was capable of scanning wood at a resolution of 1 µm. Subsequently, Illman and Dowd (1999) scanned decayed southern yellow pine samples using synchrotron X-ray micro-CT at 5 µm resolution. Their main contribution to the development of micro-CT for wood was introducing quantitative analysis of CT data. In addition, they showed that it was feasible to use a synchrotron radiation source for scanning wood. They estimated the porosity of the samples by calculating the ratio of the number of voxels representing pores versus the total number of voxels. To discover the effect of fungal decay, they also measured the disconnectivity of pores and the "burn number" which was related to the distance between a voxel representing pore and the interface of air and wood. Later, Steppe et al. (2004) studied ring-porous European oak and diffuse-porous European beech wood using a conventional X-ray CT scanner at 7 µm resolution. They quantified more parameters than Illman and Dowd (1999), including vessel diameter, surface area, density, and porosity. They contributed to X-ray micro-CT of wood by: (1) introducing segmentation and 3D volume rendering and: (2) extracting and visualizing the vessels to reveal complex networks of vessels in both diffuse-(beech) and ring-porous (oak) woods. Research at The Australian National University in 2000, which is unpublished used a cone beam, in-house CT device to image three hardwoods, European oak, ebony (*Diospyros* spp.); and balsa (*Ochroma pyramidale* [Cav. ex Lam.] Urb.). Images from this early research are shown below (Figure 2.14a,c). The pore and rays (and parenchyma in oak) are clearly evident, but the level of detail is far less than in the adjacent images (Figure 2.14b,d) obtained using a modern CT device at higher resolution.

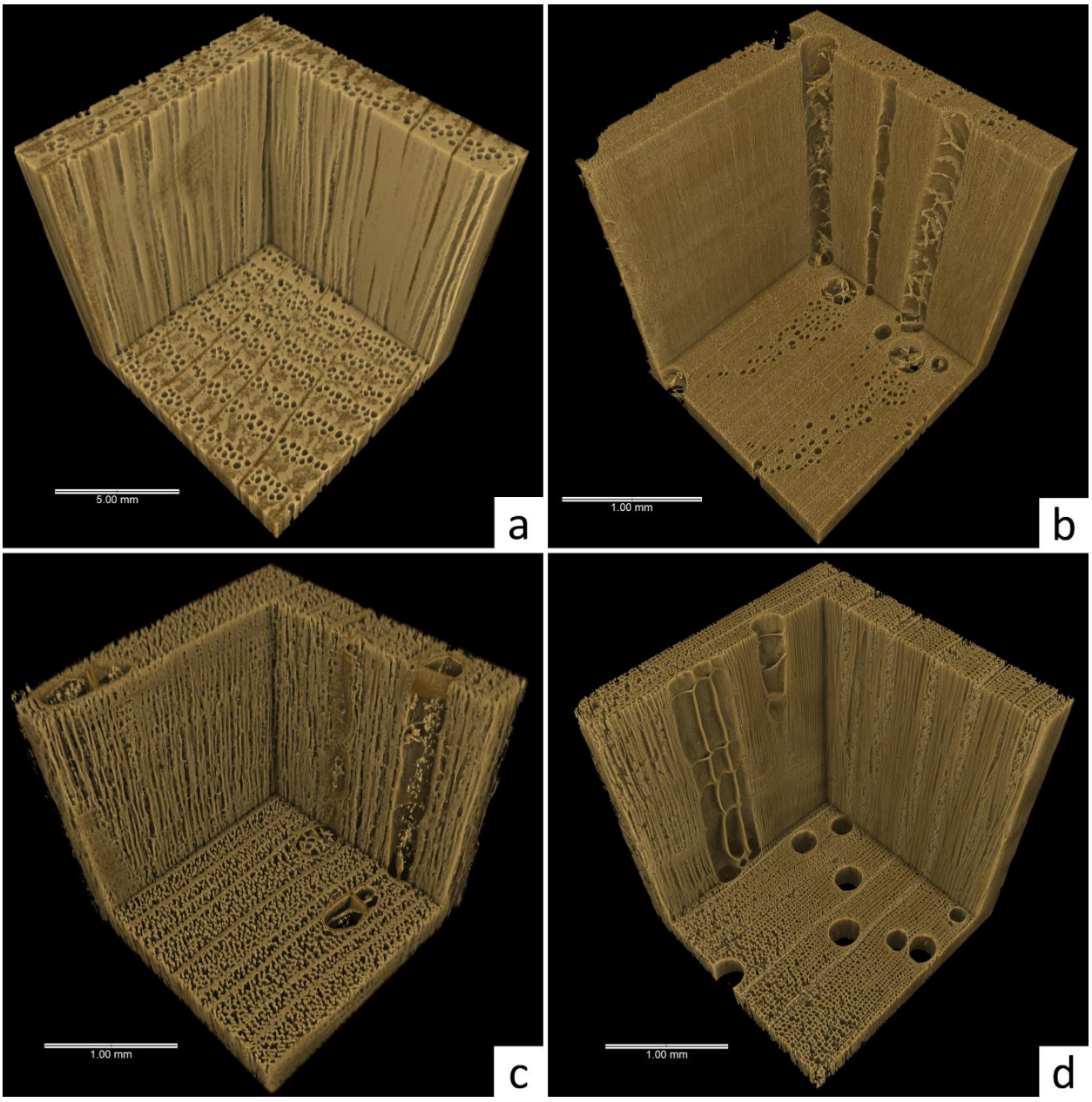

Figure 2.14 3D rendered images of oak (*Quercus* spp.) and balsa scanned using an early and a more contemporary X-ray micro-CT device at The Australian National University: (a) oak, scanned in 2000 at 32.6 µm voxel size; (b) oak, 2013, 2.4 µm; (c) balsa, 2000, 5.3 µm; (d) balsa, 2015, 2.5 µm

2.5.1.2 Developments of techniques for X-ray micro-CT of wood anatomy

After the aforementioned pioneering studies, X-ray micro-CT of wood structure increased in popularity helped by improved access to the technology. Mannes et al. (2009) used synchrotron micro-CT to complement findings from X-ray macro-CT. The device they used had high resolution (0.75-1.5 µm), which was sufficient for visualizing pits in the vessel walls of European beech. They also pointed out that sample preparation for scanning at such resolution should be carefully performed because they found small checks caused by machining in the outer area of their samples. They subsequently used their synchrotron CT device to scan two more species, European oak and English yew (*Taxus baccata* L.) (Mannes et al. 2010). Van den Bulcke et al. (2009a) visualized a softwood species Scots pine, and three hardwood species which were European beech, afzelia (*Afzelia bipindensis* Harms), and movingui (*Disthemonanthus benthamianus* Baillon). Unlike Mannes et al. (2009, 2010), they used conventional X-ray micro-CT with voxel sizes below 1 µm. They demonstrated that a lab-based micro-CT scanner with a conventional X-ray source could be used to scan micron-sized anatomical features such as the thin cell walls and pits. They were able to visualize different anatomical structures in softwood and hardwood, and quantify the sizes of cell lumens. Similarly, Mayo et al. (2009, 2010) visualized softwood and hardwood features using conventional X-ray micro-CT with a voxel size of 2 µm. They also compared their high-resolution data sets with lower resolution ones and found that the higher resolution ones showed more detail, which was because of the smaller voxel size and also the effect of a phase-contrast method they used. Belini et al. (2011) conducted a similar study and concluded that their device was capable of scanning anatomical features of softwood and hardwood. Lautner and Beckman (2012) used a synchrotron micro-CT design to scan poplar (*Populus trichocarpa* var. Trichobel) wood. They claimed that their device could easily achieve a resolution below 1µm, and the quality of CT images increased when phase-contrast and absorption contrast methods were combined.

2.5.1.3 Tomography of wood microstructures

In addition to the aforementioned studies that explored the general capability of X-ray micro-CT for anatomical studies of wood, scientists have also studied the anatomy of specific wood species using X-ray micro-CT. Trtik et al. (2007) looked at the anatomy of Norway spruce wood using synchrotron micro-CT. They analyzed the morphology of tracheids and found that they were mostly four-sided in shape. Their measurements of the sizes of tracheids were in accord with previous microscopy studies of the anatomy of spruce. They quantified the porosity and cell wall thickness of spruce wood, and their

visualization of the pits in tracheids and ray parenchyma pre-dated the work of Mannes et al. (2009). They also located the tori of pits via an indirect method that involved watershed segmentation, a segmentation method that is based on “valleys” and “ridges” in the topographic landscape of CT images (Preim and Botha 2014). Yazid et al. (2010) studied the morphology of the fragrant resinous wood, Indonisian agarwood (*Aquilara malaccensis* Lam.) using X-ray micro-CT. They were able to characterize resin, wood and voids, but their X-ray detector caused several ring artifacts in CT images. Liu et al. (2018) studied the anatomy of Chinese-grown agarwood (*Aquilaria sinensis* [Lour.] Gilg) using synchrotron micro-CT. Two methods were used to enhance the imaging of samples: propagation-based phase-contrast CT (PPCT) and phase retrieval-based PPCT (PR-PPCT). They found that PR-PPCT could detect resin near vessels while PPCT could not. They located resin in resin ducts of agarwood. They also found that PR-PPCT was better than PPCT at revealing fibres, rays, and parenchyma in their agarwood samples. Svedström et al. (2012b) studied juvenile wood in hybrid aspen (*Populus tremula* L. × *Populus tremuloides* Michx.). They used X-ray micro-CT to study the 3D cellular structure of hybrid aspen and the geometry of its cells (Figure 2.15). Their results showed that their fibres were shorter than those obtained by previous studies. Also, the microfibril angles in fibre walls of spruce, pine, birch, and juvenile *Populus* were lower than those obtained by previous studies. Koddenberg and Militz (2018) looked at the morphology of European ash (*Fraxinus excelsior* L.) wood using X-ray micro-CT. They visualized vessels, fibres and parenchyma cells in 2D and 3D. They found that the length-to-diameter (L/D) ratio of vessel elements in latewood was approximately 3.7 times higher than that in earlywood. Latewood also had longer but narrower fibres with a higher L/D ratio compared to fibres in earlywood. They also found that the segmentation of axial parenchyma cells was more difficult in earlywood compared to latewood. Subsequently, Koddenberg et al. (2019b) examined bordered pits in Scots pine using light microscopy and X-ray micro-CT. They were able to measure the size of bordered pits using 3D and 2D models. They compared two 2D models for calculating pit volumes: the ellipsoid model and the spherical cap model. They found that the results of the ellipsoid model were closer to 3D measurements acquired by micro-CT, and this was more noticeable for bordered pits in earlywood than those in latewood.

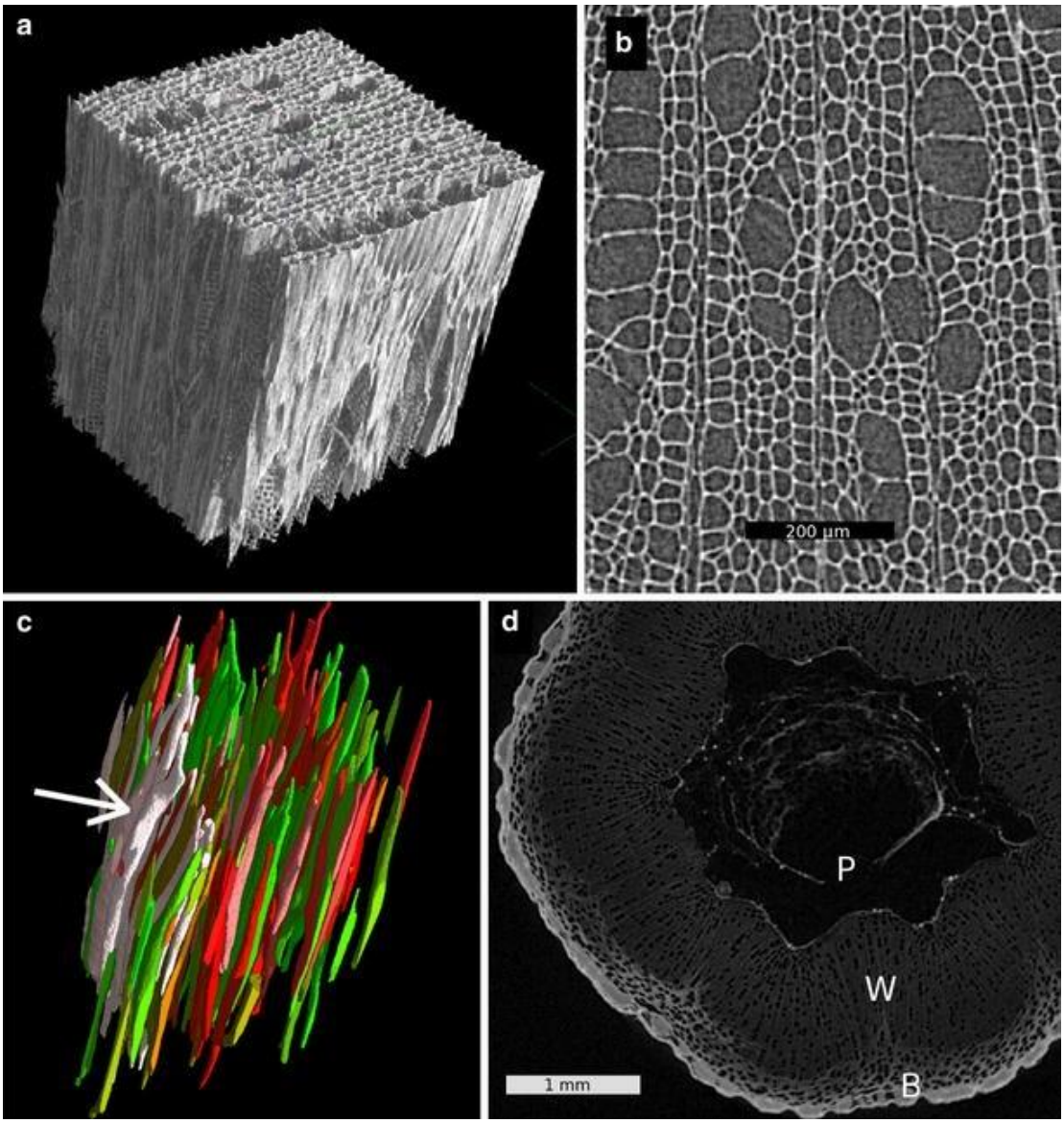

Figure 2.15 X-ray micro-CT images of hybrid aspen wood: (a) 3D volume rendered images; (b) 2D transverse section; (c) segmented lumina of fibres (coloured) and vessel elements (arrowed); (d) Cross-sectional image of stem including pith (P), wood (W) and bark (B) (Svedström et al. 2012b, adapted with publisher's permission)

2.5.1.4 X-ray micro-CT of hydraulic pathways in wood

X-ray micro-CT is very good at revealing the hydraulic pathways in wood. Steppe and Lemeur (2007) used X-ray CT data to develop a hydraulic model of wood and then examined the effects of arrangement of vessels on conductivity. X-ray micro-CT was used to image oak and beech wood samples, which are ring-porous and diffuse-porous, respectively. The number, dimensions of minor and major axes, and diameter of vessels were quantified. They found that a few large vessels had greater conductivity than many smaller vessels. Also, the larger vessels in oak had higher stem-specific hydraulic conductivity than smaller vessels in beech. Hass et al. (2010) studied the vessel network in European beech wood using synchrotron micro-CT. They quantified vessel diameters and porosity of the samples. To study the connectivity of the vessels, they performed a "blob analysis" which matched the areas, positions, and equivalent diameters of the vessels slice by slice. They also extracted the vessels using segmentation and rendered the images of vessel networks in 3D. Adey-Johnson et al. (2020) studied the hydraulic pathways in Norway spruce. They were able to measure the length, extent of overlap, diameter, and pit locations on tracheids using X-ray micro-CT. They found patterns in pit linear density and radial lumen diameter in the radial direction within growth rings.

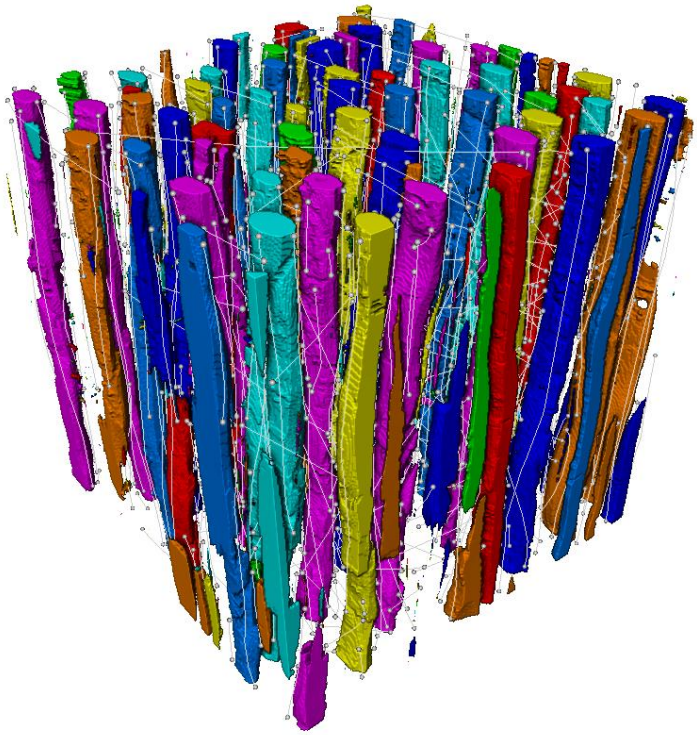

Figure 2.16 3D rendering of segmented and labeled pore network of willow (*Salix alba* L.) wood (photo, c/o Dr Mohammad Saadatfar, Department of Applied Mathematics, ANU)

2.5.2 Wood-moisture interactions

Like its macroscopic sibling mentioned in Section 2.3, X-ray micro-CT has also been used to study the interactions between wood and water, especially during the drying of wood. Rosner et al. (2010) examined the radial shrinkage and acoustic characteristics of freshly cut and pre-dried Norway spruce wood. They used X-ray micro-CT to look at the checking of their samples. However, they were not able to find micro-cracks using a resolution of 4.5 µm, although they acknowledged that microcracks could have been present in their samples. Leppänen et al. (2011) studied the drying of silver birch (*Betula pendula* Roth.), European aspen (*Populus tremula* L.), and hybrid aspen (*P. tremula* × *tremuloides*). They used X-ray micro-CT to examine the morphology of the samples before and after air drying. They found that rays were narrower in dried samples compared to undried samples. However, they were unable to find differences in cell wall thicknesses between dried and undried samples because measurement errors were too large. Taylor et al. (2013) studied the shrinkage of European beech wood over time using an in-situ X-ray micro-CT device. They observed that tangential shrinkage was greater than that in other directions. They also found that radial shrinkage in areas next to broad rays was much lower than that in other areas. In the first 40 minutes of drying, the increase of void volume followed a linear trend due to the evaporation of free water in cell lumens. After that, the wood began to shrink, and increases in void volume drastically slowed down. Patera et al. (2014) designed a device to restrain the swelling of wood during phase-contrast synchrotron micro-CT. They evaluated the effectiveness of restraint by quantifying the porosity, cell wall thickness, and swelling rate of specimens. They found that latewood tended to have higher strain compared to earlywood. They also found their restraining device useful because it reduced the anisotropy of wood. Their device itself only deformed by approximately 2 µm, which was small compared to the width of the device (500 µm). Krzemień et al. (2015) investigated how earlywood and latewood within growth rings respond to relative humidity changes. They scanned a Scots pine sample using an X-ray micro-CT device and performed 3D digital image correlation analysis on the CT data set. The results from CT complimented those from digital speckle pattern interferometry. They found that dimensional change at the wood surface was restrained by the core. Also, the latewood and earlywood in the unrestrained area shrunk uniformly, but that was not the case in the restrained area where earlywood was stretched.

2.5.3 Mechanical properties of wood

In-situ X-ray micro-CT is a powerful tool for examining the physical properties of wood. To perform in-situ scans of the bending of a Scots pine sample, Forsberg et al. (2010) mounted a compact three-point bending apparatus in a synchrotron micro-CT device. They scanned the sample three times per test to acquire cellular structures under different load states. Then, they used the CT data for digital volume correlation (DVC) analysis. In the longitudinal direction, they found a region with high tensile strain in the lower centre of the sample, plus a compression band and a tension band in the upper and lower parts of the sample, respectively. They also found that deformation was rather symmetrical in the direction parallel to the applied force. Zauner et al. (2012) conducted an in-situ compression test on Norway spruce wood. They prepared samples with three different geometries and fixed each sample on a specially designed loading device. They applied load to each sample to compress it for a certain distance and then scanned the sample in-situ and repeated the load-scan cycle until the sample was destroyed. They found that latewood tracheids tended to break first. When failure occurred, the failure area branched in multiple directions. In contrast, the resin canals were free of damage and the rays remained stable until the load reached a certain level. Sanabria et al. (2020) developed a method for quantifying the deformation of wood subjected to tension and compression. Their method, which used in-situ synchrotron micro-CT, was able to track microscopic deformations in individual wood cells.

Conventional ex-situ X-ray micro-CT is also useful for wood mechanics. For example, El Hachem et al. (2019) used it to develop a model for predicting the moisture-related change in mechanical properties of wood. They scanned spruce (*Picea* spp.) wood samples in the oven-dried state and when the wood was equilibrated at 72% relative humidity. Afterwards, they used CT data and digital volume correlation analysis to calculate the volume displacement of samples and derive a model from the results. Their model could accurately predict the swelling coefficient as well as the Poisson coefficient of spruce wood.

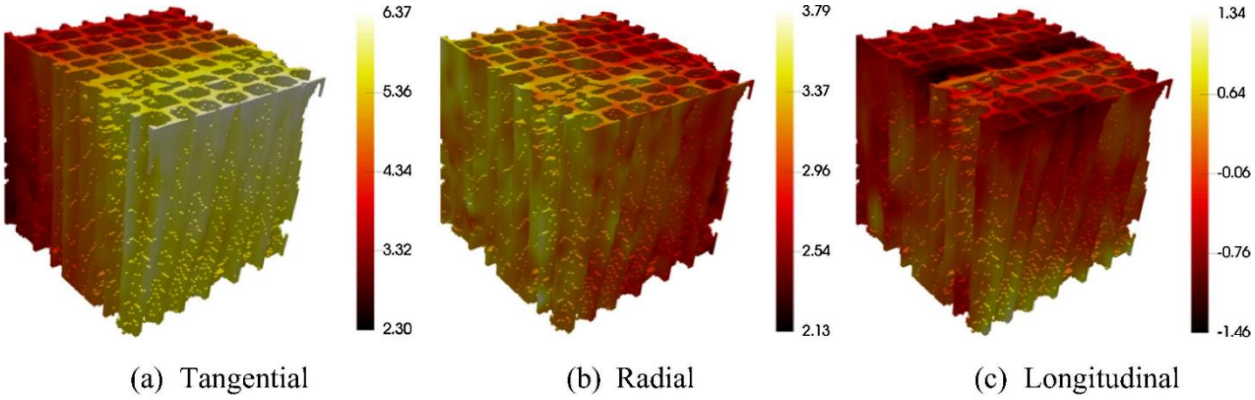

Figure 2.17 DVC mapping of the displacement of spruce wood subject to swelling at (a) tangential; (b) radial; (c) longitudinal direction (El-Hachem et al. 2019, adapted with publisher's permission)

2.5.4 Wood deterioration and protection

2.5.4.1 Deterioration of wood

Illman and Dowd (1999) pioneered the use of X-ray micro-CT to study the deterioration of wood as mentioned above (Section 2.5.1.1). Later, Illman (2003) described the principles and instrumentation for their synchrotron micro-CT study of decayed wood. Kasal et al. (2010) described novel approaches to radiography of materials including the use of X-ray micro-CT to visualize the deterioration of wood. Fuhr et al. (2012) assessed the impact of white rot on the microstructure of Norway spruce wood using synchrotron micro-CT. They visualized degraded wood using 3D volume rendering and found that damage to cell walls was mainly adjacent to bordered pits. They quantified the size and orientation of the cell wall elements in tracheids, and developed an algorithm for automated calculation of the distribution of the size of cell wall elements. Maeda and Ohta (2012) studied the anisotropy of the decay progress in Sitka spruce (*Picea Sitchensis* [Bong.] Carr.) wood using X-ray micro-CT. They found that their sample suffered higher weight losses in the longitudinal direction compared to other directions as decay progressed. In addition, density loss was greater in latewood. Tangential shrinkage was less than that in the longitudinal direction. They also observed that cracking only occurred in tangential and radial directions. Gómez-Brandón et al. (2017) studied the deterioration of coarse Norway spruce wood debris at multiple stages of decay. Their X-ray micro-CT data showed little change in microstructure in the first three decay classes, but wood in the more severely attacked fourth and fifth classes shared pronounced degradation of cell walls and tori of bordered pits.

2.5.4.2 Microorganisms in wood

The high resolution of X-ray micro-CT makes it possible to visualize micro-organisms in decayed wood, in addition to the microstructural damage that such organisms cause. Van den Burke et al. (2009b) used X-ray micro-CT to visualize a white-rot fungus (*Coriolus versicolor* [L.] Quél.) inside and on the surface of afzelia (Figure 2.18a), movingui (Figure 2.18b), European beech (Figure 2.18c), and Scots pine (Figure 2.18d) wood. They could easily observe fruiting bodies of the fungi on the outside of the wood, but the individual hyphae were difficult to identify even when they used submicron resolution CT. However, they were able to segment fungal tissues in wood based on intensity values from CT data and reveal the extent to which fungi penetrated into wood. They pointed out that their segmentation method was subjective and could falsely detect fungi at the edges of samples, and therefore they used differential imaging of CT images taken at different time frames. They visualized fungal tissues from the differences between time frames, but artifacts still occurred at the edge. Gilani et al. (2014) used synchrotron micro-CT to study the degradation of Norway spruce and sycamore (*Acer pseudoplatanus* L.) colonized by two fungi: *Xylaria longipes* Nitschke and *Physisporinus vitreus* (Pers.) P.Karst. They visualized the hyphae in cell lumens in 3D via volume rendering. They also quantified density changes in wood due to fungal activity and found that the density of sycamore wood was reduced more uniformly than that of Norway spruce wood. In Norway spruce, latewood tended to degrade more than earlywood. They also found that the density difference between earlywood and latewood decreased when the incubation time was increased. Koddenberg et al. (2020) examined the decay of Norway spruce, Scots pine, and European beech. However, their commercial X-ray micro-CT device was not able to visualize hyphae in wood. For this reason, their study focused more on the inorganic deposits they observed in their samples.

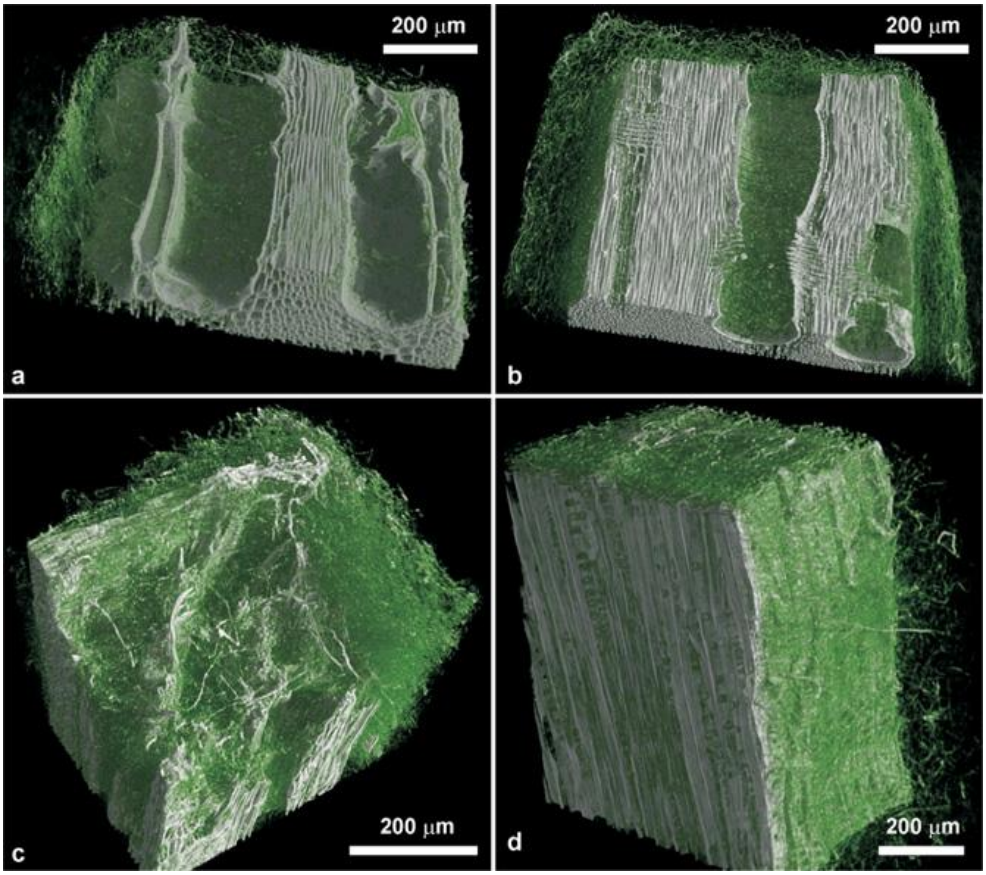

Figure 2.18 3D volume rendered images of hyphae (green) on wood (white): (a) afzelia; (b) movingui; (c) European beech; (d) Scots pine (Van den Bulcke et al. 2009b, adapted with free license granted by publisher)

2.5.4.3 Wood protection

There are many approaches to increasing the durability of wood against deterioration, for example, impregnating wood with preservatives, modifying the characteristics of wood, applying coatings to the wood surface, etc. X-ray micro-CT has been used to study various phenomena related to wood protection.

2.5.4.3(a) Preservative treatment of wood

Mannes et al. (2010) studied the penetration of a nanosilver water-repellent preservative into Norway spruce and European beech wood. They hypothesized that even a small amount of silver could act as a tracer in wood due to its high atomic number and attenuation of X-rays. However, their expectations were not met because it was difficult to detect low quantities of silver in the wood. Evans et al. (2013) studied the distribution of micronized copper azole (MCA) and alkaline copper quaternary

(ACQ) fungicidal preservative in treated southern pine (*Pinus* spp.) wood using X-ray micro-CT. They managed to detect copper in wood and found that the distribution of both preservatives coincided with the rays and the network of axial and radial resin canals in wood. Subsequently, Feng et al. (2019) revisited the CT data obtained by Evans et al. (2013). They found that both preservatives were concentrated in parenchyma cells which were adjacent to axial and radial resin canals, rather than resin canal voids. Also, in the MCA-treated sample, the epithelial cells surrounding radial resin canals were free of copper, and the surrounding axial resin canals rarely contained copper. In contrast, in ACQ-treated wood, copper was mainly located in epithelial cells around both axial and radial resin canals. They suggested that parenchyma cells were important pathways for the penetration of copper-based preservatives into wood. Their CT images were reconfigured for a virtual reality system so they could be used as an educational tool to enable students to understand the 3D distribution of copper-based preservatives in treated wood (Feng et al. 2020).

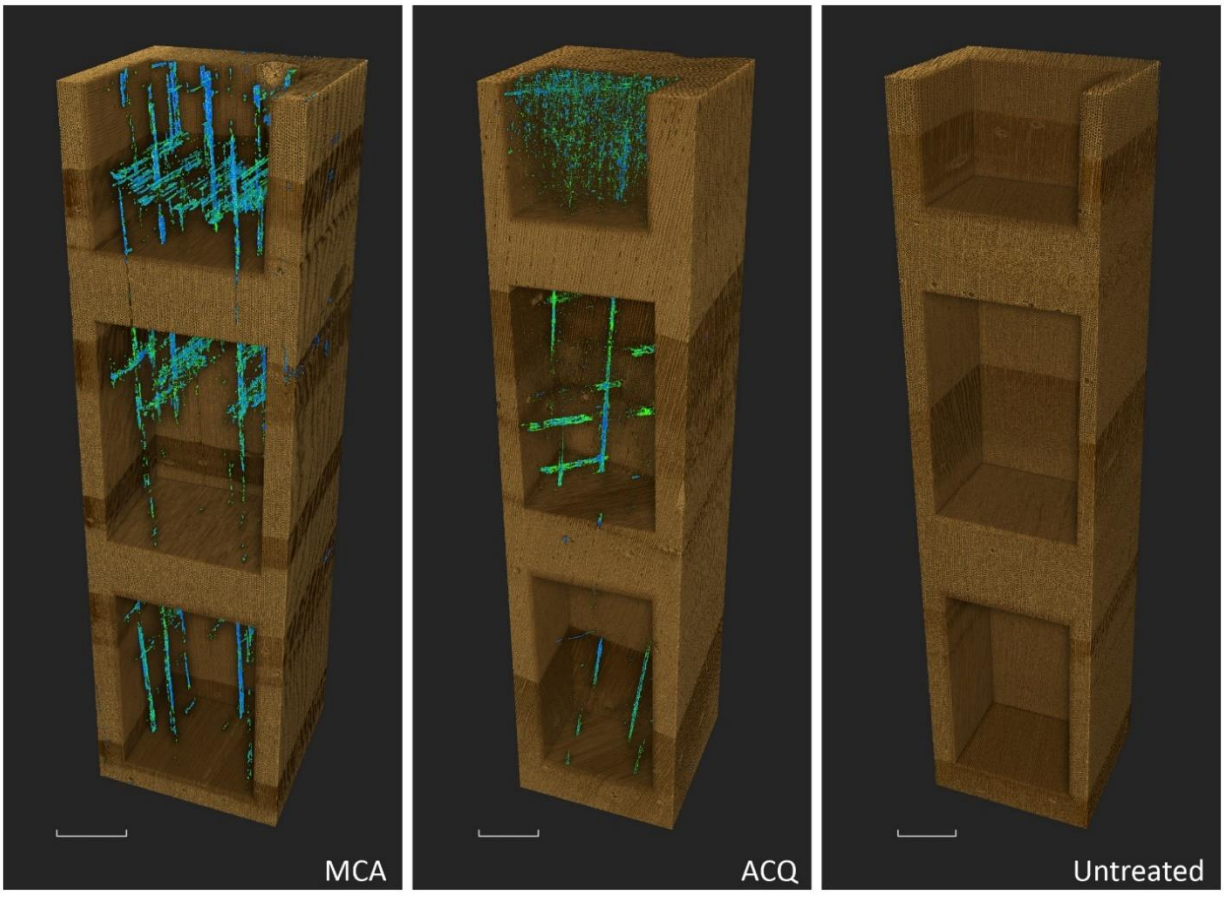

Figure 2.19 3D volume rendered images of copper-based preservatives (blue-green) in southern pine: left: MCA-treated sample; middle: ACQ-treated sample; right: untreated control. Scale bar = 2mm (modified from Feng et al. 2020)

2.5.4.3(b) Modification of wood

There are four main approaches to wood modification: (1) impregnation modification; (2) thermal modification; (3) chemical modification, and; (4) surface modification (Hill 2006). Wood modification using each of the first three approaches has been the subject of studies involving X-ray micro-CT. De Vetter et al. (2006) first used X-ray micro-CT to study the impregnation modification of wood with organic silicon compounds. They treated beech and Scots pine samples using two different methods: dipping and impregnating, and then scanned samples using X-ray micro-CT and visualized the distribution of silicon compounds in the samples. They found that the compounds were mainly located in cell lumens in the dipped samples, whereas in the impregnated samples, the compounds were in cell walls. They also studied the samples using SEM, and the results corroborated those obtained from tomography. Scholz et al. (2010a, 2010b) studied the impregnation of Scots pine and European beech wood with wax. They used X-ray micro-CT to visualize the location of wax in wood and quantify wax levels in samples. In pine wood, they observed wax in some axial and ray tracheids, while the ray parenchyma cells and some tracheids remained unfilled. In beech wood, they found wax in some but not all vessels. Wax was absent from rays and axial parenchyma. Their 3D images showed that air voids were mainly located in rays and areas adjacent to wax columns. Their quantification of the volume of different components in samples accorded with results from He pycnometry and Hg intrusion porosimetry. Tanaka et al. (2015) modified wood with an aqueous polymer to increase its homogeneity and dimensional stability. They impregnated hinoki wood with an aqueous solution of polyethylene glycol and studied the diffusivity of the solution as affected by relative humidity. X-ray micro-CT was used to image cross-sections of the samples. They also counted the number of polymer-filled cells and found that the number was negatively correlated with the relative swelling of the samples. Kielmann et al. (2016) used X-ray micro-CT to visualize resin in beech wood and found that the resin was mainly located in vessel lumens.

Micro-CT of thermally modified wood was first carried out by Van den Burke et al. (2013). They rendered 3D images of a thermally modified aspen sample and discussed the potential of X-ray micro-CT to evaluate changes caused by wood modification. Bizkis et al. (2015) subsequently used the same CT device as Van den Burke et al. (2013) to study the effect of thermo-hydro treatment on the microstructure of six wood species. They scanned the samples before and after treatment. Then, they segmented the cells and vessels from their CT data and quantified the volume of wood substrate,

porosity, and the maximum opening of pores. They found that species with higher porosity tended to show greater changes in wood microstructure. Another of their findings was that species with less cell wall substrate showed increases in porosity after treatment. In subsequent work Bizkis et al. (2019) used X-ray micro-CT to investigate density changes in Norway spruce and silver birch wood due to thermal-hydro treatment. They found that the density profiles of both species decreased when treatment temperature increased. They also found that density changes in earlywood and latewood in both species varied. Spruce wood showed similar decreases in earlywood and latewood density, but density changes in birch wood were more heterogeneous. Hamada et al. (2016) attempted to use X-ray micro-CT to study the density changes of oak wood after it was thermally modified. However, they were unsuccessful because they were unable to establish a correlation between mass losses and initial density of modified wood. Wentzel et al. (2020) used X-ray micro-CT to visualize microstructural changes in shining gum (*Eucalyptus nitens* [H.Deane & Maiden] Maiden) following thermal modification. However, they were unable to find significant differences between the microstructure of treated samples and the untreated control.

Studies on X-ray micro-CT of chemically modified wood emerged later than those on visualization of thermally modified wood or wood impregnated with polymers. Moghaddam et al. (2017) used X-ray micro-CT to study the wetting properties of furfurylated and acetylated longleaf pine (*Pinus palustris* Mill.) and maple (*Acer platanoides* L.) wood. They visualized the 2D and 3D microstructure of samples and quantified the porosity, cell wall thickness, and maximum opening of tracheids. They found significant microstructural changes in furfurylated samples, including a decrease in porosity, increase in cell wall thickness, and the deformation and polymer filling of tracheids or vessels. In contrast, their acetylated samples showed no significant microstructural changes. Their results showed that furfurylation reduced both capillary uptake and swelling while acetylation only reduced swelling. Söftje et al. (2020) studied the penetration of chemical agents in esterified Scots pine wood. They imaged their samples at high (1 µm) and low (14 µm) resolution. Their 3D rendering of the lower resolution images showed that the surfaces of the samples were highly modified. Their higher resolution images showed that latewood was completely modified while modification of earlywood was more variable. They also found that rays and resin canals were important pathways for chemicals to penetrate into wood.

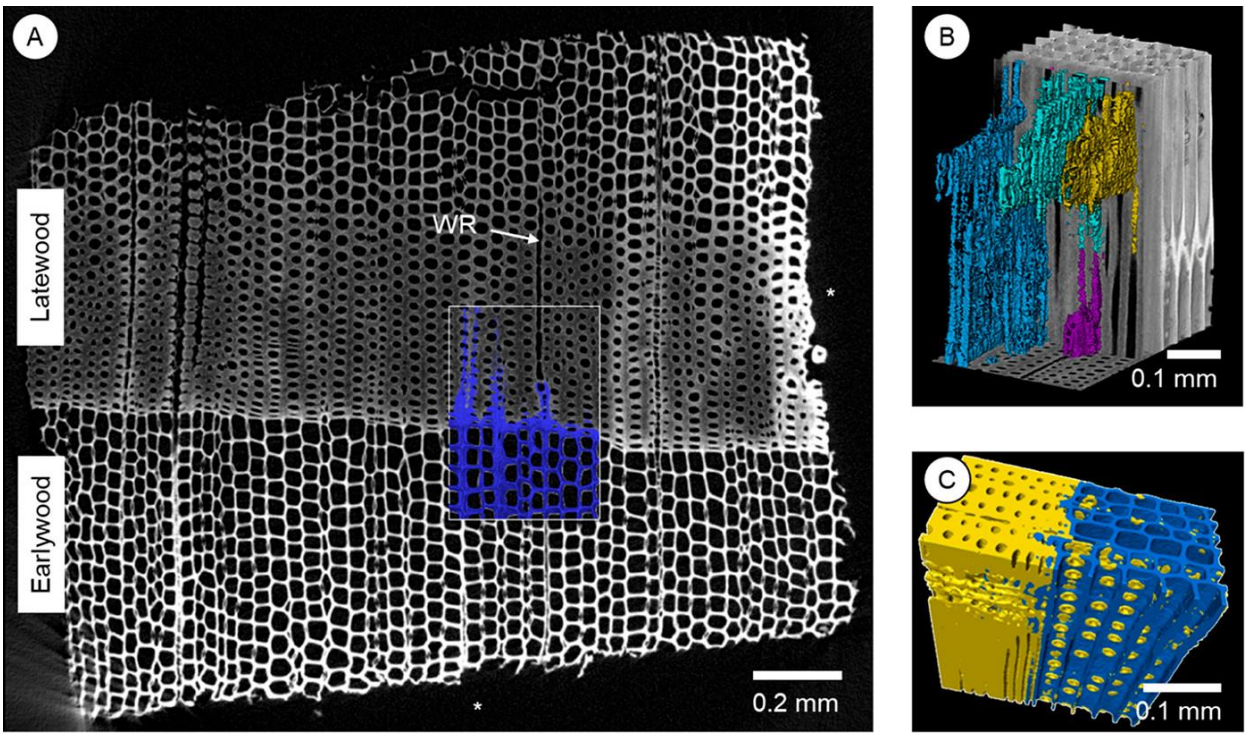

Figure 2.20 CT images of chemically modified Scots pine: (a) 2D transverse section of the sample, WR = wood ray, asterisk = border of the sample; (b) 3D volume rendered image of the selected region in (a), colored materials represent flows of chemicals; (c) 3D volume rendered image of a growth ring boundary, blue = high X-ray attenuation regions, yellow = low X-ray attenuation regions. Adapted with permission from {Söftje M, Koddenberg T, Militz H, Drafz MHH, Namyslo JC, Kaufmann DE (2020) Chemistry and spectroscopy of renewable materials, part 2: investigation of suitably esterified wood regarding penetration and distribution of the chemically modifying reagent by means of high-resolution 3D computed tomography. ACS Sustainable Chemistry & Engineering 8(19), 7353-7358}. Copyright (2020) American Chemical Society

2.5.4.3(c) Naturally durable wood

Koddenberg et al. (2019a) used X-ray micro-CT to study the silica content of turpentine, which is a silica-rich hardwood species that is resistant to attack by teredinid borers (Amos and Dadswell 1948). They used X-ray micro-CT to visualize the distribution of silica particles in their samples and confirmed findings from microscopy that silica particles are located in ray cells. They also quantified the silica content of samples, but they found that result from tomography (0.51%) underestimated the silica content when compared to that obtained from a gravimetrical method (0.60%). They listed three possible reasons for the underestimation: firstly, their method ignored the presence of silica in cell walls; secondly, the noise and artifacts in their CT images affected the results; thirdly, their CT method investigated a smaller region of interest compared to the gravimetric method. They also imaged silica

particles using SEM and found that the CT images smoothed out the details of the surface of silica particles. Feng et al. (2020) studied another silica-rich and naturally durable wood species, satinay, using X-ray micro-CT. They visualized silica particles in ray parenchyma cells and modified the CT data to make it suitable for a virtual reality system. Students using this system could interact with the 3D volume-rendered model of satinay and see silica particles located in ray cells, as well as other anatomical features of satinay. The virtual reality system received very positive feedback from students, and they preferred it to traditional methods of visualizing the anatomy of wood.

2.5.4.3(d) Wood coatings

Van den Burke et al. (2008) used X-ray micro-CT to investigate blue stain of pine wood coated with either a waterborne or a solvent-borne coating. X-ray micro-CT could visualize wood, coating, and fungal hyphae in 3D. They also quantified the porosity, thickness, and penetration depth of the coatings, the thickness of wood cell walls, and the lumen sizes of tracheids. Subsequently, Van den Burke et al. (2010) studied the microstructure of Scots pine and African padouk (*Pterocarpus soyauxii* Taub.) samples coated with either a waterborne or a solvent-borne coating. However, they did not specify the chemical composition of the coatings, nor the steps involved in coating application. They claimed their study was intended to illustrate the capability of their imaging and analysis methods, rather than to study wood-coating interaction in-depth. Nevertheless, they were able to separate coating from wood, and quantify surface roughness of wood, as well as thickness, penetration depth, porosity, and area of interface of the coating. Later, they displayed another segmented image of a coating on a Scots pine in their paper on modification of wood (Van den Burke et al. 2013).

2.6 X-ray micro-CT of wood composites

Wood composites and the sub-set of products known as engineered wood composites have replaced solid wood in many applications. The definition of engineered wood composites is varied and elastic. Guss (1995) described them as structural wood products made from smaller pieces of wood cut from roundwood, or from wood residues derived from other manufacturing processes. The resulting wood pieces are bonded together with adhesives to produce products that have specific mechanical properties, size and performance. Composites consisting of wood veneers or lamellae can also be interconnected with nails (Milner and Woodard 2016), dowels (Sotayo et al. 2020), or thermoplastics (Papadopoulos 2019). In some publications, engineered wood products also include non-structural products such as particleboard, fibreboard, and wood plastic composite (Sarfi et al. 2013, Ximenes et al. 2018, Markström et al. 2018).

2.6.1 Processing of wood composites

2.6.1.1 Adhesive bonding of wood

Modzel et al. (2011) studied phenol formaldehyde (PF) resin glue lines in glue-laminated timber. They visualized glue lines using a variety of methods including synchrotron X-ray micro-CT, fluorescence microscopy, backscattered electron imaging, SEM, and wavelength microscopy. To enhance the contrast of resin in X-ray images, they replaced the NaOH catalyst in the adhesive with RbOH, which has similar chemical characteristics to NaOH but has a much higher molecular weight and X-ray attenuation. The 3D structure of PF resin was clearly visible in the volume-rendered CT images. They concluded that X-ray micro-CT could provide a visual perspective of glue lines that other methods could not. Subsequently, Kamke et al. (2014), Paris et al. (2014), Paris and Kamke (2015), and McKinley et al. (2016, 2018) used the same synchrotron facility as Modzel et al. (2011) to investigate adhesive bonding of wood. They all used iodine as a contrast agent to tag resin in wood, except Paris et al. (2014) who used three contrast agents namely iodine, bromine, and rubidium. Kamke et al. (2014) acquired the 3D geometry of a lap-shear test sample bonded with PF resin. They then used the 3D geometry of samples to develop a mathematical model which simulated the stress and strain of the resin bondline under load. They validated their model by performing a real lap-shear test using the scanned sample. They also discussed

the limitations of their methods including the inability to detect resin in cell walls, and artefacts in tomograms. Paris et al. (2014) compared the effectiveness of the three contrast agents mentioned above, to highlight PF resin bondlines in synchrotron micro-CT images. They found that iodine and rubidium enhanced the contrast sufficiently, while rubidium was not effective because it could not attach to polymer chains in the resin. Paris and Kamke (2015) used micro-CT to study the penetration behavior of PF, polyvinyl acetate (PVA), and polymeric diphenylmethane diisocyanate (pMDI) resin in three species: loblolly pine (*Pinus taeda* L.), Douglas fir, and a hybrid poplar (*Populus deltoides* × *Populus trichocarpa*). They were able to quantify the difference in effective penetration and weighted penetration between different resin types and species. They also found horizontal cracks in 3D volume rendered images of PF glue lines. McKinley et al. (2016) exposed glue-laminated samples to an accelerated weathering process, and studied changes in the glue lines. They found cracks propagated in latewood regions in a cross-laminated latewood-earlywood sample. They also summarized their approaches to micro-CT of resin penetration, mechanical properties of bonding, and anatomy of bonded samples. McKinley et al. (2018) subsequently studied PF resin penetration in Douglas fir samples using high-resolution tomography with a voxel size of 60 nm^3. It was difficult for them to control the movement of samples during CT scanning, but they managed to detect PF resin in some of their scans and validated the results using energy-dispersive X-ray spectroscopy and X-ray fluorescence microscopy. Sterley et al. (2014) used conventional X-ray micro-CT to investigate polyurethane (PU) and phenol resorcinol formaldehyde (PRF) resin in bondlines in finger-jointed wood boards. They found that PU had deeper penetration and smaller bubbles in green wood than in dried wood, while PRF had the same penetration in greenwood and dried wood. Their CT images also showed that joints in greenwood had closer and more homogeneous contact than those in dried wood. Bastani et al. (2016) visualized the 3D flow pattern of PU resin in heat-treated wood. They found it difficult to segment wood from resin because of their similar densities, but they claimed that segmentation was still possible. Niemz et al. (2020) used in-situ synchrotron micro-CT to validate results from acoustic analysis of the shear strength of urea formaldehyde (UF) bondlines in wood. They observed that cracks formed along the boundary of growth rings in a longitudinal-longitudinal lamination. Wascher et al. (2020) used helical micro-CT to study melamine formaldehyde resin bonding enhanced by iodine in thermally modified and plasma-treated beech wood veneers. They visualized the distribution of resin and quantified the volumes of resin-impregnated and resin-filled parts of the samples. They found that the amount of resin that penetrated into wood was more than doubled by plasma treatment of samples (Figure 2.21).

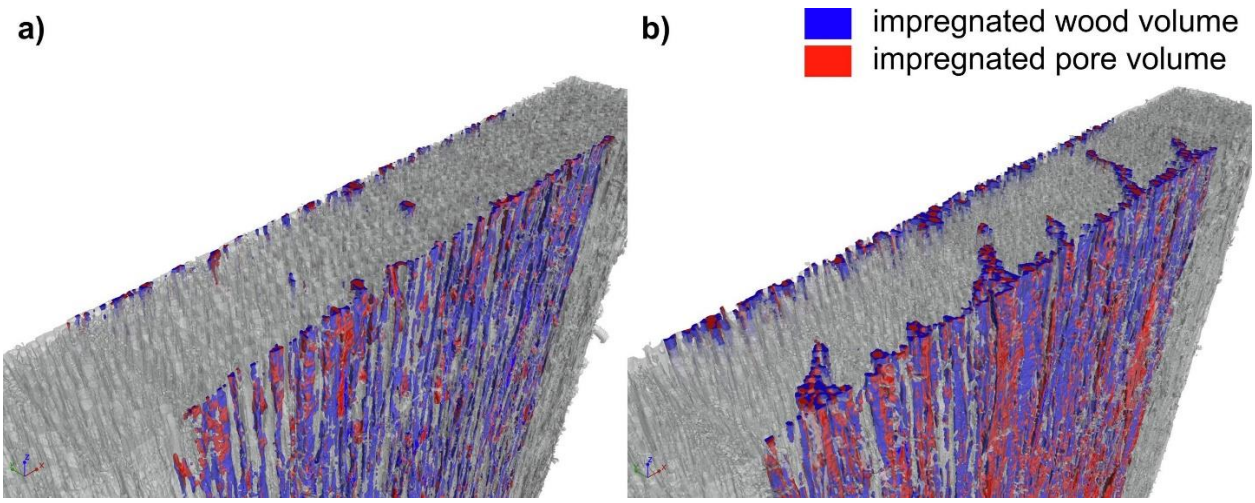

Figure 2.21 3D volume rendered images showing resin penetration in beech wood veneers: (a) control; (b) plasma-treated sample (Wascher 2020, adapted with permission granted via Creative Commons)

2.6.1.2 Fixings

Matsubara et al. (2017) studied the relationship between the withdrawal force of screws and the clamping force of timber joints. They used X-ray micro-CT to visualize the failure behavior of joints during pull-out and tightening tests. They found that overtightening the screws damaged the female threads in wood and caused splitting near the screw tips, while pulling out the screws only caused splitting. Korte et al. (2018) studied the fixing of softwoods using wooden nails. They used X-ray micro-CT to visualize the microstructure of the nail connections in 2D and 3D. They were able to visualize the areas in the wooden screw that were compressed when nails were forced into wood, as well as cracks in wood. They also quantified the porosity profile at the top and the bottom of the nail connection, and found that the porosity peaked in the areas near the wooden screws.

2.6.1.3 Wood welding

Wood pieces can be welded together by friction using similar techniques to those used for welding other materials (Vaziri et al. 2015). Vaziri et al. (2015) used X-ray micro-CT with a voxel size under 1 µm to study the density of the cell walls in the joints of welded wood. They found the bulk density of the welded joint was higher than the unwelded areas, but on the contrary, the cell wall density on the weld line was lower than that of the unwelded areas. They also found that anatomical features of wood in the weld line were almost completely unrecognisable and the wood substance

appeared as a compressed band, while the cells outside the weld line remained unaltered. They subsequently used medical CT and micro-CT to study the microstructural changes of welded wood with the addition of wollastonite (Vaziri et al. 2020). Micro-CT images showed that wollastonite was unevenly distributed in the welding interface due to uneven degradation in earlywood and latewood.

2.6.1.4 Wood machining

Matsuda et al. (2015) used X-ray micro-CT to study surface and subsurface microstructures of wood after slow-speed orthogonal machining with various machining parameters. They found that the cutting path matched the wood surface during Type 0 chip formation, but that was not the case for Type I, II, and III chip formation because fore-splitting, compression, or tearing can occur on the wood surface. They then used digital image correlation to evaluate subsurface damage to wood caused by slow-speed orthogonal cutting (Matsuda et al. 2017). They used X-ray micro-CT to non-destructively visualize the microstructure of the damaged wood. Their CT images revealed that there was a considerable amount of residual strain in the regions close to the wood surface.

2.6.2 Composite wood products

2.6.2.1 Fibreboard

Among the different types of fibreboards, medium density fibreboard (MDF) has been the subject of the majority of X-ray micro-CT studies. The first CT study of MDF was carried out by Walther et al. (2006). They scanned MDF samples with a synchrotron micro-CT device and then performed 3D visualization and segmentation of the fibres. They found that segmentation of the fibres was difficult because false positives and over- and under-segmentation always occured. Despite these problems, many correctly segmented fibres could still be acquired even in high density MDF. Walther and Thoemen (2009) subsequently used synchrotron micro-CT to justify the use of quantitative analyses of the volume and surface area of voids and fibres. They also tested iodine and barium sulfate as contrast agents to highlight adhesive in MDF, and found that iodine was better than barium sulfate as a contrast agent because it was more uniformly distributed. However, neither of the two labelling agents enabled segmentation of the adhesive from the fibres due to the lack of the resolution of their CT device. Standfest et al. (2009) in a German language publication described the use of X-ray micro-CT for density

measurement of MDF as well as particleboard and oriented strand board (OSB). They compared the results from CT with those from X-ray densitometry, and found that their CT results had a better fit in the core of the samples than at the surface. Li et al. (2016b, 2016c, 2018b, 2018c) published a series of studies of X-ray micro-CT of MDF and other types of wood composites. They used an in-situ micro-CT device to track movement of moisture in MDF and OSB (Li et al. 2016b). They found that water could move through large fibres and reach the interior of their samples within an hour. They also found that water repellent additives and adhesives could slow down water absorption. They also used X-ray micro-CT to visualize composite microstructure and map the mass loss of MDF and plywood samples during a fungal bioassay (Li et al. 2016c). They found that the decrease of elasticity of MDF after fungal decay was mainly due to the presence of internal cracks. A subsequent study observed local swelling in wet MDF, which compressed the fibres in nearby regions and caused those compressed regions to have increased water resistance (Li et al. 2018b). They also published a similar study in Chinese on moisture absorption, which also encompassed moisture absorption of plywood (Li et al. 2018c).

X-ray micro-CT has also been used to image low density fibreboard (LDF). Badel et al. (2008) performed an in-situ compression test of LDF. With the aid of synchrotron micro-CT, they were able to visualize microstructures in the sample and quantify its porosity, morphology, and density before and after compression. They found that macroscopic deformation accorded with microscopic evaluation of compression. They also developed a model to predict local densification in compressed LDF. Tran et al. (2013) used a similar in-situ experimental setup to study the compressive behavior of LDF. They found that the local porosity distribution affected the mechanical response of LDF.

Although wood fibre composites have been studied using X-ray micro-CT, it is difficult to compare results of different studies because of the lack of a standard data set. To set up a reference data set with known “ground truth”, Wernersson et al. (2009) used computer programs to generate synthetic fibres that represented real wood fibres in a composite. They created a data set with synthetic fibres and performed simulated X-ray micro-CT using the same reconstruction method as real micro-CT devices. They compared the reconstructed images to the original synthetic data set. They concluded that their method was useful for evaluating the image analysis methods for wood fibre composites.

2.6.2.2 Particleboard

There are fewer studies of micro-CT of particleboard compared to those of other wood composite types. Micro-CT densitometry of particleboard as well as MDF and OSB was carried out by Standfest et al. (2009) as mentioned above. Evans et al. (2010) used X-ray micro-CT to study the distribution of resin in pressed particleboard and unpressed wood particle mats. They labelled the resin with copper sulphate to enhance the contrast between resin and wood in CT images. Their labelling method enabled visualization and analysis of all phases (air voids, wood, and resin) in samples (Figure 2.22). They found that the bottom of the board (Figure 2.22c, e) contained a higher quantity of resin which formed a more complete network than those at the top and centre of the board. They showed that resin migrated into cracks in the pressed board (Figure 2.22f). In the unpressed mat, the resin had even coverage on the wood particles despite some areas that lacked resin. They used chord length analysis to quantify the sizes of voids, particles and gluelines in the pressed board. Nelis et al. (2018) studied the potential of kiri (*Paulownia tomentosa* Steud.) wood as a raw material for particleboard. Their mechanical test showed that the strength of particleboard was positively related to the amount of kiri particles used. They further investigated this finding using X-ray micro-CT. They found that kiri particles had good compression and many contact points between particles. They concluded that kiri wood was a suitable raw material for producing high strength particleboard.

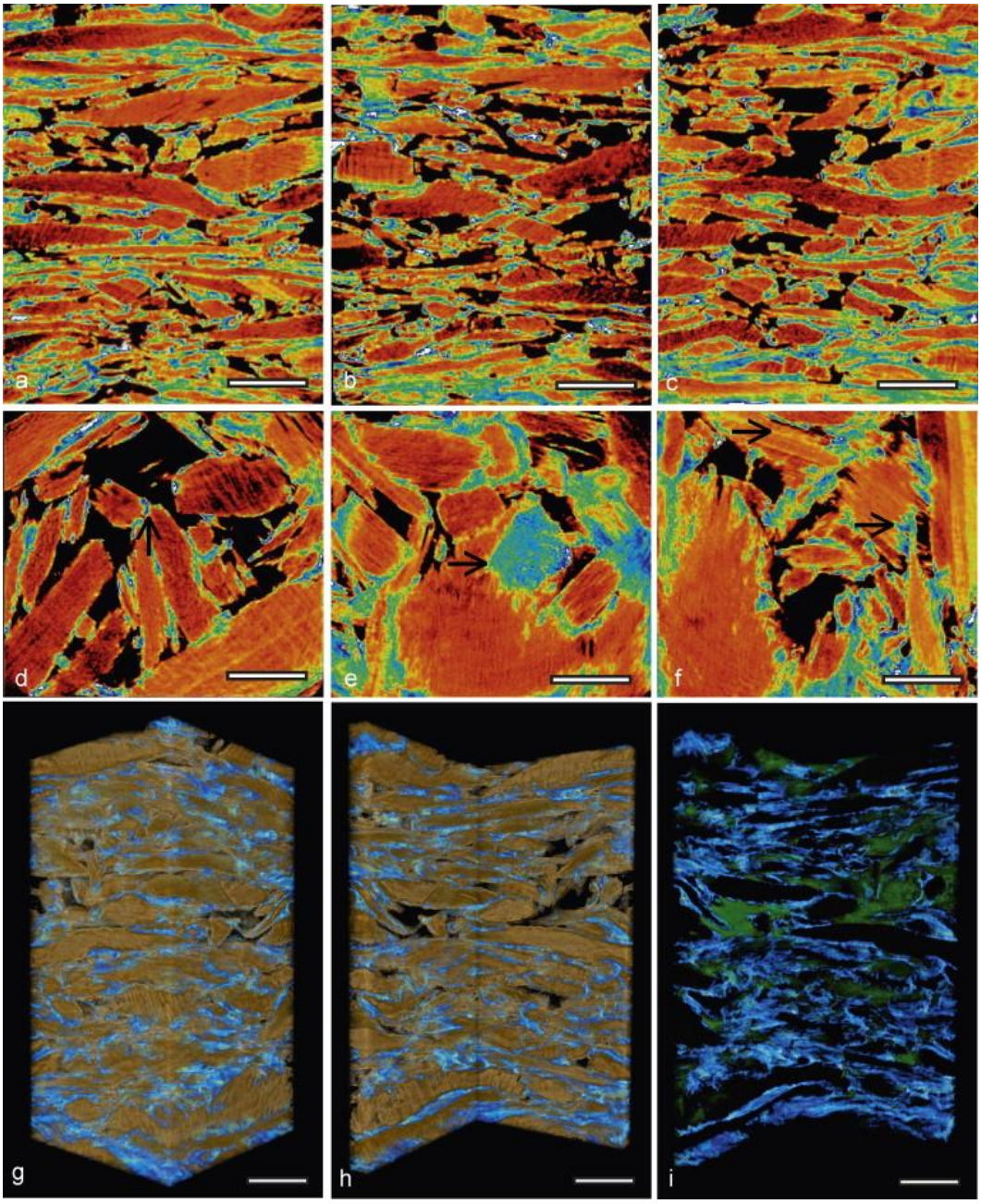

Figure 2.22 X-ray micro-CT images of resin, wood and void in particleboard: (a) 2D sectional image showing resin (blue-green), wood (red) and void (black). Note the long thin gluelines representing good interparticle contact; (b) 2D sectional image of an area with shorter and thicker particles, less well-developed gluelines, and larger voids (c) 2D sectional image showing accumulation of resin at the bottom; (d) 2D orthogonal view showing large voids and 'spot-welds' of resin between particles (arrowed); (e) 2D orthogonal view accumulation of resin (arrowed); (f) 2D orthogonal view showing resin accumulation in the splintered end (arrowed top) and resin penetration in flakes (arrowed bottom); (g) 3D volume rendered image showing wood (brown), resin (blue) and voids (black); (h) 3D volume rendered image showing inner structure of the volume; (i) 3D volume rendered image showing the network of resin (blue) and voids (green). Scale bars = 3 mm. (Evans et al. 2010, adapted with publisher's permission)

2.6.2.3 Plywood

Van den Bulcke et al. (2011) from the Ghent laboratory in Belgium used X-ray micro-CT to visualize fungal deterioration and moisture dynamics of plywood. They found that some of the panels with high moisture absorption had deeper cracks than those in panels that absorbed less moisture. They also found that thicker glue layers made the panel more moisture resistant, and cracks in glue lines lowered the moisture resistance of the plywood. Li et al. (2014, 2016c, 2016d, 2016e) also from the Ghent lab subsequently conducted a series of CT studies on plywood and other wood composites. They found that the moisture dynamics of plywood was affected by wood species, cracks in and between veneers, resin type, and grain direction (Li et al. 2014). They also observed that the plywood with grain directions perpendicular to glue lines absorbed less moisture and was less susceptible to fungal decay (Li et al. 2016c). They suggested that species type, presence of lathe checks, grain direction, gaps between veneers, and type of resin are key factors affecting the moisture stability of plywood (Li et al. 2016d). They also found that glue lines in plywood were still intact after one year of natural weathering (Li et al. 2016e). Li et al. (2018c) also published a paper in Chinese on X-ray CT of moisture absorption of plywood, OSB, and MDF. They concluded that the internal structure of plywood made it more dimensionally stable than MDF and OSB.

2.6.2.4 Oriented strand board (OSB)

Oh (2008) published a Korean paper about his work on the void structure of OSB. He found that large voids between strands could be detected using a low resolution X-ray micro-CT. Smaller (micro) voids could be detected using intermediate resolution, but they were clearer at high resolution. Evans et al. (2015) studied the distribution of zinc borate fungicide in OSB using X-ray micro-CT. They found that zinc borate particles were incorporated within glue lines in OSB and formed a layered structure within the composite. They observed that zinc borate was leached from OSB when it was exposed to water. They performed chord analysis on samples before and after exposure to water. This analysis revealed that zinc borate layers became thinner after leaching. Li et al. (2016b, 2018b, 2018c) used X-ray micro-CT to study the moisture resistance of OSB. They found that resin coverage and grain direction affected moisture uptake of their samples (Li et al. 2016b). They also found that smaller strands in a board were more resistant to moisture than large strands because they had better resin coverage (Li et al. 2016b). The swelling of OSB was mainly caused by swelling of wood strands and detachment of glue lines according to Li et al. (2018b). Voids could act as reservoirs that retained water (Li et al. 2016d, 2018b).

Phenol formaldehyde resin glue lines in OSB were more prone to delamination than pMDI resin glue lines (Li et al. 2018c).

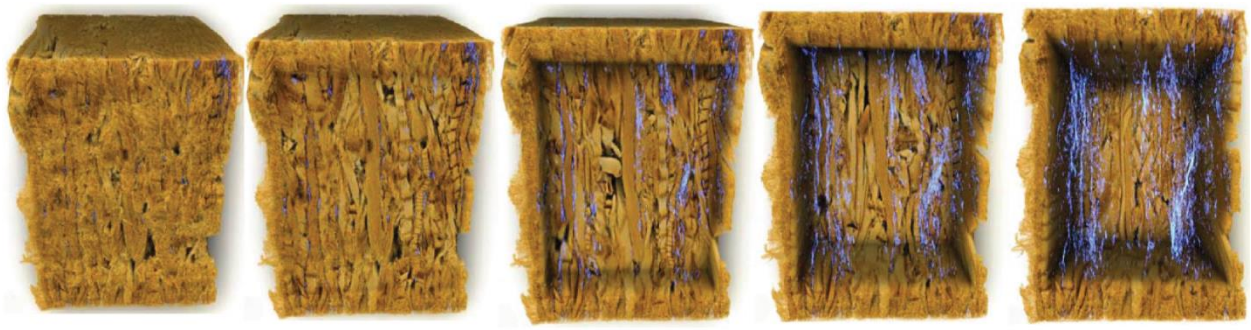

Figure 2.23 A series of 3D volume rendered images showing a block from a leached OSB sample. A virtual window which is transparent reveals the network of zinc borate within the OSB. Brown, wood; blue; zinc borate; black, voids (Evans et al. 2015, adapted with permission granted via Creative Commons)

2.6.2.5 Wood-plastic composite (WPC)

WPC is difficult to study using X-ray micro-CT because the X-ray attenuation of wood and plastic are very similar. Thus, in CT images of WPCs the contrast between wood and plastic is low (Wang et al. 2007). Wang et al. (2007) tried to solve this problem by using gold as a contrast agent in a WPC. They mixed gold particles with wood and plastic prior to making a WPC. They found that gold micro-particles were better than gold nano-particles as a contrast agent because they had more uniform distribution and less aggregation in the composite. However, neither of the particle types mixed well with the plastic, although gold micro-particles led to acceptable visualization of wood and plastic. Muszyński (2009) subsequently discussed the potential of digital methods associated with X-ray micro-CT for studies of WPCs, including digital image analysis, optical measurement of strains and deformation, inverse problem approach, and novel modelling methods.

X-ray micro-CT has also been used to study the moisture interactions and decay of WPC. Cheng et al. (2010) used X-ray micro-CT to study the changes in the microstructure of WPC after wetting and re-drying. They found that the top and bottom surfaces of WPC had lower void contents than the core. They also found that a re-dried WPC sample had 16% more voids in the core and 8.4% more voids in the top and the bottom compared to the unwetted sample. Joffre et al. (2013) studied the elastic and swelling coefficients of a WPC made with wood fibres and polylactic acid (PLA). They used finite element analysis to predict swelling coefficients and compared the outcomes with results from X-ray micro-CT

measurements. They found that the predicted and measured values were well correlated. Sun et al. (2014) examined the capability of micro-CT and other methods to visualize decay of WPC. They found that CT could visualize the microstructure of decayed WPC. It was particularly good at visualizing and quantifying the voids associated with decay. Sun et al. (2016) subsequently used X-ray micro-CT and SEM to focus on the voids in decayed WPC. They observed that voids in decayed samples were mostly interconnected, and suggested that moisture induced swelling and fungal decay created a network that was more complete than that in the undecayed control. Krause et al. (2017) studied the water resistance of a WPC made with sustainably sourced short-rotation coppice and low-value beech wood flour. They used X-ray micro-CT to visualize the inner structure of the WPC and measure the geometry of the particles. They were able to visualize larger wood particles, but small particles were not well distinguished due to the relatively low (7.5 µm) resolution of their images and poor contrast between wood and plastic. Krause et al. (2019) subsequently investigated calcium deposits in decayed WPC. Their CT images clearly showed that the deposits were in voids created by fungal degradation. Apart from the swelling and decay, X-ray micro-CT has also been used to investigate other properties in WPC. For example, Baltazar-y-Jimenez et al. (2011) studied the properties of WPC modified with bismaleimide to improve its physical performance and interfacial microstructure. Their 3D rendered CT images showed that wood fibres in untreated samples tended to aggregate, whereas fibres in the treated samples had better dispersion in the composite. They also found that samples processed at 250°C were more uniform than those processed at 180°C.

X-ray micro-CT has also been used to quantify the geometries of wood particles in a WPC. Miettinen et al. (2012) developed an approach for measuring the length of wood fibre in micro-CT data sets of a WPC. They validated their method by comparing their results with those from manual measurements. Similarly, Chinga-Carrasco et al. (2012) developed a method for length estimation of fibres in WPC, but their method was designed for desktop scanners instead of micro-CT devices. They only used micro-CT visualize the WPC. Joffre et al. (2014) used X-ray micro-CT to study fibre length degradation during the manufacture of WPC. They found that the reduction in fibre length mostly occurred during extrusion. Joffre et al. (2017) subsequently used X-ray micro-CT to study the ability of acetylated fibres in WPC to transfer stress during crack formation. They evaluated the adhesion of wood fibres to the plastic matrix by measuring the length of fibres that were pulled out or broke during the formation of cracks. They found that acetylated WPC was 30% stronger in the wet state, because fibres in this state tended to break instead of being separated from the plastic matrix and then pulled out.

Bacaicoa et al. (2017) compared the 2D and 3D quantification of the microstructure of various materials including WPC. They used X-ray micro-CT and 2D dynamic image analysis to quantify the size and aspect ratio of wood particles in WPC. They found that a 2D method was inaccurate, while a 3D method yielded acceptable information on the size and aspect ratio of wood reinforcement. Krause et al. (2018) studied the properties of WPC made with recycled wood particles. They used X-ray micro-CT to visualize the microstructure of their samples and quantify the dimensions and aspect ratios of the wood particles and the composition of the samples. They found that wood particles formed a pattern following melt flow at the surface and perpendicular to the melt flow at the core. They also found that the length and aspect ratio of particles became smaller during the processing of the WPC.

2.6.2.6 Other wood composites

X-ray micro-CT has also been used to examine the structure of organic composites made with wood and other bio-based materials. Wieland et al. (2013) studied the mechanical properties of a composite made from wood and leather particles. They only used X-ray micro-CT to study the distribution of voids because wood and leather could not be distinguished in their CT images. They found that a composite made with 75% wet blue leather particles had fewer pores with a more uniform distribution than a composite containing 25% leather particles. Revin et al. (2016) visualized a composite made from sawdust, lignosulfonate, and a bacterial culture. They found that addition of lignosulfonate and the bacterial culture reduced the number of voids and defects in samples. Goldhahn et al. (2020) used micro-CT and SEM to visualize a membrane material made from wood and gelatin. They discovered that meniscus-like structures formed in vessels after gelatin impregnation and subsequent drying.

X-ray micro-CT was also used to visualize composites composed of wood and inorganic matter. Wilkes et al. (2009) visualized silicon carbide (SiC) derived from beech wood carbon and a composite made with SiC and aluminum. X-ray micro-CT revealed the inner microstructure of pyrolyzed beech wood, the wood-derived SiC, and the composite. They quantified the porosity and connectivity of pores in the wood-derived SiC. Johnson et al. (2013) studied a copper-graphite composite containing graphite derived from wood. They used X-ray micro-CT to visualize the distribution of copper in the composite, but they could not visualize wood carbon and the air because these phases attenuated X-ray to similar degrees. They found that copper was deposited near the surface of samples and grew over time during an electroplating process. They also found that adding an electroplating leveler increased the level of copper deposition, and adding an accelerator to the leveler further increased copper deposition.

2.7 Other wood-related X-ray micro-CT studies

X-ray micro-CT is widely used in archaeology. The microtomography of archaeological objects was pioneered by Taguchi and Saito (1991) who used a purpose-built X-ray CT device that shared many of the features of modern micro-CT devices. Their device had a resolution of 0.3 mm which is lower than many modern devices. As a result, they were able to study the internal structure of archaeological objects such as a clay figure and slag from iron-making in ancient Japan. They mentioned that their device was able to successfully image other materials including wood, although they provided few details. More recently, archaeologists have been using contemporary X-ray micro-CT devices to study wooden objects. Mizuno et al. (2010) used synchrotron micro-CT to identify the wood from an ancient mask. They scanned a small piece of wood which fell off from the mask during restoration. Judging from the tangential, radial, and transverse sectional images from the CT data set, they suggested that the wood was *Salix* sp. Wörle et al. (2012) studied methods for removing pesticide contamination from wooden antiques in museum collections. Using synchrotron micro-CT, they evaluated one of the decontamination methods which involved treating the object in a vacuum chamber with controlled temperature and pressure. They found that the test specimen showed no significant change after the treatment, although damage to wood cells could occur if the sample was treated at a high temperature. Friml et al. (2014) used X-ray CT to visualize Cheb intarsia, an ancient wood decoration technique from the Czech Republic. They scanned a replica of an antique wooden game chip and also an antique wooden box from a museum collection. They were able to visualize the layered wood structure and cracking in the decorated panel.

X-ray micro-CT has also been used to visualize larger archaeological wooden objects, for example shipwrecks and waterlogged wooden items. Bugani et al. (2009) used X-ray micro-CT to study the preservation of waterlogged archaeological wood after impregnation with polyethylene glycol (PEG) and polypropylene glycol (PPG). They used synchrotron micro-CT to scan cuboid wood samples from ancient shipwrecks. They observed different filling behaviours depending on the formulation. Svedström et al. (2012a) studied the structure of oak wood from the sunken Swedish warship, the Vasa. They were able to visualize the anatomical characteristics of the wood such as vessels, tyloses, parenchyma, and fibres, but they were unable to resolve the chemical and bacterial degradation of the wood. Endo and Sugiyama (2013) studied the effect of keratin treatment on the structure of waterlogged archaeological wood. They used synchrotron micro-CT to evaluate the penetration of keratin into the specimens, and

found excessive keratin in tracheids when the treatment solution contained 30% keratin. In contrast, keratin was absent from tracheid lumens when the treatment solution contained 20% keratin. Eriksen et al. (2016) studied the relationship between wood anisotropy and the damage to wood caused by shipworms in underwater archaeological sites. They used X-ray micro-CT to visualize shipworm tunnels in wood panels cut in the tangential, radial or transverse directions. They found that the panels cut in the radial direction suffered greater damages than those cut in tangential or transverse directions.

The non-destructive nature of X-ray micro-CT makes it suitable for studying delicate antique musical instruments. Sodini et al. (2012) used CT as a non-destructive method for the inspection of antique violins. Initially they scanned a commercially purchased violin using a synchrotron micro-CT device. Then, they used the same method to scan a valuable antique violin made in 1753. They were able to observe important structural details in the violin, such as wood patches, fillers, wood deformation, and worm holes. Fioravanti et al. (2017) used CT to identify the wood species used to make eight antique music bows. They generated tangential, radial, and transverse sectional images, and identified the wood species. They found that three of the bows were made of snakewood (*Brosimum guianense* [Aubl.] Huber ex Ducke), one was Pau Brasil wood (*Caesalpinia echinate* Lam.), and four were Manilkara (*Manilkara* sp.). Viljanen et al. (2020) used X-ray micro-CT to study tropical and temperate hardwood species used as tone woods for musical instruments. They were able to visualize vessels and rays in the samples, but were unable to visualize the structure of tension wood in some tropical hardwood species due to their high density.

X-ray micro-CT is not only used to visualize man-made wooden heritage items, but also ancient natural samples such as fossils. Strullu-Derrien et al. (2013) published a review article about the hydraulic systems in plant fossils, and discussed the potential of synchrotron micro-CT to visualize the microstructure of fossils. They provided 2D and 3D tomographical images to show the capabilities of micro-CT for visualizing fossils and segmenting tracheid lumens. Strullu-Derrien et al. (2014) subsequently used synchrotron micro-CT to study the earliest wooden fossils that were estimated to be 407 million years old (Figure 2.24). They visualized bifurcated rows of tracheids (Figure 2.24c) and wall structures in different types of cells (Figure 2.24c, e). They suggested that the wood evolved from plants that belonged to Euphyllophytina. Quantitative analyses of the samples revealed that the wood had a high hydraulic conductivity, but a low resistance to hydraulic tension.

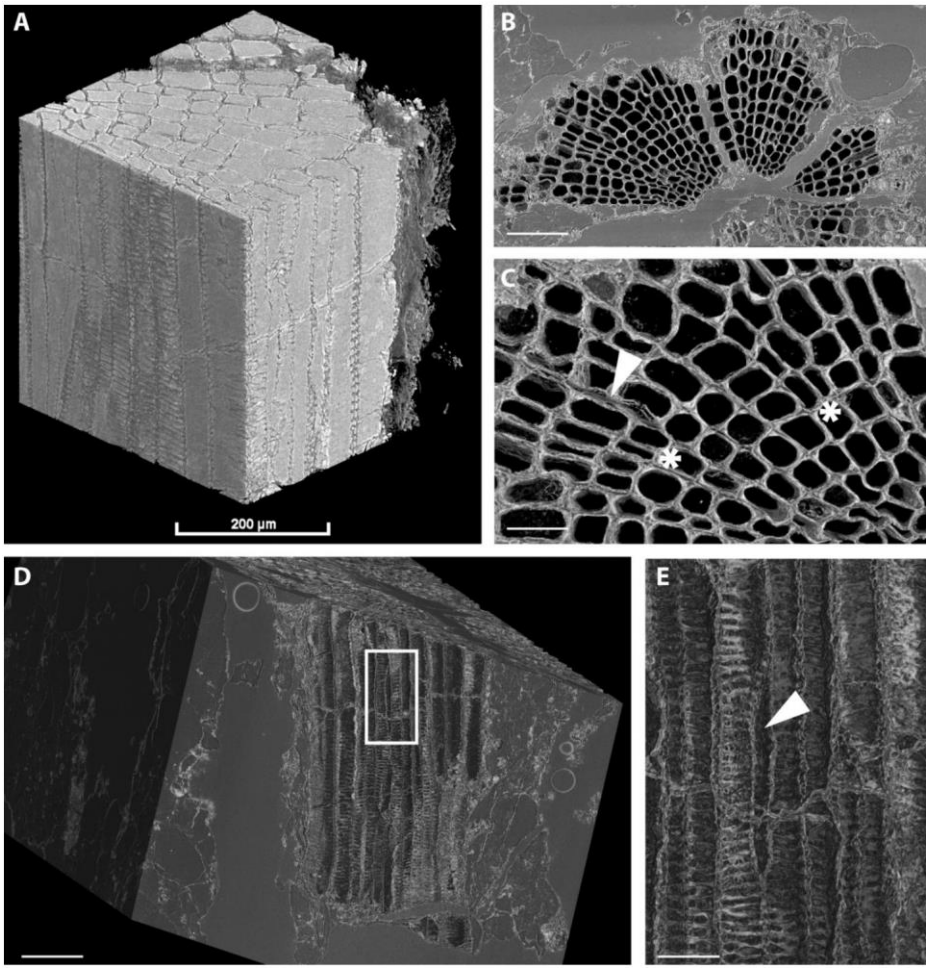

Figure 2.24 X-ray micro-CT images of a 407-million-year-old wood fossil: (a) isometric view; (b) transverse sectional image; (c) close-up image showing single rows of cells split into two rows (asterisks), and also a single-walled ray (arrow); (d) tangential-longitudinal section; (e) close-up image showing tracheids with double-walls in between, and a one-cell ray with single-walls (arrowed) (Strullu-Derrien et al. 2014, adapted with publisher's permission)

Fresh wood can also provide historical information, for example, dendrochronology is a subject that derives historical information from the structure of tree growth rings. X-ray micro-CT is particularly suitable to dendrochronology because of its non-destructive imaging and ability to detect density differences in wood. Okochi et al. (2007) tested the capability of X-ray micro-CT for dendrochronology. First, they scanned wood strips using X-ray micro-CT and conventional X-ray radiography and compared the images. They selected X-ray micro-CT in preference to radiography to scan small wooden artistic objects. They went on to use X-ray micro-CT to capture detailed images of tree rings in samples where X-ray radiography was unable to provide clear images. De Ridder et al. (2011) used X-ray CT to study the density pattern of growth rings in limba (*Terminalia superba* Engl. & Diels). They found that their data

showed a high correlation with density values acquired gravimetrically. Van den Bulke (2014) used a helical micro-CT device for dendrochronological analyses including 3D visualization, densitometry, ring width analysis, and segmentation of vessels. De Mil et al. (2016) developed a tool chain for studying the density of tree rings. X-ray micro-CT was used to acquire greyscale values of wood samples and convert such values to density data. Jacquin et al. (2017) reviewed the use of X-ray densitometry, including X-ray micro-CT, for dendrochronology. They concluded that micro-CT performed well but was more time-consuming than other methods because of the time required for image acquisition and reconstruction. Vannopen et al. (2017) were interested in measuring tree ring widths for evaluating tree growth. They compared measurements obtained from 2D microscopy and X-ray micro-CT, and found that X-ray micro-CT was less laborious and could output density data, although the resolution was lower than their 2D method. They also found that measurements from micro-CT were not significantly different from those acquired using a 2D method. Van den Bulcke et al. (2019) studied the capability of their X-ray micro-CT devices to scan tree rings at multiple levels of magnification. They scanned wood cores at different resolutions from 60 µm to 0.8 µm. They were able to acquire cross-sectional images, ring widths, wood trait data, and density profiles from their samples. They concluded that X-ray micro-CT could significantly assist research related to tree rings and the environment.

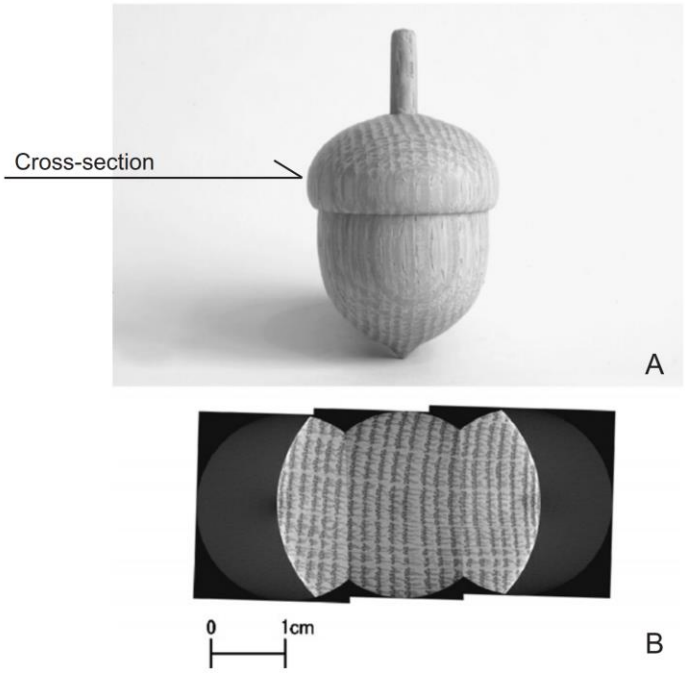

Figure 2.25 Japanese spinning top made from Japanese oak (*Quercus crispula* Blume): (a) photo of the toy; (b) X-ray micro-CT cross-sectional image (Okochi et al. 2007, adapted with publisher's permission)

Woody biomass can be a sustainable material for biofuel. Penttilä et al. (2013) studied the ability of hot water extraction to improve the suitability of wood sawdust for the production of biofuel. They used X-ray micro-CT to visualize the structure of sawdust and the thickness of cell walls. Cell wall thickness decreased after treatment, but less than they were expecting. Muzamal et al. (2016) studied steam explosion treatment of wood chips to increase their accessibility to the enzymes which are used to convert wood into biofuel. They used X-ray micro-CT to visualize treated and untreated samples and found that the 3D microstructure of the tracheids was altered by the steam explosion (cell walls cracked and the edges of the samples were ruptured although the inner regions of samples were less affected). They concluded that such structural changes could allow enzymes to easily penetrate the outer parts of samples but not the inner parts. X-ray micro-CT has also been used to study the effect of fire on the microstructure of wood. For example, Meincken and du Plessis (2013) used it to study the thermal degradation of wood caused by fire. They visualized the microstructure of wood samples which were exposed in a furnace. They also quantified volumes of the samples, the density and thickness of cell walls, and the diameter of cell lumens after treatment. They found that the volume and cell wall density decreased after thermal treatment. A temperature of 250 °C was a threshold beyond which the decrease of density and cell morphology became very noticeable causing the wood to be unsuitable for structural uses. Gilani et al. (2013) used in-situ synchrotron micro-CT to study the cracking formation in wood during fire exposure. They found that cracking mainly formed along rays and transition zones between earlywood and latewood. They also observed an increase in porosity of their samples after fire.

2.8 Concluding summary

X-ray imaging methods commonly used in wood-related research are X-ray radiography, macro-CT, and micro-CT. X-ray radiography is the earliest adopted technique of the three methods. It is used for measuring wood density (Polge 1966), visualizing voids caused by marine borers (Oliver 1959) and insects (Jacquiot 1961), metallic objects (Koene and Broekhuis 2017, 2019), moisture distribution (Yamamoto et al. 1983), and native wood features in logs (Grundberg and Grönlund 1997). The main disadvantage of X-ray radiography is that it is a 2D method. Thus, it is difficult to use it to study 3D features in wood. In contrast, X-ray computed tomography techniques, including macro- and micro-CT, can produce 3D images by stacking up a series of cross-sectional images. Medical CT devices were the first to be used for wood research (Benson-Cooper et al. 1982). More recently, purpose-built X-ray macro-CT devices designed specifically for wood were introduced to the commercial market (Giudiceandrea et al. 2011). X-ray macro-CT has been gradually replaced by X-ray micro-CT in applications where resolution and level of magnification are important, but X-ray macro-CT is still more suitable for scanning larger wood objects such as logs (Section 2.2.3.4).

X-ray micro-CT was invented by Elliott and Dover (1982) and adapted for wood research by Davis et al. (1991). In the early stage of X-ray micro-CT of wood, synchrotron X-ray sources which are powerful, but expensive and less accessible to scientists, were often used because of the advantages in resolution, scan time, and noise control (Illman and Dowd 1999, Mannes et al. 2009). Later, lab-based micro-CT devices with conventional X-ray sources were adopted for wood research (Steppe et al. 2004) and quickly developed capabilities that match those of synchrotron micro-CT devices, for example, resolution (Van den Bulcke et al. 2009a). The image quality of lab-based X-ray micro-CT has greatly improved since the introduction of helical reconstruction by Katsevich (2002). Synchrotron micro-CT is still used today because of its superior image quality and scan speed. X-ray micro-CT is used in both qualitative (Davis et al. 1991) and quantitative studies (Illman and Dowd 1999). Today, X-ray micro-CT is widely used in wood-related research (Section 2.5) including wood products (Section 2.6), as well as other areas such as archaeology, paleontology, and dendrochronology, as described in Section 2.7.

Chapter 3: X-ray Micro-CT Visualization of Inorganic Materials in Siliceous Australian Hardwood Species

3.1 Introduction

Silica is present in wood as aggregate particles in ray and axial parenchyma cells or as dense silica in vessels and ray parenchyma cells (Scurfield et al. 1974). Silica increases the resistance of wood against marine-boring organisms according to Amos and Dadswell (1948), but it also dulls cutting tools and make wood difficult to machine (Darmawan et al. 2011). Some tropical wood species have high silica contents (Fengel and Wegner 1984). For example, the tropical Australian species turpentine (*S. glomulifera*) and walnut bean (*E. palmerstonii*) have silica contents in excess of 0.33% and 0.74%, respectively (Swain 1928). Silica occurs in these two species as silica aggregates in ray parenchyma cells (Bamber and Layon 1960, Richter 1980). Similarly, the tropical Australian species brush box (*L. confertus*) also has silica aggregates in rays (Bamber and Layon 1960). In addition to silica, tropical wood species also have a high total content of inorganic materials (Fengel and Wegner 1984). For example, walnut bean has an inorganic ash content of 0.9-1.3% (Swain 1928). In contrast, pine (*Pinus* spp.) species have lower ash contents of 0.2-0.5% (Pettersen 1984). However, this is not always the case since the tropical Australian species turpentine and white beech (*G. leichhardtii*) have moderate ash contents of 0.367% and 0.18%, respectively (Swain 1928).

Traditional microscopy methods such as optical microscopy (Bamber and Layon 1960) and scanning electron microscopy (Hillis and de Silva 1979) have been used to investigate silica in wood. These methods are capable of visualizing silica, but they have shortcomings such as complicated sample preparation (Jansen et al. 1998), being destructive, and inability to reveal the spatial distribution of silica (Koddenberg et al. 2019a). X-ray micro-computed tomography (micro-CT) is able to reveal the three-dimensional distribution of silica non-destructively, because silica has a higher density (2.20 g/cm^3, Barsan 2007) than wood cell walls (1.497-1.517 g/cm^3, Kellogg and Wangaard 1969). Thus, silica and wood can be separated based on intensity contrast in CT images. X-ray micro-CT was used by De Vetter et al. (2006) to study the distribution of organic silicon treatments in wood, and by Koddenberg et al. (2019a) who investigated the distribution of silica aggregates in turpentine. Therefore, I hypothesize that X-ray micro-CT will reveal the spatial distribution of silica in siliceous wood species. I selected three tropical Australian species which are known to be silicious: turpentine, brush box, and walnut bean;

another tropical Australian species satinay (*S. hillii*) which is closely related to turpentine (Boas 1947) but whose silica (if any) is undescribed; and a non-silicious tropical Australian species white beech for contrast.

3.2 Materials and methods

3.2.1 Description of selected species

The selected species are described below. All of the species are no longer available commercially although they can be grown in plantation.

3.2.1.1 Turpentine

Turpentine (*S. glomulifera*) is a hardwood species found in eastern Australia. Its common name "turpentine" is due to the presence of a small amount of oleo-resin in its inner bark (Boas 1947). Turpentine wood has good mechanical properties. It has a modulus of rupture (MOR) of 8,600-19,900 lb/in^2 (59.29-137.21 MPa), a modulus of elasticity (MOE) of 2,223,000-2,387,000lb/in^2 (15327.04-16,457.79 MPa), and a crushing strength of 7,480-9,900 lb/in^2 (51.57-68.26 MPa) (Swain 1928). Turpentine wood has low workability. It is difficult to machine and cut with both hand and power tools and dulls cutting edges rapidly (Constantine 2005). It also requires careful air drying prior to kiln drying to avoid excessive shrinkage collapse (Constantine 2005). Australian-grown turpentine is famous for its excellent marine borer resistance. Its marine borer resistance is rated as Class 1 in Australian Standard AS-5604, which means it can remain in service for more than 60 years in southern (colder) waters of Australia, and 12-30 years in warmer northern waters in which marine borers are more active (Standards Australia 2005). Turpentine's natural marine borer resistance is thought to be associated with its high silica content. Evidence to support this statement comes from a study by Amos and Dadswell (1948). They found that Australian-grown turpentine which resists marine borer attack has a higher silica content (0.59%) than Hawaii-grown turpentine (0.09%), which is not resistant to marine borers. However, de Silva and Hillis (1980) questioned the contribution of silica to marine borer resistance of turpentine because silica is unlikely to form a physical barrier to marine borers. They suggested that the extractives content of turpentine confounded the correlation between silica content and marine borer resistance. Apart from being durable in the sea, turpentine has good resistance to

microbial attack since it is rated as Class 1 above-ground and Class 2 in-ground (Standards Australia 2005). Turpentine is also termite and fire resistant (Swain 1928). A turpentine tree can resprout after a bushfire thanks to its fire-resistant epicormic structures (Burrows 2008). Turpentine wood is not available now, but it was used in the past for applications that require durability and high strength, such as wharf piles, shipbuilding, railway sleepers, fence posts, bridges, etc. (Swain 1928).

3.2.1.2 Satinay

Satinay (*S. hillii*) is a hardwood species mainly found on Fraser Island in Queensland, Australia. Its common name "satinay" derives from its resemblance to satiné wood (*Brosimum rubescens* Taub.) from French Guinea, while its other common name "Fraser Island turpentine" is used because of its resemblance to its allied species turpentine (Boas 1947). Compared to turpentine, satinay has longer leaf petioles, and also its flower hypanthia are glabrous (hairy) unlike turpentine whose flowers are sericeous (smooth) (Bean 1995). Satinay wood can be distinguished from turpentine wood because it has thinner fibre walls and larger pores than turpentine wood. In addition, it has bi- and tri-seriate rays while turpentine has only uniseriate rays (Welch 1929). Satinay wood performs well in tension, compression, shear, and hardness tests, but it lacks toughness and tends to be brittle (Welch 1929). It can be cut cleanly and crisply, but tends to dull cutting edges quickly (Welch 1929). Satinay has excellent natural durability. It is resistant to termites and can last in the ground for 15-25 years, above ground for more than 40 years, and in southern seas of Australia for more than 60 years (Standards Australia 2005). Satinay wood is very resistant to fire. Its fire resistance is twice that of the most fire-resistant American timber redwood (*Sequoia sempervirens* [D.Don] Endl.), but only half that of turpentine, which is the most fire-resistant wood species in Australia (Swain 1928). Like turpentine trees, satinay trees can resprout after fire because the species has fire-resistant epicormic structures (Burrows 2008).

Satinay wood is no longer available commercially, but it was used for poles, fencing, building construction, trains, high-class furniture, smaller objects such as fishing rods, tool handles, cask headings, etc. (Boas 1947). Commercial availability of satinay was curtailed when logging on Fraser Island was banned (Cookson and Scown 2008).

3.2.1.3 Brush box

Brush box (*L. confertus*, synonym *Tristania conferta* R.Br.) is a hardwood species from the rainforests in New South Wales and Queensland, Australia (Bootle 1983). It has also been grown in

plantation in Hawaii and Oahu (Skolmen 1974). Brush box has good hardness, toughness, and wear resistance (Wallis 1970). It also has some degree of natural durability. For example, it has good termite resistance and moderate decay resistance (Boas 1947, Bootle 1983). Cookson and Scown (2008) tested the marine borer resistance of various wood species including brush box. They found that their brush box samples were still intact after four years of exposure to teredo, limnoria and other marine borers. However, most samples had moderate to moderate-heavy damage, some had light or heavy damage. Brush box planted in Hawaii has lower density, strength, and durability compared to Australian-grown brush box (Skolmen 1974). Brush box is difficult to cut because it is denser and contains interlocked grain and silica (Bootle 1983). However, Hawaii-grown brush box is not abrasive to saws according to Skolmen (1974).

Brush box is regarded as the best timber for jetty decking and bridges in New South Wales, and was the most popular wood for flooring in eastern Australia (Wallis 1970). It has other uses such as for general building constructions, and in the past for mallets and tram rails (Dadswell and Eckersley 1935). Large quantities of brush box were used as acoustic panels in the Sydney Opera House (Taylor and Claringbold 2010). Hawaii-grown brush box was used for pallets (Skolmen 1974).

3.2.1.4 Walnut bean

Walnut bean (*E. palmerstonii*, synonym *Cryptocarya palmerstonii* F.M.Bailey), also known as Queensland walnut, is a hardwood species native to northern Queensland, Australia. Unlike its name suggests, walnut bean belongs to the family of Lauraceae rather than true walnuts (*Juglans* spp., family Juglandaceae) (Meier 2016). Walnut bean wood can have visually appealing broken-stripe or chequered grain textures like European walnut (*Juglans regia* L.) (Porter 2014). It has a high crushing strength (68.6 MPa), moderate bending strength (MOR: 100.5 MPa), low stiffness (MOE: 11.42 GPa) and low shock resistance (Porter 2014, Meier 2016). Walnut bean is a very good electric insulator since its resistance is fifty times higher than those of most wood species (Swain 1928). Walnut bean is not durable and is rated as Class 4 (least durable) for both in-ground durability and marine borer resistance (Standards Australia 2005). Walnut bean wood is difficult to saw when dried because of the presence of silica. A possible explanation is that the saw edges push the silica particles to one side, and the displacement of silica causes resistance and blunts saw edges (Anonymous 1936). Tungsten-carbide-tipped saw blades are recommended for sawing walnut bean wood (Porter 2014).

Walnut bean is a good substitute for American walnut (*Juglans nigra* L.) for interior uses such as furniture, premium-class cabinets, office equipment, decorative panels, etc. (Richardson 1929). Walnut bean was widely used in Australian and British theatres, banks, halls, reception rooms, as well as luxury ships and trains (Boas 1947). Walnut bean was also used for making visually attractive rifle stocks (Anonymous 1959) and guitars (Evans 2006). Walnut bean is not good for exterior use due to its poor durability (Bootle 1983). Extracts from the bark of walnut bean have the potential to treat diseases caused by a parasite (*Leishmania amazonensis* Lainson & Shaw) (Monzote et al. 2014).

3.2.1.5 White beech

White beech (*G. leichhardtii*), also known as grey teak, is a hardwood species distributed in Queensland and New South Wales, Australia. Its wood is soft and easy to cut (Dadswell and Eckersley 1935). White beech has good natural resistance to weathering and termites (Swain 1928). It can remain almost intact after six years of exposure to weather and still retains prominent tyloses in vessels (Swain 1928). Boas (1947) rated its durability as Class 2 which was the same class as other durable species such as jarrah (*Eucalyptus marginata* Donn ex Sm.), satinay, and yellow stringybark (*Eucalyptus muelleriana* A.W. Howitt). Seasoned white beech wood has extraordinary dimensional stability. Swain (1928) stated that it could be quite dry even after it was submerged in water for years. Swain (1928) also used the phrase “it does not swell when wetted, nor shrink, swell, nor alter its shape when used for pattern-making” to describe its dimensional stability. The mean shrinkage rates of white beech wood from green to 12% moisture content are 3.6% tangentially and 1.5% radially (Greenhill 1940).

The uses of white beech wood are due to its functionality rather than aesthetics (Swain 1928). White beech wood was ideal for templates and patternmaking because of its high stability (Swain 1928) and workability (Boas 1947). It was also used to make churns, and seaplane hulls and floats because of its stability under water (Swain 1928, Boas 1947). Its decay and wearing resistance made it a common material for internal and external floors (Boas 1947). Other uses were for shipbuilding, furniture, turned articles, plywood veneers, match splints, etc. (Swain 1928, Boas 1947). White beech is no longer available commercially, but there has been some interest in growing it in plantation (Nikles and Robson 2005, Gibson and Warren 2020).

3.2.2 Anatomy of selected species

The anatomical characteristics of the selected species, which are recorded in the literature are summarized in the following Tables 3.1, 3.2, and 3.3. The tables are formatted according to the IAWA (International Association of Wood Anatomists) List of Microscopic Features for Hardwood Identification (Wheeler et al. 1989). The citations are labeled as followings: [1] Ingle and Dadswell (1953); [2] Dadswell and Eckersley (1935); [3] Bamber and Lanyon (1960); [4] Welch (1929); [5] Ogata et al. (2008); [6] Dadswell and Eckersley (1940). Blank entries in the tables indicate that those features are not recorded in the literature.

Table 3.1 Anatomical characteristics of the growth rings and vessels of the selected species

Anatomical features	Turpentine	Satinay[4]	Brush box	Walnut bean[6]	White beech[2]
Growth ring boundaries	Indistinct or absent[1]	Indistinct		Sometimes visible	
Porosity		Diffuse-porous	Diffuse-porous[5]		
Vessel arrangement		Tendency to have diagonal pattern			Multiples in radial pattern
Vessel grouping	Exclusively solitary[2]	Exclusively solitary	Exclusive solitary[5]	Radial multiples of 2-7	Many solitary, some multiples of 2-3
Solitary vessel outline			Fine, distinct[2]		
Vessel perforation plates	Simple[2]		Simple[2]	Simple	Simple
Intervessel pits			Small[5]	Alternate, large	
Vestured pits	Present[1]		Intervessel[5]		
Vessel-ray pitting	Half-bordered, narrow border, simple, round to elongated[1]	Very large, semi-bordered, irregularly oval, very distinct from other vascular pitting, elongated, scaliform	Small, round to oval[5]	Much reduced borders to apparently simple; pits horizontal (scalariform, gash-like)	
Vessel tangential diameter	145 µm[1]	55-170 (110) µm			
Vessel density (No. / mm^2)	11-22[1]				
Mean length of vessels	650-810 µm[1]	300-750 µm			
Tyloses	Present[2]	Common	Occasional[5]	Common	Common
Deposits			Gummy deposits[5]		

Table 3.2 Anatomical characteristics of the fibre and parenchyma cells of the selected species

Anatomical features	Turpentine	Satinay[4]	Brush box	Walnut bean[6]	White beech[2]
Ground tissue fibres				With simple bordered pits	
Septate fibres				Non-septate	Present
Fibre wall thickness		Fibres thin- to thick-walled			
Mean fibre lengths		0.6-1.7 mm			
Vasicentric tracheids	Present[1]				
Apotracheal parenchyma	Diffuse, not abundant[2]	Diffuse	Diffuse[2]		
Paratracheal parenchyma	Not abundant[2]	Slightly vasicentric			A little paratracheal, tendency to be confluent
Banded parenchyma				More than three cells wide, slightly paratracheal	

Table 3.3 Anatomical characteristics of the rays, mineral and organic inclusions of the selected species

Anatomical features	Turpentine	Satinay[4]	Brush box	Walnut bean[6]	White beech[2]
Ray width	1-2 cells[2]	1-3 cells	1-2 cells[2]	1-3 cells	1-5 cells, commonly 3-4 cells
Ray hight	≤ 30 cells[2]	≤ 2100 µm	>1 mm[2]		
Cellular composition of rays	Weakly heterogenous, 1 to several rows of square cells[1]	Body ray cells procumbent with one or more rows of upright and/or square marginal cell	Heterogeneous[2]	Almost all ray cells procumbent, square and upright cells at margin	All ray cells procumbent, occasionally one row of upright
Storied structure in rays				Tendency for storeying to produce ripple marks	
Oil and mucilage cells				Oil cells associated with ray parenchyma, occasional	
Prismatic crystals	Absent[1]				
Silica	Silica bodies in ray cells[3]		Silica bodies in ray cells[3]	Present	

3.2.3 X-ray micro-CT of the wood specimens

A sample of each species, measuring 14.5 cm (length) x 6.8 cm (width) x 1 cm (thickness) was retrieved from the wood collection at the University of British Columbia. A plug cutter attached to a drill press was used to remove cylinders with diameters of 5.8 mm or 1.9 mm from each sample. The samples were wrapped in protective plastic film and air-bubble wrap, and then sealed in a padded envelope and airmailed by courier to the National Laboratory for X-ray Micro-Computed Tomography at The Australian National University (ANU). Each sample was sealed in a PEEK (polyether ether ketone) tube and imaged using a helical cone-beam X-ray micro-CT devices designed and built in the Department of Applied Mathematics at The ANU (Sheppard et al. 2014). Individual samples were placed on a rotating stage while an X-ray tube projected a cone-shaped X-ray beam onto the sample. When the sample was interacting with X-rays, a charge-coupled device captured two-dimensional (2D) projection data. The projection data were then processed using the Raijin supercomputer located in the ANU Supercomputer Facility to reconstruct the 3D volumes from samples. The Katservich (2002) formula and an autofocus alignment method (Kingston et al. 2010) were used to compute the helical trajectory data and to reduce artefacts. After reconstruction, the tomographic data sets were transferred to the University of British Columbia for visualization.

Table 3.4 Dimensions of specimens and information on corresponding CT data sets

Species	Diameter (mm)	Length (mm)	Voxel size (µm)	Spatial resolution
Turpentine	5.8	9.3	2.95	2560×2560×3400
Satinay	1.9	4	1.11	2480×2480×3696
Brush box	5.8	10.3	2.95	2560×2560×3740
Walnut bean	5.8	7.3	2.95	2560×2560×2880
White beech	1.9	4	1.12	2680×2680×3600

3.2.4 Tomographic data visualization

Each tomographic data set consisted of a 3D array of voxels which contained intensity values. Thresholding these values allowed the selective display of materials that the voxels represented. These materials, or more correctly, phases were air, wood and inorganics. Transfer functions that assign colour and transparency were then applied to each phase for volume rendering. I used the volume rendering software Drishti to explore and visualize all data sets (Limaye 2012). Volume cropping, slicing, and shading were used to display features found in the data sets for each wood species. The volume rendering of all tomographic data sets occurred at the University of British Columbia on a workstation computer equipped with an octa-core processor (Ryzen 3700X, Advanced Micro Devices, Santa Clara, CA) and a dedicated graphics accelerator (Titan RTX 24GB, NVIDIA Corporation, Santa Clara, CA).

Two viewing modes were used for rendering images: perspective view and orthographic view. Perspective view is the natural way for a human to perceive 3D objects since it has a foreshortening effect (closer object appear larger). For this reason, perspective view mode was used for generating images illustrating the inner 3D structure of samples. In this view, the scalebar is precise for the central portion. The orthographic mode projects 3D objects parallel to the viewing plane (e.g., the shadows caused by sunlight are orthographic projections). Orthographic view mode does not have a foreshortening effect. Thus, it was used for generating sectional images of samples. In an orthographic view, the scalebar is precise for any portion of the image.

3.2.5 Synchrotron X-ray fluorescence microscopy

The turpentine and satinay wood blocks from which the cylindrical cores were extracted for X-ray micro-CT were also used for synchrotron X-ray fluorescence microscopy (XFM). Three wood blocks measuring 6.5×2.8×20 mm were hand-sawn from each parent sample. The wood blocks were placed in individual glass beakers and submerged in ultra-pure distilled water for five days. Then, each sample was clamped on a sliding sledge microtome (Spencer Lens Co., Buffalo, NY, USA) and radial-tangential sections approximately 20 µm thick were sliced from the blocks using a microtome blade-holder (Feather No. 160, Feather Safety Razor Co., Ltd., Osaka, Japan) with a fresh disposable microtome blade (Feather Type S35). The sections were placed on clean-glass backing plates, air dried, and then stored in

glass vials. The vials were couriered to the Australian Synchrotron in Melbourne, Australia by courier. The sections were fixed on a Perspex sample holder using double-sided adhesive tape (Figure 3.1) and then analysed using the synchrotron XFM beamline (Figure 3.2). A monochromatized and focused X-ray beam was projected to the sample (Paterson et al. 2011, Howard et al. 2020), and an element spectrometer array recorded the fluorescence of the X-ray beam (Ryan et al 2014). Elemental mappings of the samples occurred after the XFM data were analyzed using the software GeoPIXE (Ryan et al. 1990).

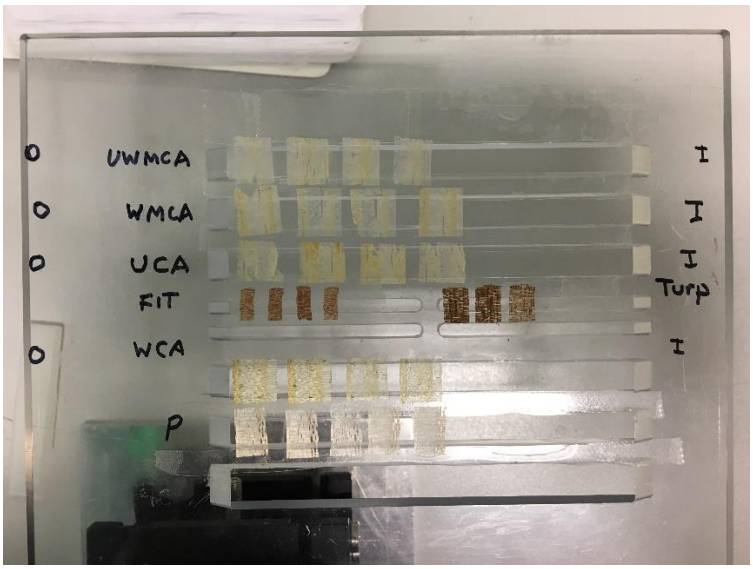

Figure 3.1 Sample holder containing turpentine (TURP) and satinay (FIT) sections

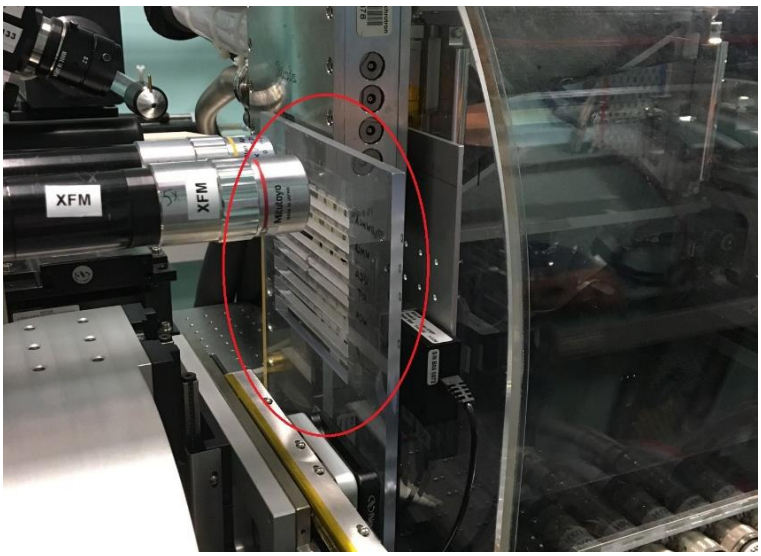

Figure 3.2 Close-up image of the synchrotron XRF gun and the sample holder (circled)

3.3 Results

3.3.1 Turpentine

Anatomical structures in turpentine such as vessels, tyloses, rays and fibres were visible at a resolution of 2.95 µm. Spherical-like silica particles (Figure 3.3 – 3.6, pink) were found in rays via thresholding of the density profile. The distribution of silica particles resembled the outline of rays in 3D (Figure 3.3). Close-up sectional images showed that silica had a rather even distribution across the rays (Figure 3.4).

Another finding from thresholding was that materials denser than walls of fibres and slightly less dense than silica were detected (Figure 3.3 – 3.6, green). Silica within the detected materials could not be cleanly separated using thresholding due to their similarity in density. Thus, segmentation which involved erosion and dilation of the materials was used for separation. The materials highlighted in green matched the appearance of vessel elements and tyloses in 3D images (Figure 3.3). Sectional images (Figure 3.4 – 3.6) also showed that these materials were localized in vessels and tyloses. The detected materials were potentially inorganics, but their chemical compositions cannot be identified using X-ray micro-CT. For this reason, synchrotron XRF was used to map chemical elements.

Synchrotron XRF images show the micro-distribution of inorganic elements in the radial-longitudinal sections of turpentine heartwood (Figure 3.7, 3.8, Appendix 1). Silica inclusions are clearly visible in Figure 3.7a and 3.8a due to the high concentration of Si element. Figure 3.7a and 3.8a also show the presence of silica in vessels which appears as purple areas resembling the outline of vessels. Copper had a higher concentration in the vessel walls appearing as blue bands along the outline of vessels (Figure 3.7b, 3.8b). Copper at a lower concentration was also found in rays, which can be clearly seen in Figure 3.8b. There is also a small amount of zinc in the vessel walls, showing as purple strips matching the outline of vessels in Figure 3.7c and 3.8c. The micro-distribution of other inorganic elements such as Hg, Ni, Pb, Sn are displayed in Appendix 1.

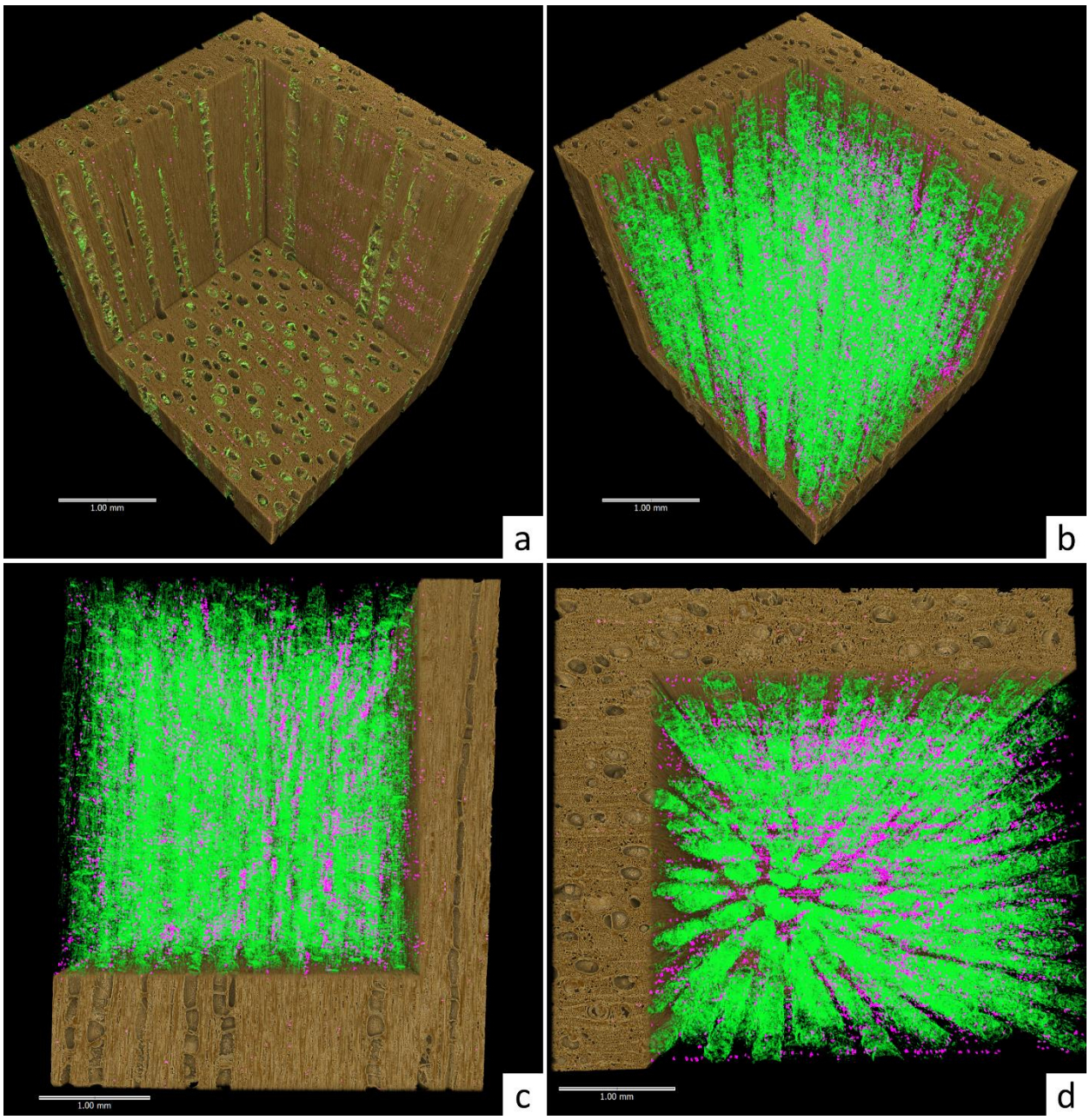

Figure 3.3 3D images of turpentine: (a) isometric view. A corner is cropped to show silica and dense materials potentially inorganics in radial, tangential, and transverse sections; (b) isometric view showing spatial distribution of silica and dense materials in the cropped area; (c) side view in the radial direction; (d) top view showing end grain. Brown, wood; Pink, silica; Green, materials possibly inorganics

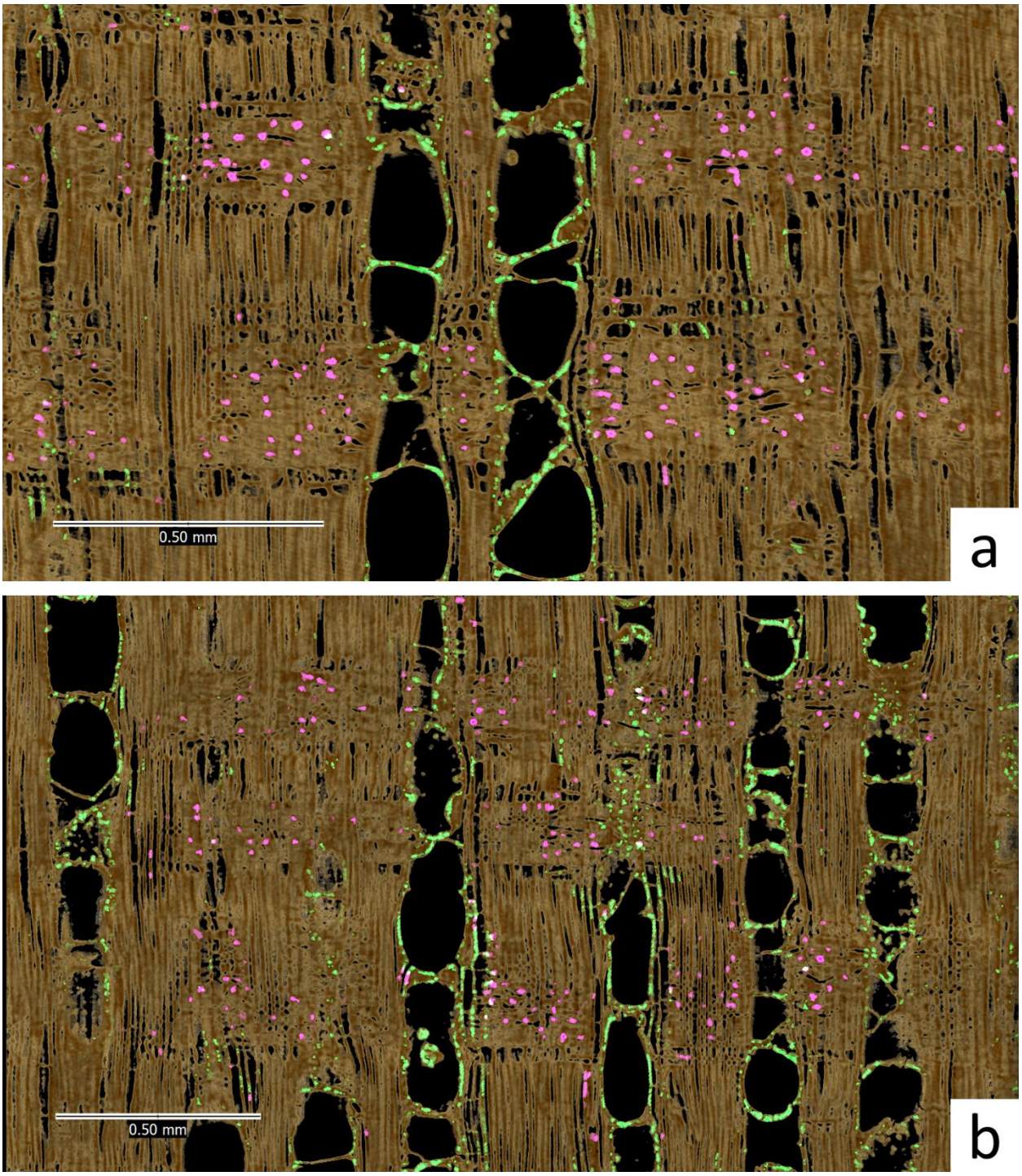

Figure 3.4 Radial-longitudinal sectional images of turpentine. Brown, wood; Pink, silica; Green, materials possibly inorganics

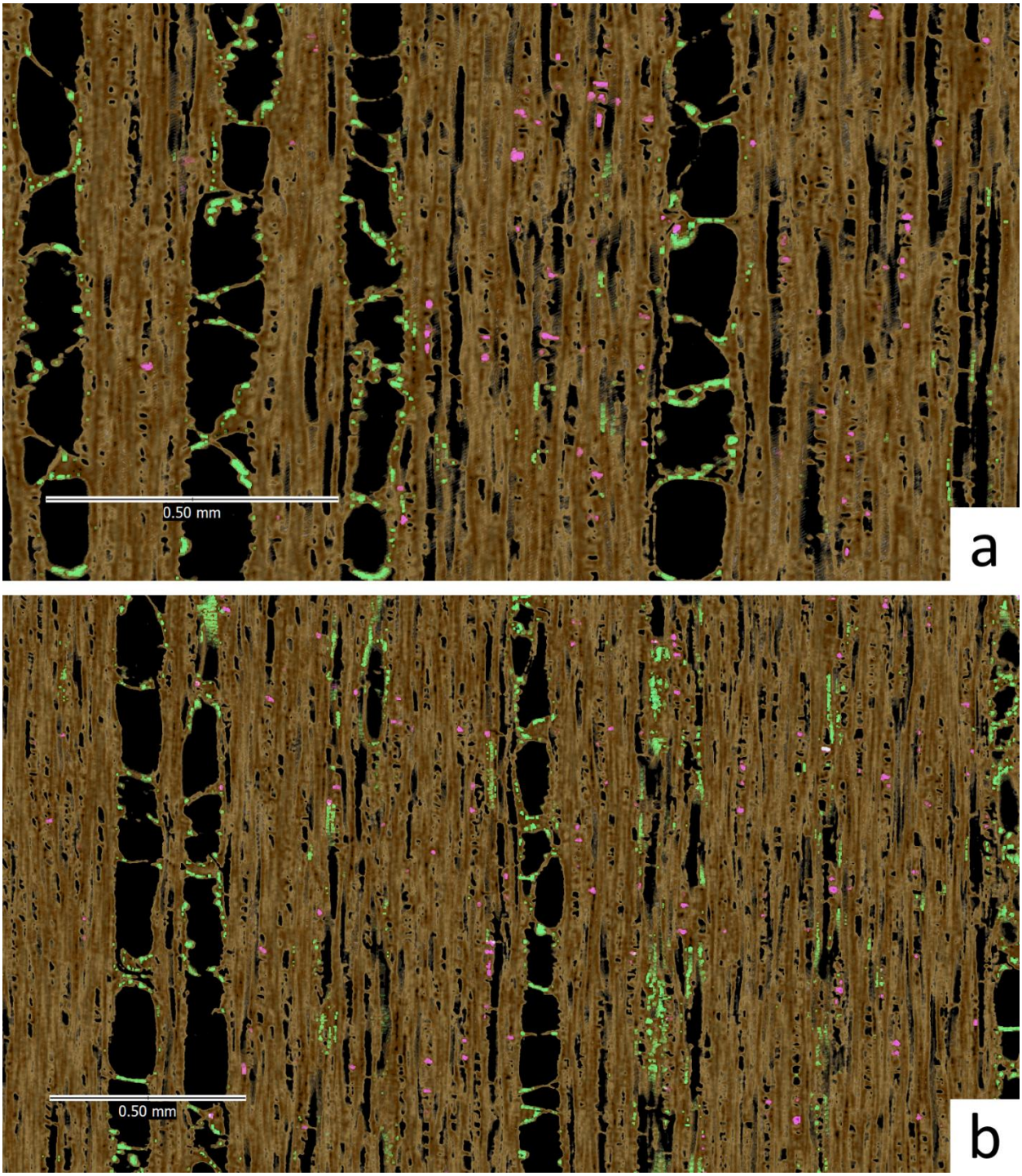

Figure 3.5 Tangential-longitudinal sectional images of turpentine. Brown, wood; Pink, silica; Green, materials possibly inorganics

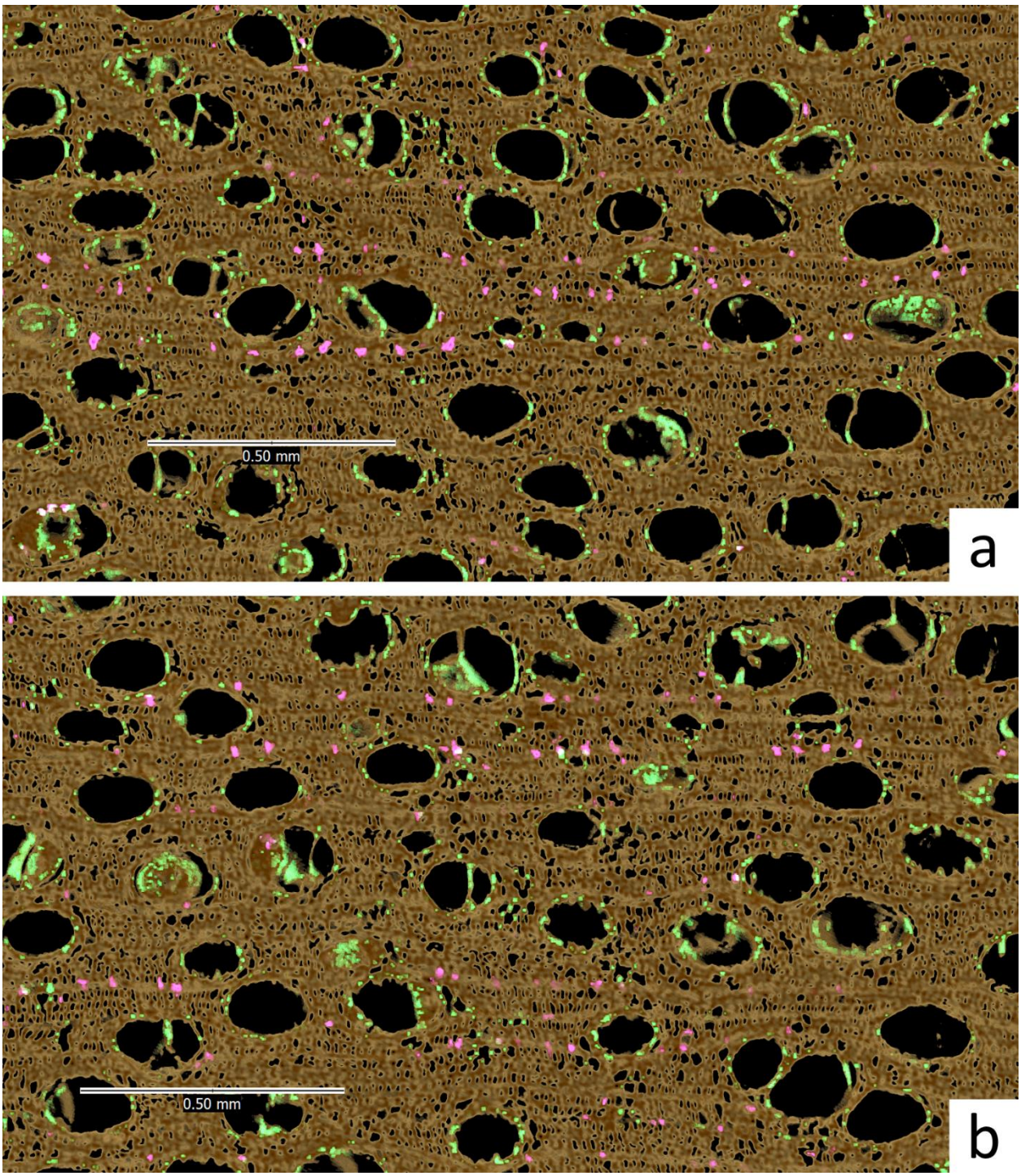

Figure 3.6 Transverse sectional images of turpentine. Brown, wood; Pink, silica; Green, materials possibly inorganics

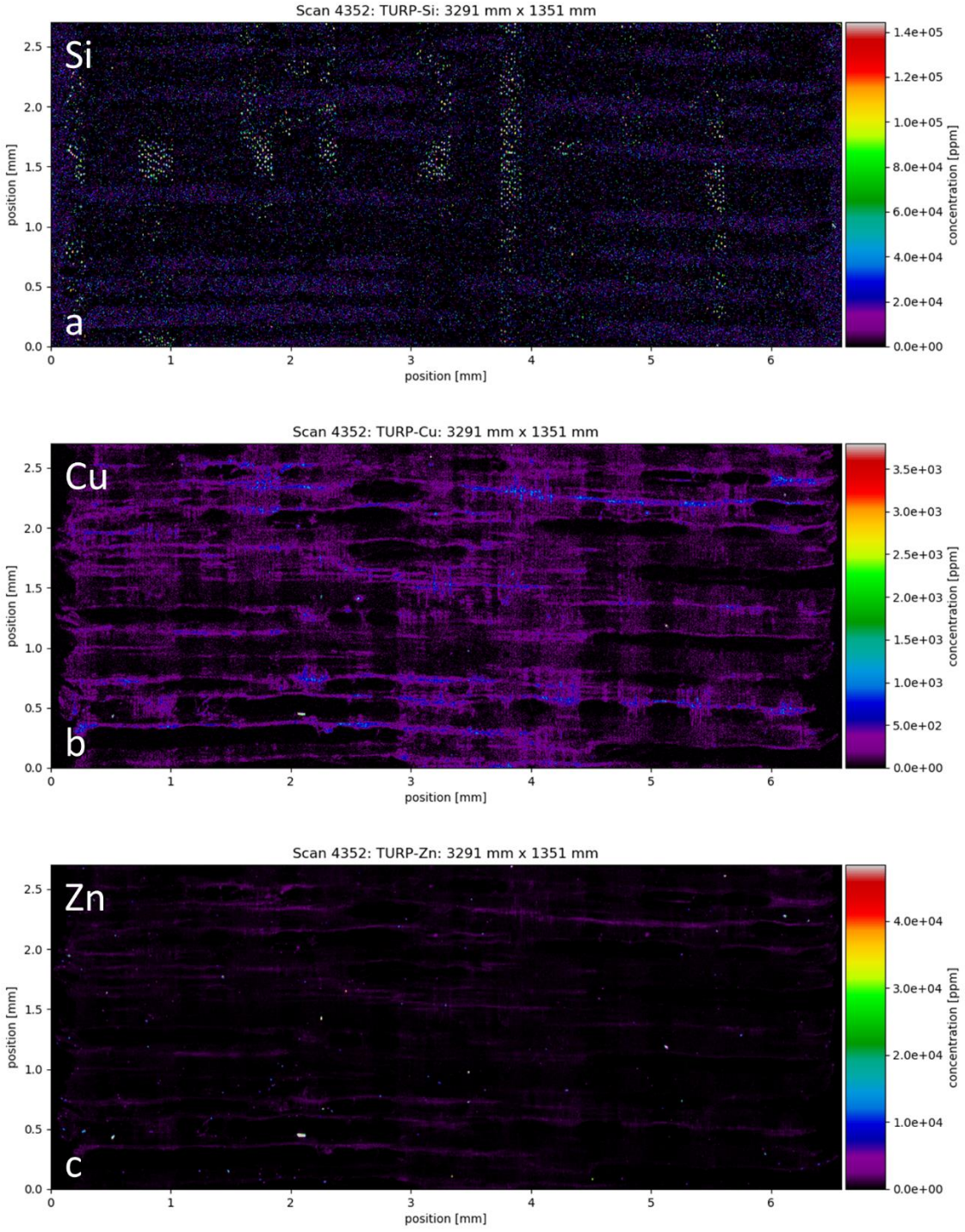

Figure 3.7 Synchrotron XFM elemental maps of Si, Cu, and Zn in the radial-longitudinal direction of turpentine heartwood sample: (a) distribution of Si; (b) distribution of Cu; (c) distribution of Zn

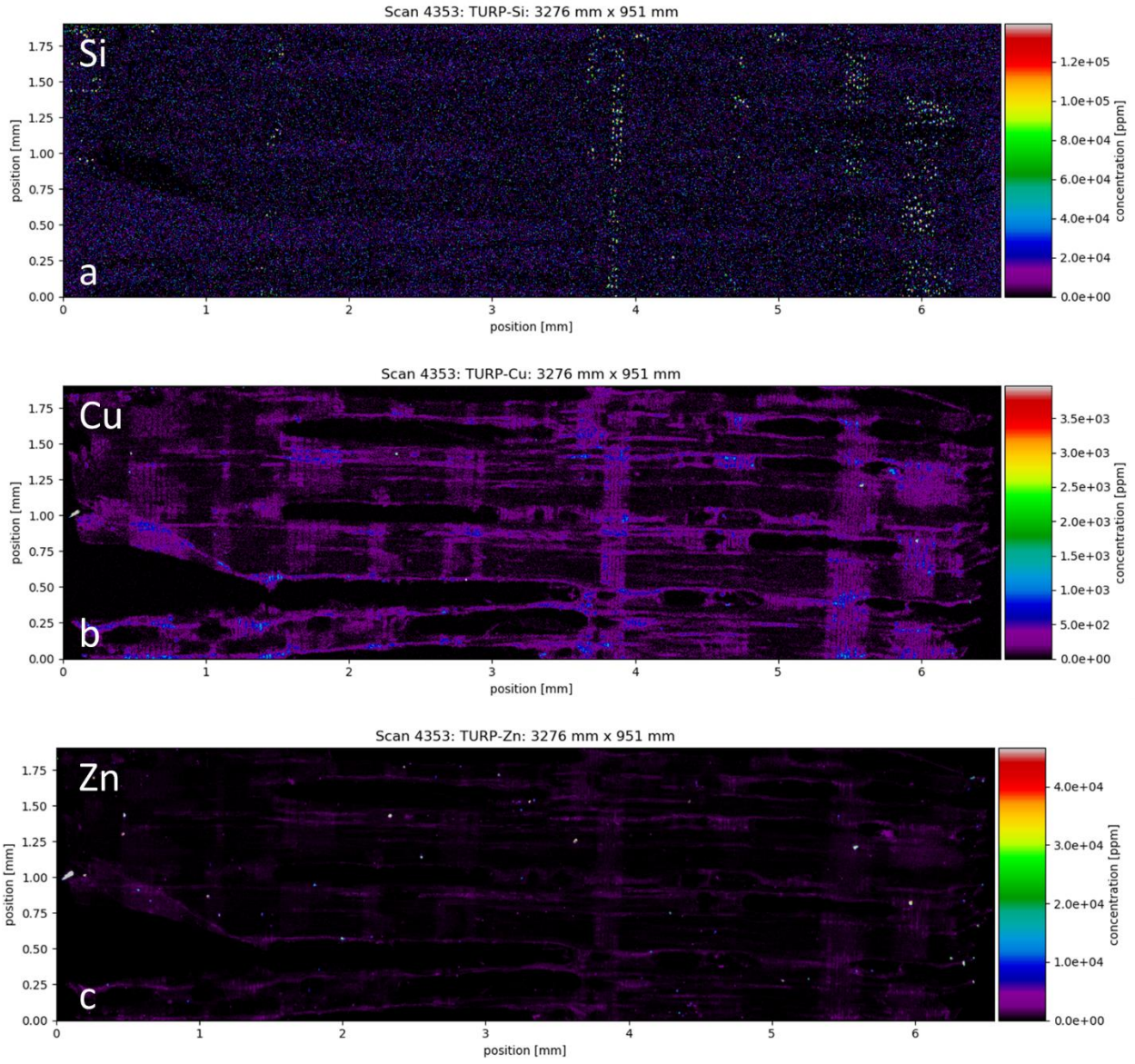

Figure 3.8 Synchrotron XFM elemental maps of Si, Cu, and Zn in the radial-longitudinal direction of another turpentine heartwood sample: (a) distribution of Si; (b) distribution of Cu; (c) distribution of Zn

3.3.2 Satinay

The higher 1.11 µm resolution scan of satinay made it easier to see its cellular structure. As in turpentine, spherical-like silica particles were found in rays (Figure 3.9 – 3.12, pink). Radial-longitudinal images showed that silica particles were in the lumens of procumbent ray parenchyma cells, but not all ray cells contained silica particles (Figure 3.10). Materials denser than cell walls and less dense than silica, similar to those found in turpentine, were also found in satinay (Figure 3.9 – 3.12, green). The higher resolution scan made it possible to cleanly separate these materials using thresholding without the need for segmentation. The detected materials were more commonly associated with tyloses than vessel walls. The materials were also present to a lesser extent in the walls of ray parenchyma cells (Figure 3.10, 3.11). Nevertheless, as was the case for turpentine, the identity of these materials was not revealed by X-ray micro-CT.

Synchrotron XRF images show bright Si spots resembling silica inclusions in satinay (Figure 3.13a, b). Silica was also present to a lesser extent in vessels and cell walls of rays (blue and purple in Figure 3.13a, b), but it was not clearly defined. As was the case for turpentine, copper was found in the vessels and rays in satinay (Figure 3.13c, d). The horizontal purple bands resembling rays appear wavy due to the alignment of the sample. Bright Zn particles associated with vessels and Cu particles were present in samples. These particles can be seen in Figure 3.13e and f. Additional images of the mapping of other inorganic elements can be found in Appendix 1.

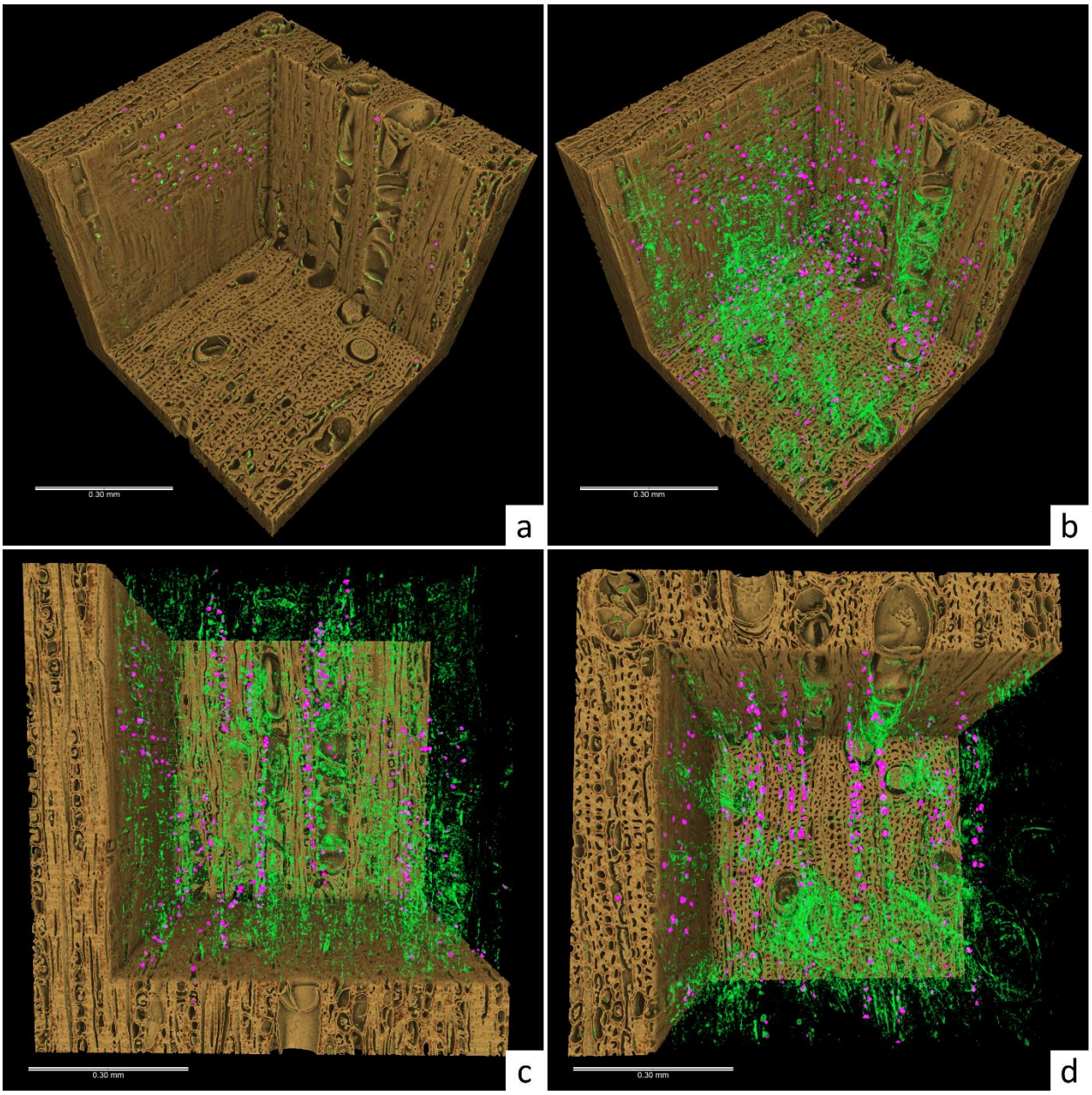

Figure 3.9 3D images of satinay: (a) isometric view. A corner is cropped to show silica and dense materials potentially inorganics in radial, tangential, and transverse sections; (b) isometric view showing spatial distribution of silica and dense materials in the cropped area; (c) side view in the radial direction; (d) top view showing end grain. Brown, wood; Pink, silica; Green, materials possibly inorganics

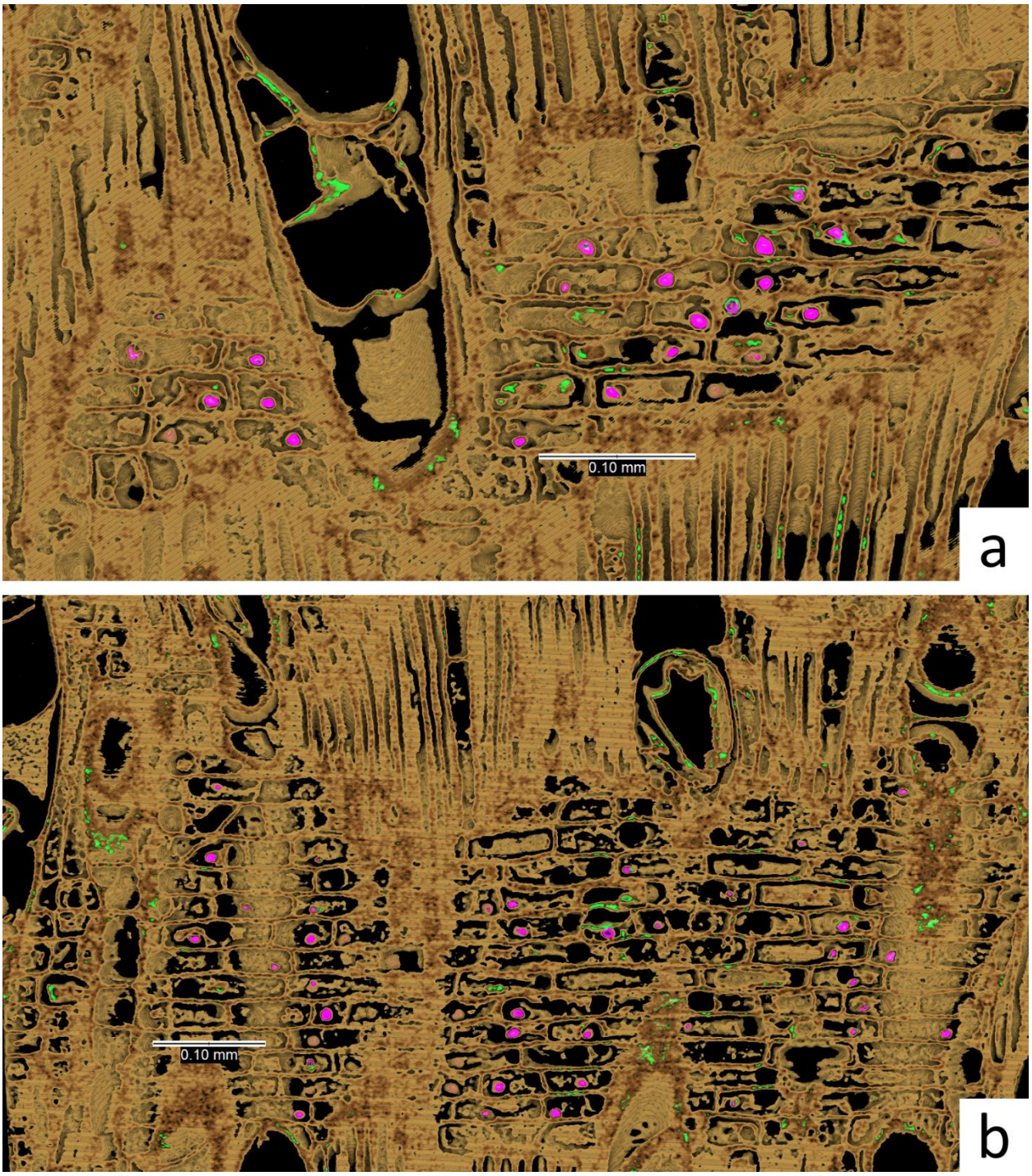

Figure 3.10 Radial-longitudinal sectional images of satinay. Brown, wood; Pink, silica; Green, materials possibly inorganics

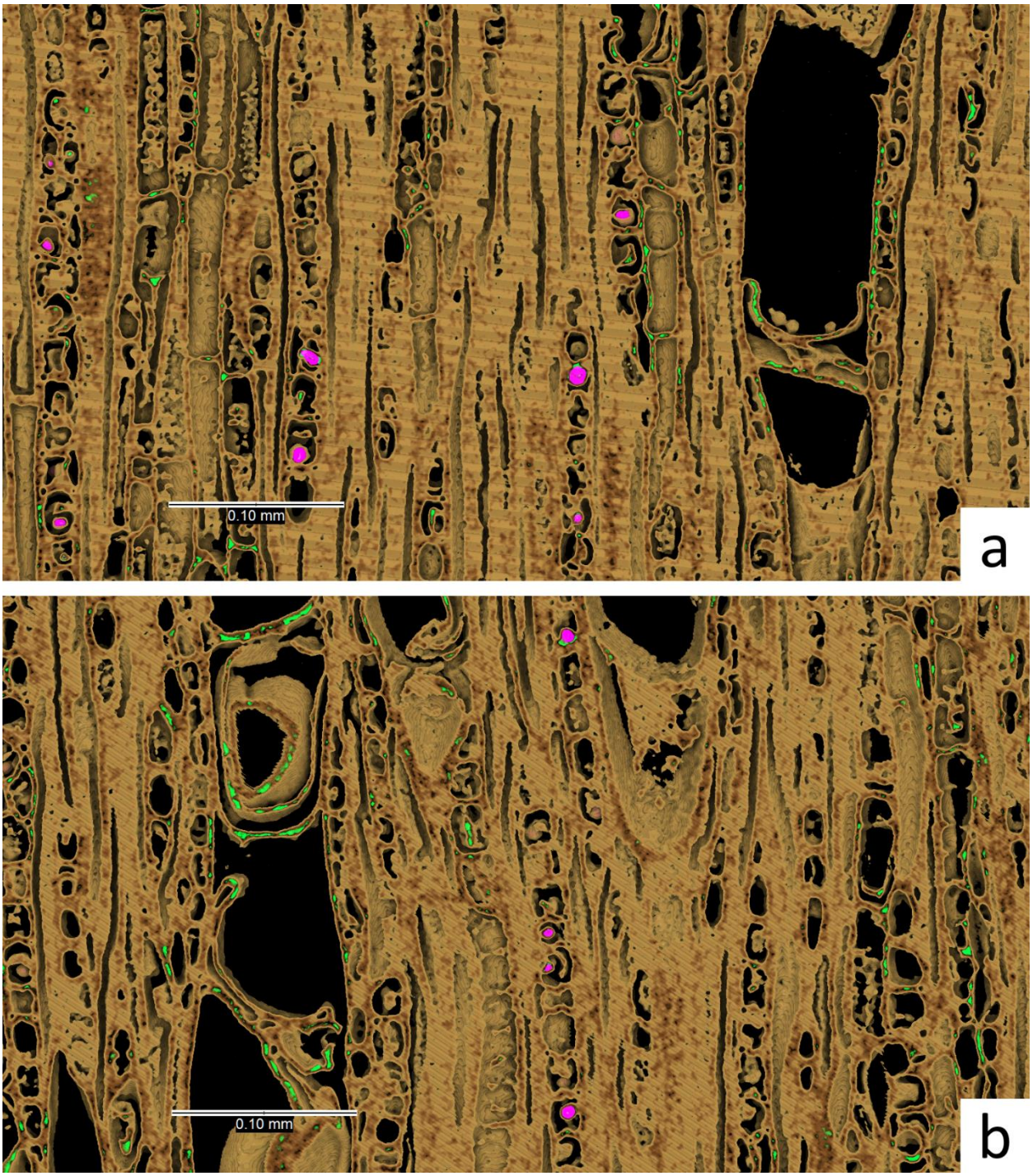

Figure 3.11 Tangential-longitudinal sectional images of satinay. Brown, wood; Pink, silica; Green, materials possibly inorganics

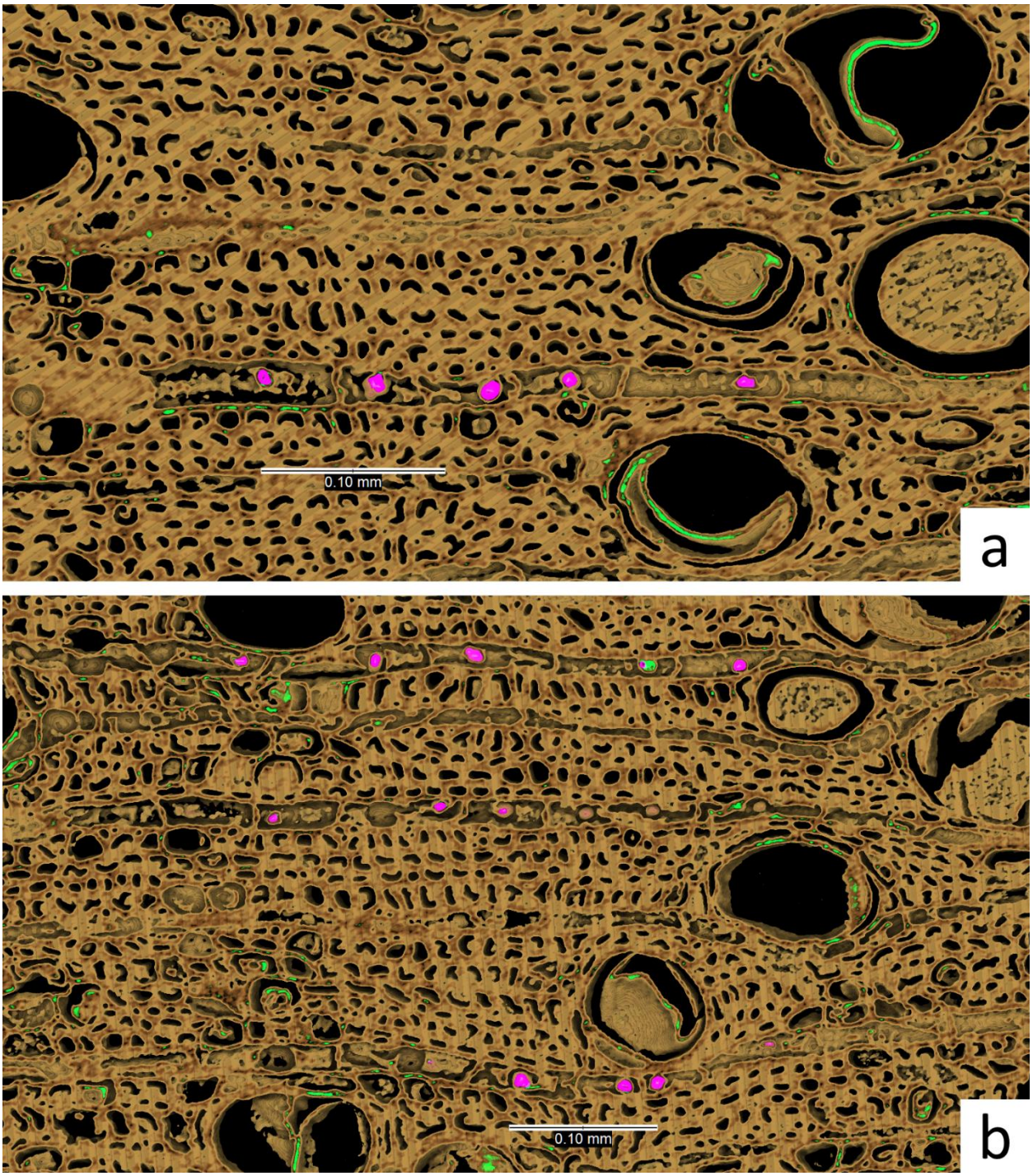

Figure 3.12 Transverse sectional images of satinay. Brown, wood; Pink, silica; Green, materials possibly inorganics

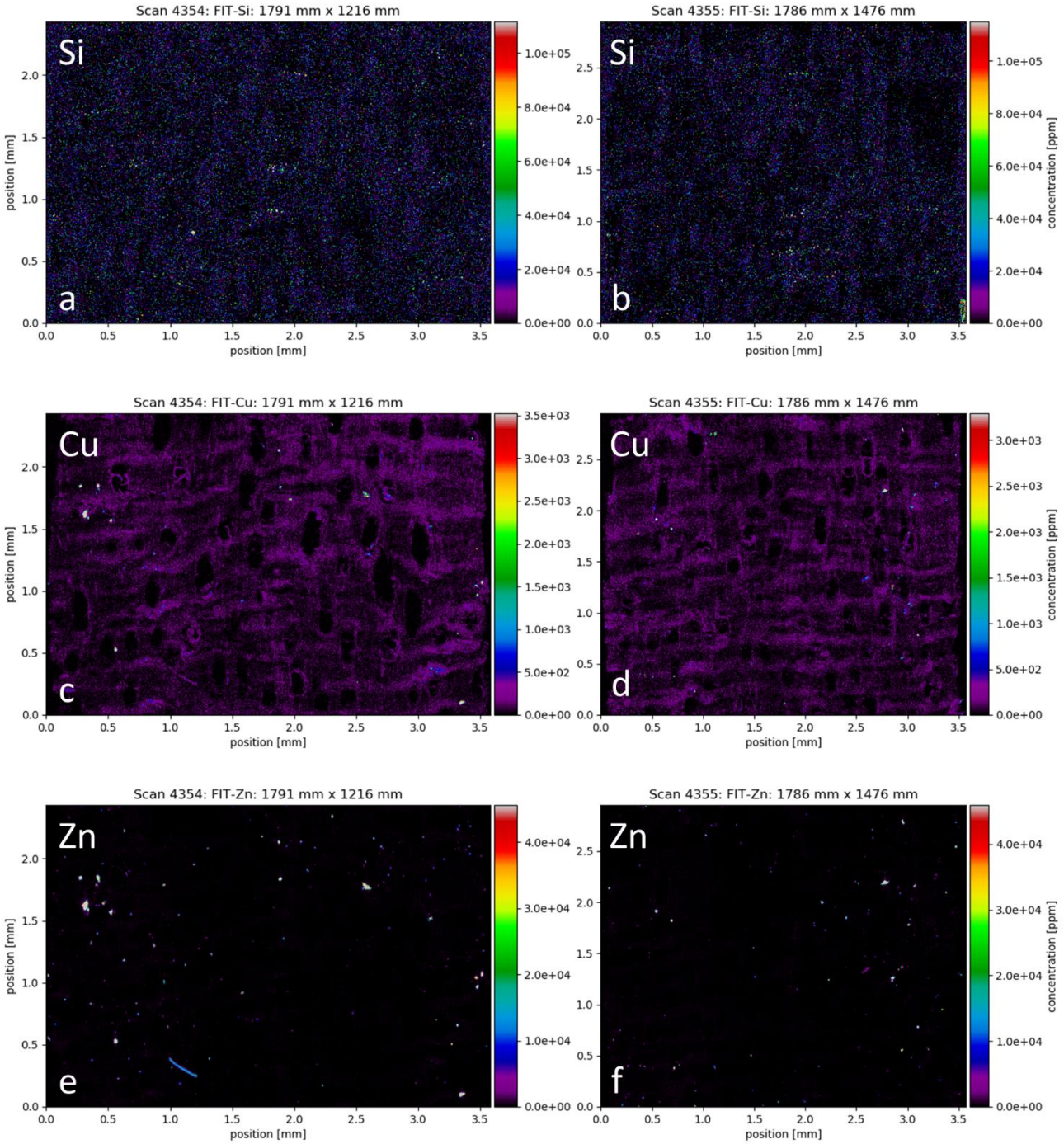

Figure 3.13 Synchrotron XFM elemental maps of Si, Cu, and Zn in the radial-longitudinal direction of satinay heartwood samples: (a) (b) distribution of Si; (c) (d) distribution of Cu; (e) (f) distribution of Zn

3.3.3 Brush box

Spherical silica particles were detected in brush box at a resolution of 2.95 µm. In 3D images, the spatial distribution of silica followed the outline of rays (Figure 3.14). Close-up images showed silica particles in most cells within rays. The silica particles showed larger variation in size than those in turpentine and satinay (from less than 0.01 mm to approximately 0.03 mm, Figure 3.15). The variation in size of silica particles appeared to be related to their location in the wood sample: some areas had both large and small silica particles (Figure 3.15a, 3.16a, 3.17a), whereas other areas only had small silica particles (Figure 3.15b, 3.16b, 3.17b).

A larger region of interest in the sample was selected to investigate the spatial variation in size of silica particles (Figure 3.18). Silica occurred as curved bands in which the silica particles were larger and more numerous compared to other areas (Figure 3.18b). The curved bands of silica matched the transition zones between earlywood and latewood which were marked by an absence of vessels (Figure 3.18a, c).

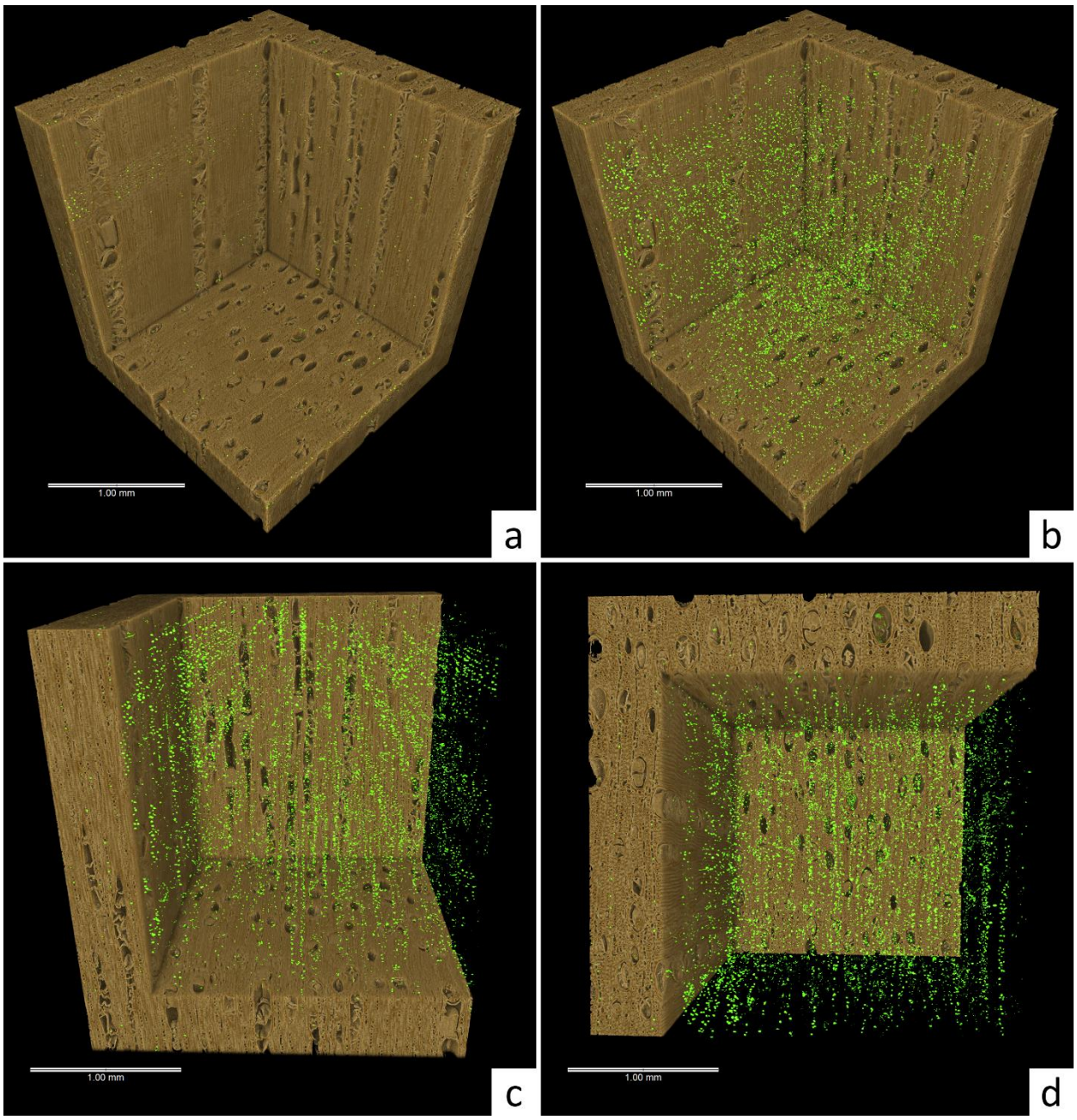

Figure 3.14 3D images of brush box: (a) isometric view. A corner is cropped to show silica in radial, tangential, and transverse sections; (b) isometric view showing spatial distribution of silica in the cropped area; (c) side view along radial direction; (d) top view showing end grain. Brown, wood; Green, silica

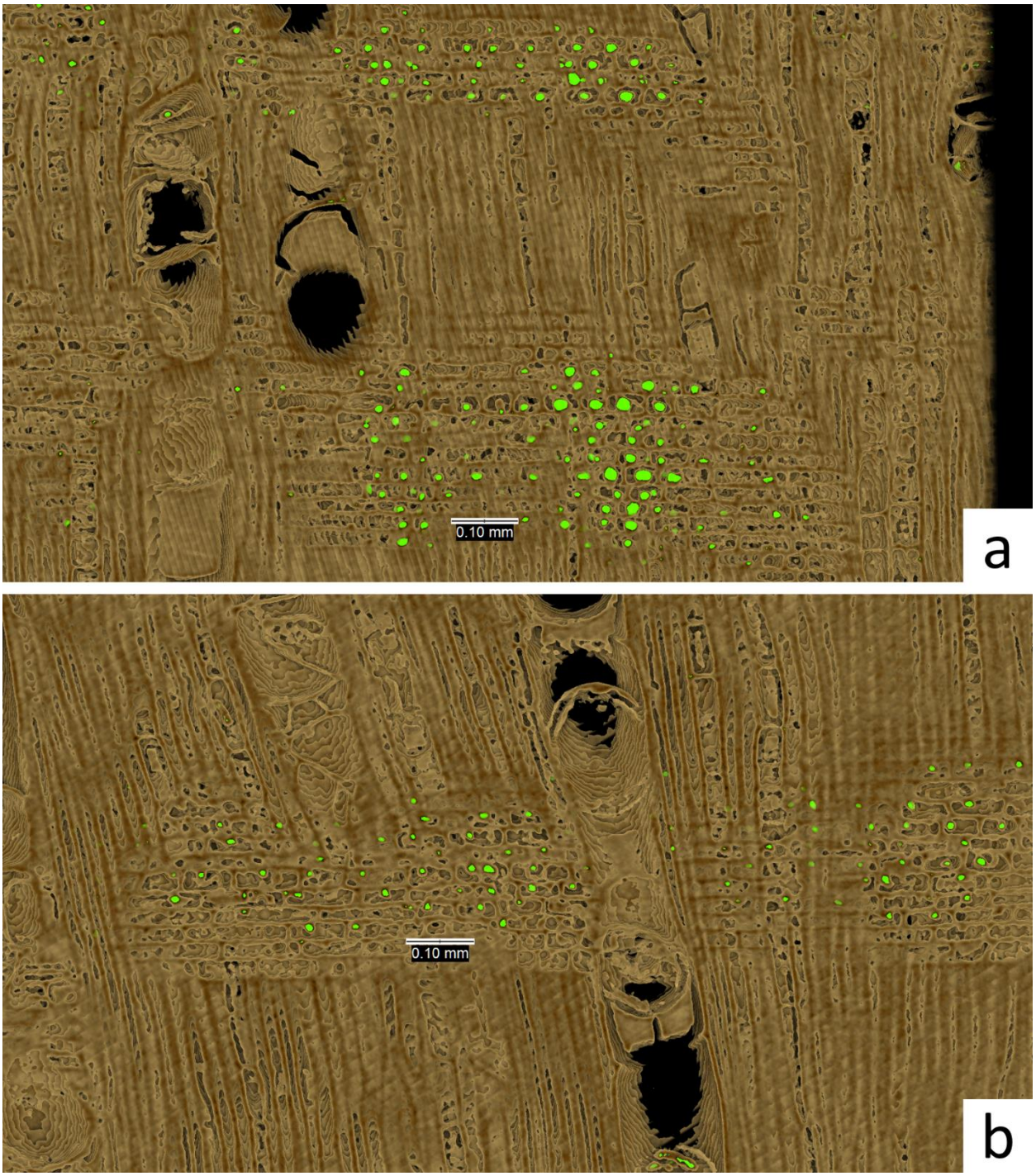

Figure 3.15 Radial-longitudinal sectional images of brush box. (a) zone containing a large amount of silica; (b) zone containing a small amount of silica. Brown, wood; Green, silica

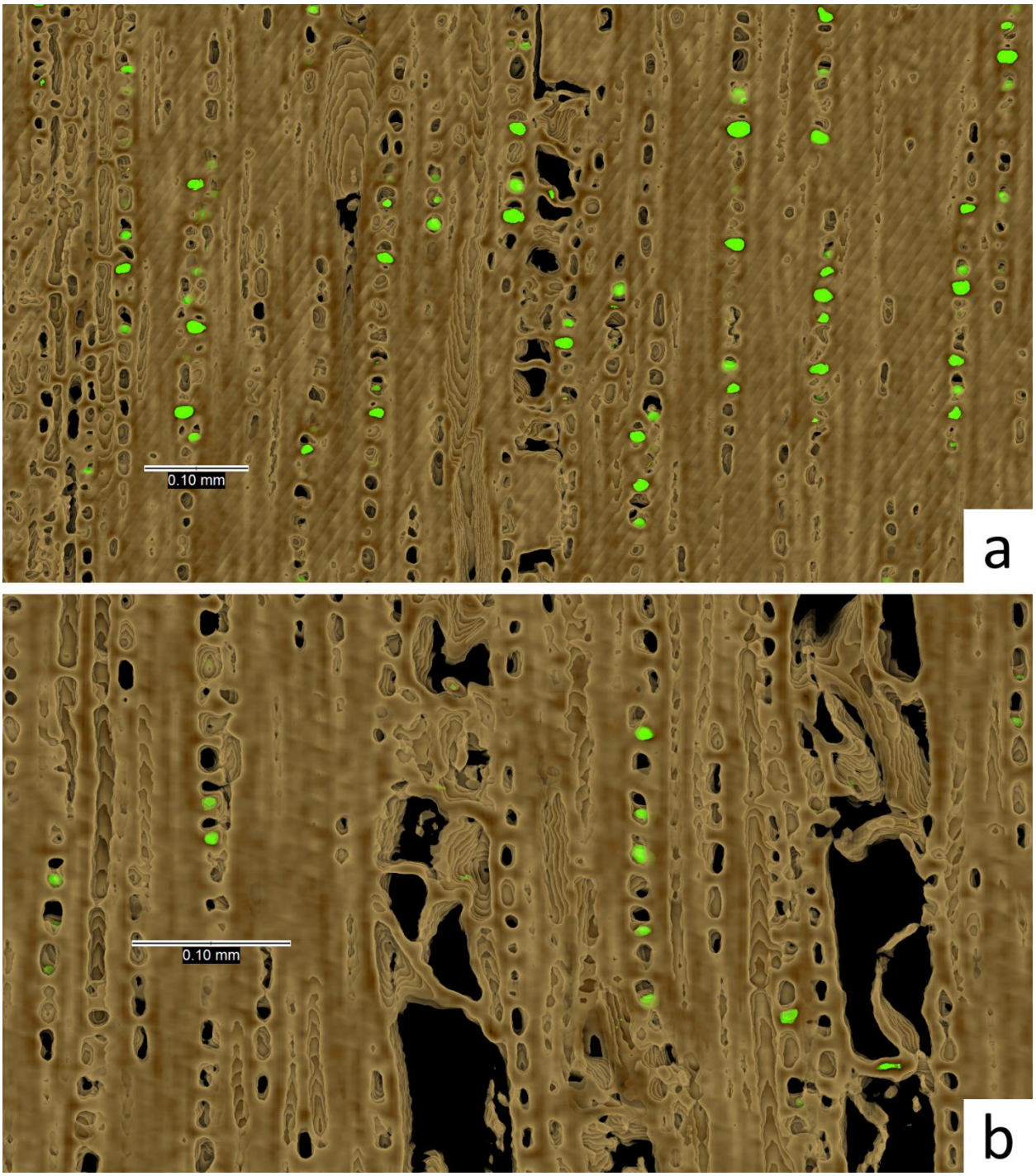

Figure 3.16 Tangential-longitudinal sectional images of brush box. (a) zone containing a large amount of silica; (b) zone containing a small amount of silica. Brown, wood; Green, silica

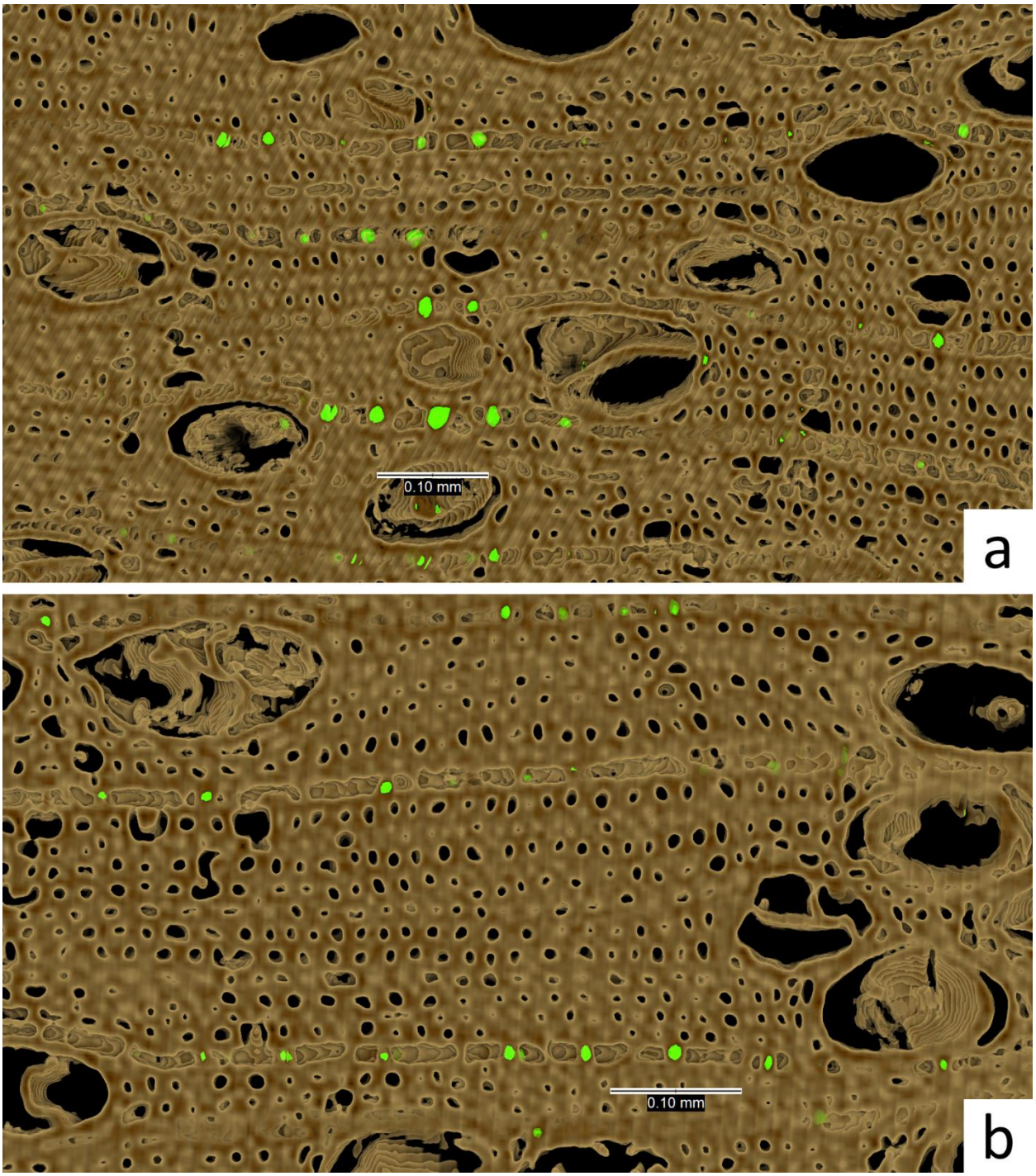

Figure 3.17 Transverse sectional images of brush box. (a) zone containing a large amount of silica; (b) zone containing a small amount of silica. Brown, wood; Green, silica

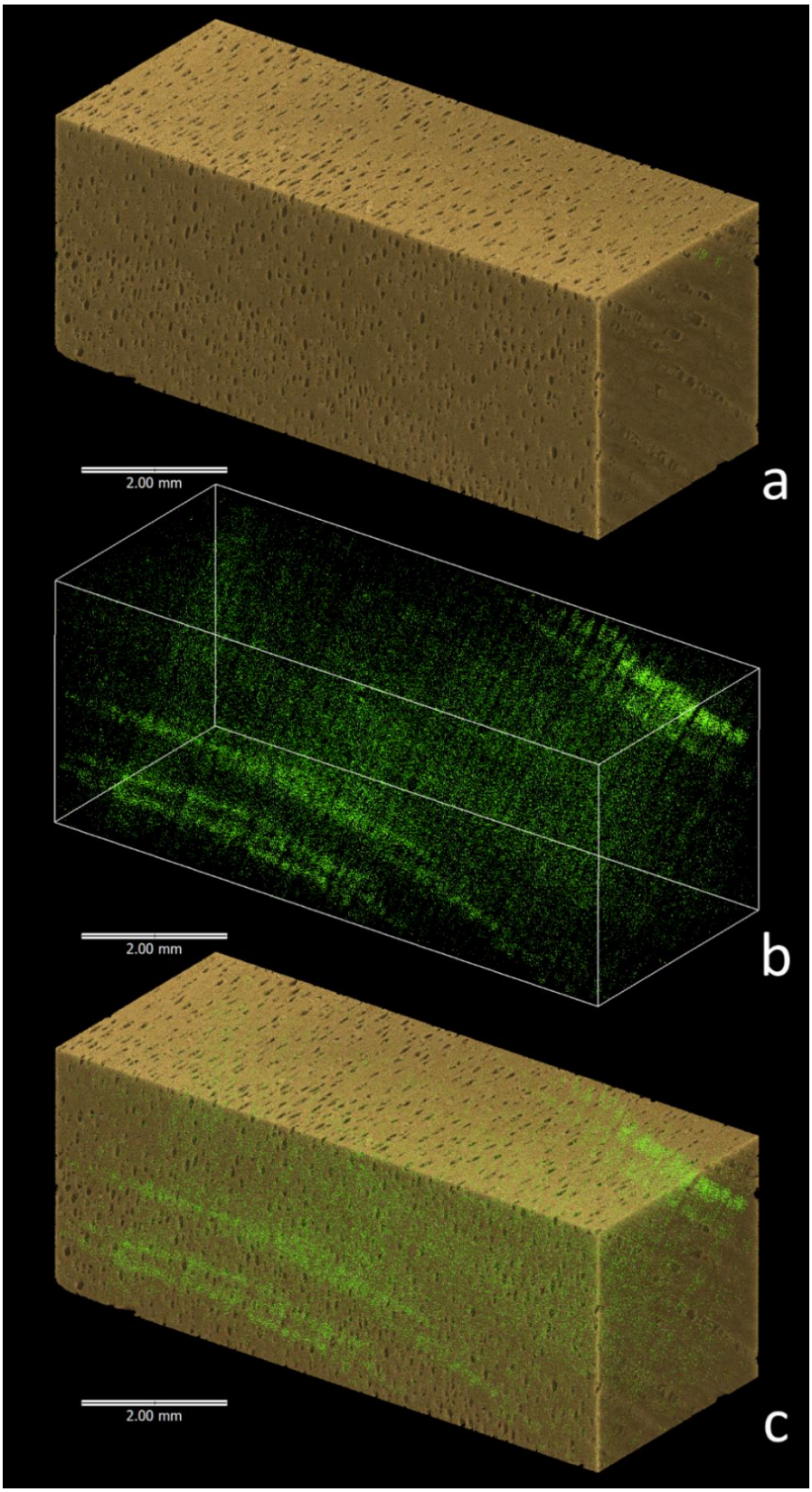

Figure 3.18 Silica size and distribution related to growth rings in brush box. Brown, wood; Green, silica

3.3.4 Walnut bean

Silica was found in rays in walnut bean using the same 2.95 μm resolution as that of the brush box sample. The 3D images of silica distribution showed rather pronounced lines of silica in the direction of rays (Figure 3.19). Close-up sectional images showed that the silica particles were mostly in upright and square parenchyma cells at the edges of rays (Figure 3.20), while the procumbent cells in the centre of the rays rarely contained silica particles (Figure 3.20, 3.21). There was no correlation between the distribution of silica and growth rings, unlike that found in brush box.

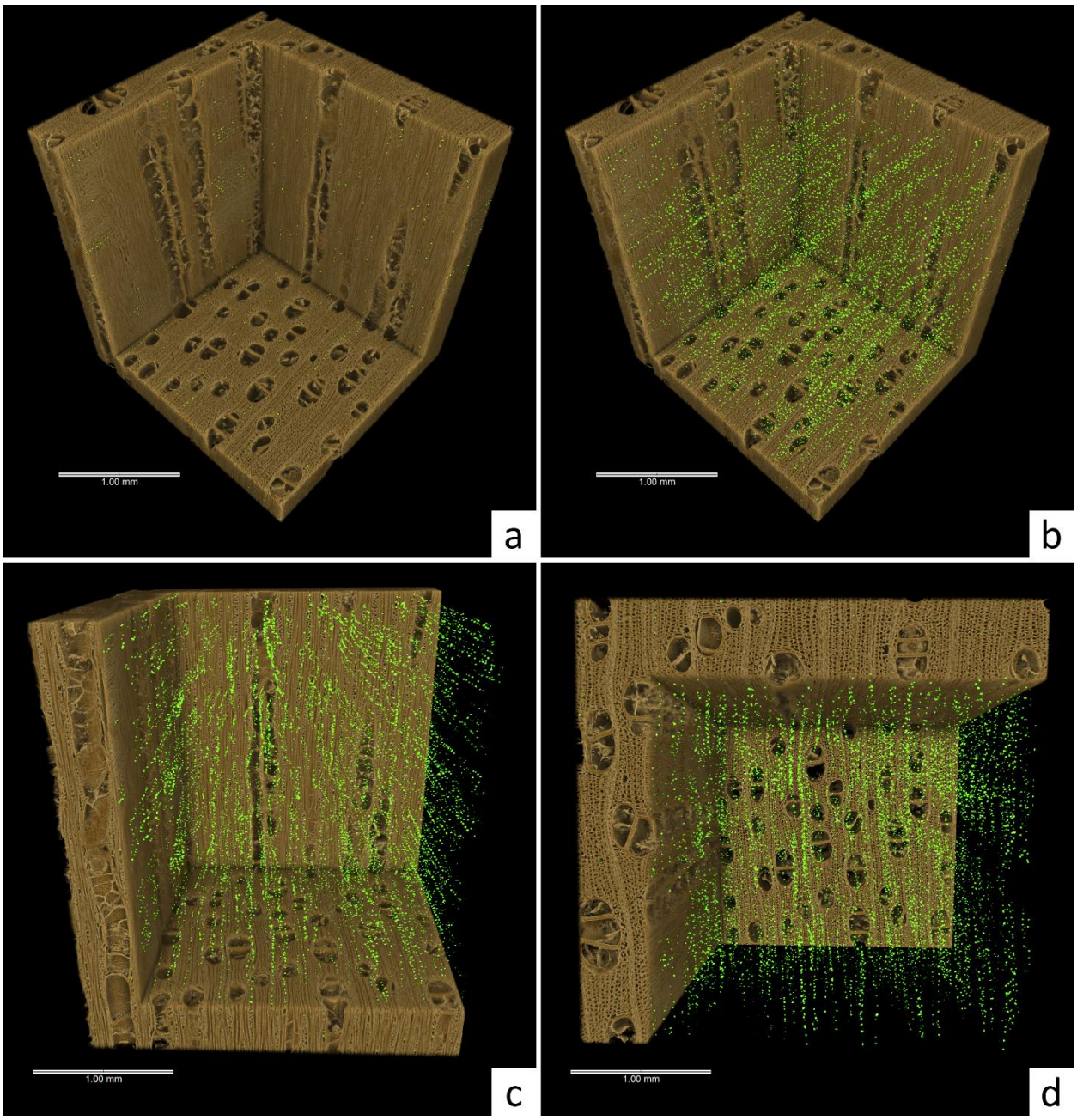

Figure 3.19 3D images of walnut bean: (a) isometric view. A corner is cropped to show silica in radial, tangential, and transverse sections; (b) isometric view showing spatial distribution of silica in the cropped area; (c) side view in the radial direction; (d) top view showing end grain. Brown, wood; Green, silica

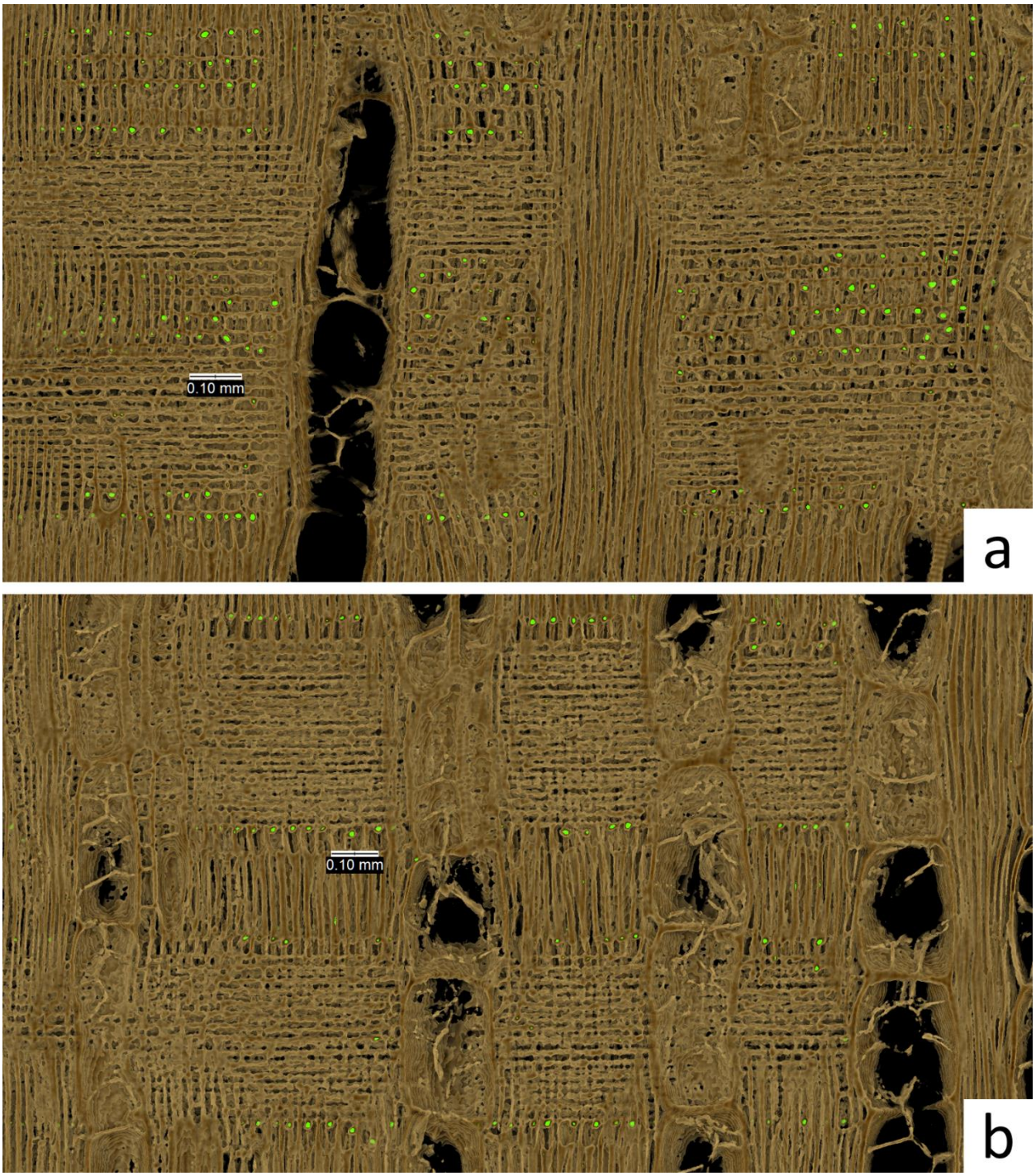

Figure 3.20 Radial-longitudinal sectional images of walnut bean. Brown, wood; Green, silica

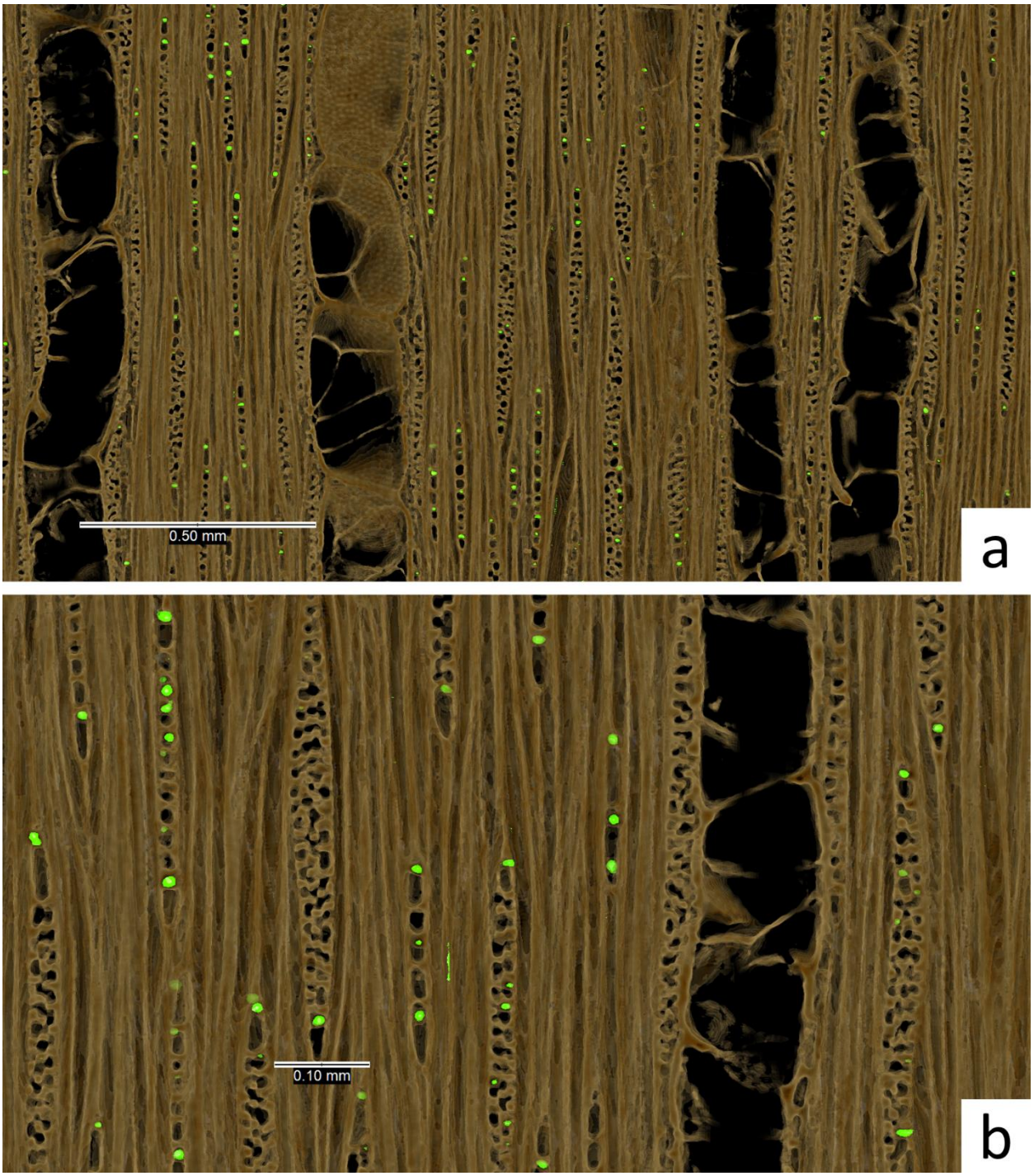

Figure 3.21 Tangential-longitudinal sectional images of walnut bean. Brown, wood; Green, silica

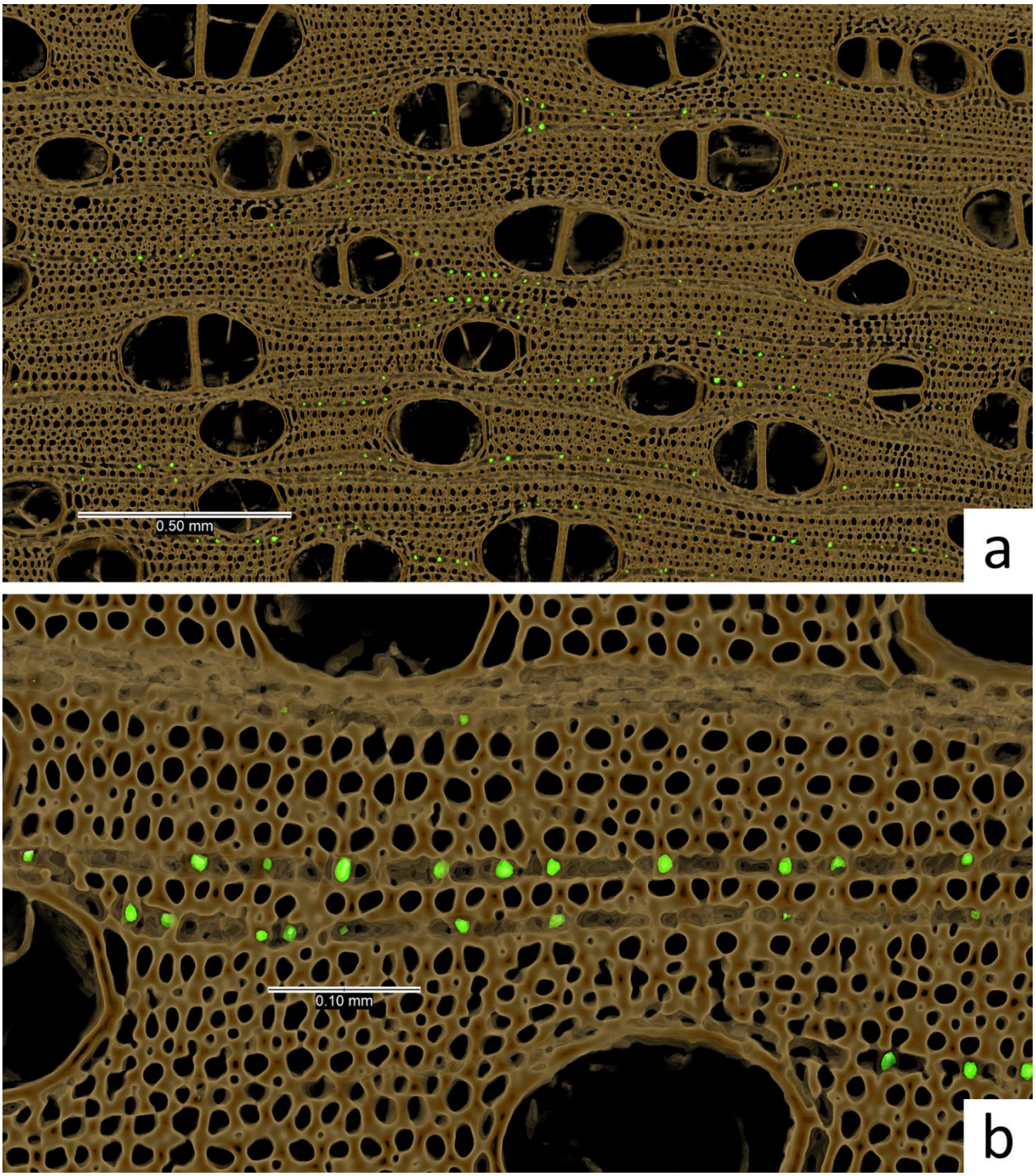

Figure 3.22 Transverse sectional images of walnut bean. Brown, wood; Green, silica

3.3.5 White beech

The high resolution (1.12 µm) micro-CT scan of white beech clearly showed cellular structures such as parenchyma cells in multiseriate rays and fibre cells. Unlike the other species described above, silica particles were not found in white beech. However, the high-resolution scan was able to detect inorganic (dense) materials in the white beech sample (Figure 3.23 a, b, c). Close-up images showed that the materials were located in the horizontal cross-walls of fibres (Figure 3.23 d, e, f, g).

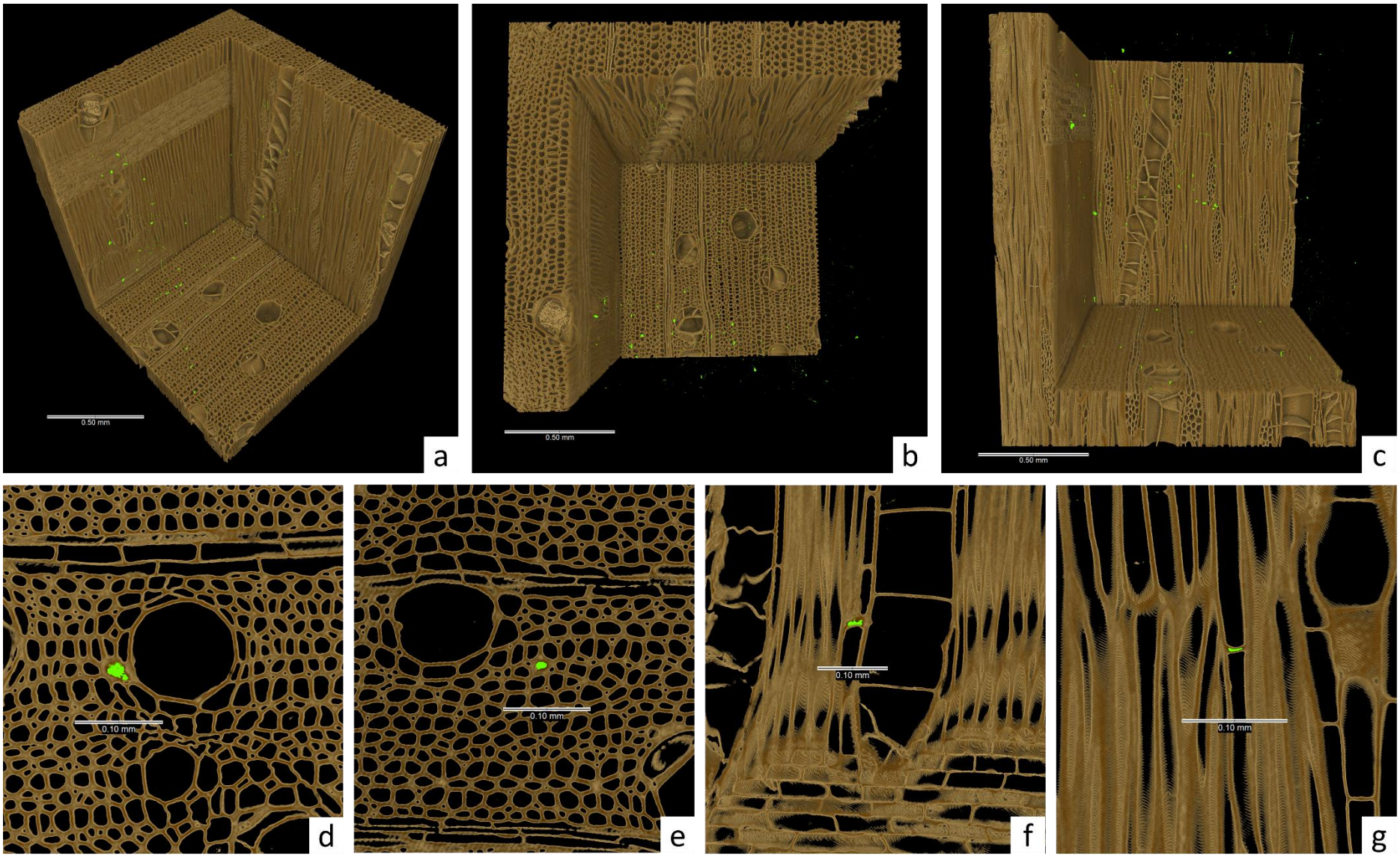

Figure 3.23 X-ray micro-CT images of white beech. (a) (b) (c): 3D views showing the cellular structures of white beech: (a) isometric view; (b) top view showing end grain; (c) side view in the radial direction. (d) (e) (f) (g) sectional views: (d) (e) transverse sections; (f) radial-longitudinal section; (g) tangential-longitudinal section. Brown, wood; Green, possible location of inorganics

3.4 Discussion

My results partially support the hypothesis that X-ray micro-CT will reveal the spatial distribution of silica in siliceous wood species. X-ray micro-CT successfully separated silica particles from other substances in wood samples, and also revealed their spatial distribution. X-ray micro-CT suggested, but could not confirm the presence of silica in other locations such as vessel elements and walls of parenchyma cells (Scurfield et al. 1974). Although dense materials (possibly silica) were found in the vessels and cell walls of ray parenchyma in turpentine and satinay, chemical information cannot be acquired using the X-ray micro-CT system I used. This limitation was mitigated through the use of synchrotron XFM. XFM confirmed that dense materials in samples were other inorganic elements in addition to silica. Other elemental analysis, such as scanning electron microscopy (SEM) in combination with energy dispersive X-ray analysis (EDX), can also be used to identify inorganic elements in wood. For example, Evans et al. (2021) used SEM-EDX to examine silica particles in turpentine and found that other elements such as P, Al, and Ti co-existed with silica particles. The combination of X-ray micro-CT and SEM-EDX has been used for studies on wood preservation (De Vetter et al. 2006, Evans et al. 2015), adhesion (McKinley et al. 2016), bio-deterioration (Koddenberg et al. 2020), etc. Future studies on inorganics in wood can use a similar approach. X-ray micro-CT could be used to detect materials denser than cell walls, and then elemental analyses like XFM and SEM-EDX can be deployed to confirm the chemical composition of the dense materials. Alternatively, elemental analysis could be used to locate inorganic elements in 2D and then X-ray micro-CT could be used to render their 3D distribution. The chemical identities of the dense materials in white beech could also be revealed using these approaches.

Previous studies of silica in wood have mainly used light or electron microscopy. Bamber and Lanyon (1960) used light microscopy to show that silica in turpentine and brush box heartwood occured as irregular-shaped aggregates that were rounded to some extent. Richter's (1980) SEM study found that *Endiandra* spp. had aggregated silica particles. Ogata et al. (2008) also used SEM and found silica particles in rays of *Tristania* spp. My results accorded with these previous studies because silica particles mainly occured in the ray cells of turpentine, walnut bean and brush box. Additionally, X-ray micro-CT revealed some previously undescribed features of the microstructure of silica in wood. These novel findings are: (1) silica particles are found in the ray cells in satinay; (2) silica particles mainly occur in the upright and square ray cells in walnut bean; (3) silica is associated with growth rings in brush box. However, compared to the X-ray micro-CT system I used, microscopy is superior in resolution. Hence,

the level of detail in the CT images of silica particles was not sufficient to see if they were smooth, rough, or aggregated. Such absence of detail in CT images was remarked upon by Koddenberg et al. (2019a) who used X-ray micro-CT to visualize silica in turpentine. This disadvantage in terms of resolution is likely to disappear when nanometer resolution X-ray micro-CT devices become more common. Koddenberg et al's (2019a) X-ray CT study observed that silica particles in ray cells in turpentine could be separated from the wood substrate. My results accord with their observations. However, my findings suggested that silica is present in vessels and walls of ray cells of turpentine and satinay. These findings may explain why Koddenberg et al. (2019a) found that silica content quantified using X-ray micro-CT was lower than the value obtained using a gravimetric analytical method.

My results showed some advantages of X-ray micro-CT for studying the 3D structure of wood. For example, the variation in the size and number of silica particles in brush box is difficult to discern from 2D images (Figure 3.15, 3.16, 3.17). Brush box is a diffuse-porous species with growth ring boundaries that are difficult to identify from sectional images. However, X-ray micro-CT makes it possible to remove wood substance cleanly while retaining the position of silica particles, allowing easy observation of their spatial distribution at growth ring boundaries. X-ray micro-CT makes it possible to rotate samples to discover the spatial distribution of silica particles. This feature made it possible to observe silica particles coinciding with growth rings in brush box (Figure 3.18). Similarly, it was possible to see the presence of silica particles in walnut bean at the edges of rays because of the pronounced sharp line patterns in 3D images (Figure 3.19). The 3D patterns of silica and other dense materials obtained using X-ray micro-CT opens up new horizons for wood anatomy. However, the number of species and replication in this chapter is not sufficient for my results to be used as a key for wood identification. A broader survey using more wood species with greater replication is required to confirm my findings.

My results demonstrate that X-ray micro-CT is an easier way to examine the anatomy of dense siliceous wood species than microscopy. The sectioning process in traditional microscopy methods is labour-intensive and time-consuming. Tardif and Conciatori (2015) commented that "making thin sections of wood is not an easy task and there is a wide array of details to which the practitioner must pay attention". Sectioning very dense tropical silicious wood species is particularly difficult since the commonly used chemical for softening such species, hydrofluoric acid, can cause severe injury or fatalities when mishandled due to its high and unique toxicity (Bertolini 1992). Furthermore,

hydrofluoric acid can alter the microstructure of wood by affecting cellulose and lignin and dissolving silica (Prakash 1986, cited in Tardif and Conciatori 2015). Electron microscopy does not require thin sectioning, but softening of wood is still necessary to obtain clean surfaces, plus an extra coating step is needed to make the wood electrically conductive (Jansen et al. 1998). By comparison, X-ray micro-CT samples can be prepared more easily (Van den Bulcke et al. 2009a, Koddenberg et al. 2019a). In addition, post-processing steps in X-ray micro-CT can be used to section samples virtually on a computer without going through the steps involved in physical sectioning. Lastly, X-ray micro-CT can be used to study the 3D microstructure of wood. While this is possible in microscopy using stacking of sectional images (Broadsen 2013), it is easier with X-ray micro-CT because continuous images in 3D are easily produced by volume rendering software.

3.5 Conclusions

X-ray micro-CT easily detected silica particles in all four silica-rich species and revealed new information on the silica particles and the microstructure of the four species: (1) satinay contained silica particles and their distribution was similar to that of turpentine; (2) bands of silica particles were found in brush box which coincided with growth rings; and (3) silica particles were mainly found in upright and square ray cells in walnut bean. Dense materials were also found in the vessels in turpentine and satinay, and in the cross-walls of white beech fibres, but their chemical compositions was not revealed using X-ray micro-CT. Another limitation was that the resolution of CT scans was insufficient to show the surface structure of individual silica particles. The former limitations can be overcome by combining X-ray micro-CT with elemental analysis methods, as the dense materials in turpentine and satinay were confirmed to be inorganics using synchrotron XFM, while the latter can be mitigated by improving the resolution of X-ray CT devices. Despite these limitations, X-ray micro-CT is an effective method for visualizing silica particles in wood in both 2D and 3D, and potentially other inorganic microstructures in more wood species in the future, potentially leading to better descriptions of the wood anatomy of siliceous species.

Chapter 4: Sodium Iodide as a Contrast Agent for X-ray Micro-CT of a Wood Plastic Composite

4.1 Introduction

Wood plastic composites (WPCs) are an important class of natural fibre reinforced composites, and in North America alone approximately 2000 Kt of WPCs are produced each year with an estimated market value of $6 billion (Popescu 2017). WPCs consist of a commodity polymer (most commonly high-density polyethylene, 35-45%), comminuted wood (50-60%) and various additives (5%) (Clemons et al. 2013). The wood in WPCs is a heterogeneous mix of particles that vary in size (0.1 to 2 mm in length and 0.1 to 0.6 mm in width), geometry, microstructure and chemical composition (Wang 2007). The size of wood particles in WPCs influences composite performance, for example, WPCs containing larger particles of wood are more susceptible to decay by basidiomycete fungi than composites containing smaller particles (Verhey and Laks 2002). Smaller wood particles act as a filler in WPCs, but larger particles provide reinforcement (Clemons et al. 2013). Hence, tailoring the size and geometry of particles can improve the mechanical properties of WPCs. For example, previous studies have examined the relationships between the initial size and length to width ratio of wood particles (measured using microscopy), and the mechanical properties of WPCs (Stark and Rowland 2003, Chaudemanche et al. 2018). These studies have shown that when wood particles have a larger aspect ratio, 'there is potential for more effective load transfer between the plastic and particles leading to better mechanical properties' (Schwarzkopf and Burnard 2016). However, the geometry of particles changes when they are incorporated into WPCs and, hence, measurements of particle dimensions prior to processing may not reflect their dimensions within manufactured WPC (Krause et al. 2018). In addition and more generally, as pointed out by Hanhan et al. (2019), prediction of the properties of polymer composites requires accurate characterization of their microstructural features. Various techniques have been used to characterize the microstructure of composites including light and electron microscopy, ultra-sound imaging, NMR and IR imaging and various X-ray imaging techniques (Jezzard et al. 1992, Guild and Summerscales 1993, Young 1997, Garcea et al. 2018).

X-ray micro-computed tomography (CT) is increasingly used to characterize the microstructure of polymer and aerospace composites and examine either experimentally or computationally the relationship between microstructure and bulk composite properties (Garcea et al. 2018, Naresh et al.

2020). X-ray micro-CT has also been used to characterize the microstructure of wood composites including wood plastic composites which can contain zinc borate as a biocide (Wang 2007, Muszynski 2009, Evans et al. 2010, 2015, Paris et al. 2014, Kamke et al. 2016, Bacaicoa et al. 2017). Characterization of wood plastic composites using X-ray micro-CT is challenging because, as pointed out by Wang (2007) 'plastics and wood are both weak in X-ray attenuation, and this always causes insufficient contrast in X-ray images and inability to separate wood particles from plastic'. Wang et al. (2007) incorporated gold nanoparticles into a WPC to improve the contrast between wood and plastic in a laboratory-made composite, as mentioned in Chapter 2. Alternative methods used to make it easier to distinguish wood and plastic are to reduce the wood particle fraction in the WPC or to subsample volumes and select larger wood particles that are easier to threshold (Krause et al. 2018). Nevertheless, it is challenging to distinguish plastic from small wood particles and discern interfacial regions within WPCs, as pointed out by Krause et al. (2018). Hence, better methods of increasing the contrast between wood and plastic in WPCs are needed. One obvious approach is to label either the plastic or the wood component to increase their X-ray opacity. In previous research, Evans et al. (2010) successfully labelled the thermosetting polymer adhesive, melamine-urea formaldehyde with copper sulphate to distinguish it from wood in particleboard. Similarly, barium sulphate or iodine have also been used as X-ray contrast agents for urea formaldehyde resin in medium density fiberboard, as mentioned in Chapter 2 (Walther and Thoemen 2009). However, these approaches are only suitable for laboratory-made boards. For commercial particleboard, Morrison (2004) took the opposite approach and labeled the wood rather than the polymer by injecting particleboard with the halogenated, low viscosity, X-ray opaque compound, bromoform ($CHBr_3$). This approach was only partially successful because the bromoform did not completely penetrate the composite (Morrison 2004). Nevertheless, in areas where wood particles absorbed bromoform it was possible to distinguish wood from polymer (Morrison 2004). Hence, I hypothesize that thoroughly impregnating a WPC with a halogenated fluid will be able to increase the contrast between wood and plastic. If this approach is successful, it will allow better visualization of the microstructure of the WPC, including the precise location of zinc borate particles in the composite and numerical analysis of the geometry of zinc borate and wood particles in the WPC. The aim of the work was to test this hypothesis, describe new insights into the microstructure of WPCs particularly zinc borate, and compare my results with those of other researchers who have examined the location of zinc borate in composites and also the effect of wood reinforcement on the properties of WPCs.

4.2 Materials and Methods

4.2.1 Wood plastic composite sample and intial X-ray micro-CT

An uncapped sample of wood-plastic composite decking measuring 24 mm (thick) and 140 mm square provided by Rio Tinto was air-freighted to the University of British Columbia. The WPC was composed of a high-density polyethylene polymer, wood particles, zinc borate and other unspecified additives. A cylindrical core, (5.8 mm [diam.] 9.68 mm [long]) was removed from the WPC sample using a plug cutter and vertical drill press. The sample was wrapped in pliable plastic, air-bubble, packaging, and sealed in a padded envelope, which was air-freighted by courier to the National Laboratory for X-ray Micro-Computed Tomography at The Australian National University in Canberra. The sample was sealed in a PEEK (polyether ether ketone) tube and imaged using a helical cone-beam X-ray micro-CT device as described in Chapter 3. The sample was fixed to the stage of the X-ray micro-CT device. X-rays from a cone-beam source passed through the sample to a detector where they created a two-dimensional (2-D) radiograph of the sample's interaction with X-rays. A series of 2880 such projections were collected over a period of 16 h by rotating and moving the sample relative to the X-ray source. The resolution of the CT scan was 2600 × 2600 voxels with a voxel size of 3.1 µm. Projection data were used to create 3D volumes (tomograms) of the x-ray attenuation property of the sample. Projection data was segmented to identify discrete phases (wood, plastic, void space and zinc borate).

4.2.2 Impregnation of WPC sample with sodium iodide and X-ray micro-CT

A 0.2 mol/L aqueous solution of sodium iodide (NaI) was used as a contrast agent for the WPC sample. Following the initial X-ray CT scan described above, the cylindrical WPC sample was placed in a stainless-steel pressure vessel containing sodium iodide solution under 6000 psi (41.37 MPa) of pressure. After 10 days the WPC sample was removed from the pressure vessel and sealed into a PEEK tube, containing free NaI fluid at the bottom of the tube. This reservoir of liquid ensured that the WPC sample did not dry out and move when it was irradiated with X-rays. The PEEK tube containing the WPC sample was placed on the rotating stage of a helical X-ray micro-CT device (as above) for 5 h prior to scanning. The sample was then scanned for 25 h and projection data segmented as described above for the first scan.

4.2.3 Visualization and numerical analysis of different phases in WPC sample

Phases in tomograms from the scans of the WPC sample before and after impregnation with sodium iodide (NaI) were visualized using the volume rendering software Drishti as described in Chapter 3. Drishti was used to create 2D images and 3D animations of the WPC sample. A CT data set of oriented strand board (OSB) scanned by Evans et al. (2015) was revisited to compare the zinc borate distribution in OSB with that in WPC. Numerical analyses of volumes of different phases in the WPC sample used the software Avizo (Thermo Fisher Scientific, Waltham, MA, USA). For the analysis of phase volumes the central region (2.56 mm long) of the untreated cylindrical core, which had the best contrast, was selected. The matching region within the NaI impregnated core was also selected. Both data sets were thresholded, and the percentages of the different phases were calculated. The wood volume from the second data set was adjusted to account for the swelling caused by NaI, as follows. The wood content in the WPC after the second X-ray CT scan is inflated because the wood swells as a result of impregnation with sodium iodide. The adjustment for such swelling of wood involved the following. First, calculation of the plastic content of the WPC before impregnation, which is assumed to remain constant as a result of labelling, is required (1):

$$P_0(\%) = \frac{V_{PW0} - \frac{V_{W1}}{1+S^W}}{V_0} \quad (1)$$

In which P_0 is the plastic content before impregnation; V_0 is the total volume before impregnation; V_{PW0} is the volume of plastic and wood before impregnation; V_{W1} is the wood volume after impregnation; S^W is the swelling ratio of wood. According to Siau (1995), S^W can be calculated using the equation (2):

$$S^W = (M_f - M_{0)} G_0^W \quad (2)$$

In which M_f is the moisture content of wood at the saturation point; M_0 is the moisture content of the wood before impregnation; G_0^W is the specific gravity of wood cell wall substance. Equation 1 can then be modified as:

$$P_0(\%) = \frac{V_{PW0}}{V_0} - \frac{V_{W1}}{V_0 + (M_f - M_{0)} G_0^W V_0} \quad (3)$$

V_{pw0}, V_0 and V_{w1} were obtained from the X-ray CT scan. Given that the initial moisture of wood in WPC is ~1-1.5% (Adebayo et al. 2008), I assume M_f = 30%, M_0 = 1.5%, G_0^W = 1.53. The plastic content was then

calculated as 35.10%. The adjusted proportions of the components before impregnation are shown in Table 4.1 in the results section below.

Avizo was used to calculate the number and sizes of the zinc borate particles before and after impregnation of the WPC sample. A series of 760 continuous 2D tomograms were selected from the central region of the WPC core before impregnation and a matching series of tomograms were selected from the core after treatment. Analysis of variance was used to analyze the effect of NaI impregnation on the number and sizes of zinc borate particles in the WPC sample. Statistical computation used Genstat (v. 20) (VSN International, Hemel Hempstead, UK). To calculate the extent of the interconnected void network, I used Avizo's label analysis module which measured the percentage volume of the largest 3D object representing voids. The same module was used to calculate the percentage of wood particles that were connected.

4.2.4 Numerical analysis of geometry of wood particles in WPC sample

A volume within the labelled WPC sample data set, measuring 4.92 mm (diameter) × 0.64 mm (thickness), was selected using Avizo. All wood particles in this area were labeled, except those on the edges of the volume that were cut during sample preparation. Labelling of wood particles involved thresholding them, smoothing thresholded volumes and filling pores for easier segmentation. Secondly, thresholded volumes were divided into small 3D segments based on the topological skeleton of wood particles (Youssef et al. 2007). Finally, all wood particles were labelled according to the following rules: (1) Particles which contained more than one segment (Figure 4.1, blue), were only labelled on one segment, which was usually the central or the largest particle of wood (Figure 1, labelled in blue); (2) Particles that were wholly separated from other particles and only contained one segment were fully tagged (Figure 4.1, green); (3) Particles that were attached to other particles were manually labelled in their centres (Figure 4.1, magenta). The tags were numbered, and 50 of them were randomly selected. The selected wood particles were manually traced to obtain their complete dimensions (Figure 4.1d).

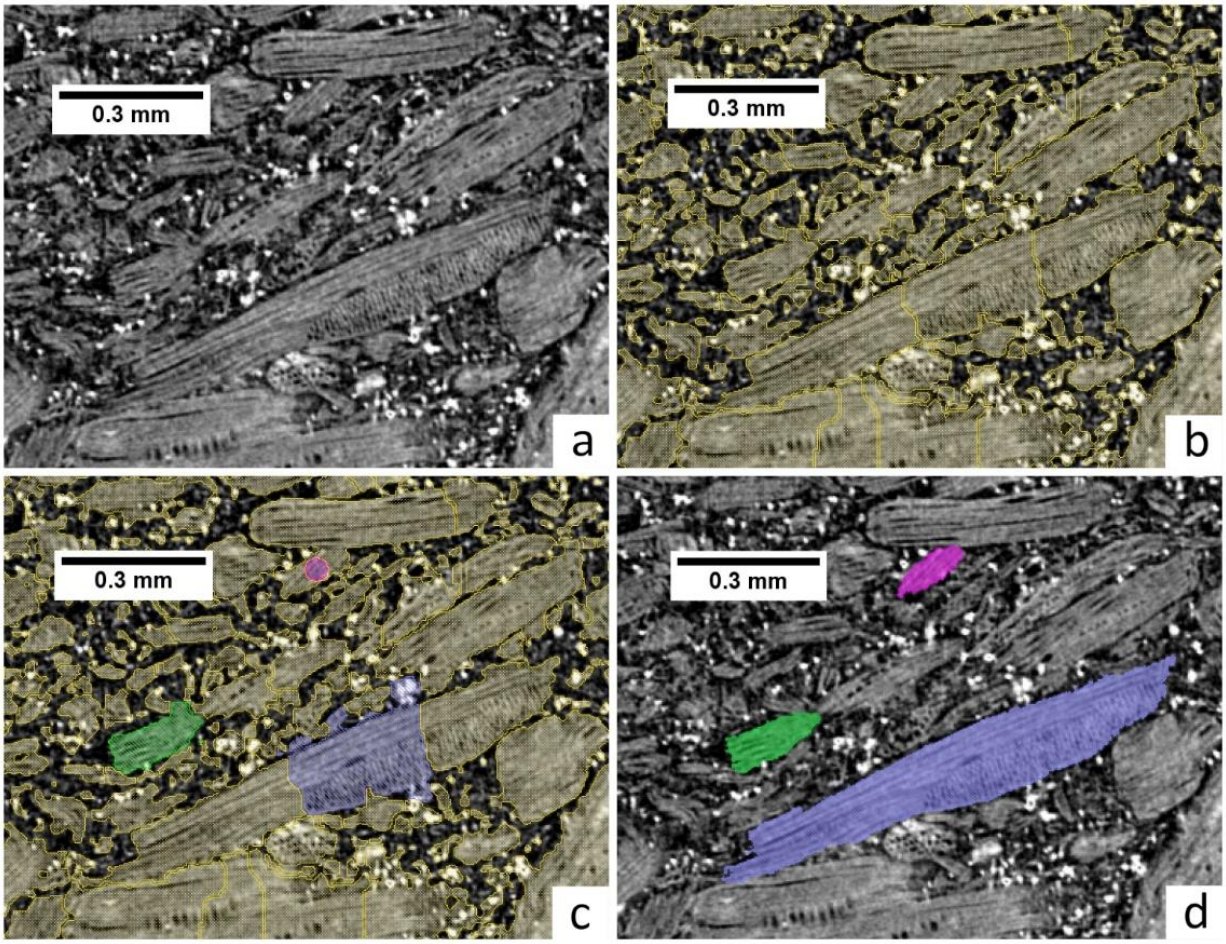

Figure 4.1 Labelling and restoration of wood particles. (a) Original grayscale tomogram; (b) Thresholded volume showing segments (yellow); (c) Three different types of labels: Blue, a wood particle with more than one segment; Green, a particle with only one segment; Magenta, an unseparated particle that shared a segment with another particle. (d) Results of the manual restoration of labeled particles

The volume, surface area, aspect ratio, and Wadell (1935) circularity of wood particles were measured using Avizo. I used the definition of aspect ratio from Merkus (2009), which is the maximum Feret diameter divided by the minimum Feret diameter. Particle length (L) is the largest Feret diameter of a wood particle; breadth (B) is the largest Feret diameter perpendicular to L; and thickness (T) is the largest Feret diameter perpendicular to both L and B. The L:B:T ratios were calculated to obtain a shape parameter.

4.3 Results

4.3.1 Visualization of phases in WPC before and after impregnation with NaI

4.3.1.1 Wood, polymer and voids

Impregnation of the WPC sample with sodium iodide made it possible to clearly differentiate wood and polymer as hypothesized. Before impregnation of the WPC sample it was possible to clearly identify air and zinc borate, which are coloured light blue and white in Figure 4.2a, c, e, respectively, but there was a lack of contrast between wood and plastic. In particular, it was difficult to distinguish smaller wood particles from the plastic matrix. However, larger wood particles could be seen in the unimpregnated sample because of their cellular characteristics. As a result, it was possible to see that the WPC contained both softwood (4.2a, arrowed) and hardwood particles (4.2c, arrowed).

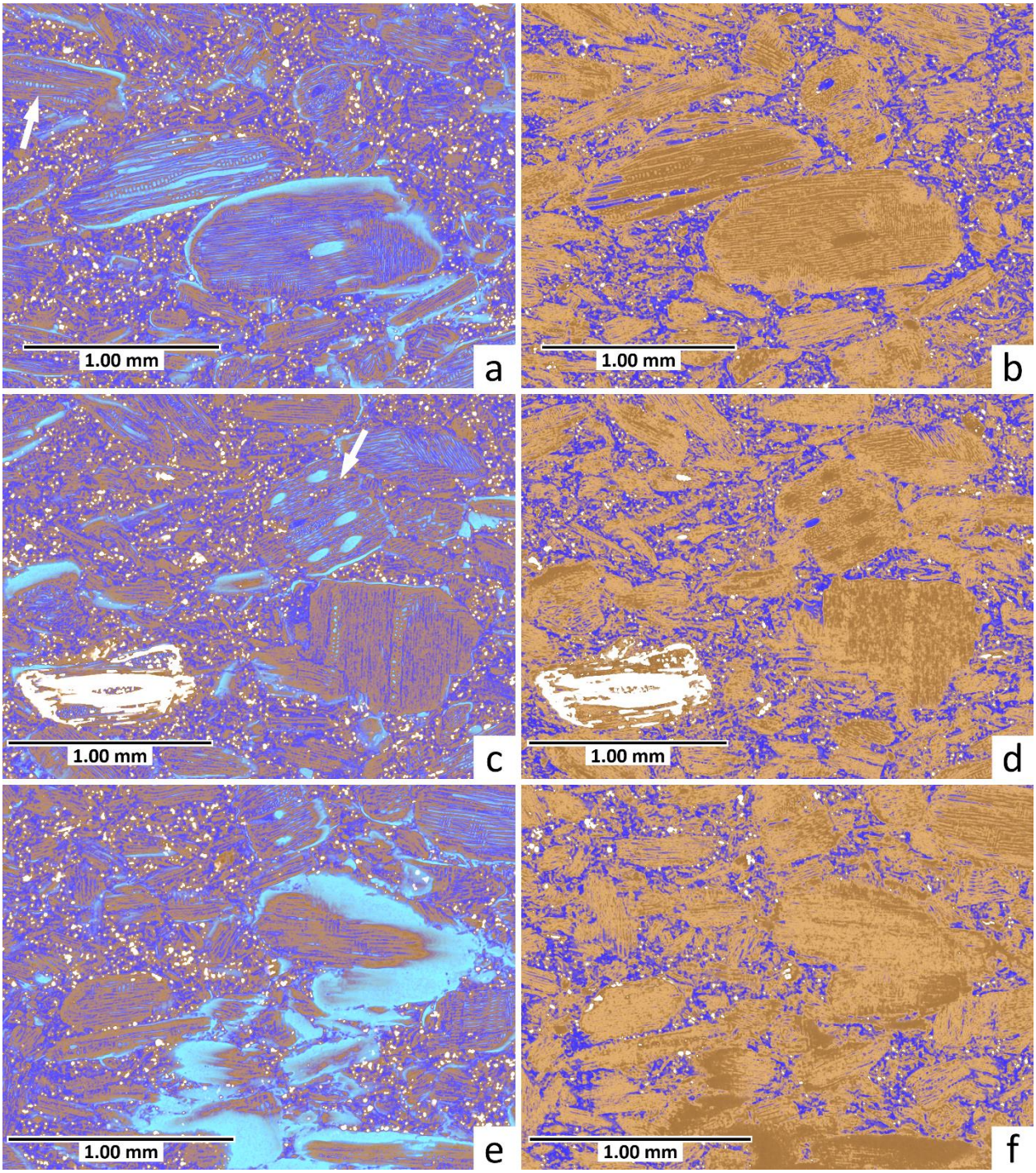

Figure 4.2 2D tomographic images of the wood plastic composite: before (a, c, e) and after (b, d, e) impregnation with sodium iodide impregnation; Brown = wood; navy blue = plastic; light blue = void; white = zinc borate

The unimpregnated sample contained voids within and around wood particles, particularly larger particles, whereas such voids were absent from the impregnated sample. Interfacial voids around particles in the unimpregnated sample were connected creating a network of cracks within the WPC (Figure 4.2e). Numerical analysis of the network revealed that 61.80% of the voids formed a single connected network. A similar analysis revealed that almost all (99.75%) of the wood particles in the WPC were connected. The improved contrast between wood and polymer in the impregnated sample made it possible to see two features that were not apparent in the unimpregnated sample. Firstly, there are areas where wood particles meet that contained little or no polymer (Figure 4.3a, b). Secondly, wood particles in the WPC were not randomly oriented. Instead, many of the larger particles were oriented in length in approximately the horizontal direction (Figure 4.3c, d).

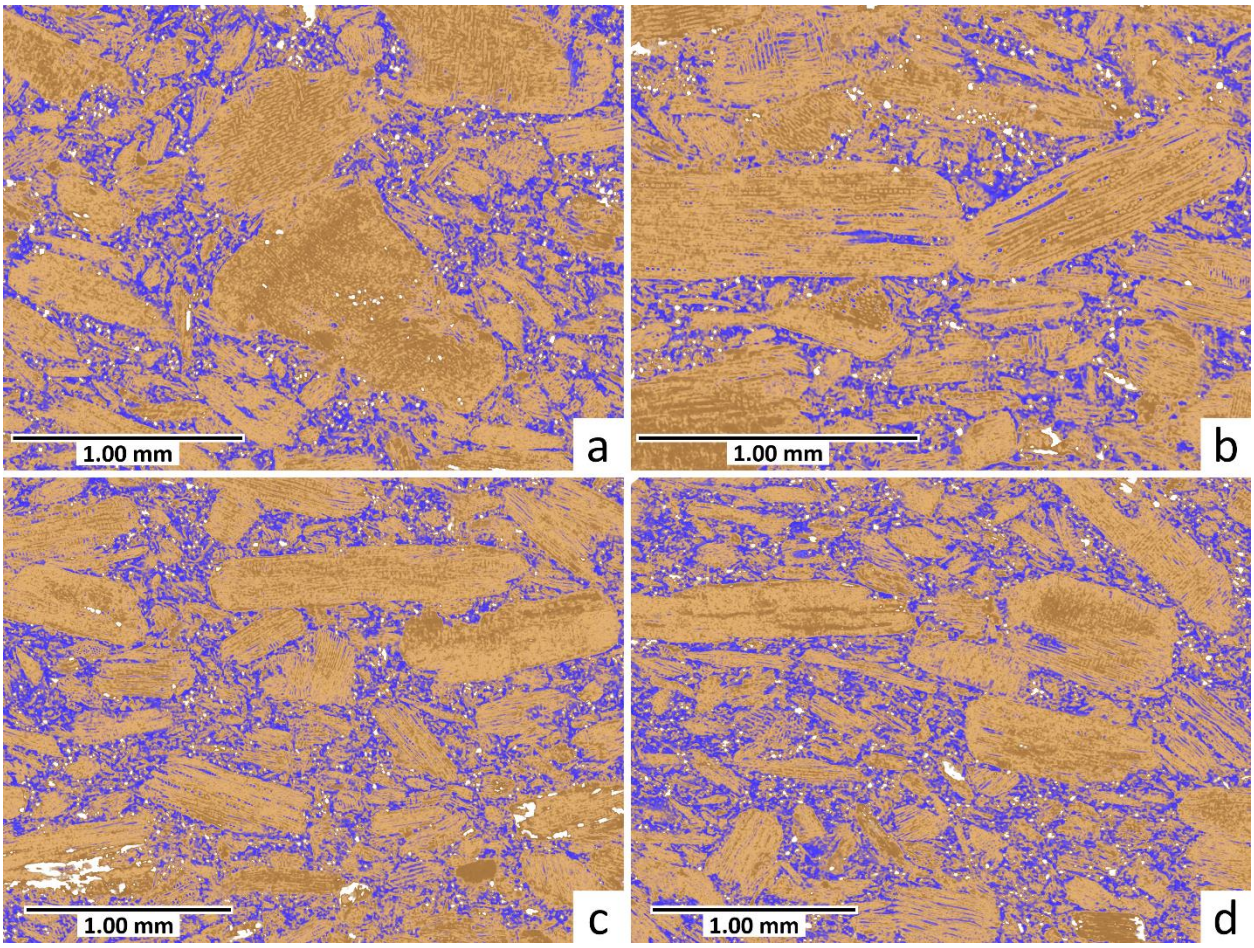

Figure 4.3 Tomographic images of the wood plastic composite after it was impregnated with sodium iodide showing wood to wood connections (a, b) and orientation of particles in the sample (c, d)

4.3.1.2 Zinc borate

As expected, zinc borate (ZB) was easy to see in the unimpregnated sample because it is far denser than plastic or wood. ZB occurred mainly as discrete particles between rather than within or around wood particles (Figure 4.2, 4.4a). However, occasionally, large wood particles were encased in a layer of zinc borate particles (Figure 4.2c, d, 4.4a). In contrast, ZB particles in OSB were mainly aggregated along glue lines, showing interrupted lines as in Figure 4.4b. There were fewer discrete zinc borate particles in the OSB than in the WPC. Zinc borate particles were clearly smaller and less numerous in the WPC sample after it was impregnated with sodium iodide. Accordingly, analysis of variance showed a highly significant ($p<0.001$) effect of impregnation with sodium iodide on the number of ZB particles and their average diameter in the selected volume within the WPC. These observations are supported by analysis of ZB particles in the entire data set, which showed that the number of particles decreased from 1,130,639 to 512,731 as a result of labelling. Similarly, the average volume and diameter of the ZB particles dropped from 1204.4 μm^3 and 10.4 µm (before labeling) to 770.8 μm^3 and 8.8 µm, respectively, after labeling.

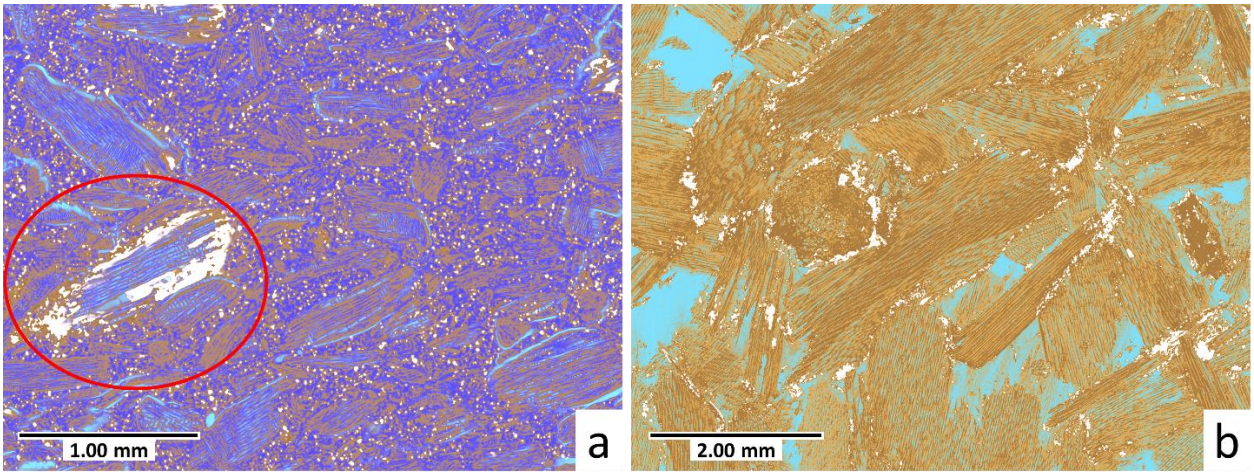

Figure 4.4 Tomographic images of zinc borate in the WPC (a) and an OSB sample (b). A wood particle encased by zinc borate is circled in (a). Brown = wood; navy blue = plastic; light blue = void; white = zinc borate

4.3.2 Quantification of different phases in WPC following labelling with NaI

It was not possible to segment wood and plastic in the unlabeled WPC, as mentioned above, but after impregnation with sodium iodide there was sufficient contrast to segment both phases. However, swelling of wood particles caused by aqueous sodium iodide solution, which is obvious in Figure 4.2 (b, d, f) altered the volumetric composition of the WPC. Therefore, quantification of the levels of wood and plastic in the labelled WPC needs to adjust the wood content for such swelling, as described above.

Table 4.1 Volumes (mm^3) of phases in the WPC sample (percentage in parenthesis)

Composition/phases	Before labeling	After labeling	Adjusted*
Voids within WPC	5.1 (8.5%)	-	5.1 (8.5%)
Wood particles	-	46.2 (65.6%)	32.2 (54.1%)
Plastic matrix	-	-	20.9 (35.1%)
Zinc borate biocide/fire retardant	1.4 (2.29%)	0.39 (0.56%)	1.4 (2.3%)

* Composition based on initial volumes of void and ZB contents and adjusted wood content

Finally, compositional volumes of the WPC after impregnation with sodium iodide needed to be adjusted to reflect the natural composition of the WPC including voids and zinc borate, which were altered by the labelling process (Table 4.1). The adjusted volumes in Table 4.1 indicate that the WPC was mainly composed of wood (54%) and plastic (35%) in accord with figures in the literature, but the void volume was significant (8.5%).

4.3.3 Quantification of wood particle sizes and geometry

The particles that were randomly selected in a slice within the labelled WPC sample are shown in Figure 4.5. There is clearly great variation in the size and geometry of the particles. This was confirmed by using Avizo software to quantify: (1) the largest Feret diameter of each wood particle (length, L); (2) breadth (B) as the largest Feret diameter perpendicular to L; and (3) thickness (T) as the largest Feret diameter perpendicular to both L and B. Shape was defined using a combination of L, B and T, as mentioned above.

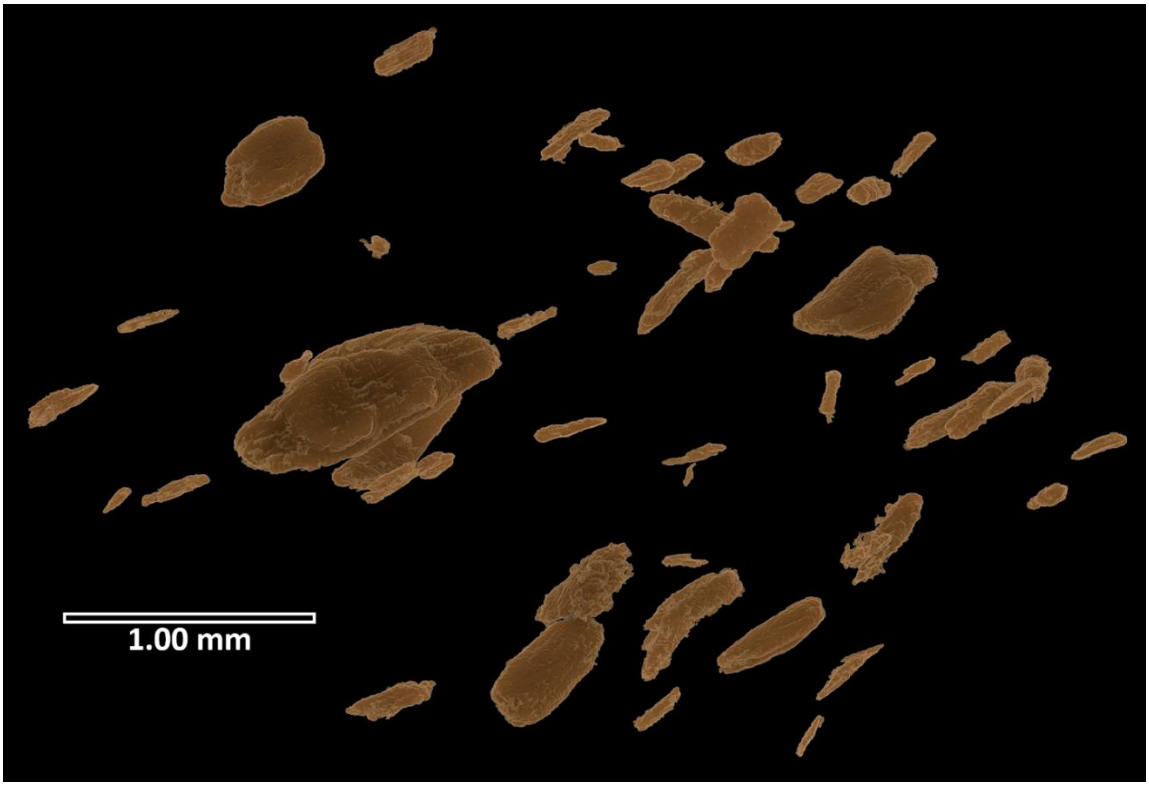

Figure 4.5 Image showing the wood particles that were randomly selected from a volume within the labelled WPC sample

All of the selected wood particles were longer than they were wide (Figure 4.6). Three particles had an aspect ratio slightly greater than two: ie, similar to the rectangular format of films (movies) used to depict landscapes. Four particles (8%) had needle-like aspect ratios of >5.

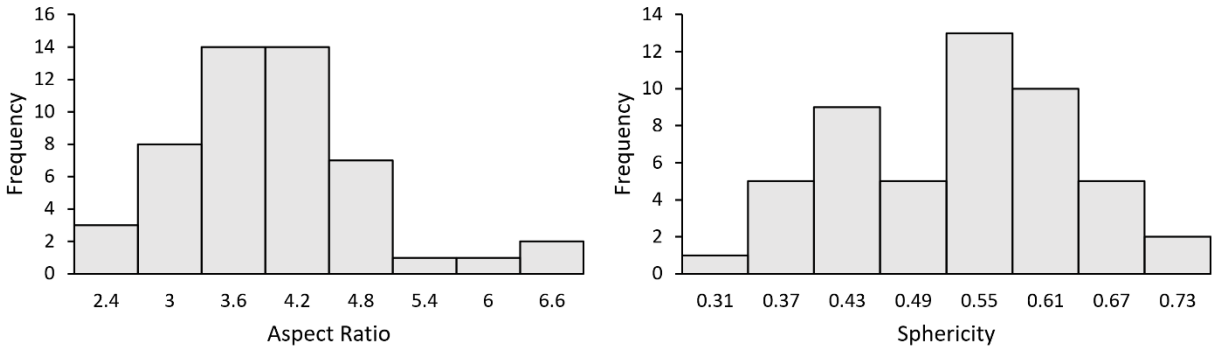

Figure 4.6 Aspect ratios and sphericity of the wood particles that were randomly selected from a slice within the labelled WPC sample

Shape descriptions based on Ferret L:B:T values showed that most of the wood particles were either columns or plates (Figure 4.7). None of the particles could be classified as spheres, i.e. particles with diameter deviations within 5%, rotational symmetry, and round surfaces (Merkus 2009). The unclassified category in Figure 4.7 is composed of particles that do not fit any of the categories developed by Merkus (2009).

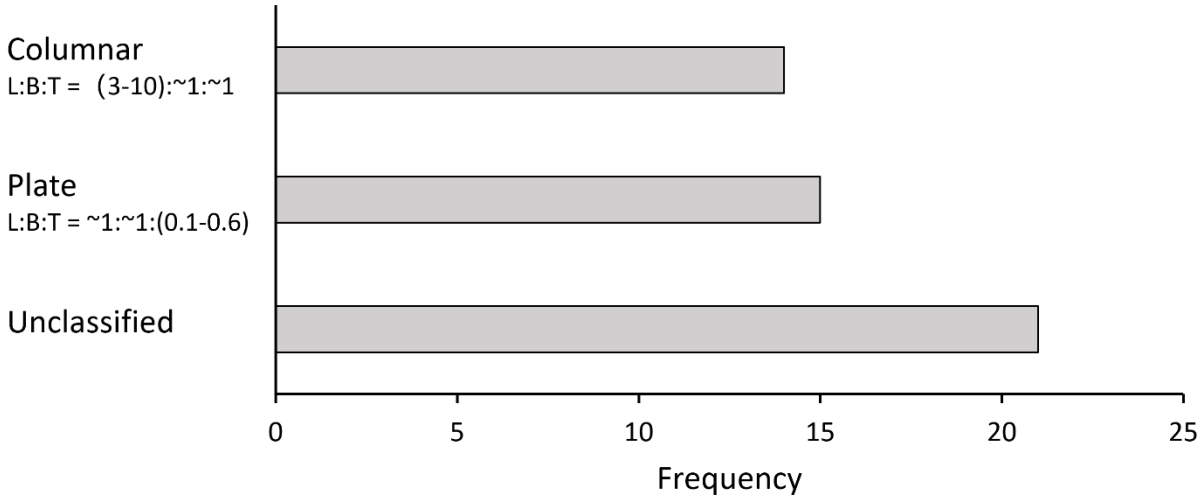

Figure 4.7 Shape descriptions of the selected 50 particles based on their L:B:T ratios

4.4 Discussion

My results only partially support the hypothesis that aqueous sodium iodide is a suitable X-ray micro-CT contrast agent to help visualize the microstructure of a wood plastic composite, and precisely locate zinc borate in the composite. Sodium iodide labelling made it possible to: more clearly visualize wood and plastic in the WPC; quantify the levels of different phases (wood, plastic, zinc borate and voids) in the composite; and measure the geometry of the wood reinforcement. These outcomes of labelling are noteworthy, but sodium iodide was not an ideal contrast agent because it altered the microstructure of the WPC. For example, it swelled wood particles closing interfacial voids, filled any remaining voids with liquid, and (unfortunately) dissolved zinc borate particles. Furthermore, the labelling process was lengthy and two separate CT scans were needed to quantify the composite's composition and analyze the shape of wood reinforcement. Future research should seek to overcome some of these limitations possibly by selecting a solvent for sodium iodide or an alternative halogenated

chemical that does not swell wood or dissolve zinc borate. Wood or plastic could be labelled prior to the manufacture of the WPC as has been done previously (Wang et al. 2007), which would eliminate the time-consuming step of impregnating wood with the contrast agent, but this approach is not suitable for visualizing the microstructure of commercial WPCs, which was one of the aims of this study

Previously, Evans et al. (2015) used X-ray micro-CT to visualize the distribution of the biocide zinc borate in oriented strand board (OSB), a structural wood composite that contains high levels of wood reinforcement and low adhesive content. OSB is manufactured using a completely different method to that of WPC's (Lötter and Evans 2019, Gardner et al. 2015), and zinc borate in OSB is located within glue lines (Evans et al. 2015). The distribution of zinc borate in my WPC sample was different to that in OSB (Figure 4.4), but in both composites zinc borate was dissolved by water, which reduced the size of zinc borate particles. The dissolution of zinc borate in WPC and absorption or complexation of zinc or borate ions with wood that is not fully encapsulated in plastic may explain, in part, why it is an effective biocide for WPC's (Evans et al. 2015). Some of my findings also help explain other aspects of the durability of WPCs. For example, previous studies, as mentioned above, have shown that WPCs with larger wood particles absorb more moisture and are more susceptible to decay than composites made from smaller particles (Verhey and Laks 2002, Steckel et al. 2007). These observations can be explained by my finding that interfacial voids were concentrated around large wood particles and many of the voids were connected, possibly assisting moisture ingress into the WPC as suggested by Sun et al. (2016). In addition to the network of voids, moisture ingress would also be facilitated by the aggregation of wood particles and the numerous wood-to-wood connections in the composite, which made shape analysis of individual particles difficult. The absorption of moisture into WPC's is the rate-limiting factor restricting decay of the composites (Morrell and Stark 2006), and therefore measures that reduce the porosity of the composite improve the durability of WPC's. In practice, this is achieved in the latest generation of 'capped' WPCs by extruding a layer of pure polymer over the surface of the composites (Mankowski et al. 2015). This barrier approach is highly effective at reducing moisture ingress into WPCs, but in areas where the protective polymer cap is absent, or breached, for example by cut ends and fixings, some moisture absorption can still occur (Gnatowski et al. 2015). Therefore, additional measures to reduce the porosity and durability of WPCs may be useful. My results suggest that reducing the number of large wood particles and the interfacial voids around the particles could have the desirable effect of reducing porosity and possibly increasing durability of WPCs. Further, research is needed to fully test this hypothesis. Where large wood particles are required as reinforcement for WPCs

(Chen et al. 2006), alternative approaches to reduce the formation of interfacial voids may be needed, for example, modifying wood or plastic to make the two phases more compatible (Takatani et al. 2008, Lin et al. 2020).

It is difficult to compare my results on the visualization of WPC with those of previous studies because my approach to labelling the composite has not been used before. However, there is similarity between methods I used to analyze the geometry of wood reinforcement and those of previous studies (Chaudemanche et al. 2018, Madyan et al. 2020). Previous studies have cast doubt on the use of mesh size as an accurate way of characterizing the sizes of wood reinforcement in WPCs. For example, Madyan et al. (2020) pointed out that a small mesh allows the passage of long particles, overestimating the potential of small (mesh) particles to reinforce the composite. My results support this assertion because all the randomly selected particles in my commercial WPC were elongated (aspect ratio >2) with a mean aspect ratio of 3.67; 28% of the particles were columnar in shape; only 30% of the particles had a centro-symmetrical plate-like shape which would allow passage through a mesh in any direction. Previous studies have also used particle diameter as a measure of the size of wood particles used to reinforce WPCs. A diameter measurement is suitable for a sphere, ellipsoid, or cylinder. However, I found that 42% of the wood particles did not fit these shape categories. Furthermore, wood particles were not spherical because they had a mean sphericity of 0.50. Therefore, I suggest it would be better in future to use Feret diameter measurements rather than mesh size or particle diameter to classify the wood reinforcement used in the manufacture of WPCs. This suggestion is supported by the research of Bacaicoa et al. (2017) who obtained Feret-based parameters from wood particles segmented in X-ray micro-CT images.

The segmentation of wood particles in a WPC following imaging is a key step in quantifying their shape. This was not straightforward even after my WPC sample was labelled with sodium iodide. Automated segmentation of wood particles in a WPC was successfully used by Bacaicoa et al. (2017), but their WPC had a lower wood content (10%) than mine (>50%) and far less overlap of wood particles. When I tested the same automated software used by Bacaicoa et al. (2017) it was unable to find the correct wood particle boundaries because there were numerous overlapping and irregular-shaped particles in my WPC. On the other hand, manually segmentation was too time consuming (Strohmann et al. 2019). These limitations of automated and manual segmentation stimulated the development of my tagging-selecting method, which is more accurate than automated segmentation and less time-

consuming than complete manual segmentation. Nevertheless, my approach is still slower than automated segmentation and it would be desirable to develop an accurate and automated segmentation method for the reinforcement in WPC's. One possible approach involves the use of AI-based techniques, for example, machine learning and neural networking, which have been used to recognize and segment objects automatically in CT images (Furat et al. 2019, Strohmann et al. 2019). I anticipate that in the future, similar techniques could be used to develop a more advanced automated segmentation algorithm that could recognize the contours of wood particles, so that wood particles in commercial WPC samples could be rapidly separated and analyzed. Such developments could facilitate better understanding of the relationships between the geometry of wood reinforcement in WPCs and their properties, possibly leading to the development of improved composites.

4.5 Conclusions

Aqueous sodium iodide is an effective contrast agent for wood in a commercially manufactured wood plastic composite (WPC) making it possible to clearly visualize both wood and plastic in the WPC, quantify the amounts of wood, plastic, zinc borate and voids in the composite, and measure the geometry of the wood reinforcement. I describe the limitations of sodium iodide as a contrast agent for WPCs and the difficulties of segmenting or separating wood and plastic even in a labelled composite. I suggest ways of overcoming both these limitations using, respectively, non-swelling halogenated contrast agents, and automated machine-learning segmentation algorithms. These advances could lead to a better understanding of the relationships between the microstructure of WPCs and their properties, possibly leading to the development of improved wood plastic composites.

Chapter 5: Discussion, conclusions, and suggestions for further research

5.1 General discussion

In this thesis, I hypothesized that X-ray micro-CT could visualize inorganic materials in 3D in silica rich Australian hardwoods and a wood plastic composite treated with zinc borate, and produce images that show the spatial distribution of inorganics in the silica rich wood and WPC. This hypothesis is partially supported by results in both experimental chapters in which the discrete inorganic particles were detected and their 3D distributions were rendered using X-ray micro-CT. In Chapter 3, discrete silica particles were found in the ray cells of the four siliceous hardwood species. The 3D rendering of the distribution of silica particles showed different patterns in some of the species, for example arc-shaped patterns matching growth rings in brush box and sharp lines corresponding to the upright and square cells at the edges of rays in walnut bean. Dense materials associated with vessels and walls of ray cells were also found in turpentine and satinay, which were not easily resolved using X-ray micro-CT. Synchrotron XRF confirmed that these dense materials were inorganics. In Chapter 4, zinc borate particles were found in the WPC sample both before and after labeling with sodium iodide. The zinc borate particles were mainly discrete occurring in-between wood particles and occasionally encasing large wood particles. However, both chapters revealed limitations of X-ray micro-CT in detecting small inorganic particles (< voxel size). The X-ray micro-CT resolutions employed here was not adequate to visualize aforementioned dense inorganic materials in vessels of the two *Syncarpia* species, or the surface morphology of silica particles in rays. In contrast, SEM can visualize the rough irregular surface of silica particles (Richter 1980, Koddenberg et al. 2019a). X-ray micro-CT was also unable to detect zinc borate particles in WPC which were smaller than the voxel size, as well as any dissolved or redistributed zinc borate particles resulting from labelling of wood with sodium iodide.

In Chapter 1 I also hypothesized that the addition of an inorganic halogenated contrast agent could overcome limitations during X-ray imagining of WPCs resulting from the similarity in density of wood and plastic. My results in Chapter 4 generally met this hypothesis because sodium iodide successfully made wood in WPC clearly visible and thus enabled both qualitative and quantitative analyses of the different components in the WPC. However, there were a few caveats which make sodium iodide less than ideal as a contrast agent for WPC. Sodium iodide altered the microstructure of

the WPC by swelling the wood, dissolving zinc borate particles, and filling the voids. The treatment process was time-consuming and difficult to perform since a constant high pressure was required to treat the WPC with sodium iodide. These findings point to the need to develop better contrast agents for WPC and new quantitative analysis methods for different components of WPC.

Results in both of my experimental chapters on inorganics in solid wood and a WPC demonstrated the potential of X-ray micro-CT for the study of 'wood' anatomy. The non-destructive nature of X-ray micro-CT made it possible to scan the same WPC sample twice (before and after labeling). The high degree of freedom in the 3D operation of volume rendering software allowed free rotation and zooming of the volume to observe 3D microstructures, and micro-adjustments of virtual slicing tool to produce sectional images similar to microscopy images, as well as virtually subtracting wood while retaining the position of inorganics to enable unobstructed observation of the distribution of inorganics. The computer-based analysis of CT data enabled automatic quantification of composition of a WPC and the geometry of its wood reinforcement. X-ray micro-CT is not limited to these applications. Results in Chapter 4 were presented in the form of animated videos (Feng et al. 2022, video abstract, Appendix 4), In addition, some of the results in Chapter 3 was presented in a virtual reality system (Feng et al. 2020, Appendix 2). Moreover, the 3D geometries in micro-CT data sets can be converted into other digital formats that could be used in a large variety of applications such as computer-assisted design (CAD) (Shammaa et al. 2007), finite element analysis (Magne 2007), 3D printing (Shelmerdine et al. 2018), technology-enhanced learning (Feng et al. 2020, O'Rourke et al. 2020), video games (Javan et al. 2020), etc. These applications may attract a wide variety of audiences to wood science in the future. They may also enhance future research in wood anatomy and wood composites.

Some limitations of X-ray micro-CT also emerged in the two experimental chapters. First, the image acquisition time for each sample was long. For example, each of the two CT scans of the WPC took 16 hours to complete, similar to each CT scan of the wood species in Chapter 3. Secondly, the limited resolution of X-ray micro-CT resulted in lower level of detail compared to electron microscopy. In Chapter 3, the coarse texture of the surface of silica particles, which has been observed in SEM study of siliceous wood species (Richter 1980), were smoothed out in X-ray CT images. Similarly, X-ray micro-CT was not able to detect zinc borate particles which were smaller than the voxel size employed in Chapter 4. Thirdly, X-ray micro-CT is costly, since the scans in Chapter 3 and 4 each cost $AUD 500, which is a

heavily discounted rate for staff at The ANU. There are some other limitations of X-ray micro-CT, but these were either avoided or minimized in this thesis. For example, Paterson et al. (2014) pointed out that the file size of a micro-CT data set is large, and storing and transferring such big files can be difficult. These issues were solved in this thesis thanks to the array of solid-state drives installed in my workstation at UBC, which offered a large storage space and a high transfer speed. Paterson et al. (2014) also stated that rendering the images of micro-CT data sets is time consuming. This issue was minimized in this thesis by employing a dedicated graphic processing unit and large graphic memory, both of which reduced rendering times.

5.2 Conclusions

This thesis demonstrated that X-ray micro-CT is a versatile tool for studying inorganics in wood. X-ray micro-CT revealed dense siliceous inclusions in silica-rich tropical hardwood species, and was able to locate silica particles in rays and render their distribution patterns in 3D. X-ray micro-CT in combination with synchrotron X-ray fluorescence microscopy identified dense inorganic materials in vessels of the two *Syncarpia* spp. Therefore, I conclude that the distribution of inorganics in the four siliceous species here are tied to horizontal xylem conduits (rays), or the 3D network comprised of vertical conduits (vessels) and horizontal rays. X-ray micro-CT was also used to examine a WPC containing the inorganic biocide, zinc borate. With the aid of a halogenated inorganic contrast agent, NaI, X-ray micro-CT was able to perform qualitative and quantitative analyses on organic and inorganic constituents in the WPC sample. However, the labeling technique was not perfect because it was time-consuming and it altered the microstructure of WPC. Hence, I conclude that X-ray micro-CT is an effective tool for visualizing WPC when a NaI contrast agent is used but future research should seek a contrast agent that does not alter the microstructure of WPCs.

In conclusion, X-ray micro-CT is an attractive method for non-destructive detection of inorganics in wood. My thesis opened up new horizons for future studies by providing examples of how X-ray micro-CT can reveal new structural information on the microstructure of wood and wood composites. Since the inorganics detected in both experimental chapters were all denser than other wood constituents, future studies can use X-ray micro-CT to browse through the density profile of solid wood or wood composites, and locate the materials at the dense end of the density profile which may

represent inorganics. Then, the identity of these dense materials can be revealed by comparing their visual appearance with microscopy images, or by using elemental analyses such as XRF microscopy or SEM-EDX. The 3D distribution of inorganics and quantitative information can be acquired from X-ray micro-CT analyses once the presence of inorganics is confirmed.

5.3 Suggestions for further research

Chapter 3 examined the distribution of silica inclusions in four silicious hardwood species. The X-ray micro-CT device was able to detect silica particles, but was unable to acquire detailed information on the morphology of silica particles. Higher resolution X-ray micro-CT devices (nano X-ray CT) can be used in the future to obtain such information. Chapter 3 presented novel findings on the microstructure of five tropical Australian hardwood species and found high-density tissues containing inorganics. Such organic/inorganic composites only appeared in the two *Syncarpia* species (turpentine and satinay) and possibly in white beech. The other species in *Syncarpia* spp., *Syncarpia verecunda* A.R.Bean, should be examined in future to see if it has inorganics inclusions in vessels. The silica particles in brush box and walnut bean showed sharp line patterns and rainbow-shaped patterns, respectively. Future studies should investigate if other species in *Lophostemon* spp. and *Endiandra* spp. also have such patterns. Furthermore, the pattern of inorganics may be used to identify wood species, but a broader survey including more species is needed to examine the feasibility of such approach.

Chapter 4 described the use of an inorganic contrast agent (NaI) for labelling wood in a commercially manufactured WPC. The impregnation of aqueous NaI successfully increased the contrast between wood and plastic and enabled qualitative and quantitative descriptions of components in the WPC. However, the NaI contrast agent also closed interfacial voids by swelling the wood, dissolved zinc borate particles, and filled remaining voids with liquid, all of which made it less ideal as a contrast agent. Future research is needed to find a non-swelling halogenated contrast agent for WPC. In addition, a random selection procedure was used in this chapter for easing the difficulties of separating wood particles, but this procedure was still time-consuming. Advanced automated segmentation methods which are AI-based could be developed in the future for rapid segmentation of wood particles.

In both chapters, the phases were thresholded based on visual recognition. The inorganics were always found in the high-density regions, but the precise density values were unknown. X-ray CT can be used to measure wood density (Lindgren 1991a). The previous studies on utilizing X-ray micro-CT for wood densitometry were mostly related to dendrochronology (De Ridder et al. 2011, Van den Bulcke et al. 2014, 2019, De Mil et al. 2016, Vannopen et al. 2017), which focuses on density variation between or withing growth rings, rather than cellular structures like cell walls or inclusions. The micro-CT images in Chapter 3 clearly show dense cellular structures in samples. I anticipate that future studies can establish a threshold of density between inorganics and the wood substance. Future studies on wood composites could also use X-ray micro-CT to measure density. Previous studies on micro-CT density detection of wood composites mainly focused on the one-dimensional distribution of density across the thickness of samples (also known as vertical density profile, VDP) (Standfest et al. 2009, Yusof et al. 2015, Han et al. 2016, Oluwafemi et al. 2021, Zuber et al. 2021), rather than 2D and 3D mapping of density. Wood composites are not always uniform across their length and width. For example, Han et al. (2016) measured the VDP in WPC and found that VDP curves were flatter near the edges and steeper in the middle of the samples. The 2D and 3D capability of X-ray micro-CT may aid studies of the density distribution in wood composites, possibly facilitating the development of wood composites whose density profiles are more closely tailored to stresses they will be subjected to in-service.

References

Abdel-Gadir AY, Krahmer RL (1993a) Estimating the age of demarcation of juvenile and mature wood in Douglas-fir. Wood and Fiber Science 25(3), 242-249

Abdel-Gadir AY, Krahmer RL (1993b) Genetic variation in the age of demarcation between juvenile and mature wood in Douglas-fir. Wood and Fiber Science 25(4), 384-394

Adebayo AB, Dawson-Andoh B, Georg BP, Nkansah K, Medley C (2008) Adsorption and desorption performance of two commercial wood plastic composites. Forest Products Journal 58 (9), 32-36

Adey-Johnson R, Mclean JP, Van den Bulcke J, Van Acker J, McDonald PJ (2020) Micro-CT measurements of within-ring variability in longitudinal hydraulic pathways in Norway spruce. IAWA Journal 41(1), 12-29. doi: 10.1163/22941932-00002104

Aernouts J, Gonzalez-Benecke CA, Schimleck LR (2018) Effects of vegetation management on wood properties and plant water relations of four conifer species in the Pacific Northwest of the USA. Forests 9(6), 323. doi: 10.3390/f9060323

Aguilera C, Ramos M, Salinas D (2002) Internal visualization of knots in Radiata pine logs using X-rays. Maderas: Ciencia y Tecnología 4(2), 193-200 (in Spanish). doi: 10.4067/S0718-221X2002000200010

Alkan S, Zhang Y, Lam F (2007) Moisture distribution changes and wetwood behavior in subalpine fir wood during drying using high X-ray energy industrial CT scanner. Drying Technology 25, 483-488. doi: 10.1080/07373930601184023

Alteyrac J, Cloutier A, Zhang SY (2006) Characterization of juvenile wood to mature wood transition age in black spruce (*Picea mariana* (Mill.) B.S.P.) at different stand densities and sampling heights. Wood Science and Technology 40(2), 124-138. doi: 10.1007/s00226-005-0047-4

Amos G, Dadswell H (1948) Siliceous inclusions in wood in relation to marine borer resistance. Journal of the Concil for Scientific and Industrial Research, Australia 27(3), 190-196

Anonymous (1936) The sawing of Queensland walnut. Commonwealth Scientific and Industrial Research Organization (CSIRO) Forest Products Newsletter 50, 2

Anonymous (1959) Uses of Australian timbers: gun and rifle stocks. Commonwealth Scientific and Industrial Research Organization (CSIRO) Forest Products Newsletter 251, 3

Appelqvist C, Havenhand JN, Toth GB (2015) Distribution and abundance of teredinid recruits along the Swedish coast - are shipworms invading the Baltic Sea? Journal of the Marine Biological Association of the United Kingdom 95(4), 783-790. doi: doi:10.1017/S0025315414001830

Bacaicoa I, Lütje M, Sälzer P, Umbach C, Brückner-Foit A, Heim H, Middendorf B (2017) Comparative investigation of two-dimensional imaging methods and X-ray tomography in the characterization of micro-structure. Materials Testing 59(10), 829-836. doi: 10.3139/120.111076

Badel E, Delisee C, Lux J (2008) 3D structural characterisation, deformation measurements and assessment of low-density wood fibreboard under compression: The use of X-ray

microtomography. Composites Science and Technology 68(7-8), 1654-1663. doi: 10.1016/j.compscitech.2008.02.013

Baker JM (1965) Application of X-radiography to the estimation of larval size in Anobium punctatum (Deg.). Holz und Organismen Internationales Symposium 1, 383-390

Baltazar-y-Jimenez A, Seviaryna I, Sain M, Maeva EY (2011) Acoustic, tomographic, and morphological properties of bismaleimide-modified PLA green composites. Journal of Reinforced Plastics and Composites 30(16), 1329-1340. doi:10.1177/0731684411415451

Bamber RK, Lanyon JW (1960) Silica depositions in several woods of New South Wales. Tropical Woods 113, 48-53

Barsan ME (2007) NIOSH pocket guide to chemical hazards. Department of Health and Human Services, Center for Disease Control and Prevention, DHHS (NIOSH). Publication No. 2005-149. NIOSH Publications, US

Bastani A, Adamopoulos B, Koddenberg T, Militza H (2016) Study of adhesive bondlines in modified wood with fluorescence microscopy and X-ray micro-computed tomography. International Journal of Adhesion and Adhesives 68, 351-358. doi: 10.1016/j.ijadhadh.2016.04.006

Bazerque F (1974) Etude dendrochronologique et dendroclimatique de deux peuplements de *Pins sylvestres* (Thesis), University of Nancy, France (in French)

Bean AR (1995) A revision of *Syncarpia* Ten. (Myrtaceae). Austrobaileya 4(3), 337-344

Belini UL, Filho MT, Chagas MP (2009) X ray densitometry applied to technological evaluation of MDF panels of eucalyptus. Scientia Forestalis 37(84), 343-350

Belini UL, Filho MT, de Castro VR, de Muniz GIB, Lasso PRO, Vaz CMP (2011) X-ray microtomography to anatomical characterization of softwood and hardwood. Floresta e Ambiente 18(1), 30-36. doi: 10.4322/floram.2011.020

Belley D, Duchesne I, Vallerand S, Barrette J, Beaudoin M (2019) Computed tomography (CT) scanning of internal log attributes prior to sawing increases lumber value in white spruce (*Picea glauca*) and jack pine (Pinus banksiana). Canadian Journal of Forest Research 49(12), 1516-1524. doi: 10.1139/cjfr-2018-0409

Benson-Cooper DM, Knowles RL, Thomson FJ, Cown DJ (1982) Computed tomographic scanning for the detection of defects within logs. FRI Bulletin, Forest Research Institute, New Zealand, No.8, 9

Bertolini JC (1992) Hydrofluoric acid: a review of toxicity. Journal of Emergency Medicine 10(2), 163-168. doi: 10.1016/0736-4679(92)90211-b

Bizkis V, Van Acker J, Militz H, Grinins J, Van den Bulcke J (2019) Density and density profile changes in birch and spruce caused by thermo-hydro treatment measured by X-ray computed tomography. Wood Science and Technology 53, 491-504. doi: 10.1007/s00226-018-1070-6

Bizkis V, Van den Bulcke J, Grinins J, Militz H, Andersons B, Andersone I, Dhaene J, Van Acker J (2015) Assessment of wood microstructural changes after one-stage thermo-hydro treatment (THT) by micro X-ray computed tomography. Holzforschung 70(2), 167-177. doi: 10.1515/hf-2014-0337

Blomberg and Persson (2005) An algorithm for comparing density in CT-images taken before and after compression of *Pinus sylvestris*. Holz als Roh- und Werkstoff 63, 23-29. doi: 10.1007/s00107-004-0544-4

Boas IH (1947) The Commercial Timbers of Australia: their Properties and Uses. Commonwealth of Australia Council for Scientific and Industrial Research. J.J. Gourlay, Government Printer, Melbourne, Australia

Bootle KR (1983) Wood in Australia: types, properties and uses. McGraw-Hill, Sydney, Australia

Boukadida H, Longuetaud F, Colin F, Freyburger C, Constant T, Leban JM, Mothe F (2012) PithExtract: A robust algorithm for pith detection in computer tomography images of wood – Application to 125 logs from 17 tree species. Computers and Electronics in Agriculture 85, 90-98. doi: 10.1016/j.compag.2012.03.012

Bouslimi B, Koubaa A, Bergeron Y (2014) Effects of biodegradation by brown-rot decay on selected wood properties in eastern white cedar (Thuja occidentalis L.). International Biodeterioration and Biodegradation 87, 87-98. doi: 10.1016/j.ibiod.2013.11.006

Brazolin S, Filho MT, Yojo T, Neto MAO; Albuquerque ÁR, Sette CR (2014) Mechanical and physical properties of *Tipuana tipu* wood deteriorated by decaying fungi. Cerne 20(2), 183-190. doi: 10.1590/01047760.201420021089

Breinig L, Berglund A, Grönlund A, Brüchert F, Sauter UH (2013) Effect of knot detection errors when using a computed tomography log scanner for sawing control. Forest Products Journal 63(7/8), 263-274. doi: 10.13073/FPJ-D-13-00068

British Standards Institution (2016) Wood preservatives - Determination of the preventive action against recently hatched larvae of *Hylotrupes bajulus* (Linnaeus) - Application by surface treatment (laboratory method). BS EN 46-1:2016, British Standards Institution, London, UK

Brodersen CR (2013) Visualizing wood anatomy in three dimensions with high-resolution X-ray micro-tomography (µCT): a review. IAWA Journal 34(4), 408-424. doi: 10.1163/22941932-00000033

Brüchert F, Biechele T, Longo BL, Sauter UH, Pizarro ME (2019) Using X-ray computed tomography to identify wood quality parameters of high-value teak roundwood. In: Proceedings of 21st International Nondestructive Testing and Evaluation of Wood Symposium. Freiburg, Germany. 524-534

Brunke O, Brockdorf K, Drews S, Müller B, Donath T, Herzen J, Beckmann F (2008) Comparison between X-ray tube based and synchrotron radiation based µCT. In: Proceedings of SPIE 7078, Developments in X-Ray Tomography VI, 70780U, San Diego, California, USA. doi: 10.1117/12.794789

Bryant JA, Drage NA, Richmond S (2012) CT number definition. Radiation Physics and Chemistry 81(4), 358-361. doi: 10.1016/j.radphyschem.2011.12.026

Bucur V, Garros S, Navarrete A, de Troya MT, Guyonnet R (1997) Kinetics of wood degradation by fungi with X-ray microdensitometric technique. Wood Science and Technology 31(5), 383-389. doi: 10.1007/BF01159156

Bugani S, Modugno F, Lucejko JJ, Giachi G, Cagno S, Cloetens P, Janssens K, Morselli L (2009) Study on the impregnation of archaeological waterlogged wood with consolidation treatments using synchrotron radiation microtomography. Analytical and Bioanalytical Chemistry 395, 1977-1985. doi: 10.1007/s00216-009-3101-5

Burrows GE (2008) *Syncarpia* and *Tristaniopsis* (Myrtaceae) possess specialised fire-resistant epicormic structures. Australian Journal of Botany 56, 254-264. doi: 10.1071/BT07164

Caceres CB, Uliana L, Hernández RE (2018) Orthogonal cutting study of wood and knots of white spruce. Wood and Fiber Science 50(1), 55-65. doi: 10.22382/wfs-2018-006

Cai ZY (2008) A new method of determining moisture gradient in wood. Forest Products Journal 58(7/8), 41-45

Calhoun PS, Kuszyk BS, Heath DG, Carley JC, Fishman EK (1999) Three-dimensional volume rendering of spiral CT data: Theory and method. Radiographics 19(3), 745-764. doi: 10.1148/radiographics.19.3.g99ma14745

Chagas SF, Evangelista WV, Silva JC, Pinheiro MA (2015) Study of the retention and penetration of CCA in teakwood, for use as treated fence posts. Scientia Forestalis 43(105), 155-165

Chang SJ, Gazo R (2009) Measuring the effect of internal log defect scanning on the value of lumber produced. Forest Products Journal 59(11/12), 56-59. doi: 10.13073/0015-7473-59.11.56

Chappard C, Basillais A, Benhamou L (2006) Comparison of synchrotron radiation and conventional x-ray microcomputed tomography for assessing trabecular bone microarchitecture of human femoral heads. Medical Physics 33(9), 3568-3577. doi: 10.1118/1.2256069

Chaudemanche S, Perrot A, Pimbert S, Lecompte T, Faure F (2018) Properties of an industrial extruded HDPE-WPC: The effect of the size distribution of wood flour particles. Construction and Building Materials 162, 543-52. doi: 10.1016/j.conbuildmat.2017.12.061

Chen HC, Chen TY, Hsu CH (2006) Effects of wood particle size and mixing ratios of HDPE on the properties of the composites. Holz als Roh- und Werkstoff 64, 172-177, doi: 10.1007/s00107-005-0072-x

Cheng Q, Muszyński L, Shaler S, Wang J (2010) Microstructural changes in wood plastic composites due to wetting and re-drying evaluated by X-ray microtomography. Journal of Nondestructive Evaluation 29, 207-213. doi: 10.1007/s10921-010-0078-0

Ching TW, Nobuchi T, Sahri MH, Yu LC (2011) Formation and distribution of calcium crystals in the trunk of *Hopea odorata*. Wood Research Journal 2(1), 13-20. doi: 10.1234/wrj.v2i1.158

Chinga-Carrasco G, Solheim O, Lenes M, Larsen A (2013) A method for estimating the fibre length in fibre-PLA composites. Journal of Microscopy 250(1), 15-20. doi: 10.1111/jmi.12012

Clark A, Daniels RF, Jordan L (2006a) Juvenile/mature wood transition in loblolly pine as defined by annual ring specific gravity, proportion of latewood, and microfibril angle. Wood and Fiber Science 38(2), 292-299

Clark A, Daniels RF, Miller JH (2006b) Effect of controlling herbaceous and woody competing vegetation on wood quality of planted loblolly pine. Forest Products Journal 56(2), 40-46

Clemons CM, Rowell RM, Plackett D, Segerholm BK (2013) Wood/nonwood thermoplastic composites. In: Rowell R (ed) Handbook of Wood Chemistry and Wood Composites (Second Edition). CRC Books, Boca Raton, FL, USA. 473-508

Constantine AJ (2005) Know Your Woods: A Complete Guide to Trees, Woods, and Veneers. The Lyons Press. Guilford, USA

Cookson LJ, Scown D (2008) Development of marine borer natural durability classes for timber in Australia. Journal of the Institute of Wood Science 18(2), 94-104. doi: 10.1179/wsc.2008.18.2.94

Couceiro J, Elustondo D (2015) Implementation of computer aided tool for non-destructive X-ray measurement of moisture content distribution in wood. Pro Lingo 11, 330-336

Couceiro J, Hansson L, Sehlstedt-Persson M, Vikberg T, Sandberg D (2020) The conditioning regime in industrial drying of Scots pine sawn timber studied by X-ray computed tomography: a case-study. European Journal of Wood and Wood Products 78, 673-682. doi: 10.1007/s00107-020-01549-2

Couceiro J, Lindgren O, Hansson L, Söderström O, Sandberg D (2019) Real-time wood moisture-content determination using dual-energy X-ray computed tomography scanning. Wood Material Science and Engineering 14, 437-444. doi: 10.1080/17480272.2019.1650828

Cown DJ, Clement BC (1983) A wood densitometer using direct scanning with X-rays. Wood Science and Technology 17, 91-99

Currie G, Hewis J, Bushong S (2015) Tomographic reconstruction: a nonmathematical overview. Journal of Medical Imaging and Radiation Sciences 46(4), 403-412. doi: 10.1016/j.jmir.2015.07.007

Dadswell HE, Eckersley AM (1935) The Identification of the Principal Commercial Australian Timbers other than Eucalypts. Commonwealth of Australia Council for Scientific and Industrial Research. Melbourne, Australia

Dadswell HE, Eckersley AM (1940) The Wood Anatomy of some Australian Lauraceae with Methods for their Identification. Commonwealth of Australia Council for Scientific and Industrial Research. Melbourne, Australia

Darmawan W, Rahayu I, Nandika D, Marchal R (2011) Wear characteristics of wood cutting tools caused by extractive and abrasive materials in some tropical woods. Journal of Tropical Forest Science 23(3), 345–353

Davis JR, lerdin Am Wells P, Ilic J (1991) X-ray microtomography of wood. Journal of the Institute of Wood Science 12(4), 259-261

De Mil T, Vannoppen A, Beeckman H, Van Acker J, Van den Bulcke J (2016) A field-to-desktop toolchain for X-ray CT densitometry enables tree ring analysis. Annals of Botany 117(7), 1187-1196. doi: 10.1093/aob/mcw063

De Ridder M, Van den Bulcke J, Vansteenkiste D, Van Loo D, Dierick M, Masschaele B, De Witte Y, Mannes D, Lehmann E, Beeckman H, Van Hoorebeke L, Van Acker J (2011) High-resolution proxies for wood density variations in *Terminalia superba*. Annals of Botany 107(2), 293-302. doi: 10.1093/aob/mcq224

De Silva D, Hillis WE (1980) The contribution of silica to the resistance of wood to marine borers. Holzforschung 34, 95–97

De Vetter L, Cnudde V, Masschaele B, Jacobs PJS, Van Acker J (2006) Detection and distribution analysis of organosilicon compounds in wood by means of SEM-EDX and micro-CT. Materials Characterization 56(1), 39-48. doi: 10.1016/j.matchar.2005.09.007

Deganello S (1980) The structure of whewellite, $CaC_2O_4 \cdot H_2O$ at 328 K. Acta Crystallographica Section B 37, 826-829. doi: 10.1107/S056774088100441X

Diaz Vaz Olmedo J (1974) Vergleichende Untersuchung der Schwankungen yon Tracheidendimensionen und röntgenoptisch ermittelter Rohdichte innerhalb des Jahrrings (Dissertation). Faculty of Forestry, University of Göttingen, Germany (in German)

Dong Z, Baas P (1993) Wood Anatomy of Trees and Shrubs from China. V. Anacardiaceae. IAWA Journal 14(1), 87-102. doi: 10.1163/22941932-90000580

Drebin RA, Carpenter L, Haneahan P (1988) Volume rendering. ACM SIGGRAPH Computer Graphics 22(4), 65-74. doi: 10.1145/378456.378484

Du Pless A, Yadroitsava I, le Roux SG, Yadroitsev I, Fieres J, Reinhart C, Rossoiuv P (2017a) Prediction of mechanical performance of Ti6Al4V cast alloy based on microCT-based load simulation. Journal of Alloys and Compounds 724, 267-274. doi: 10.1016/j.jallcom.2017.06.320

Du Plessis A, Broeckhoven C, Guelpa A, Le Roux SG (2017b) Laboratory X-ray micro-computed tomography: a user guideline for biological samples. Gigascience 6(6), 1-11. doi: 10.1093/gigascience/gix027

Eberhardt TL, So C, Leduc DJ (2019) Wood property maps showing wood variability in mature longleaf pine: does getting old change juvenile tendencies? Wood and Fiber Science 51(2), 193-208. doi: 10.22382/wfs-2019-020

Echols RM (1972) Patterns of wood density distribution and growth acceleration on the properties of wood. Forest Products Laboratory, Berkeley

Edwin L, Pillai AGG (2004) Resistance of preservative treated rubber wood (*Hevea brasiliensis*) to marine borers. Holz als Roh- und Werkstoff 62(4), 303-306. doi: 10.1007/s00107-003-0460-z

El Hachem C, Abahri K, Bennacer R (2019) Original experimental and numerical approach for prediction of the microscopic hygro-mechanical behavior of spruce wood. Construction and Building Materials 203, 258-266. doi: 10.1016/j.conbuildmat.2019.01.107

Elliott JC, Dover SD (1982) X-ray microtomography. Journal of Microscopy 126(2), 211-213. doi: 10.1111/j.1365-2818.1982.tb00376.x

Endo R, Sugiyama J (2013) Evaluation of cell wall reinforcement in feather keratin-treated waterlogged wood as imaged by synchrotron X-ray microtomography (μXRT) and TEM. Holzforschung 67(7), 795-803. doi: 10.1515/hf-2012-0181

Eom YG, Kwon O, Hanna RB, Meyer RW (2006) Crystals in North American commercial woods of *Abies* species. Korean Journal of Electron Microscopy 36(4), 251-258

Eriksen AM, Gregory DJ, Villa C, Lynnerup N, Botfeldt KB, Rasmussen AR (2016) The effects of wood anisotropy on the mode of attack by the woodborer *Teredo navalis* and the implications for underwater cultural heritage. International Biodeterioration and Biodegradation 107, 117-122. doi: 10.1016/j.ibiod.2015.11.018

Eriksson J, Johansson H, Danvind J (2006) Numerical determination of diffusion coefficients in wood using data from CT-scanning. Wood and Fiber Science 38, 334-344.

Espinoza GR, Hernández R, Condal A, Verret D, Beauregard R (2005) Exploration of the physical properties of internal characteristics of sugar maple logs and relationships with CT images. Wood and Fiber Science 37(4), 591-604

Espinoza GR, Iribarren OO (2009) Identification of defective core in pruned Pinus radiata logs from CT images using the maximum likelihood classifier. Maderas: Ciencia y Tecnología 11(2), 117-127 (in Spanish). doi: 10.4067/S0718-221X2009000200003

Espinoza GR, Iribarren OO (2012) Identification of knotty core in Pinus radiata logs from CT images: comparative study. Maderas: Ciencia y Tecnología 14(1), 65-77 (in Spanish). doi: 10.4067/S0718-221X2012000100005

Evans P (2006) The use of blackwood in the Australian guitar-making industry. In Proceedings of a Blackwood Industry Group (BIG) Workshop: Acacia Utilisation and Management – Adding value. Victoria, Australia

Evans PD, Limaye A, Averdunk H, Turner M, Senden TJ (2013) Visualization of copper in the voids and cell walls of treated wood using x-ray micro-computed tomography. In: Proceedings of the 44th Annual Meeting of the International Research Group on Wood Protection. Stockholm, Sweden. IRG/WP 13-40640

Evans PD, Limaye A, Averdunk H, Turner M, Senden TJ, Knackstedt MA (2012). Use of X-ray micro-computed tomography to visualize copper in preservative treated wood. In: Proceedings of the 43rd Annual Meeting of the International Research Group on Wood Protection. Kuala Lumpur, Malaysia. 20488

Evans PD, Lube V, Averdunk H, Limaye A, Turner M, Kingston A, Senden TJ (2015) Visualizing the microdistribution of zinc borate in oriented strand board using X-ray microcomputed tomography and SEM-EDX. Journal of Composites 2015, 630905. doi: 10.1155/2015/630905

Evans PD, Matsunaga H, Averdunk H, Turner M, Limaye A, Kataoka Y, Kiguchi M, Senden TJ (2014) Microdistribution of copper in southern pine treated with particulate wood preservatives. In: Schultz TP, Goodell B, Nicholas DD (eds) Deterioration and Protection of Sustainable Biomaterials. American Chemical Society, Washington, DC, USA. 227-238. doi: 10.1021/bk-2014-1158.ch013

Evans PD, Matsunaga H, Feng D, Turner M, Henley RW, Kewish CM (2021) Inorganic compounds in the marine borer resistant timber turpentine (*Syncarpia glomulifera*). Journal of Wood Chemistry and Technology 41(4), 185-197. doi: 10.1080/02773813.2021.1954952

Evans PD, Matsunaga H, Kiguchi M (2008) Large-scale application of nanotechnology for wood protection. Nature Nanotechnology 3, 577. doi: 10.1038/nnano.2008.286

Evans PD, Morrison O, Senden TJ, Vollmer S, Roberts RJ, Limaye A, Arns CH, Averdunk H, Lowe A, Knackstedt MA (2010) Visualization and numerical analysis of adhesive distribution in particleboard using X-ray micro-computed tomography. International Journal of Adhesion and Adhesives 30(8), 754-762. doi: 10.1016/j.ijadhadh.2010.08.001

Feldkamp LA, Davis LC, Kress JW (1984) Practical cone-beam algorithm. Journal of the Optical Society of America A 1(6), 612-619. doi: 10.1364/JOSAA.1.000612

Feng D, Liu Y, Mazloomi MS, Limaye A, Turner M, Evans PD (2020) A virtual reality system to augment teaching of wood structure and protection. International Wood Products Journal 11(2), 46-56. doi: 10.1080/20426445.2020.1737773

Feng D, Turner M, Evans PD (2022) Sodium iodide as a contrast agent for X-ray micro-CT of a wood plastic composite. Applied Sciences 12(1), 208. doi: 10.3390/app12010208.

Feng D, Turner M, Limaye A, Knackstedt MA, Evans PD (2019) Accumulation of copper in parenchyma cells in southern pine wood treated with micronized and amine-copper preservatives. In: Proceedings of the 50th Annual Meeting of the International Research Group on Wood Protection. Quebec City, QC. IRG/WP 19-20657

Fengel D, Wegener G (1984) Wood – Chemistry, Ultrastructure, Reactions. De Gruyter, Berlin, Germany

Fioravanti M, Di Giulio G, Signorini G, Rognoni GR, Sodini N, Tromba G, Zanini F (2017) Non-invasive wood identification of historical musical bows. IAWA Journal 38(3), 285-296. doi: 10.1163/22941932-20170172

Fiorelli J, Bueno SB, Cabral MR (2019) Assessment of multilayer particleboards produced with green coconut and sugarcane bagasse fibers. Construction and Building Materials 205, 1-9. doi: 10.1016/j.conbuildmat.2019.02.024

Fleischmann D, Boas FE (2011) Computed tomography—old ideas and new technology. European Radiology 21, 510-517. doi: 10.1007/s00330-011-2056-z

Forsberg F, Sjödahl M, Mooser R, Hack E, Wyss P (2010) Full three-dimensional strain measurements on wood exposed to three-point bending: analysis by use of digital volume correlation applied to synchrotron radiation micro-computed tomography image data. Strain 46(1), 47-60. doi: 10.1111/j.1475-1305.2009.00687.x

Fougerousse M, Gueneau P (1971) Further research on X-ray examination of wood panels exposed to Teredinidae marine borers. Journal of the Institute of Wood Science 5(6), 3-12

Fredriksson M (2016) Handling positioning errors when optimizing sawing of Scots pine and Norway spruce logs using CT scanning. Journal of Wood Science 62, 400-406. doi: 10.1007/s10086-016-1566-3

Fredriksson M, Cool J, Avramidis S (2019) Automatic knot detection in coarse-resolution cone-beam computed tomography images of softwood logs. Forest Products Journal 69(3), 185-187. doi: 10.13073/FPJ-D-19-00008

Fredriksson M, Cool J, Duchesne I, Belley D (2017) Knot detection in computed tomography images of partially dried jack pine (*Pinus banksiana*) and white spruce (*Picea glauca*) logs from a Nelder

type plantation. Canadian Journal of Forest Research 47(7), 910-915. doi: 10.1139/cjfr-2016-0423

Fredriksson M, Johansson E, Berglund A (2014) Rotating *Pinus sylvestris* sawlogs by projecting knots from X-ray computed tomography images onto a plane. Bioresources 9(1), 816-827.

Freyburger C, Longuetaud F, Mothe F, Leban JM (2009) Measuring wood density by means of X-ray computer tomography. Annals of Forest Science 66, 804. doi: 10.1051/forest/2009071

Friml J, Procházková K, Melnyk G, Zikmund T, Kaiser J, (2014) Investigation of Cheb relief intarsia and the study of the technological process of its production by micro computed tomography. Journal of Cultural Heritage 15(6), 609-613. doi: 10.1016/j.culher.2013.12.006

Fromm JH, Sautter I, Matthies D, Kremer J, Schumacher P, Ganter C (2001) Xylem water content and wood density in spruce and oak trees detected by high-resolution computed tomography. Plant Physiology 127, 416-425. Doi: 10.1104/pp.010194

Fuhr MJ, Stührk C, Münch B, Schwarze FWMR, Schubert M (2012) Automated quantification of the impact of the wood decay fungus *Physisporinus vitreus* on the cell wall structure of Norway spruce by tomographic microscopy. Wood Science and Technology 46, 769-779. doi: 10.1007/s00226-011-0442-y

Furat O, Wang M, Neumann M, Petrich L, Weber M, Krill CE, Schmidt V (2019) Machine learning techniques for the segmentation of tomographic image data of functional materials. Frontiers in Materials 6, 145. doi: 10.3389/fmats.2019.00145

Gaitán-Alvarez J, Moya R, Puente-Urbina A, Rodriguez-Zuñiga A (2017) Physical and compression properties of pellets manufactured with the biomass of five woody tropical species of Costa Rica torrefied at different temperatures and times. Energies 10(8), 1205. doi: 10.3390/en10081205

Gapare WJ, Wu HX, Abarquez A (2006) Genetic control of the time of transition from juvenile to mature wood in Pinus radiata D. Don. Annals of Forest Science 63(8), 871-878. doi: 10.1051/forest:2006070

Garcea SC, Wang Y, Withers PJ (2018) X-ray computed tomography of polymer composites. Composites Science and Technology 156, 305-19. doi: 10.1016/j.compscitech.2017.10.023

Gardner DJ, Han Y, Wang L (2015) Wood–plastic composite technology. Current Forestry Reports 1, 139-150. doi: 10.1007/s40725-015-0016-6

Gardner DJ, Tascioglu C, Wålinder MEP (2003). Wood composite protection. In: Goodell B, Nicholas DD, Schultz TP (eds) Wood Deterioration and Preservation: Advances in Our Changing World. American Chemical Society, Washington, DC, USA. 399-419. doi: 10.1021/bk-2003-0845.ch025

Garvey C, Hanlon R (2002) Computed tomography in clinical practice. British Medical Journal 324, 1077-1080. doi: 10.1136/bmj.324.7345.1077

Ge Z, Chen L, Luo R, Wang Y, Zhou Y (2018) The detection of structure in wood by X-ray CT imaging technique. Bioresources 13, 3674-3685.

George JP, Schueler S, Karanitsch-Ackerl S, Mayer K, Klumpp RT, Grabner M (2015) Inter- and intra-specific variation in drought sensitivity in *Abies* spec. and its relation to wood density and

growth traits. Agricultural and Forest Meteorology 214-215, 430-443. doi: 10.1016/j.agrformet.2015.08.268

Gibson C, Warren A (2020) Keeping time with trees: Climate change, forest resources, and experimental relations with the future. Geoforum 108, 325-337. doi: 10.1016/j.geoforum.2019.02.017

Gilani MS, Boone M, Mader K,Schwarze FWMR (2014) Synchrotron X-ray micro-tomography imaging and analysis of wood degraded by *Physisporinus vitreus* and *Xylaria longipes*. Journal of Structural Biology 187(2), 149-157. doi: 10.1016/j.jsb.2014.06.003

Gilani MS, Fife JL, Boone MN, Wakili KG (2013) Dynamics of microcrack propagation in hardwood during heat treatment investigated by synchrotron-based X-ray tomographic microscopy. Wood Science and Technology 47, 889-896. doi: 10.1007/s00226-013-0545-8

Giudiceandrea F, Ursella E, Vicario E (2011) A high speed CT scanner for the sawmill industry. In: Proceedings of the 17th International Non-destructive Testing and Evaluation of Wood Symposium, Sopron, Hungary. 1:105–112

Gnatowski M, Ibach R, Leung M, Sun G (2015) Magnetic resonance imaging used for the evaluation of water presence in wood plastic composite boards exposed to exterior conditions. Wood Material Science and Engineering 10(1), 94-111. doi: 10.1080/17480272.2014.920418

Goldhahn C, Schubert M, Lüthi T, Keplinger T, Burgert I, Chanana M (2020) Wood-gelatin bio-composite membranes with tunable flux. ACS Sustainable Chemistry and Engineering, 8(18), 7205–7213. doi: 10.1021/acssuschemeng.0c01856

Gómez-Brandón M, Ascher-Jenull J, Bardelli T, Fornasier F, Fravolini G, Arfaioli P, Ceccherini MT, Pietramellara GP, Lamorski K, Sławiński C, Bertoldi D, Egli M, Cherubini P, Insam H (2017) Physico-chemical and microbiological evidence of exposure effects on *Picea abies* - coarse woody debris at different stages of decay. Forest Ecology and Management 391, 376-389. doi: 10.1016/j.foreco.2017.02.033

Gonçalves FG, Lelis RCC, de Carvalho AM; Filho MT (2018) X-ray densitometry in the evaluation of density in particleboard panel. Ciência Florestal 28(3), 1151-1162. doi: 10.5902/1980509833382

Goyens J, Mancini L, Nieuwenhove V, Sijbers J, Aerts P (2017). Comparison of conventional and synchrotron X-ray microCT scanning of thin membranes in the inner ear. (2017) Comparison of conventional and synchrotron X-ray microCT scanning of thin membranes in the inner ear. in: Proceeding of Bruker Micro-CT User Meeting 2017. Brussels, Belgium. 137-140

Grabner M, Wimmer R, Gierlinger N, Evans R, Downes G (2005) Heartwood extractives in larch and effects on X-ray densitometry. Canadian Journal of Forest Research 35(12), 2781-2786. doi: 10.1139/x05-196

Grandmont JF, Cloutier A, Gendron G, Desjardins R (2010) Effect of density on the properties of oriented strandboard web stock used in wood I-joists. Forest Products Journal 60(7/8), 592-598. doi: 10.13073/0015-7473-60.7.592

Greenhill WL (1940) The Shrinkage of Australian Timber: 2. Shrinkage Data for 170 Timbers. Commonwealth of Australia Council for Scientific and Industrial Research. Melbourne, Australia

Grundberg S, Grönlund A (1997) Simulated grading of logs with an X-ray log scanner-grading accuracy compared with manual grading. Scandinavian Journal of Forest Research 12(1), 70-76. doi: 10.1080/02827589709355386

Guddanti S, Chang SJ (1998) Replicating sawmill sawing with TOPSAW using CT images of a full-length hardwood log. Forest Products Journal 48(1), 72-75

Guild FJ, Summerscales J (1993) Microstructural image analysis applied to fibre composite materials: a review. Composites 24(5), 383-393. doi: 10.1016/0010-4361(93)90246-5

Guss LM (1995) Engineered wood products: The future is bright. Forest Products Journal 45(7/8), 17

Hailey JR, Morris PI (1987) Application of scanning and imaging techniques to assess decay and wood quality in logs and standing trees. Forintek Canada Corporation, Vancouver, BC, Canada

Hamada J, Pétrissans A, Mothe F, Ruelle J, Pétrissans M, Gérardin P (2016) Variations in the natural density of European oak wood affect thermal degradation during thermal modification. Annals of Forest Science 73(2), 277-286. doi: 10.1007/s13595-015-0499-0

Han Y, Ta J, Qi D (2016) Computer tomography of the density and its spatial distribution of wood-plastic composites. Bioresources 11(2), 3538-3549

Hanhan I, Agyei R, Xiao X, Sangid MD (2019) Comparing non-destructive 3D X-ray computed tomography with destructive optical microscopy for microstructural characterization of fiber reinforced composites. Composites Science and Technology 184,107843. doi: 10.1016/j.compscitech.2019.107843

Hansson L, Fjellner BA (2013) Wood shrinkage coefficient and dry weight moisture content estimations from CT-images. Pro Ligno 9(4), 557-561

Hao X, Lv J, Yu C, Jiang J, Jiang J (2014) Moisture content distribution of wood via X-ray method based on the volume density. Scientia Silvae Sinicae 50, 125-132 (in Chinese)

Harris MJ (1969) The use of beta rays in determining wood properties. New Zealand Journal of Science 12, 395-451

Hass P, Wittel FK, McDonald SA, Marone F, Stampanoni M, Herrmann HJ, Niemz P (2010) Pore space analysis of beech wood: The vessel network. Holzforschung 64(5), 639-644. doi: 10.1515/hf.2010.103

Hattori Y, Kanagawa Y (1985) Non-destructive measurement of moisture distribution in wood with a medical X-ray CT scanner I. Accuracy and influencing factor. Mokuzai Gakkaishi 31, 974-982 (in Japanese)

He Q, Zhan T, Zhang H, Ju Z, Dai C, Lu X (2018) The effect of high voltage electrostatic field (HVEF) treatment on bonding interphase characteristics among different wood sections of Masson pine (*Pinus massoniana* Lamb.). Holzforschung 72(7), 557-565. doi: 10.1515/hf-2017-0168

He X, Qi D (2013) Density and moisture content forecasting based on X-ray computed tomography. European Journal of Wood and Wood Products 71, 647-652. doi: 10.1007/s00107-013-0722-3

Helama S, Vartiainen M, Kolström T, Meriläinen J (2010) Dendrochronological investigation of wood extractives. Wood Science and Technology 44(2), 335-351. doi: 10.1007/s00226-009-0293-y

Helama S, Vartiainen M, Kolström T, Peltola H, Meriläinen J (2008) X-ray microdensitometry applied to subfossil tree-rings: growth characteristics of ancient pines from the southern boreal forest zone in Finland at intra-annual to centennial time-scales. Vegetation History and Archaeobotany 17(6), 675-686. doi: 10.1007/s00334-008-0147-9

Henze KJ (2006) Visualization of the spiral variation of wood density in western hemlock (Master of Science Thesis). The University of British Columbia

Hervé V, Mothe F, Freyburger C, Gelhaye E, Frey-Klett P (2014) Density mapping of decaying wood using X-ray computed tomography. International Biodeterioration and Biodegradation 86C, 358-363. doi: 10.1016/j.ibiod.2013.10.009

Hill CAS (2006) Wood Modification: Chemical, Thermal and Other Processes. John Wiley & Sons, West Sussex, UK

Hillis WE, de Silva D (1979). Inorganic extraneous constituents of wood. Holzforschung 33(2), 47-53. doi: 10.1515/hfsg.1979.33.2.47

Hounsfield GN (1973) Computerized transverse axial scanning (tomography): Part I. Description of system. British Journal of Radiology 46, 1016-1022. doi: 10.1259/0007-1285-46-552-1016

Howard DL, de Jonge MD, Afshar N, Ryan CG, Kirkham R, Reinhardt J, Kewish CM, McKinlay J, Walsh A, Divitcos J, Basten N, Adamson L, Fiala T. Sammut L, Paterson DJ (2020) The XFM beamline at the Australian Synchrotron. Journal of Synchrotron Radiation 27, 1447-1458. doi: 10.1107/S1600577520010152

Illman (2003) Synchrotron applications in wood preservation and deterioration. ACS Symposium Series-Wood Deterioration and Preservation 845, 337–345

Illman BJ, Dowd BA (1999) High resolution microtomography for density and spatial information about wood structures. In: Proceedings of SPIE 3772, Developments in X-Ray Tomography II. Denver, CO, USA. doi: 10.1117/12.363722

Ingle HD, Dadswell HE (1953) The anatomy of the timbers of the southwest Pacific area III: Myrtaceae. Austalian Journal of Botany 1(3), 353-401

Ivaska A, Harju L (1999) Analysis of inorganic constituents. In: Sjöström E, Alén R (eds) Analytical Methods in Wood Chemistry, Pulping, and Papermaking. Springer, Berlin, Heidelberg, Germany. doi: 10.1007/978-3-662-03898-7_10

Jacquin et al. (2019) CarDen: A software for fast measurement of wood density on increment cores by CT scanning

Jacquin P, Longuetaud F, Leban JM, Mothe F (2017) X-ray microdensitometry of wood: A review of existing principles and devices. Dendrochronologia 42, 42-50. doi: 10.1016/j.dendro.2017.01.004

Jacquiot C (1961) The use of X-rays in research and tests on woodboring insects (in French). Corrosion et Anticorrosion 9(3), 75-79

Jacquiot C, Serment MM (1971) Research on treatments for the control of larvae of *Hylotrupes bajulus*. Material und Organismen 6(4), 277-293 (in French)

Jakes JE, Frihart CR, Hunt CG, Yelle DJ, Plaza NZ, Lorenz LF, Ching DJ (2018) Integrating multi-scale studies of adhesive penetration into wood. Forest Products Journal 68, 340-348. doi: 10.13073/FPJ-D-17-00067

Jansen S, Kitin P, de Pauw H, Idris M, Beeckman H, Smets E (1998). Preparation of wood specimens for transmitted light microscopy and scanning electron microscopy. Belgian Journal of Botany 131(1), 41-49

Javan R, Rao A, Jeun BS, Herur-Raman A, Singh N, Heidari P (2020) From CT to 3D printed models, serious gaming, and virtual reality: framework for educational 3D visualization of complex anatomical spaces from within—the pterygopalatine fossa. Journal of Digital Imaging 33m 776-791. doi: 10.1007/s10278-019-00315-y

Jerzy J, Tomasz N, Katarzyna H (2013) Selected methods of diagnosis of historic timber structures – principles and possibilities of assessment. Advanced Materials Research 778, 225-232. doi: 10.4028/www.scientific.net/AMR.778.225

Jezzard P, Wiggins CJ, Carpnter TA, Hall LD, Jackson P, Clayden NJ, Walton NJ (1992) Nuclear magnetic resonance imaging of polymers and polymer composites. Advanced Materials 4(2), 82-90. doi: 10.1002/adma.19920040204

Joffre T, Miettinen A, Berthold F, Gamstedt EK (2014) X-ray micro-computed tomography investigation of fibre length degradation during the processing steps of short-fibre composites. Composites Science and Technology 105, 127-133. doi: 10.1016/j.compscitech.2014.10.011

Joffre T, Segerholm K, Persson C, Bardage SL, Hendriks CLL, Isaksson P (2017) Characterization of interfacial stress transfer ability in acetylation-treated wood fibre composites using X-ray microtomography. Industrial Crops and Products 95, 43-49. doi: 10.1016/j.indcrop.2016.10.009

Joffre T, Wernersson ELG, Miettinen A, Hendriks CLL, Gamstedt EK (2013) Swelling of cellulose fibres in composite materials: Constraint effects of the surrounding matrix. Composites Science and Technology 74, 52-59. doi: 10.1016/j.compscitech.2012.10.006

Johnson MT, Childers AS, De Carlo F, Xiao X, Faber KT (2013) Wood-derived copper–graphite composites produced via additive-assisted electrodeposition. Composites Science and Technology 89, 61-68. doi: 10.1016/j.compscitech.2013.09.010

Junqueira, AOR, Omena EP, da Silva SHG (1991) A comparative study of the methods used to evaluate the activity of Teredinidae molluscs. Journal of Experimental Marine Biology and Ecology 150, 107-115. doi: 10.1016/0022-0981(91)90109-A

Jyske T, Hölttä T, Mäkinen H, Nöjd P, Lumme I, Spiecker H (2010) The effect of artificially induced drought on radial increment and wood properties of Norway spruce. Tree Physiology 30(1), 103-115. doi: 10.1093/treephys/tpp099

Jyske T, Manner M, Mäkinen H, Nöjd P, Peltola H, Repo T (2012) The effects of artificial soil frost on cambial activity and xylem formation in Norway spruce. Trees: Structure and Function 26(2), 405-419. doi: 10.1007/s00468-011-0601-7

Kachelrieß M. (2008) Micro-CT. In: Semmler W., Schwaiger M. (eds) Molecular Imaging I. Handbook of Experimental Pharmacology, vol 185/1. Springer, Berlin, Heidelberg, Germany. doi: 10.1007/978-3-540-72718-7_2

Kamke FA, McKinley PE, Ching DJ, Zauner M, Xiao X (2016) Micro X-ray computed tomography of adhesive bonds in wood. Wood and Fiber Science 48, 2-16

Kamke FA, Nairn JA, Muszynski L, Paris JL, Schwarzkopf M, Xiao X (2014) Methodology for micromechanical analysis of wood adhesive bonds using X-ray computed tomography and numerical modeling. Wood and Fiber Science 46(1), 15-28

Kanagawa Y, Furuyama Y, Hattori Y (1992) Nondestructive measurement of moisture diffusion coefficient in wood drying. Drying Technology 10, 1231-1248. doi: 10.1080/07373939208916515

Kasal B, Adams A, Drdácký M (2010) New applications in radiographic evaluation of structural components. European Journal of Environmental and Civil Engineering 4, 395-410. doi: 10.1080/19648189.2010.9693233

Kasal B, Blass R (2013) Experimental and analytical investigation of crack development in composite reinforced laminated arch. Materials and Structures 46, 173-180. doi: 10.1617/s11527-012-9892-4

Katsevich A (2002) Theoretically exact filtered backprojection-type inversion algorithm for spiral CT. SIAM Journal on Applied Mathematics 62(6), 2012-2026. doi:10.1137/S0036139901387186

Katsevich and Frenkel (2016) Testing of the circle and line algorithm in the setting of micro-CT. In: the International Symposium of the Society of Core Analysts 2016, SCA2016-080.

Kaufman AE (1994) Voxels as a computational representation of geometry. In: SIGGRAPH 1994 Course Notes. Orlando, USA.

Kedrov GB (2012) Functioning wood. Wulfenia 19, 57-95

Keller R (1968) Des caractéistiques nouvelles pour l'étude des propriétés mécaniques des bois: les composantes de la densité. Annals of Forest Science 25, 237-249 (in French)

Keller R (1971) Ermittlung der mechanischen Eigenschaften und der Dichte von Holz mit Hitfe von Röntgenstrahlen. Holztechnologie 12, 225-252 (in German)

Keller R (1973) Caractéristiques du bois de pin maritime. Variabilité et transmission héréditaire. Annals of Forest Science 30, 68-81 (in French)

Keller R, Millier C (1970) Utilisation des composantes de la densité en xylochronologie. Annals of Forest Science 27, 157-196 (in French)

Keller R, Thiercelin F (1975) Influence des gros rayons ligneux sur quelques propriétés du bois de hètre. Annals of Forest Science 32, 113-129 (in French)

Kellogg RM, Wangaard FF (1969) Variation in the cell-wall density of wood. Wood and Fiber Science 3, 180-204

Kent SM, Leichti RJ, Morrell JJ, Rosowsky DV, Kelley SS (2006) Analytical tools to predict changes in properties of oriented strandboard exposed to the fungus *Postia placenta*. Holzforschung 60(3), 332-338. doi: 10.1515/HF.2006.053

Kerner G, Thiele H, Unger W (1980) Reliable and non-destructive location of larvae of wood-destroying insects in timber. Holztechnologie 21(3), 131-137 (in German)

Ketcham R (2017) X-ray computed tomography (CT). Available at: https://serc.carleton.edu/research_education/geochemsheets/techniques/CT.html (Accessed 28 Jan 2022)

Kielmann BC, Militz H, Mai C (2016) The effect of combined melamine-resin-colouring-agent modification on water related properties of beech wood. Wood Research 61(1), 1-12

Kim CK, Oh JK, Hong JP, Lee JJ (2014) Density calculation of wood by portable X-ray tube with consideration of penetrating depth. Journal of Wood Science 60, 105-110. doi: 10.1007/s10086-013-1381-z

Kingston AM, Sakellariou A, Sheppard AP, Varslot TK, Latham, SJ (2010). An auto-focus method for generating sharp 3D tomographic images. Proceedings of SPIE 7804(1), 78040J. doi:10.1117/12.860285

Klisz M (2011) Genetic correlations between wood density components and tracheid length in European larch. Annals of Warsaw University of Life Sciences: Forestry and Wood Technology 74, 166-169

Klüppel A, Mai C (2013) The influence of curing conditions on the chemical distribution in wood modified with thermosetting resins. Wood Science and Technology 47(3), 643-658. doi: 10.1007/s00226-013-0530-2

Kłusek M, Grabner M (2016) X-ray densitometry of Norway spruce subfossil wood from the Austrian Alps. Tree-Ring Research 72(1), 23-34. doi: 10.3959/1536-1098-72.01.23

Knackstedt MA, Arns CH, Saadtfar M, Senden TJ, Limaye A, Sakellariou A, Sheppard AP, Sok RM, Schrof W, Steininger H (2006) Elastic and transport properties of cellular solids derived from three-dimensional tomographic images. Proceedings of the Royal Society A 462, 2833-2862. doi: 10.1098/rspa.2006.1657

Koddenberg T, Krause KC, Krause A (2019a) Tomographic analysis of siliceous particulates in Australian turpentine wood (*Syncarpia glomulifera*) through X-ray micro-computed tomography. Micron 117, 22-28. doi: 10.1016/j.micron.2018.10.006

Koddenberg T, Militz H (2018) Morphological imaging and quantification of axial xylem tissue in Fraxinus excelsior L. through X-ray micro-computed tomography. Micron 111, 28-35. doi: 10.1016/j.micron.2018.05.004

Koddenberg T, Wentzel M, Militz H (2019b) Volumetric estimate of bordered pits in *Pinus sylvestris* based on X-ray tomography and light microscopy imaging. Micron 124, 102704. doi: 10.1016/j.micron.2019.102704

Koddenberg T, Zauner M, Militz H (2020) Three-dimensional exploration of soft-rot decayed conifer and angiosperm wood by X-ray micro-computed tomography. Micron 134, 102875. doi: 10.1016/j.micron.2020.102875

Koene L, Broekhuis FR (2017) Bullet penetration into wooden targets. In: 30th International Symposium on Ballistics. Long Beach, CA, USA. 1905-1916

Koene L, Broekhuis FR (2019) Bullet penetration into medium density fibreboard targets. In: 31st International Symposium on Ballistics. Long Beach, Hyderabad, India. 1363-1373

Kondo T, Maeda Y, Fukushima N (2021) Accelerating finite impulse response filtering using tensor cores. In: Proceedings of the Asia Pacific Signal and Information Processing Association Annual Summit and Conference 2021. Tokyo, Japan. 74-79

Korte H, Koch G, Krause KC, Koddenberg T, Siemers S (2018) Wood nails to fix softwoods: characterization of structural deformation and lignin modification. European Journal of Wood and Wood Products 76, 979-988. doi: 10.1007/s00107-018-1288-x

Koubaa A, Isabel N, Zhang SY, Beaulieu J, Bousquet J (2005) Transition from juvenile to mature wood in black spruce *(Picea mariana*). Wood and Fiber Science 37(3), 445-455

Krajewski A, Witomski P, Bobiński P, Wójcik A, Nowakowska M (2012) An attempt to detect fully-grown house longhorn beetle larvae in coniferous wood based on electroacoustic signals. Drewno 55(188), 5-15

Kramer PJ, Kozlowski TT (1979) Mineral nutrition and salt absorption. In: Kramer PJ, Kozlowski TT (eds) Physiology of Woody Plants. Academic Press Books, Cambridge, MA, USA. 334-372. doi: 10.1016/B978-0-12-425050-5.50013-3

Krause KC, Brischke C, Koddenberg T, Buschalsky A, Militz H, Krause A (2019) Resistance of injection molded wood-polypropylene composites against basidiomycetes according to EN 15534-1: new insights on the test procedure, structural alterations, and impact of wood source. Fibers 7, 92. doi: 10.3390/fib7100092

Krause KC, Müller M, Militz H, Krause A (2017) Enhanced water resistance of extruded wood–polypropylene composites based on alternative wood sources. European Journal of Wood and Wood Products 75, 125-134. doi: 10.1007/s00107-016-1091-5

Krause KC, Sauerbier P, Koddenberg T, Krause A (2018) Utilization of recycled material sources for wood-polypropylene composites: Effect on internal composite structure, particle characteristics and physico-mechanical properties. Fibers 6(4), 86. doi: 10.3390/fib6040086

Krzemień L, Strojecki M, Wroński S, Tarasiuk J, Łukomski M (2015) Dynamic response of earlywood and latewood within annual growth ring structure of Scots pine subjected to changing relative humidity. Holzforschung 69(5), 555-561. doi: 10.1515/hf-2014-0132

Lautner S, Beckmann F (2012) Analysis of wood microstructure by synchrotron radiation-based x-ray microtomography (SRμCT). In: Proceedings of SPIE 8506, Developments in X-Ray Tomography VIII, 85060F. San Diego, CA, USA. doi: 10.1117/12.929571

Leißner T, Diener A, Löwer E, Ditcherlein R, Krüger K, Kwade A, Peuker UA (2020) 3D ex-situ and in-situ X-ray CT process studies in particle technology – A perspective. Advanced Powder Technology 31(1), 78-86. doi: 10.1016/j.apt.2019.09.038

Leppänen K, Bjurhager I, Peura M, Kallonen A, Suuronen JP, Penttilä P, Love J, Fagerstedt K, Serimaa R (2011) X-ray scattering and microtomography study on the structural changes of never-dried

silver birch, European aspen and hybrid aspen during drying. Holzforschung 65(6), 865-873. doi: 10.1515/HF.2011.108

Lewis RJ (2007) Hawley's Condensed Chemical Dictionary, 15th Edition. John Wiley & Sons Inc. New York, NY, USA

Li P, Tao Y, Wu Q (2016a) A three-dimensional void reconstruction method for analyzing fractal dimensions of void volume in wood-strand composites. Holzforschung 70(4), 377-382. doi: 10.1515/hf-2015-0024

Li P, Wu Q, Tao Y (2013a) Fractal dimension analysis of void size in wood-strand composites based on X-ray computer tomography images. Holzforschung 67, 177-182. doi: 10.1515/hf-2012-0074

Li R, Cao P, Xu W, Ekevad M, Wang X (2018a) Experimental and numerical study of moisture-induced stress formation in hexagonal glulam using X-ray computed tomography and finite-element analysis. Bioresources 13, 7395-7403.

Li W, Van den Bulcke J, De Schryver T, Van Acker J (2016b) Investigating water transport in MDF and OSB using a gantry-based X-ray CT scanning system. Wood Science and Technology 50, 1197-1211. doi: 10.1007/s00226-016-0855-8

Li W, Van den Bulcke J, De Windt I, Defoirdt N, Dhaene J, Dierick M, Sol H, Van Acker J (2016c) Relating MOE decrease and mass loss due to fungal decay in plywood and MDF using resonalyser and X-ray CT scanning. International Biodeterioration and Biodegradation 110, 113-120. doi: 10.1016/j.ibiod.2016.03.012

Li W, Van den Bulcke J, De Windt I, Dhaene J, Mannes D, Lehmann E, Van Acker J (2016d) Investigating plywood behaviour in outdoor conditions. International Wood Products Journal 7(4), 220-224. doi: 10.1080/20426445.2016.1261235

Li W, Van den Bulcke J, De Windt I, Dhaene J, Van Acker J (2016e) Moisture behavior and structural changes of plywood during outdoor exposure. European Journal of Wood and Wood Products 74, 211-221. doi: 10.1007/s00107-015-0992-z

Li W, Van den Bulcke J, De Windt I, Van Loo D, Dierick M, Brabant L, Van Acker J (2013b) Combining electrical resistance and 3-D X-ray computed tomography for moisture distribution measurements in wood products exposed in dynamic moisture conditions. Building and Environment 67, 250-259. doi: 10.1016/j.buildenv.2013.05.026

Li W, Van den Bulcke J, Dhaene J, Zhan X, Mei C, Van Acker J (2018b) Investigating the interaction between internal structural changes and water sorption of MDF and OSB using X-ray computed tomography. Wood Science and Technology 2018, 701-716. doi: 10.1007/s00226-018-0992-3

Li W, Van den Bulcke J, Mannes D, Lehmann E, De Windt I, Dierick M, Van Acker J (2014) Impact of internal structure on water-resistance of plywood studied using neutron radiography and X-ray tomography. Construction and Building Materials 73, 171-179. doi: 10.1016/j.conbuildmat.2014.09.095

Li W, Zhan X, Yang Y, Mei C (2018c) Changes of size and relative position of the internal unit during water uptake of wood-based panels. Journal of Forestry Engineering 3(3), 24-28 (in Chinese)

Limaye A (2012) Drishti: a volume exploration and presentation tool. In: Developments in X-Ray Tomography VIII, Proceedings of SPIE Optical Engineering + Applications. San Diego, CA, USA. 85060X. doi: 10.1117/12.935640

Lin H, Li R, Li D, Huang Z, Pang J, Zhang X, Liu W, Yang W (2020) Hydrophobic wood flour derived from a novel p-TsOH treatment for improving interfacial compatibility of wood/HDPE composites. Cellulose 27, 4053-4065. doi: 10.1007/s10570-020-03046-4

Lindgren LO (1985) Preliminary observations on the relationship between density/moisture content in wood and X-ray attenuation in computerised axial tomography. In 5th Non-destructive Testing of Wood Symposium. Pullman, Washington, USA

Lindgren LO (1991a) Medical CAT-scanning: X-ray absorption coefficients, CT-numbers and their relation to wood density. Wood Science and Technology 25, 341-349. doi: 10.1007/BF00226173

Lindgren LO (1991b) The accuracy of medical CAT-scan images for non-destructive density measurements in small volume elements within solid wood. Wood Science and Technology 25, 425-432. doi: 10.1007/BF00225235

Lindgren LO, Davis J, Wells P, Shadbolt P (1992) Non-destructive wood density distribution measurements using computed tomography. Holz als Roh- und Werkstoff 50, 295-299. doi: 10.1007/BF02615356

Liu H, Lin F, Lin J, Sulaiman K, Xiao T, Sun Y, Pang Y, Liu H (2018) Phase-retrieval-based synchrotron X-ray micro-tomography for 3D structural characterization and quantitative analysis of agalloch eaglewood. Wood Science and Technology 52, 839-854. doi: 10.1007/s00226-018-1004-3

Liu Y, Pan H, Ruan X (1996) The distribution of the moisture content of each growth ring in wood using X-ray densitometry. Journal of Nanjing Forestry University 20, 69-72 (in Chinese)

Liu Y, Pan H, Zhou M (1998) Determination of water distribution in wood by X-ray densitometry. Journal of Northeast Forestry University 26, 34-37 (in Chinese)

Longo BL, Brüchert F, Becker G, Sauter UH (2019) Validation of a CT knot detection algorithm on fresh Douglas-fir (*Pseudotsuga menziesii* (Mirb.) Franco) logs. Annals of Forest Science 76, 28. doi: 10.1007/s13595-019-0812-4

Lötter BT, Evans PD (2019) Sprayable hot melt waxes as water repellents for oriented strand board International Wood Products Journal 10(3), 102-110. doi: 10.1080/20426445.2019.1637609

Lykidis C, Moya R, Tenorio C (2020) The effect of melamine formaldehyde impregnation and hot-pressing parameters on the density profile of densified poplar wood. European Journal of Wood and Wood Products 78(3), 433-440. doi: 10.1007/s00107-020-01515-y

Macedo A, Vaz CMP, Pereira JCD, Naime JM, Cruvinel PE, Crestana S (2002) Wood density determination by x- and gamma-ray tomography. Holzforschung 56(5), 535-540. doi: 10.1515/HF.2002.082

MacLean JD (1952) Preservation Treatment of Wood by Pressure Methods. US Department of Agriculture Forest Service, Washington DC, USA

Madyan OA, Wang Y, Corker J, Zhou Y, Du G, Fan M (2020) Classification of wood fibre geometry and its behaviour in wood poly(lactic acid) composites. Composites Part A: Applied Science and Manufacturing 133, 105871. doi: 10.1016/j.compositesa.2020.105871

Maeda K, Ohta M (2012) Analysis of decay progress anisotropy by X-ray computer tomography. In: Proceedings of the joint IRG – IUFRO Research Sessions International Union of Forest Research Organizations All Division 5 Conference. Estoril, Portugal. IRG/WP 12-20501

Maeda K, Ohta M, Momohara I (2015) Relationship between the mass profile and the strength property profile of decayed wood. Wood Science and Technology 49, 331-344. doi: 10.1007/s00226-014-0696-2

Magne P (2007) Efficient 3D finite element analysis of dentalrestorative procedures using micro-CT data. Dental Materials 23, 539-548. doi: 10.1016/j.dental.2006.03.013

Mankowski ME, Manning MJ, Slowik DP (2015) Durability of capped wood plastic composites. In Proceedings of the 111th Annual Meeting of the American Wood Protection Association. Asheville, NC, USA. 124-132

Mannes D, Marone F, Lehmann E, Stampanoni M, Niemz P (2010) Application areas of synchrotron radiation tomographic microscopy for wood research. Wood Science and Technology 44, 67–84. doi: 10.1007/s00226-009-0257-2

Mannes D, Niemz P, Eberhard L (2009) Tomographic investigations of wood from macroscopic to microscopic scale. Wood Research 54(3), 33-44

Marčok M, Kúdela J, Čunderlík I (1996) Identification of reaction beech wood by X-ray computed tomography. Holz als Roh- und Werkstoff 54, 97-98. doi: 10.1007/s001070050145

Markström E, Kuzman MK, Bystedt A, Sandberg D, Fredriksson M (2018) Swedish architects view of engineered wood products in buildings. Journal of Cleaner Production 181, 33-41. doi: 10.1016/j.jclepro.2018.01.216

Matsubara D, Wakashima Y, Fujisawa Y, Shimizu H, Kitamori A, Ishikawa K (2017) Relationship between clamp force and pull-out strength in lag screw timber joints. Journal of Wood Science 63, 625-634. doi: 10.1007/s10086-017-1660-1

Matsuda Y, Fujiwara Y, Fujii Y (2015) Observation of machined surface and subsurface structure of hinoki (Chamaecyparis obtusa) produced in slow-speed orthogonal cutting using X-ray computed tomography. Journal of Wood Science 61, 128-135. doi: 10.1007/s10086-014-1457-4

Matsuda Y, Fujiwara Y, Murata K, Fujii Y (2017) Residual strain analysis with digital image correlation method for subsurface damage evaluation of hinoki (*Chamaecyparis obtusa*) finished by slow-speed orthogonal cutting. Journal of Wood Science 63, 615-624. doi: 10.1007/s10086-017-1659-7

Matsunaga H, Kiguchi M, Evans PD (2009) Microdistribution of copper-carbonate and iron oxide nanoparticles in treated wood. Journal of Nanoparticle Research 11, 1087–1098. doi: 10.1007/s11051-008-9512-y

Mayo S, Evans R, Chen F, Lagerstrom R (2009) X-ray phase-contrast micro-tomography and image analysis of wood microstructure. Journal of Physics: Conference Series 186, 012105. doi: 10.1088/1742-6596/186/1/012105

Mayo SC, Chen F, Evans R (2010) Micron-scale 3D imaging of wood and plant microstructure using high-resolution X-ray phase-contrast microtomography. Journal of Structural Biology 171:182–188

McElrone AJ, Choat B, Gambetta GA, Brodersen CR (2013) Water Uptake and Transport in Vascular Plants. Nature Education Knowledge 4(5), 6

McKinley PE, Ching DJ, Kamke FA, Zauner M, Xiao X (2016) Micro X-ray computed tomography of adhesive bonds in wood. Wood and Fiber Science 48, 2-16

McKinley PE, Kamke FA, Sinha A, De Andrade V, Jakes JE (2018) Analysis of adhesive penetration into wood using nano-X-ray computed tomography Wood and Fiber Science 50(1), 66-76

McKinnell FH, Rudman P (1973) Potassium fertilizer and wood density of *Pinus radiata*. Appita 26, 283-286

McNeely R, Neale J, Benkel M, Rustenburg J, Terasmae J (1973) Studies in dendrochronology 1: application of X-ray densitometry in dendrochronology. Brock University Department of Geological Sciences, Research Report Series: No. 16

Megraw RA, Nearn WT (1972) Detailed DBH density profiles of several trees from Douglasfir fertilizer/thinning plots. Proceedings of the Symposium on the effect of growth acceleration on the properties of wood. Forest Products Laboratory, Forest Service, Madison, WI, USA

Meier E (2016) Wood: Identifying and Using Hundreds of Woods Worldwide. The Wood Database, Eric Meier (self-published)

Meincken M, du Plessis A (2013) Visualising and quantifying thermal degradation of wood by computed tomography. European Journal of Wood and Wood Products 71, 387-389. doi: 10.1007/s00107-013-0683-6

Merkus HG (2009) Particle Size Measurements: Fundamentals, Practice, Quality. Springer, London, UK

Miettinen A, Hendriks CLL, Chinga-Carrasco G, Gamstedt EK, Kataja M (2012) A non-destructive X-ray microtomography approach for measuring fibre length in short-fibre composites. Composites Science and Technology 72(15), 1901-1908. doi: 10.1016/j.compscitech.2012.08.008

Milner HR, Woodard AC (2016) Sustainability of engineered wood products. In: Khatib JM (ed) Sustainability of Construction Materials (Second Edition). Woodhead Publishing, Sawston, UK. 159-180. doi: 10.1016/B978-0-08-100370-1.00008-1

Mizuno S, Torizu R, Sugiyama J (2010) Wood identification of a wooden mask using synchrotron X-ray microtomography. Journal of Archaeological Science 37(11), 2842-2845. doi: 10.1016/j.jas.2010.06.022

Modzel G, Kamke FA, De Carlo F (2011) Comparative analysis of a wood: adhesive bondline. Wood Science and Technology 45, 147-158. doi: 10.1007/s00226-010-0304-z

Moghaddam MS, Van den Bulcke J, Wålinder MEP, Claesson PM, Van Acker J, Swerin A (2017) Microstructure of chemically modified wood using X-ray computed tomography in relation to wetting properties. Holzforschung 71(2), 119-128. doi: 10.1515/hf-2015-0227

Monzote L, Piñón A, Setzer WN (2014) Antileishmanial potential of tropical rainforest plant extracts. Medicines 2014, 32-55. doi: 10.3390/medicines1010032

Morgado-González G, Gómez-Guerrero A, Villanueva-Díaz J, Terrazas T, Ramírez-Herrera C, de la Rosa PH (2019) Wood density of *Pinus hartwegii* Lind. at two altitude and exposition levels. Agrociencia 53(4), 645-660

Morgan JB, Connolly EL (2013) Plant-soil interactions: nutrient uptake. Nature Education Knowledge 4(8), 2

Morrell JJ, Stark NM (2006) Durability of wood-plastic composites. Wood Design Focus 16(3), 7-10

Morrison O (2004) Resin distribution in particleboard (B.Eng Honours Thesis). Australian National University, Canberra, Australia

Mull RT (1984) Mass estimated by computed tomography: physical density from CT numbers. American Journal of Roentgenology 143, 1101-1104. doi: 10.2214/ajr.143.5.1101

Muszyński L (2009) Imaging wood plastic composites (WPCs): X-ray computed tomography, a few other promising techniques, and why we should pay attention. Bioresources 4(3), 1210-1221

Muzamal M, Bååth JA, Olsson L, Rasmuson A (2016) Contribution of structural modification to enhanced enzymatic hydrolysis and 3-D structural analysis of steam-exploded wood using X-ray tomography. Bioresources 11(4), 8509-8521

Nakada R (2006) Within-stem water distribution in living trees of some conifers. IAWA Journal 27, 313-327

Nakada R, Fujisawa Y, Hirakawa Y (1999) Soft X-ray observation of water distribution in the stem of Cryptomeria japonica D-Don I: General description of water distribution. doi: 10.1163/22941932-90000157

Naresh K, Khan KA, Umer R, Cantwell WJ (2020) The use of X-ray computed tomography for design and process modeling of aerospace composites: a review. Materials and Design 190, 108553. doi: 10.1016/j.matdes.2020.108553

Nelis PA, Michaelis F, Krause KC, Mai C (2018) Kiri wood (*Paulownia tomentosa*): can it improve the performance of particleboards? European Journal of Wood and Wood Products 76, 445-453. doi: 10.1007/s00107-017-1222-7

Nepveu G (1973) Etude génétique de quelques qualités du bois de pin maritime. Corrélations avec des caractères de croissance et d'aptitude à l'élagage. Document à distribution limitée. Station de Recherches sur la Qualité des Bois du C.N.R.F., Champenoux, No. 1973/5 (in French)

Nicholls JWP (1971a) The effect of environmental factors on wood characteristics I - The influence of irrigation on *Pinus radiata* from South Australia. Silvae Genetica 20, 1-52

Nicholls JWP (1971b) The effect of environmental factors on wood characteristics II - The effect of thinning and fertilizer treatment on the wood of *Pinus pinaster*. Silvae Genetica 20, 53-100

Nicholls JWP, Brown AG (1971) The ortet-ramet relationship in wood characteristics of *Pinus radiata*. Appita 25, 200-209

Niemz P, Baensch F, Brunner AJ (2020) Acoustic emission analysis and synchrotron-based microtomography on glued shear strength samples from spruce solid wood. Bulletin of the Transilvania University of Brasov. Forestry, Wood Industry, Agricultural Food Engineering. Series II 13(1), 81-88. doi: 10.31926/but.fwiafe.2020.13.62.1.7

Nikles DG, Robson KJ (2005) Vegetative propagation and preliminary field performance of sixteen rainforest tree species in north Queensland. In: Erskine PD, Lamb D, Bristow M (eds) Reforestation in the Tropics and Subtropics of Australia Using Rainforest Tree Species. Rural Industries Research and Development Corporation, Barton, Australia

Nordmark U, Oja J (2004) Prediction of Board Values in Pinus sylvestris Sawlogs Using X-ray Scanning and Optical Three-dimensional Scanning of Stems. Scandinavian Journal of Forest Research 19(5), 473-480. doi: 10.1080/02827580410030172

Nowakowska M, Krajewski A, Witomski P (2017) The relationship between the mass of old house borer larvae Hylotrupes bajulus (L.) and their lengths measured using radiograph. Drewno 60(199), 81-88

O'Rourke JC, Smyth L, Webb AL, Valter K (2020) How can we show you, if you can't see It? Trialing the use of an interactive three-dimensional micro-CT model in medical education. Anatomical Sciences Education 13(2), 206-217. doi: 10.1002/ase.1890

Ogata K, Fujii T, Abe H, Bass P (2008) Identification of the timbers of Southeast Asia and the western Pacific. Kaiseisha Press, Hiyoshidai, Japan

Oh SC (2008) Internal void structure of strandboard using X-ray computed tomography. Mokchae Konghak 36, 13-22 (in Korean)

Oja J (1997) A comparison between three different methods of measuring knot parameters in *Picea abies*. Scandinavian Journal of Forest Research 12(3), 311-315. doi: 10.1080/02827589709355415

Oja J, Grundberg S, Grönlund A (1998) Measuring the outer shape of Pinus sylvestris saw logs with an X-ray LogScanner. Scandinavian Journal of Forest Research 13(1-4), 340-347. doi: 10.1080/02827589809382993

Oja J, Grundberg S, Grönlund A (2000) Predicting the strength of sawn products by X-ray scanning of logs: a preliminary study. Wood and Fiber Science 32(2), 203-208.

Oja J, Grundberg S, Grönlund A (2001) Predicting the stiffness of sawn products by X-ray scanning of Norway spruce saw logs. Scandinavian Journal of Forest Research 16(1), 88-96. Journal of Wood Science 48, 479-483. doi: 10.1080/028275801300004442

Okochi T, Hoshino Y, Fujii H, Mitsutani T (2007) Nondestructive tree-ring measurements for Japanese oak and Japanese beech using micro-focus X-ray computed tomography. Dendrochronologia 24(2-3), 155-164. doi: 10.1016/j.dendro.2006.10.010

Oliver AC (1959) Use of X-rays in the detection of Teredo in wood. Journal of the Institute of Wood Science 3, 47-52

Olsson T, Megnis M, Varna J, Lindberg H (2001) Measurement of the uptake of linseed oil in pine by the use of an X-ray microdensitometry technique. Journal of Wood Science 47(4), 275-281. doi: 10.1007/BF00766713

Oluwafemi SD, Jafri MZM, Hashim R, Sulaiman O, Aziz MZA, Yusof MFM, Shukri A (2021) Mass attenuation coefficients, CT Numbers and density profiles of soy protein concentrate-based *Rhizophora* spp. particleboards enhanced by NaOH/IA-PAE. AIP Conference Proceedings 2319, 050001. doi: 10.1063/5.0039370

Osborne NL, Høibø ØA, Maguire DA (2016) Estimating the density of coast Douglas-fir wood samples at different moisture contents using medical X-ray computed tomography. Computers and Electronics in Agriculture 127, 50-55. doi: 10.1016/j.compag.2016.06.003

Özer SY (2011) Detection of vertical root fractures by using cone beam computed tomography with variable voxel sizes in an in vitro model. Journal of Endodontics 37(1), 75-79. doi: 10.1016/j.joen.2010.04.021

Pacilè S, Tromba G (2018) Introduction to X-Ray micro-tomography. In: Giuliani A, Cedola A (eds) Advanced High-Resolution Tomography in Regenerative Medicine. Springer, Cham. doi: 10.1007/978-3-030-00368-5_2

Papadopoulos AN (2019) Advances in wood composites. Polymers 12(1), 48. doi: 10.3390/polym12010048

Paris JL, Kamke FA (2015) Quantitative wood-adhesive penetration with X-ray computed tomography. International Journal of Adhesion and Adhesives 61, 71-80. doi: 10.1016/j.ijadhadh.2015.05.006

Paris JL, Kamke FA, Mbachu R, Gibson SK (2014) Phenol formaldehyde adhesives formulated for advanced X-ray imaging in wood-composite bondlines. Journal of Materials Science 49, 580-591. doi: 10.1007/s10853-013-7738-2

Parker ML, Barton GM, Jozsa LA (1974) Detection of lignans in western hemlock by radiography. Wood Science and Technology 8, 229-232

Patera A, Jefimovs K, Rafsanjani A, Voisard F, Mokso R, Derome D, Carmeliet J (2014) Micro-scale restraint methodology for humidity induced swelling investigated by phase contrast x-ray tomography. Experimental Mechanics 54, 1215-1226. doi: 10.1007/s11340-014-9894-y

Paterson DJ, De Jonge MD, Howard DL, Lewis W, McKinlay JA, Starritt A, Kusel M, Ryan CG, Kirkham R, Moorhead G, Siddons DP (2011) The X-ray fluorescence microscopy beamline at the Australian Synchrotron. AIP Conference Proceedings 1365, 219-222. doi: 10.1063/1.3625343

Paterson GL, Sykes D, Faulwetter S, Merk R, Ahmed F, Hawkins LE, Dinley J, Ball A, Arvanitidis C (2014). The pros and cons of using micro-computed tomography in gross and microanatomical assessments of polychaetous annelids. Memoirs of the Museum of Victoria 71, 237-246

Penttilä PA, Kilpeläinen P, Tolonen L, Suuronen JP, Sixta H, Willför S, Serimaa R (2013) Effects of pressurized hot water extraction on the nanoscale structure of birch sawdust. Cellulose 20, 2335-2347. doi: 10.1007/s10570-013-0001-9

Peters T (2002) CT image reconstruction (PowerPoint slides). Presented at the 44th Annual Meeting of the American Association of Physicists in Medicine. Montréal, Québec, Canada. Retrieved from: https://www.aapm.org/meetings/02AM/pdf/8372-23331.pdf (Accessed 10 September 2020)

Pettersen RC (1984) The chemical composition of wood. Advances in chemistry series 57-126. doi: 10.1021/ba-1984-0207.ch002

Phelps ME, Gado MH, Hoffman EJ (1975) Correlation of effective atomic number and electron density with attenuation coefficients measured with polychromatic X-rays. Radiology 117, 585-588. doi: 10.1148/117.3.585

Polge H (1964) Délimitation de l'aubier et du bois de coeur par analyse densitométrique de cliches radiographiques. Annales des Sciences Forestières 21, 607-623 (in French)

Polge H (1966) Établissement des courbes de variation de la densité du bois par exploration densitométrique de radiographies d'échantillons prélevés à la tarière sur des arbres vivants: applications dans les domaines technologique et physiologique. Annales des Sciences Forestières 23, 1-206. doi: 10.1051/forest/19660101

Polge H (1968) Tests précoces de la qualité du bois sur 25 provenances d'Abies grandis. Annals of Forest Science 25, 3-23 (in French)

Polge H (1969) Influence de la fertilisation sur la qualité du bois de Pin maritime. Annals of Forest Science 26, 45-64 (in French)

Polge H (1970) The use of X-ray densitometric methods in dendrochronology. Tree-Ring Bulletin 30, 1-4

Polge H (1971) Le "Message" des arbres. La Recherche 11, 331-338 (in French)

Polge H (1978) Fifteen years of wood radiation densitometry. Wood Science and Technology 12, 187-196

Polge H, Garros S (1971) Influence de défoliaisons sur la structure du bois de Pin maritime. Annals of Forest Science 28, 195-206 (in French)

Polge H, Keller R (1968) Influence de l'approvisionnement en eau sur la structure interne des accroissements annuels - Expérience d'irrigation sur *Pins sylvestres*. Annals of Forest Science 25, 125-133 (in French)

Polge H, Keller R (1969) La xylochronologie, perfectionnement logique de la dendrochronology. Annals of Forest Science 26, 225-256 (in French)

Polge H, Keller R (1973) Qualité du bois et largeur d'accroissements en foret de Tronçais. Annals of Forest Science 30, 91-126 (in French)

Polge H, Keller R, Thiercelin F (1973) Influence de l'élagage de branches vivantes sur la structure des accroissements annuels et sur quelques caractérlstiques du bois de douglas et de grandis. Annals of Forest Science 30, 127-140 (in French)

Popescu CM (2017) Wood as bio-based building material. In: Jones D, Brischke C (eds) Performance of Bio-Based Building Materials. Woodhead Publishing, Cambridge, UK. 21–96. doi:10.1016/B978-0-08-100982-6.00002-1

Porter T (2014) Wood Identification and Use. Guild of Master Craftsman Publications, Lewes, UK

Prakash N (1986) Methods in Plant Microtechnique, 2nd Edition. University of New England, Armidale, Australia

Preim B, Botha C (2014) Image analysis for medical visualization. In: Preim B, Botha C (eds) Visual Computing for Medicine (Second Edition). Morgan Kaufmann Publishers, Burlington, MA, USA. 111-175. doi: 0.1016/B978-0-12-415873-3.00004-3

Qi Y, Zhou Y, Xu J, Ge Z (2018) Development of a wood computed tomography imaging system using a butterworth filtered back-projection algorithm. Forest Products Journal 68, 147-156. doi: 10.13073/FPJ-D-17-00029

Rahayu I, Darmawan W, Nugroho N, Nandika D, Marchal R (2014) Demarcation point between juvenile and mature wood in sengon (*Falcataria moluccana*) and jabon (*Antocephalus cadamba*). Journal of Tropical Forest Science 26(3), 331-339

Rahman F, Allan D, Rosen C, Sadowsky M (2004). Arsenic availability from chromated copper arsenate (CCA)-treated wood. Journal of Environmental Quality, 33(1), 173-180. doi:10.2134/jeq2004.1730

Rais A, Ursella E, Vicario E, Giudiceandrea F (2017) The use of the first industrial X-ray CT scanner increases the lumber recovery value: case study on visually strength-graded Douglas-fir timber. Annals of Forest Science 74, 28. doi: 10.1007/s13595-017-0630-5

Rautkari L, Kamke FA, Hughes M (2011) Density profile relation to hardness of viscoelastic thermal compressed (VTC) wood composite. Wood Science and Technology 45(4), 693-705. doi: 10.1007/s00226-010-0400-0

Redenbach C (2009) Modelling foam structures using random tessellations. In: Proceeding of the 10th European Conference of ISS. Bologna, Italy

Revin V, Novokuptsev N, Kadimaliev D (2016) Preparation of biocomposites using sawdust and lignosulfonate with a culture liquid of levan producer *Azotobacter vinelandii* as a bonding agent. Bioresources 11(2), 3244-3258

Richardson J (1929) Timbers of Australia. Empire Forestry Journal 8(1), 98-100

Richter HG (1980) Occurrence, morphology and taxonomic implications of crystalline and siliceous inclusions in the secondary xylem of the Lauraceae and related families. Wood Science and Technology 14, 35-44. doi: 10.1007/BF00353461

Rinnhofer A, Petutschnigg A, Andreu JP (2003) Internal log scanning for optimizing breakdown. Computers and Electronics in Agriculture 41(1-3), 7-21. doi: 10.1016/S0168-1699(03)00039-5

Rosner B, Konnerth J, Plank B, Salaberger D, Hansmann C (2010) Radial shrinkage and ultrasound acoustic emissions of fresh versus pre-dried Norway spruce sapwood. Trees 24, 931-940. doi: 10.1007/s00468-010-0464-3

Rothlisberger F (1976) 8000 Jahre Walliser Gletschergeschichte. II. Tell: Gletscher- und Klimaschwankungen im Raum Zermatt, Ferpecle und Arolla. Die Alpen 52(3/4), 61-151 (in German)

Ruano A, Zitek A, Hinterstoisser B, Hermoso E (2019) NIR hyperspectral imaging (NIR-HI) and µXRD for determination of the transition between juvenile and mature wood of *Pinus sylvestris* L. Holzforschung 73(7), 621-627. doi: 10.1515/hf-2018-0186

Rudman P, McKinnell FH (1970) Effect of fertilizers on wood density of young radiata pine. Australian Forestry 34, 170-178

Ryan CG, Cousens DR, Sie SH, Griffin WL (1990) Quantitative analysis of PIXE spectra in geoscience applications. Nuclear Instruments and Methods in Physics Research Section B: Beam Interactions with Materials and Atoms 49(1-4), 271-276. doi: 10.1016/0168-583X(90)90259-W

Ryan CG, Siddons DP, Kirkham R, Li ZY, DeJonge MD, Paterson DJ, Kuczewski A, Howard DL, Dunn PA, Falkenberg G (2014) Maia X-ray fluorescence imaging: Capturing detail in complex natural samples. Journal of Physics: Conference Series 499, 012002. doi: 10.1088/1742-6596/499/1/012002

Sackey EK, Smith GD (2010) Characterizing macro-voids of uncompressed mats and finished particleboard panels using response surface methodology and X-ray CT. Holzforschung 64, 343-352. doi: 10.1515/HF.2010.052

Sakellariou A, Senden TJ, Sawkins TJ, Knackstedt MA, Turner ML, Jones AC, Saadatfar M, Roberts RJ, Limaye A, Arns CH, Sheppard AP, Sok RM (2014) An x-ray tomography facility for quantitative prediction of mechanical and transport properties in geological, biological, and synthetic systems. in: Proceedings of SPIE 5535, Developments in X-Ray Tomography IV, 473-484, Denver, Colorado, USA. doi: 10.1117/12.559200

Salim K, Abdelatif Z, Nourdine S, Abdelhamid A (2014) Characterization of Algerians oak wood by X-ray tomographic scanner and free software Image-J. Wood Research 59(2), 335-342

Salomé M, Peyrin F, Cloetens P, Odet C, Laval-Jeantet AM, Baruchel J, Spanne P (1999) A synchrotron radiation microtomography system for the analysis of trabecular bone samples. Medical Physics 26(10), 2194-2204. doi: 10.1118/1.598736

Sanabria SJ, Baensch F, Zauner M, Niemz P (2020) In-situ quantification of microscopic contributions of individual cells to macroscopic wood deformation with synchrotron computed tomography. Scientific Reports 10, 21615. doi: 10.1038/s41598-020-78028-4

Sano Y, Fujikawa S, Fukazawa K (1995) Detection and features of wetwood in *Quercus mongolica* var. grosseserrata. Trees 9, 261-268. doi: 10.1007/BF00202016

Santini L, Rodriguez DRO, Quintilhan MT, Brazolin S, Filho MT (2019) Evidence to wood biodeterioration of tropical species revealed by non-destructive techniques. Science of the Total Environment 672, 357-369. doi: 10.1016/j.scitotenv.2019.03.429

Sarfi F, Azizi M, Arian A (2013) A multiple criteria analysis of factors affecting markets of engineered wood products with respect to customer preferences: a case study of particleboard and MDF. Forest Science and Practice 15(1), 61-69. doi: 10.1007/s11632-013-0110-4

Sasov A (2002) Comparison of fan-beam, conebeam, and spiral scan reconstruction in X-ray micro-CT. In: Proceedings of SPIE 4503, Developments in X-Ray Tomography III, 124-131. doi: 10.1117/12.452835

Sauter UH, Mutz R, Munro BD (1999) Determining juvenile-mature wood transition in Scots pine using latewood density. Wood and Fiber Science 31(4), 416-425

Schad KC, Schmoldt DL, Ross RJ (1996) Nondestructive methods for detecting defects in softwood logs. USDA Forest Service Research paper FPL-RP-546. Forest Products Laboratory, Forest Service, United States Department of Agriculture

Scheepers G, Moren T, Rypstra T (2007) Liquid water flow in Pinus radiata during drying. Holz als Roh- und Werkstoff 65, 275-283. doi: 10.1007/s00107-007-0171-y

Schladitz K (2011) Quantitative micro-CT. Journal of Microscopy 243, 111-117. doi: 10.1111/j.1365-2818.2011.03513.x

Schmidt H (1962) Larvae of *Hylotrupes bajulus* made visible in the wood by X-rays. Die Umschau 62(3), 82-83 (in German)

Scholz G, Van den Bulcke J, Boone M, Zauer M, Bäucker E, Van Acker J, Militz H (2010a) Investigation on wax-impregnated wood. Part 1: Microscopic observations and 2D X-ray imaging of distinct wax types. Holzforschung 64(5), 581-585. doi: 10.1515/hf.2010.091

Scholz G, Zauer M, Van den Bulcke J, Van Loo D, Pfriem A, Van Acker J, Militz H (2010b) Investigation on wax-impregnated wood. Part 2: Study of void spaces filled with air by He pycnometry, Hg intrusion porosimetry, and 3D X-ray imaging. Holzforschung 64(5), 587-593. doi: 10.1515/hf.2010.090

Schwarzkopf MJ, Burnard MD (2016) Wood-plastic composites—Performance and environmental impacts. In: Kutnar A, Muthu S (eds) Environmental Impacts of Traditional and Innovative Forest-based Bioproducts. Springer, Singapore. 19-43

Scurfield G, Anderson CA, Segnit ER (1974) Silica in woody stems. Australian Journal of Botany 22(2), 211-229. doi: 10.1071/BT9740211

Sean T, Brunette G, Cote F (1999) Protection of oriented strandboard with borate. Forest Products Journal 49(6), 47-51

Seger MM, Danielsson PE (2003) Scanning of logs with linear cone-beam tomography. Computers and Electronics in Agriculture 41(1-3), 45-62. doi: 10.1016/S0168-1699(03)00041-3

Sepúlveda P, Oja J, Grönlund A (2002) Predicting spiral grain by computed tomography of Norway spruce Journal of Wood Science 48, 479-483. doi: 10.1007/BF00766643

Shammaa MH, Suziki H, Michikawa T (2007) Registration of CAD mesh models with CT volumetric model of assembly of machine parts. Visual Computer 23, 965-974. doi: 10.1007/s00371-007-0171-2

Shelmerdine SC, Simcock IC, Hutchinson JC, Aughwane R, Melbourne A, Nikitichev DI, Ong J, Borghi A, Cole G, Kingham E, Calder AD, Capelli C, Akhtar A, Cook AC, Schievano S, David A, Ourselin S, Sebire NJ, Arthurs OJ (2018) 3D printing from microfocus computed tomography (micro-CT) in human specimens: education and future implications. British Journal of Radiology 91, 20180306. doi: 10.1259/bjr.20180306

Sheppard A, Latham S, Middleton J, Kingston A, Myers G, Varslot T, Fogden A, Sawkins T, Cruikshank R, Saadatfar M, Francois N (2014) Techniques in helical scanning, dynamic imaging and image

segmentation for improved quantitative analysis with X-ray micro-CT. Nuclear Instruments and Methods in Physics Research Section B: Beam Interactions with Materials and Atoms 324, 49-56. doi: 10.1016/j.nimb.2013.08.072

Siau JF (1995) Wood: Influence of Moisture on Physical Properties. Virginia Polytechnic Institute and State University, Blacksburg, VA, USA

Skolmen RG (1974) Some woods of Hawaii: Properties and uses of 16 commercial species. USDA Forest Service General Technical Report PSW-8, Berkeley, USA

Skuratov N, Sapozhnikov I, Alexeeva I, Mamontov M, Matveeva K, Samoilenko D (2015) Measurements during wood drying based on X-ray and slicing techniques and computation of diffusion coefficients. Pro Lingo 11, 383-388.

Sodini N, Dreossi D, Chen R, Fioravanti M, Giordano A, Herrestal P, Rigon L, Zanini F (2012) Non-invasive microstructural analysis of bowed stringed instruments with synchrotron radiation X-ray microtomography. Journal of Cultural Heritage 13(3), S44-S49. doi: 10.1016/j.culher.2012.04.008

Söftje M, Koddenberg T, Militz H, Drafz MHH, Namyslo JC, Kaufmann DE (2020) Chemistry and spectroscopy of renewable materials, part 2: investigation of suitably esterified wood regarding penetration and distribution of the chemically modifying reagent by means of high-resolution 3D computed tomography. ACS Sustainable Chemistry & Engineering 8(19), 7353-7358. doi: 10.1021/acssuschemeng.0c01574

Sotayo A, Bradley D, Bather M, Sareh P, Oudjene M, El-Houjeyri I, Harte AM, Mehra S, O'Ceallaigh C, Haller P, Namari S, Makradi A, Belouettar S, Bouhala L, Deneufbourg F, Guan Z (2020) Review of state of the art of dowel laminated timber members and densified wood materials as sustainable engineered wood products for construction and building applications. Developments in the Built Environment (1), 100004. doi: 10.1016/j.dibe.2019.100004

Standards Australia (2005) Australian Standard AS 5604-2005 Timber—Natural Durability Ratings. Standards Australia, Sydney, Australia

Standfest G, Petutschnigg A, Dunky M, Zimmer B (2009) Determination of density in wood based panels by means of computer tomography. European Journal of Wood and Wood Products 67(1), 83-87 (in German). doi: 10.1007/s00107-008-0289-6

Stängle SM, Brüchert F, Heikkila A, Usenius T, Usenius A, Sauter UH (2015) Potentially increased sawmill yield from hardwoods using X-ray computed tomography for knot detection. Annals of Forest Science 72, 57-65. doi: 10.1007/s13595-014-0385-1

Stängle SM, Weiskittel AR, Dormann CF, Brüchert F (2016) Measurement and prediction of bark thickness in *Picea abies*: assessment of accuracy, precision, and sample size requirements. Canadian Journal of Forest Research 46(1), 39-47. doi: 10.1139/cjfr-2015-0263

Stark NM, Rowlands RE (2003) Effects of wood fiber characteristics on mechanical properties of wood/polypropylene composites. Wood and Fiber Science 35(2), 167-174

Stark NM, White RH, Mueller SA, Osswald TA (2010) Evaluation of various fire retardants for use in wood flour–polyethylene composites. Polymer Degradation and Stability 95(9), 1903-1910. doi: 10.1016/j.polymdegradstab.2010.04.014

Steckel V, Clemons CM, Thoemen H (2007) Effects of material parameters on the diffusion and sorption properties of wood-flour/polypropylene composites. Journal of Applied Polymer Science 103, 752-763. doi: 10.1002/app.25037

Steffenrem A, Kvaalen H, Dalen KS, Høibø OA (2014) A high-throughput X-ray-based method for measurements of relative wood density from unprepared increment cores from *Picea abies*. Scandinavian Journal of Forest Research 29(5), 506-514. doi: 10.1080/02827581.2014.919350

Steppe K, Cnudde V, Girard C, Lemeur R, Cnudde JP, Jacobs P (2004) Use of X-ray computed microtomography for non-invasive determination of wood anatomical characteristics. Journal of Structural Biology 148(1), 11-21. doi: 10.1016/j.jsb.2004.05.001

Steppe K, Lemeur R (2007) Effects of ring-porous and diffuse-porous stem wood anatomy on the hydraulic parameters used in a water flow and storage model. Tree Physiology 27(1), 43-52. doi: 10.1093/treephys/27.1.43

Sterley M, Serrano E, Enquist B, Hornatowska J (2014) Finger jointing of freshly sawn Norway spruce side boards - a comparative study of fracture properties of joints glued with phenol-resorcinol and one-component polyurethane adhesive. In: Aicher S, Reinhardt HW, Garrecht H (eds) Materials and Joints in Timber Structures. RILEM Bookseries, Vol 9. Springer, Dordrecht, Netherlands. 325-339. doi: 10.1007/978-94-007-7811-5_30

Stiller W (2018) Basics of iterative reconstruction methods in computed tomography: A vendor-independent overview. European Journal of Radiology 109, 147-154. doi: 10.1016/j.ejrad.2018.10.025

Strohmann T, Bugelnig K, Breitbarth E, Wilde F, Steffens T, Germann H, Requena G (2019) Semantic segmentation of synchrotron tomography of multiphase Al-Si alloys using a convolutional neural network with a pixel-wise weighted loss function. Scientific Reports 9, 19611. doi: 10.1038/s41598-019-56008-77

Strullu-Derrien C, Kenrick P, Badel E, Cochard H, Tafforeau P (2013) An overview of the hydraulic systems in early land plants. IAWA Journal 34(4), 333-351. doi: 10.1163/22941932-00000029

Strullu-Derrien C, Kenrick P, Tafforeau P, Cochard H, Bonnemain JL, Le Hérissé A, Lardeux H, Badel E (2014) The earliest wood and its hydraulic properties documented in c. 407-million-year-old fossils using synchrotron microtomography. Botanical Journal of the Linnean Society 175(3), 423-437. doi: 10.1111/boj.12175

Sugimori M, Lam F (1999) Macro-void distribution analysis in strand-based wood composites using an X-ray computer tomography technique. Journal of Wood Science 45, 254-257. Doi: 10.1007/BF01177735

Sun G, Ibach RE, Faillace M, Gnatowski M, Glaeser JA, Haight J (2016) Laboratory and exterior decay of wood–plastic composite boards: voids analysis and computed tomography. Wood Material Science and Engineering 12(5), 263-287. doi: 10.1080/17480272.2016.1164755

Sun G, Ibach RE, Gnatowski M, Glaeser JA, Leung M, Haight J (2014) Modern instrumental methods to investigate the mechanism of biological decay in wood plastic composites. In: Proceedings of the 45th Annual Meeting of the International Research Group on Wood Protection. St George, UT, USA. IRG/WP 14-40674

Surdi PG, Bortoletto G, Castro VR, Mendes RF, de Almeida NF, Filho MT (2014) Relationship between density profile and internal bond of Pinus spp. OSB panels. Floresta e Ambiente 21(3), 349-357. doi: 10.1590/2179-8087.063413

Sutton WRJ, Harris, JM (1974) Effect of heavy throning on wood density in radiata pine. New Zealand Journal of Forestry Science 4, 112-115

Svedström K, Bjurhager I, Kallonen A, Peura M, Serimaa R (2012a) Structure of oak wood from the Swedish warship Vasa revealed by X-ray scattering and microtomography. Holzforschung 66(3), 355-363. doi: 10.1515/hf.2011.157

Svedström K, Lucenius J, Van den Bulcke J, Van Loo D, Immerzeel P, Suuronen JP, Brabant L, Van Acker J, Saranpää P, Fagerstedt K, Mellerowicz E, Serimaa R (2012b) Hierarchical structure of juvenile hybrid aspen xylem revealed using X-ray scattering and microtomography. Trees 26, 1793-1804. 10.1007/s00468-012-0748-x

Swain EHF (1928) The Timbers and Forest Products of Queensland. A.J. Cumming, Government Printer. Brisbane, Australia

Taguchi I, Saito T (1991) Non-destructive analysis of archaeological materials. Analytical Sciences 7, 659-662

Takatani M, Ikeda K, Sakamoto K, Okamoto T (2008) Cellulose esters as compatibilizers in wood/poly(lactic acid) composite. Journal of Wood Science 54, 54-61. doi: 10.1007/s10086-007-0911-y

Tanaka S, Seki M, Miki T, Shigematsu I, Kanayama K (2015) Solute diffusion into cell walls in solution-impregnated wood under conditioning process I: effect of relative humidity on solute diffusivity. Journal of Wood Science 61, 543-551. doi: 10.1007/s10086-015-1503-x

Tanaka T, Avramidis S, Shida S (2009) Evaluation of moisture content distribution in wood by soft X-ray imaging. Journal of Wood Science 55, 69-73. doi: 10.1007/s10086-008-0997-x

Tardif JC, Conciatori F (2015) Microscopic examination of wood: sample preparation and techniques for light microscopy. In: Yeung E, Stasolla C, Sumner M, Huang B. (eds) Plant Microtechniques and Protocols. Springer, Cham. doi: 10.1007/978-3-319-19944-3_22

Taylor A, Plank B, Standfest G, Petutschnigg A (2013) Beech wood shrinkage observed at the micro-scale by a time series of X-ray computed tomographs (μXCT). Holzforschung 67(2), 201-205. doi: 10.1515/hf-2012-0100

Taylor AJ (2006) Wood density determination in *Picea sitchensis* using computerised tomography: how do density measurements compare with measurements of pilodyn pin penetration? (Honours Thesis), University of Wales, Bangor, UK

Taylor L, Claringbold D (2010) Acoustics of the Sydney Opera House concert hall, part one: the client's perspective. In: Proceedings of 20th International Congress on Acoustics. Sydney, Australia

Thiercelin F (1970) Tardiveté du débourrement et densité du bois dans une population adulte de Picea abies Karst. Annals of Forest Science 27, 243-254 (in French)

Thoby M (1975) Validitg de tests prEcoces d'apprEciation des caractères technologiques du bois de douglas. Application à une plantation comparative de 24 provenances de Douglas (Peyrat le Chateau) en liaison avec des caractères morphologiques et auxométriques. Rapport Ecole Nationale des Ingénieurs des Travaux des Eaux et Forets. Nogent S/Vernisson (in French)

Tinti VP, Gonçalves FG, Paes JB, Arantes MDC, Vieira MC, López YM (2018) Physical properties and X-ray densitometry in particle board of the eucalypt wood waste. Ciência da Madeira 9(2), 71-81. doi: 10.12953/2177-6830/rcm.v9n2p71-81

Tomoko O, Maeda K, Tsunetsugu Y, Shida S (2019) Influence of surface checks on wood moisture content during wetting and re-drying. European Journal of Wood and Wood Products 77, 681-689. doi: 10.1007/s00107-019-01423-w

Tran H, Doumalin P, Delisee C, Dupre JC, Malvestio J, Germaneau A (2013) 3D mechanical analysis of low-density wood-based fiberboards by X-ray microcomputed tomography and digital volume correlation. Journal of Materials Science 48, 3198-3212. doi: 10.1007/s10853-012-7100-0

Trtik P, Dual J, Keunecke D, Mannes D, Niemz P, Stähli P, Kaestner A, Groso A, Stampanoni M (2007) 3D imaging of microstructure of spruce wood. Journal of Structural Biology 159(1), 46-55. doi: 10.1016/j.jsb.2007.02.003

Tsunoda K, Nishimoto K (1978) Growth rates of shipworm Teredo navalis L. at Naruto, Tokushima Pref., Japan. Material und Organismen 13(4), 285-296

Tsunoda K, Watanabe H, Fukuda K, Hagio K (2002) Effects of zinc borate on the properties of medium density fiberboard. Forest Products Journal 52(11), 62-65

Tuy HK (1983) An inversion formula for cone-beam reconstruction. SIAM Journal on Applied Mathematics 43(3), 546-552. doi: 10.1137/0143035

Van den Bulcke J, Biziks V, Andersons B, Mahnert KC, Militz H, Van Loo D, Dierick M, Masschaele B, Boone MN, Brabant L, De Witte Y, Vlassenbroeck J, Van Hoorebeke L, Van Acker J (2013) Potential of X-ray computed tomography for 3D anatomical analysis and microdensitometrical assessment in wood research with focus on wood modification. International Wood Products Journal 4(3), 183-190. doi: 10.1179/2042645313Y.0000000046

Van den Bulcke J, Boone M, Van Acker J, Stevens M, Van Hoorebeke L (2009a) X-ray tomography as a tool for detailed anatomical analysis. Annals of Forest Science 66, 508. doi: 10.1051/forest/2009033

Van den Bulcke J, Boone M, Van Acker J, Van Hoorebeke L (2009b) Three-dimensional X-ray imaging and analysis of fungi on and in wood. Microscopy and Microanalysis 15(5), 395-402. doi: 10.1017/S1431927609990419

Van den Bulcke J, Boone M, Van Acker J, Van Hoorebeke L (2010) High-resolution X-ray imaging and analysis of coatings on and in wood. Journal of Coatings Technology and Research 7, 271-277. doi: 10.1007/s11998-009-9182-4

Van den Bulcke J, Boone MA, Dhaene J, Van Loo D, Van Hoorebeke L, Boone MN, Wyffels F, Beeckman H, Van Acker J, De Mil T (2019) Advanced X-ray CT scanning can boost tree ring research for earth system sciences. Annals of Botany 124, 837-847. doi: 10.1093/aob/mcz126

Van den Bulcke J, Masschaele B, Dierick M, Van Acker J, Stevens M, Van Hoorebeke L (2008) Three-dimensional imaging and analysis of infested coated wood with X-ray submicron CT. International Biodeterioration and Biodegradation 61(3), 278-286. doi: 10.1016/j.ibiod.2007.09.004

Van den Bulcke J, Wernersson ELG, Dierick M, Van Loo D, Masschaele B, Brabant L, Boone MN, Van Hoorebeke L, Haneca K, Brun A, Hendriks CLL, Van Acker J (2014) 3D tree-ring analysis using helical X-ray tomography. Dendrochronologia 32(1), 39-46. doi: 10.1016/j.dendro.2013.07.001

Van den Bulcke J, Windt ID, Defoirdt N, de Smet J, Van Acker J (2011) Moisture dynamics and fungal susceptibility of plywood. International Biodeterioration and Biodegradation 65(5), 708-716. doi: 10.1016/j.ibiod.2010.12.015

Vannoppen A, Maes S, Kint V, De Mil T, Ponette Q, Van Acker J, Van den Bulcke J, Verheyen K, Muys B (2017) Using X-ray CT based tree-ring width data for tree growth trend analysis. Dendrochronologia 44, 66-75. doi: 10.1016/j.dendro.2017.03.003

Varslot TK, Kingston AM, Latham SJ, Middleton J, Knackstedt MA, Sheppard AP (2011a) Combining high-fidelity helical microtomography with region-of-interest scanning for improved core characterisation. In: 2011 International Symposium of the Society of Core Analysts, Austin, Texas, USA

Varslot TK, Kingston AM, Myers G, Sheppard A (2011b) High-resolution helical cone-beam micro-CT with theoretically-exact reconstruction from experimental data. Medical Physics 38(10), 5459-5476. doi: 10.1118/1.3633900

Varslot TK, Kinston AM, Sheppard A, Sakellariou A (2010) Fast high-resolution micro-CT with exact reconstruction methods. In: Proceedings of SPIE 7804, Developments in X-Ray Tomography VII, 780413. doi: 10.1117/12.860298

Vaziri M, Abrahamsson L, Hagman O, Sandberg D (2020) Welding of wood in the presence of wollastonite. Bioresources 15, 1617-1628.

Vaziri M, Du Plessis A, Sandberg D, Berg S (2015) Nano X-ray tomography analysis of the cell-wall density of welded beech joints. Wood Material Science and Engineering 10(4), 368-372. doi: 10.1080/17480272.2015.1062418

Vaziri M, Lindgren O, Pizzi A (2012) Influence of machine setting and wood parameters on crack formation in scots pine joints produced by linear friction welding. Journal of Adhesion Science and Technology 26, 2189-2197. doi: 10.1163/156856111X610126

Verhey SA, Laks PE (2002) Wood particle size affects the decay resistance of woodfiber/thermoplastic composites Forest Products Journal 52 (11/12), 78-81

Véstias M, Neto H (2014) Trends of CPU, GPU and FPGA for high-performance computing. In: Proceedings of the 24th International Conference on Field Programmable Logic and Applications. München, Germany. 1-6

Viljanen M, Ahvenainen P, Penttilä P, Help H, Svedström K (2020) Ultrastructural X-ray scattering studies of tropical and temperate hardwoods used as tonewoods. IAWA Journal 41(3), 301-319. doi: 10.1163/22941932-bja10010

Wadell H (1935) Volume, shape, and roundness of quartz particles. The Journal of Geology 43, 250-280. doi: 10.1086/624298

Wallis NK (1970) Australian Timber Handbook. Angus and Robertson. Sydney, Australia

Walther T, Terzic K, Donath T, Meine H, Beckmann F, Thoemen H (2006) Microstructural analysis of lignocellulosic fiber networks. Proceedings of SPIE 6318, Developments in X-Ray Tomography V, 631812. doi: 10.1117/12.679050

Walther T, Thoemen H (2009) Synchrotron X-ray microtomography and 3D image analysis of medium density fiberboard (MDF). Holzforschung 63(5), 581-587. doi: 10.1515/HF.2009.093

Wang Q, Liu X, Yang S (2020) Predicting density and moisture content of *Populus xiangchengensis* and *Phyllostachys edulis* using the X-ray computed tomography technique. Forest Products Journal 70, 193-199. doi: 10.13073/FPJ-D-20-00001

Wang Q, Liu X, Yang S, Jiang M, Cao J (2019) Non-destructive detection of density and moisture content of heartwood and sapwood based on X-ray computed tomography (X-CT) technology. European Journal of Wood and Wood Products 77(6), 1053-1062. doi: 10.1007/s00107-019-01459-y

Wang Y (2007) Morphological characterization of wood plastic composite (WPC) with advanced imaging tools: developing methodologies for reliable phase and internal damage characterization (Master of Science Thesis). Oregon State University

Wang Y, Muszynski L, Simonsen J (2007) Gold as an X-ray CT scanning contrast agent: Effect on the mechanical properties of wood plastic composites. Holzforschung 61(6), 723-730. doi: 10.1515/HF.2007.117

Wascher R, Bittner F, Avramidis G, Bellmann M, Endres HJ, Militz H, Viöl W (2020) Use of computed tomography to determine penetration paths and the distribution of melamine resin in thermally-modified beech veneers after plasma treatment. Composites Part A: Applied Science and Manufacturing 132, 105821. doi: 10.1016/j.compositesa.2020.105821

Watanabe K, Lazarescu C, Shida S, Avramidis S (2012) A novel method of measuring moisture content distribution in timber during drying using CT scanning and image processing techniques. Drying Technology 30, 256-262. doi: 10.1080/07373937.2011.634977

Watanabe K, Saito Y, Avramidis S, Shida S (2008) Non-destructive measurement of moisture distribution in wood during drying using digital X-ray microscopy. Drying Technology 26, 590-595. doi: 10.1080/07373930801944796

Welch MB (1929). Some properties of red satinay, *Syncarpia hillii*. Journal and proceedings of the Royal Society of New South Wales 63-64, 122-130

Wentzel M, Koddenberg T, Militz H (2020) Anatomical characteristics of thermally modified Eucalyptus nitens wood in an open and closed reactor system. Wood Material Science & Engineering 15(4), 223-228. doi: 10.1080/17480272.2019.1572649

Wernersson ELG, Luengo Hendriks CL, Brun A (2009) Generating synthetic µCT images of wood fibre materials. In: Proceedings of 6th International Symposium on Image and Signal Processing and Analysis. Salzburg, Austria. 365-370. doi: 10.1109/ISPA.2009.5297698

Wheeler E, Baas P, Gasson P (1989) IAWA list of microscopic features for hardwood identification. IAWA Bulletin 10(3), 219-332

Wieland S, Grünewald T, Ostrowski S, Plank B, Standfest G, Mies B, Petutschnigg A (2013) Assessment of mechanical properties of wood-leather panels and the differences in the panel structure by means of X-ray computed tomography. Bioresources 8(1), 818-832

Wilberg P (1995) Moisture distribution changes during drying. Holz als Roh- und Werkstoff 53, 402. doi: 10.1007/s001070050118

Wilkes TE, Stock SR, De Carlo F, Xiao X, Faber KT (2009) X-ray micro-computed tomography of beech wood and biomorphic C, SiC and Al/SiC composites. Philosophical Magazine 89(17), 1373-1389. doi: 10.1080/14786430902956457

Wilkinson S, Ogée J, Domec JC, Rayment M, Wingate L (2015) Biophysical modelling of intra-ring variations in tracheid features and wood density of Pinus pinaster trees exposed to seasonal droughts. Tree Physiology 35(3), 305-318. doi: 10.1093/treephys/tpv010

Wörle M, Hubert V, Hildbrand E, Hunger K, Lehmann E, Mayer I, Petrak G, Pracher M, von Arx U, Wülfert S (2012) Evaluation of decontamination methods of pesticide contaminated wooden objects in museum collections: Efficiency of the treatments and influence on the wooden structure. Journal of Cultural Heritage 13(3), S219-S215. doi: 10.1016/j.culher.2012.01.006

Wu Y, Matsui H, Kataoka Y (2003) Study on the impregnation of phenol resin in Chinese Fir and its improvement. Scientia Silvae Sinicae 39(6), 136-140

Ximenes FA, Cowie AL, Barlaz MA (2018) The decay of engineered wood products and paper excavated from landfills in Australia. Waste Management 74, 312-322. doi: 10.1016/j.wasman.2017.11.035

Yamamoto K, Ohgoshi M, Nakato K, Sadoh T (1983) Natural penetration of water into softwoods - analysis by soft X-ray densitometry. Journal of the Society of Materials Science 32, 869-874 (in Japanese).

Yata S, Nishimoto K (1983) Application of SEM-EDXA technique to the study of metal distribution in preservative-treated wood. Wood Research: bulletin of the Wood Research Institute Kyoto University 69, 71-79

Yates HO (1968) X-ray stalks old house borer. Pest Control 36(10), 52-59

Yazid K, Masschaele B, Awang MRB, Abdullah MZ, Saleh JM, Mohamed AA, Khalid MABH (2009) Three-dimensional imaging using microcomputed tomography for studying Gaharu morphology. AIP Conference Proceedings 1202 (1), 127. doi: 10.1063/1.3295582

Young RJ (1997) Analysis of composites using Raman and fluorescence microscopy—a review. Journal of microscopy 185(2), 199-205. doi: 10.1046/j.1365-2818.1997.d01-618.x

Youssef S, Rosenberg E, Gland NF, Kenter JA, Skalinski M. Vizika O (2007) High resolution CT and pore-network models to assess petrophysical properties of homogeneous and heterogeneous carbonates. In: 2007 SPE/EAGE Reservoir Characterization and Simulation Conference. Abu Dhabi, UAE. 111427

Yu L, Hao X, Cai L, Shi SQ, Jiang J, Lu J (2014) An investigation of moisture gradient in wood during drying using X-ray radiation and numeric methods. Forest Products Journal 64, 199-205. doi: 10.13073/FPJ-D-14-00007

Yu L, Lu J, Li X, Xu J, Hao X, Jiang J (2012) Studies on measurement of moisture content by X-ray scanning method. Journal of Central South University of Forestry and Technology 32, 43-47 (in Chinese). doi: 10.14067/j.cnki.1673-923x.2012.01.024

Yu L, Lu J, Li X, Xu K, Wu Y, Jiang J (2013) Comparison of X-ray scanning and slice methods for moisture distribution measurements when drying *Cunninghamia lanceolata* plantation wood. Journal of Zhejiang A&F University 30, 543-547 (in Chinese).

Yu L, Qi D (2008) Analysis and processing of decayed log CT image based on multifractal theory. Computer and Electronics in Agriculture 63(2), 147-154. doi: 10.1016/j.compag.2008.02.003

Yu L, Qi D (2011) Applying multifractal spectrum combined with fractal discrete Brownian motion model to wood defects recognition. Wood Science and Technology 45, 511-519. doi: 10.1007/s00226-010-0341-7

Yusof MFMY, Hamid PNKA, Bauk S, Hashim R, Tajuddin AA (2015) Determination of CT number and density profile of binderless, pre-treated and tannin-based *Rhizophora* spp. particleboards using computed tomography imaging and electron density phantom. AIP Conference Proceedings 1659, 040004. doi: 10.1063/1.4916864

Zauner M, Keunecke D, Mokso R, Stampanoni M, Niemz P (2012) Synchrotron-based tomographic microscopy (SbTM) of wood: development of a testing device and observation of plastic deformation of uniaxially compressed Norway spruce samples. Holzforschung 66(8), 973-979. doi: 10.1515/hf-2011-0192

Zeng GL (2010) 3D image reconstruction. In: Zeng GL (ed) Medical Image Reconstruction. Springer, Berlin, Heidelberg, Germany. doi: 10.1007/978-3-642-05368-9_5

Zuber SH, Hashikin NAA, Yusof MFM, Aziz MZA, Hashim R (2021) Characterization of soy-lignin bonded *Rhizophora* spp. particleboard as substitute phantom material for radiation dosimetric studies – Investigation of CT number, mass attenuation coefficient and effective atomic number. Applied Radiation and Isotopes 170, 109601. doi: 10.1016/j.apradiso.2021.109601

Appendices

Appendix 1: Synchrotron XFM elemental maps of turpentine and satinay

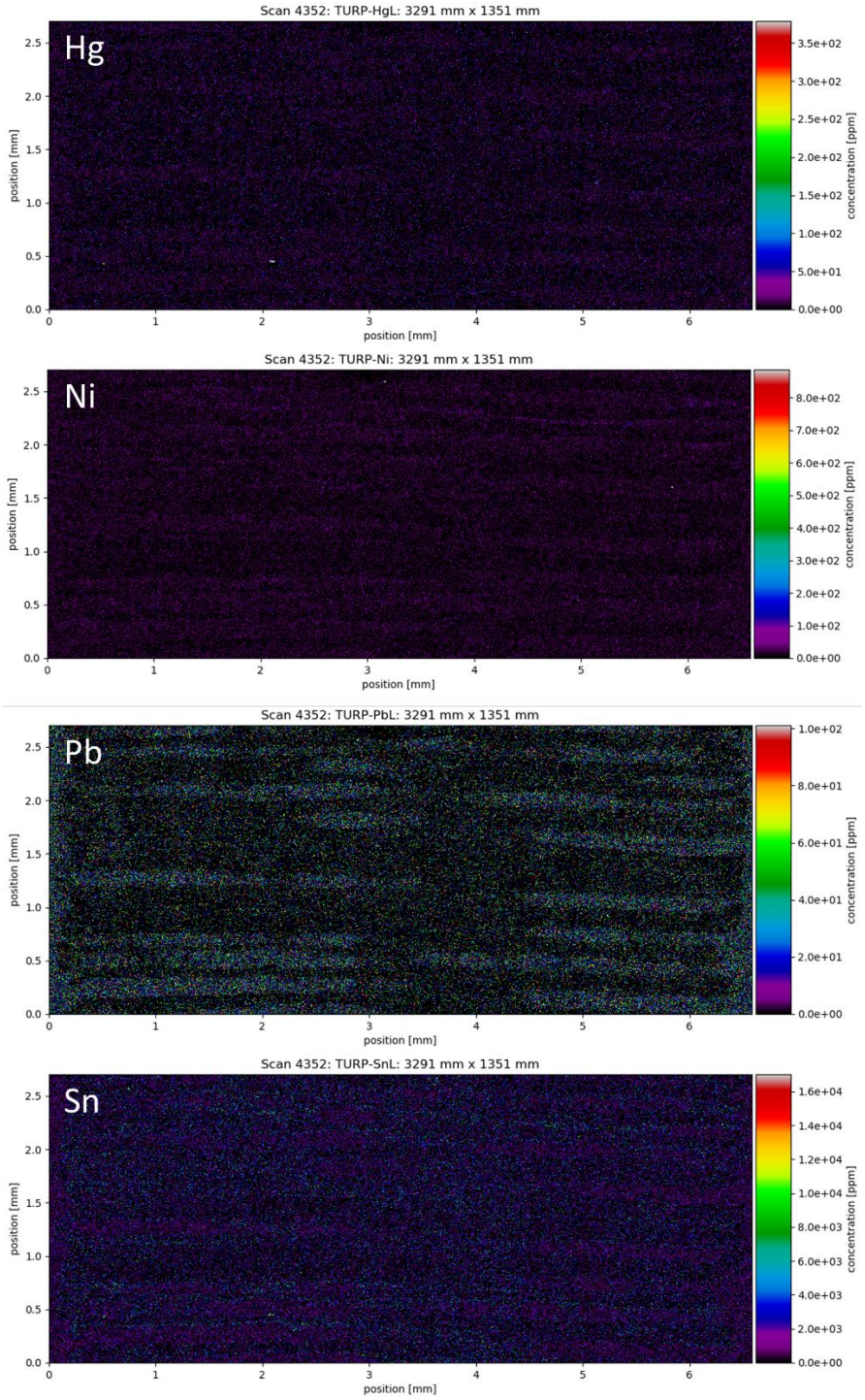

Appendix Figure 1: Synchrotron XFM elemental maps of Hg, Ni, Pb and Sn in the radial-longitudinal direction of turpentine heartwood samples

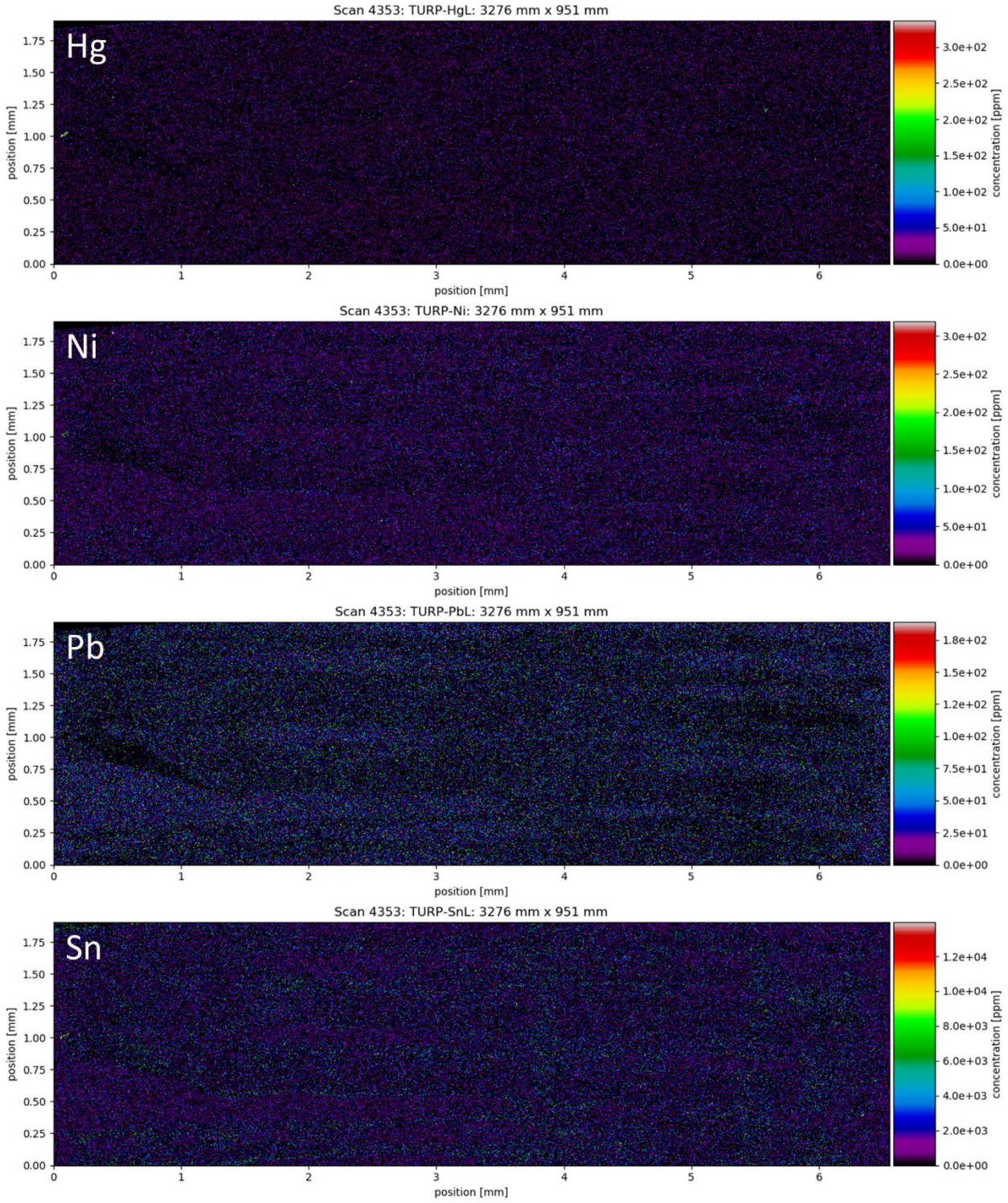

Appendix Figure 2: Synchrotron XFM elemental maps of Hg, Ni, Pb and Sn in the radial-longitudinal direction of another turpentine heartwood samples

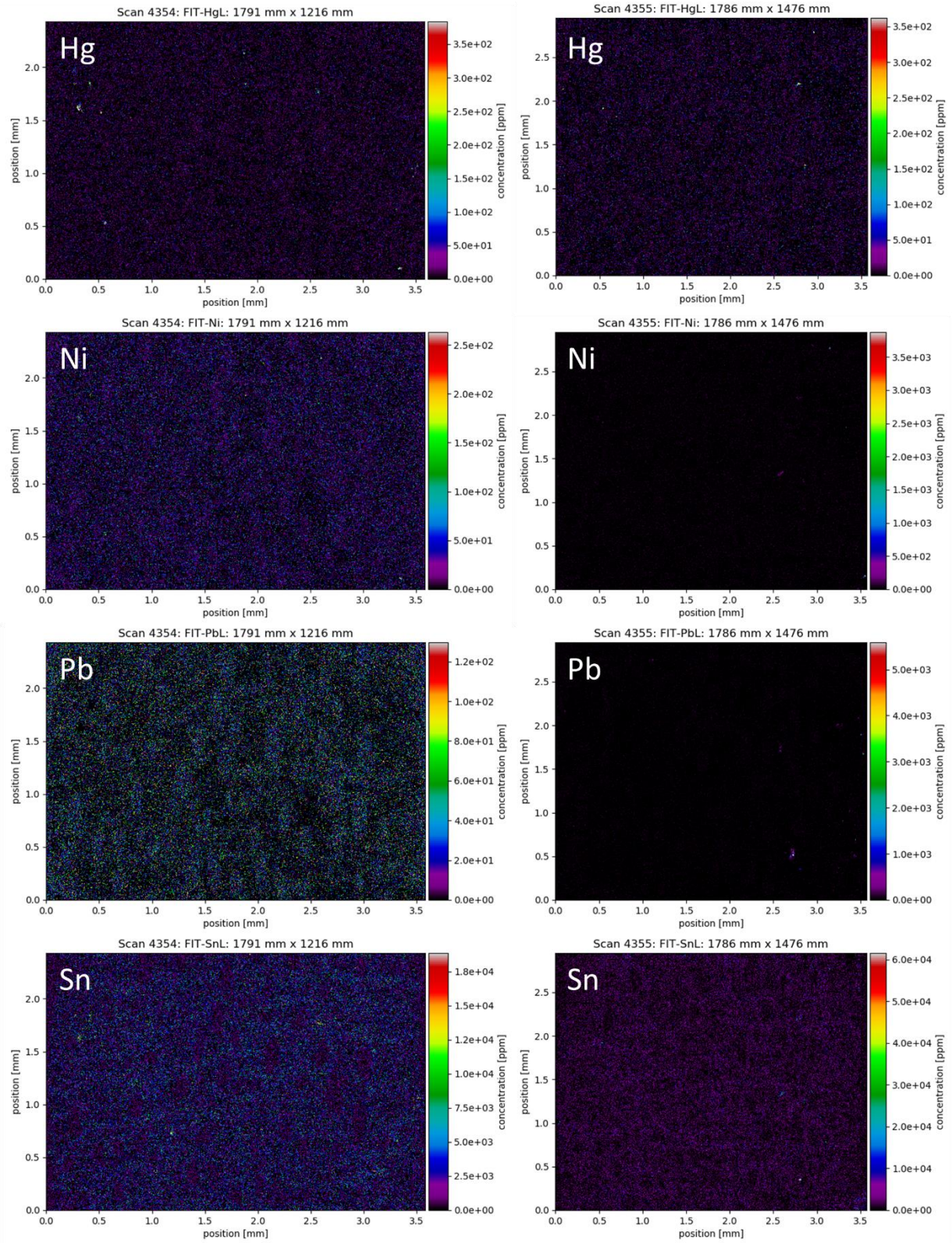

Appendix Figure 3: Synchrotron XFM elemental maps of Hg, Ni, Pb and Sn in the radial-longitudinal direction of satinay heartwood samples

Appendix 2: Video demonstrating a student using a virtual reality system to explore silica particles in satinay (Fraser Island turpentine)

Please see the video entitled “VR and wood science (1/2) VR system demo” in the YouTube channel “The Wood Technology Society”, or use the link below:

https://www.youtube.com/watch?v=zFrKSnkxCLE

Appendix 3: Animated video of inorganics in satinay (Fraser Island turpentine)

Please see the video entitled “VR and wood science (2/2) Fraser Island turpentine” in the YouTube channel “The Wood Technology Society”, or use the link below:

https://www.youtube.com/watch?v=M2tdrxWw7qU

Appendix 4: Animated video of phases in WPC before and after labeling

Please see the video under the abstract section of the publisher’s webpage of the paper below:

Feng D, Turner M, Evans PD (2022) Sodium iodide as a contrast agent for X-ray micro-CT of a wood plastic composite. Applied Sciences 12(1), 208. doi: 10.3390/app12010208

Alternatively, please use the following link: https://www.doi.org/10.3390/app12010208

Appendix 5: Additional X-ray micro-CT images of WPC

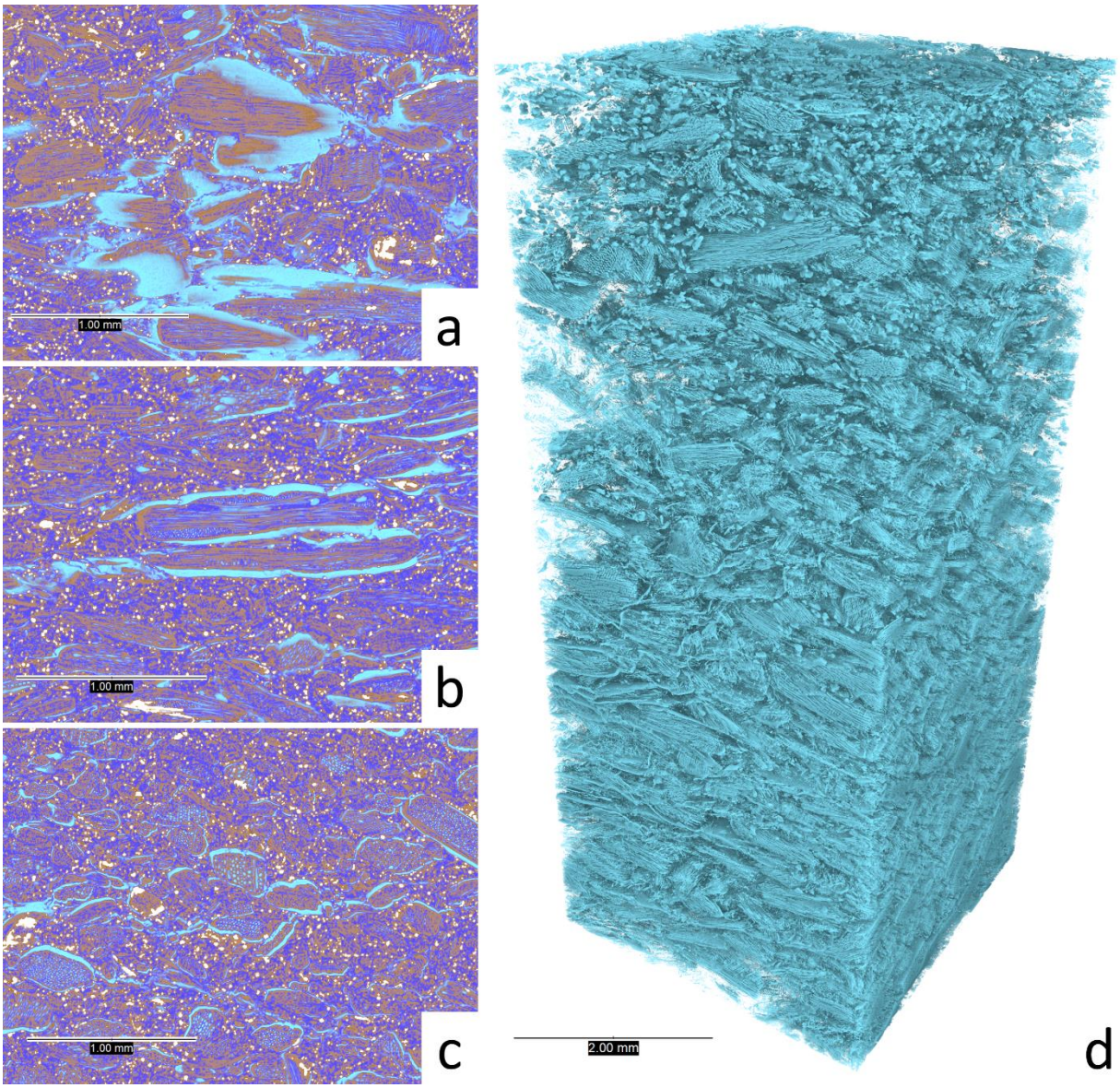

Appendix Figure 4. 2D and 3D images showing the network of interconnected voids in the WPC before labeling: (a) (b) (c) 2D sectional images; (d) 3D volume rendered image. Brown = wood; light blue = void; navy blue = plastic; white = zinc borate

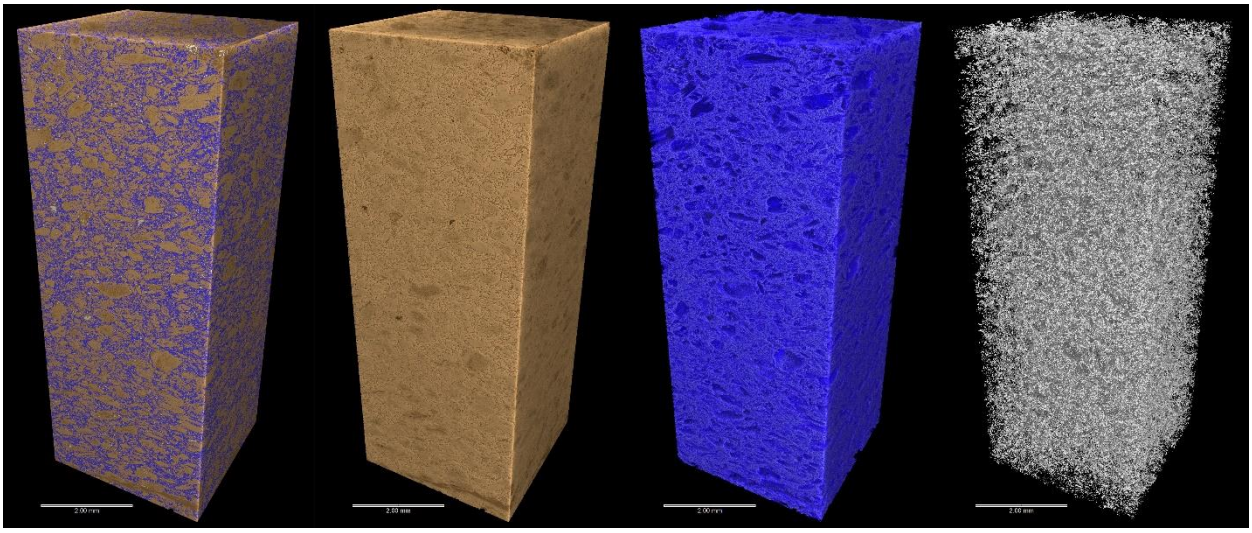

Appendix Figure 5. 3D volume rendered images showing phases in the WPC after labeling. Brown = wood; navy blue = plastic; white = zinc borate

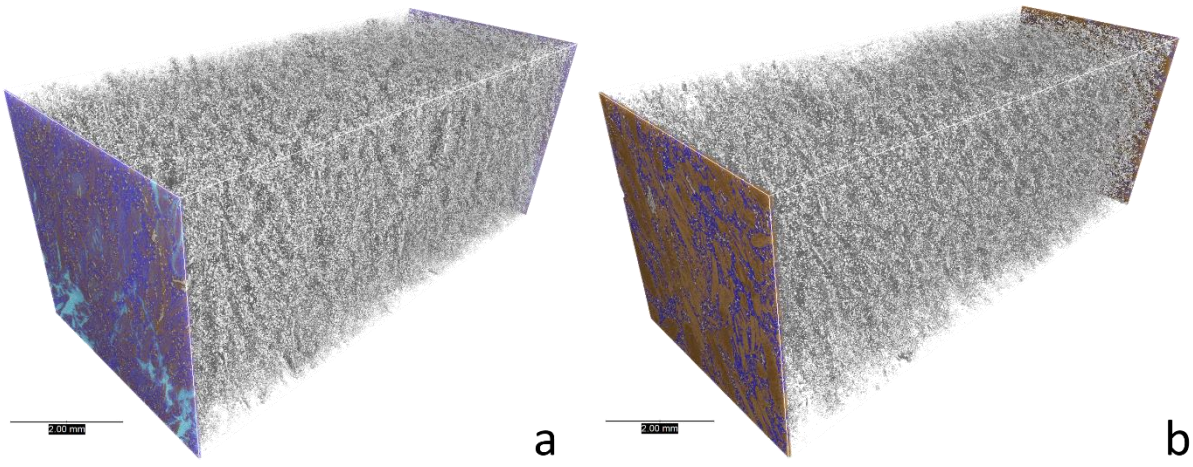

Appendix Figure 6. 3D volume rendered images showing zinc borate particles in the WPC: (a) before treatment; (b) after treatment. Brown = wood; light blue = void; navy blue = plastic; white = zinc borate

Appendix 6: Quantitative data of selected wood particles from the WPC sample

Index	Volume3d	EqDiameter	Area3d	Length3d	Breadth3d	Thickness3d	AspectRatio3d	Sphericity
1	0.001382	0.138195	0.16946	0.327434	0.148498	0.091664	3.38301	0.354054
2	0.01775	0.323643	0.48201	0.502262	0.337885	0.229133	1.98467	0.682695
3	0.001822	0.151535	0.15463	0.34606	0.194937	0.111235	2.61354	0.466529
4	0.001205	0.132032	0.140464	0.423548	0.111835	0.094761	4.11891	0.389895
5	0.001006	0.124306	0.083624	0.331304	0.099723	0.069495	4.03114	0.580504
6	0.000186	0.070766	0.027844	0.149704	0.109735	0.040986	2.57826	0.565027
7	0.000471	0.096563	0.04316	0.230478	0.082019	0.066573	3.29537	0.678715
8	0.000221	0.075006	0.043969	0.271828	0.059649	0.043236	4.25631	0.401979
9	0.004387	0.2031	0.264033	0.591775	0.1976	0.132446	3.7599	0.490809
10	9.31E-05	0.056239	0.015481	0.126368	0.072103	0.033056	3.74163	0.641854
11	0.00041	0.092149	0.077524	0.258599	0.133641	0.057624	3.10193	0.344113
12	0.001618	0.145659	0.116889	0.255731	0.156234	0.112114	2.16047	0.570233
13	0.000754	0.112938	0.066428	0.259008	0.130328	0.06269	3.52592	0.603221
14	0.000452	0.09521	0.067796	0.291938	0.101194	0.051982	3.63231	0.420064
15	0.000158	0.067098	0.021862	0.164992	0.065474	0.044903	3.3787	0.64698
16	0.000421	0.092986	0.044036	0.268228	0.111141	0.069085	3.32641	0.616845
17	0.000464	0.09604	0.056349	0.20124	0.158737	0.03964	2.78635	0.514239
18	0.002544	0.16938	0.214521	0.487511	0.146181	0.102419	3.64142	0.42015
19	0.006272	0.228811	0.404722	0.704282	0.221139	0.130511	4.21976	0.406392
20	0.001252	0.133718	0.104367	0.328071	0.140786	0.081563	3.48581	0.53823
21	0.009004	0.258113	0.510214	0.862919	0.231175	0.142469	5.24103	0.410221
22	0.018952	0.330792	0.6736	0.671471	0.415233	0.1624	2.85368	0.510338
23	0.001725	0.148787	0.112837	0.280869	0.172316	0.101707	2.6896	0.616351
24	0.083196	0.541629	1.83299	1.23082	0.447612	0.398321	2.96772	0.502797
25	0.002591	0.170417	0.162392	0.346944	0.228864	0.089265	3.07769	0.561841
26	0.000392	0.09079	0.059894	0.293934	0.09748	0.04122	4.25576	0.432362
27	0.001048	0.126038	0.096108	0.29037	0.153757	0.055448	3.84191	0.519272
28	0.000802	0.115281	0.073767	0.323083	0.09934	0.057795	4.78373	0.565986
29	0.000662	0.10813	0.106826	0.298971	0.112388	0.077518	3.21019	0.343848
30	0.000346	0.087128	0.040256	0.218828	0.104264	0.052446	3.39034	0.592427
31	0.000387	0.090387	0.040055	0.231597	0.078577	0.059233	3.76031	0.640768
32	0.000234	0.076448	0.034524	0.266125	0.065685	0.05914	4.1028	0.531822
33	0.000465	0.096096	0.056688	0.379204	0.069131	0.06072	4.78129	0.511759
34	3.09E-05	0.038953	0.008108	0.145212	0.039329	0.021247	4.38395	0.587899
35	0.004281	0.201457	0.310289	0.681639	0.208231	0.089978	5.61258	0.410909
36	0.002166	0.16054	0.204329	0.414289	0.192875	0.093367	3.95868	0.396266
37	0.000184	0.070507	0.030846	0.191307	0.085635	0.033832	4.53325	0.506304
38	0.001483	0.141486	0.12796	0.330098	0.142942	0.11006	2.88717	0.491474

Index	Volume3d	EqDiameter	Area3d	Length3d	Breadth3d	Thickness3d	AspectRatio3d	Sphericity
39	0.002888	0.176675	0.167545	0.46281	0.151431	0.117956	3.4285	0.585285
40	0.001108	0.128398	0.094508	0.373754	0.131597	0.061353	4.05685	0.548027
41	0.011709	0.281736	0.558882	0.513433	0.41615	0.178728	2.63017	0.446185
42	0.000984	0.123394	0.098886	0.270065	0.163007	0.066508	3.15577	0.483729
43	0.012708	0.289527	0.503435	0.659218	0.275186	0.1607	3.04499	0.523099
44	0.000522	0.099908	0.069724	0.244296	0.111701	0.063171	3.72013	0.449744
45	0.006197	0.227887	0.449276	0.722803	0.280725	0.170688	3.6884	0.363141
46	0.004608	0.206455	0.446354	0.766375	0.187042	0.096968	6.27994	0.3
47	0.000775	0.113941	0.080523	0.191345	0.151645	0.085726	2.11216	0.506517
48	0.006507	0.231631	0.287172	0.542026	0.18994	0.150257	3.25428	0.586948
49	0.000482	0.097285	0.081932	0.439559	0.093515	0.047436	6.51316	0.362906
50	0.000267	0.079906	0.047055	0.256133	0.083562	0.036291	4.13168	0.426291

Appendix 7: Studies in wood density using X-ray techniques and a Joyce Loebl autodensidater (Nyakuengama 1991)

Studies in wood density using x-ray techniques and a Joyce Loebl autodensidater

1. Preparation of standard wood samples:

There are three species involved: radiata pine (Pinus radiata), alpine ash (Eucalyptus delegatensis) and Atlantic cedar (Cedrus atlantica)

The procedure was as follows:

1.1 One or more trees of each species were felled and sample discs about 5 cms thick were removed as required.

1.2 Blocks roughly square in section were sawn from each disc passing through the centre of the pith from bark to bark.

1.3 The blocks were dried in an oven at $40^{o}C$.

1.4 A piece was sawn from each block, 10mm x 10mm in section, the length depending on the dimater of the original disc. Each piece again passed through the centre of the pith.

1.5 Some of the radiata pine pieces were extracted with benzene alcohol (2:1) in a Soxhlet apparatus.

1.6 All pieces were placed in a closed desiccator over saturated solution of sodium dichromate for at least 2 days to equilibrate. This brings the wood to an equilibrium moisture content of 8%.

1.7 The piece were reduced to 6.9 ± 0.04mm in the longitudinal grain direction, using a Black and Decker router modified to act as a spindle moulder. These are the final samples.

1.8 The samples were returned to the disiccator until ready to x-ray but at least overnight.

2. X-Ray Procedure:

2.1 CAUTION: (a) There is always risk when dealing with x-rays if you do not follow the procedure meticulously.
(b) ensure you are wearing a radiation badge.
(c) ensure that if the red light is flashing you do not enter the dark room
(d) ensure an aluminium plate is taped over the x-ray tube aperture.

2.2 WARMING UP:

1. Ensure kV switch points to 50kV
2. Switch on the machine at the wall and turn operating switch to "stand-by" (P).

CAUTION:

The green and yellow lights should come on. If they don't, do not proceed.

3. You may switch on normal ceiling lights at this stage.

4. Check that lead plate in darkroom is correctly positioned by switching on the position lights on the X-ray source head. The diagonal lines should divide the plate up symmetrically.

5. Turn on the cooling water in the dark room. The yellow light on the control panel should go out when sufficient water is flowing.

6. Leave dark-room, close lead lined door and warm up the x-ray unit:

   (a) Check timer is set to 7 minutes
   (b) Turn operation switch from "stand-by" (P) to "On" and (1) and press red button on time switch simultaneously.
   (c) Wind up the kV and mA knobs with the kV slightly ahead of the mA until 20 mA is registered. Complete the adjustment by turning the kV knob to 23 (top side) and re-adjusting the mA to 20.

CAUTION:

Beware of exceeding 20mA; The needle must be kept out of the red area otherwise you will cause severe thumping in the control box.

   (d) Flashing red light denotes that x-rays are being produced.
   (e) Machine cuts off x-rays after 7 minutes, then turn switch back to (P), wind kV back to 0 but leave mA alone.
   (f) If green light only is "on" you may re-enter the x-ray room.

2.3 X-RAYING

1. Your sample or samples should be placed within the inner borderline of the cardboard sheet provided along with 2 step wedges and lead identification numbers as per log book record. The sequence in which the samples are placed on the sheet should be recorded.

2. The cardboard and samples should be placed immediately adjacent to the lead plate on the floor of the dark room so that transfer of the samples, wedges and numbers from the cardboard to the lead can be accomplished in the red safelight only.

3. Place box of x-ray films adjacent to lead plate.

CAUTION: The X-Ray box must not be opened yet.

4. Switch off all overhead lights, close both doors, and crouch down in the corner of the dark room near the sink so that you can see what you are about to do.

5. Remove one x-ray film from the box and then close the box.

6. Remove the paper cover from the X-Ray film and align it on the lead plate so that it is within the taped border.

7. Place the samples, 2 step wedges* and identification number on the lead plate in the same sequence as they were on the cardboard.

8. Leave the dark room taking the box fo unexposed x-ray film with you. Ensure the box is light-tight.

9. Close the lead-lined door.

10. Open the door into the corridor and x-ray the samples as for warming-up procedure turning up the kV to 23 and re-adjusting the mA ro 20. Make sure the mA remains at 20 throughout x-raying.

11. Re-enter the dark room when the green light is on after closing the outside door.

12. Close the lead-lined door, remove samples and place x-ray film in the light-tight bag provided for carrying to the photographic darkroom.

13. Turn all dials to 0 and switches to "OFF"

15. Turn off lights and water.

Developer		Stop Bath		Fixer
5 mins	→	30 secs.	→	5 mins
				longer is old
				Wash for ½ an hour
				Dry.

---

* The step wedges are cellulose acetate working standards of known optical density. The optical density figures derived by Rudman (1969) will be used. These are:

Step	Density level (g/cm^3)
2	0.229
3	0.344
4	0.468
5	0.592
6	0.717
7	0.867

Developer - 200 mls of developer
800 mls of water

Stop Bath - 13 mls of glacial acetic acid in 1 litre of water.

Fixer - If mixed use as in bottle
If new must be mixed as follows:

200 mls of fixer
20 mls of hardener
800 mls of distilled water

After developing the negatives should be checked. If they are not clear-cut or if there are any shadowing effects, they should be rejected. Otherwise each print should be stored between 2 pieces of paper until ready for use.

4. Operation of the Joyce-Loebl Autodensidater

4.1 Introduction

These notes are not comprehensive instructions for the Autodensidater; they are only a brief guide to the use of this instrument in this practical, and should not be used without prior demonstration or reference to the Joyce-Loebl instruction manual.

The Autdensidater can be used in many application other than measuring wood density. This versatility is achieved by varying such features as the sha and intensity of the measuring beam, the sensitivity of the pen response system and the ratio of trace size to specimen size. These controls have been set on this instrument for the measurement of wood density, and must not be tampered with.

4.2 Switching on

4.2.1 Switch on machine at power point

4.2.2 Press on 'Supply' at base panel and switch on 'supply' at point panel of instrument.

4.2.3 Switch on 'Lamp' at instrument Allow 15 mins. for instrument to warm up.

4.3. Aligning Specimen Beam

4.3.1 Turn focussing knob until red spot is focussed on viewing screen

4.3.2 Turn vertical and horizontal adjustment knobs until white slit is exactly covered by black line on viewing screen.

4.4 Setting base-line position

4.4.1 Place a negative on the specimen table, and arrange so that the light spot falls just off one and of a step wedge image. Orientate the negative until you can scale the long axis of the image by manually sliding the specimen table.

4.4.2 Switch on 'pen' switch. If the pen immediately moves to the outer limit of the pen carriage, procede to 4.4.4. If not, follow 4.4.3.

4.4.3 The pen control motor is out of phase. Correct this by changing switch 'pen synch'.

4.4.4 Scan wedge image by manually sliding specimen table, and watch position of pen carriage. This should move in seven definite steps as the wedge steps are scanned.

4.4.4-1 If there are less than seven steps the base-line is set too high. Adjust base-line control until pen carriage moves in seven stages.

4.4.4-2 If pen carriage tends to move to the extreme inside of its travel, the base-line is set too low. Adjust base-line control until pen moves in 7 stages without contacting inside limit of travel.

4.5. Setting up specimen and paper.

4.5.1 Align negative so that the light beam will scan the long axis through the centre of the specimen. The specimen table moves from left to right, so the light spot must be positioned on the left end of the specimen.

4.5.2 Place paper on recording table and clamp down. Use fine grade plain or graph paper.

The recording tables moves from right to left, so it must begin the trace from the extreme right of its travel.

Switch drive motor switch to "reverse" until table reaches end of travel and stops. Then switch off motor manually.

4.5.3 Insert filled pen into holder so that it clears the paper when up, contacts it firmly when down. Switch 'pen' on. Lower pen on to paper.

4.5.4 Clamp specimen table to ratio arm with lock clamp at left end of specimen table. The specimen table and recording table are now locked together, and will move synchronously in the ratio set on the ratio arm (1:5 in this work).

4.6. Making the record

4.6.1 Switch motor switch to "fwd normal". If specimen trace is completed before table reaches end of travel, switch motor of 'off', raise pen, switch 'pen' off and remove paper from record table.

4.6.2 If record table reaches end of travel before specimen scan is completed, proceed as follows.

4.6.2-1 Switch motor to 'stop'.

4.6.2-2 Switch motor to "reverse" momentarily, then back to off. This will provide a small overlap to allow correct joining to the next chart record.

4.6.2-3 Raise pen and remove last record. Insert new paper.

4.6.2-4 Release specimen table from ratio arm be releasing lock clamp.

4.6.2-5 Return recording table to start position by switching motor to 'reverse' then to 'off' when table stops. Be careful not to move specimen table.

4.6.2-6 Clamp specimen table back onto ratio arm, lower pen and resume trace by switching motor to 'fwd normal'.

4.6.2-7 When specimen scan is completed, switch motor to 'off', raise pen, switch pen to 'off' and remove paper.

4.6.3 Record the next specimen proceeding as for steps 4.5 and 4.6. A step wedge trace must be made for each new negative. It may be necessary to re-set the base line when changing to a new negative.

4.7 Switching off.

4.7.1 Remove pen from holder, dismantle pen and soak clean in water.

4.7.2 Switch off 'lamp', 'instrument supply', 'instrument supply', 'main supply' in that order.

4.7.3 Switch off at mains and remove plug.

4.7.4 Replace cover on instrument.

5. Some Theoretical Aspects of the X-ray Technique for examination of wood density.

5.1 INTRODUCTION

Because of the variability of wood, Investigations aiming to clarify causes of variation in density as a function of various factors of forest production, must be cased on a great number of samples to permit statistical interpretation.

All methods of determination used must be rapid as well as non-destructive. Small samples taken with a mortising chain fulfill both objectives, since sampling is carried out on living trees and allows careful selection of individuals in various age classes and locations. Since more than one sample may be taken and because samples may be taken later from the same tree, data may be verified, added to and complemented.

The method gives satisfactory accuracy limited only by the quality and clearness of the x-ray photographs obtained.

5.2 THEORETICAL ASPECTS

The samples are X-rayed in groups; the variations in the density of the negative are then automatically recorded with an auto-densidater. There is a relationship between the density of the wood and the density of the x-ray film.

5.2.1 Relation between the dose of radiation and the dose transmitted by the sample:

X-ray absorption by the material takes place according to an exponential law of simple form:

$$I = I_0 e^{-ux}$$

where I = intensity of radiation after passing through a sample of thickness x.

I_0 = Initial intensity

u = The characteristic absorption coefficient of the material scanned.

Coefficient u increases with density p of the absorbing material in such a way that the ratio $\frac{u}{p}$ remains practically constant, so that, if the thickness does not vary, the intensity of radiation after passing through a sample depends solely on variations in density.

5.2.2 Relation between the dose transmitted by the sample and density of the film:

The relation between the intensity of a beam of light transmitted by the film in a section not exposed to x-rays

(I_0) to the intensity transmitted by an exposed section (I) is called the opacity of a radio-graphic film. The optic density (d) of the section is given by the following formula:

$$d = \log_{10} \frac{I_0}{I}$$

If for very low capacities the optic density of an x-ray photograph is proportional to the exposure, i.e. the product of beam intensity by time, the otpic density is, for high values, proportional to the logarithm of the exposure.

If the intensity received is an exponential function of the density of the sample scanned, then for a given range of optic densities, a linear relation exists between the optic density of the x-ray photograph and the density of the sample at the corresponding point. Since the exponent of the x-ray absorption formula is negative, the optic density of the x-ray film decreases as the density of the wood increases and the relationship is linear. It is therefore sufficient to record the variations in optic density across an x-ray photograph of a radial sample to obtain directly the variations in the density of the wood.

5.3 PRACTICAL APPLICATION

5.3.1 The x-ray apparatus:

The absorption coefficient of x-rays increases with the density of the material scanned. The constitutents of wood, mainly cellulose and lignin, are based on three elements only; carbon, oxygen and hydrogen, of relatively low atomic mass and are transparent to x-rays. Radiation of low energy (so-called "soft-rays") will pass through these. The penetration of the x-rays depends on the speed of the electrons projected on to the anode, and this depends on the potential difference applied across the terminals of the tube. Apparatus destined for x-ray photography of wood must be designed so that it will emit long-wave radiation at low potential differences since wavelength is inversely proportional to the energy of radiation.

The medical apparatus, these long wave radiations are blocked by the glass wall of the emission tube which consists of high atomic mass, notably sillicon. When photographing thin wood sections with x-rays, tubes with a beryllium window are used since this metal has a low atomic weight, and is transparent to long wave radiations; while able to resist differences in pressure between the outside air and the vacuum inside the tube even in very thin sections.

Since exposure times are long, overheating of the filament is prevented by a continuous circulation of cold water.

5.3.2 The Autodensidater

This gives readings of optic densities and not opacity, as only the former is inversely proportional to the density of the wood scanned by radiation.

Since the linear relationship between wood density and optic density is valid only if the thickness of the scanned sample is constant, it is necessary to scan the sample along an axis of precise thickness. An instrument is therefore required which posssesses high resolution, is collimated, and has a film holding stage which can be aligned with the axis of the image even when this is not absolutely rectilinear.

To ensure this method remains accurate and reproducible, the readings of the instrument must be independent of fluctuations in the input current or the aging of the light source.

These conditions lead to the selection of a double beam auto-densidater whose principle is as follows:

A single source of light passes through a number of prisms and is split into the two beams. One passes through the optical system associated with the x-ray image to be scanned, the other through an adjustable optical wedge of variable density consisting of an opaque material increasing uniformly in thickness from end to end, inserted between two sheets of glass. Its opacity increases at an exponential rate and its optic density increases linearly with the thickness traversed. A single photo-multiplier which receives the light from each beam at the rate of 100 pulses/sec. produces a signal which is proportional to the difference in the light intensities of the two beams. This signal controls a servomotor which displaces the optical wedge in such a way the two beams scan regions of the same optical density, one in the film and the other in the wedge. During this displacement a pen fitted to the wedge records the profile of the density variations.

The scale of distance from pith (x-axis) can also be extended by using an optical wedge which has a low variation in density from end to end, if there is insufficient contrast.

5.3.3 Special precautions

5.3.3-1 The Sample:

The sample should be thicknessed very accurately since the entire system depends on the uniformity of thickness scanned by the x-rays.

5.3.3-2 Exposure:

If we assume all annual increments are parallel to each other, there is only one annual increment for which the alignment

between the boundary of the growth rings and the radiation emitted from a point source is perfect. For the others the growth boundaries do not appear on the image in a linear form but in the form of ellipses, more or less flattened according to their displacement with respect to the beam axis, causing blurring in the radiograph and affecting the accuracy of the readings.

To reduce this blurring as much as possible, the distance between source and sample should be increased. A distance of 2.438 m. has been allowed between source and film, which for a growth ring of 5mm diameter and an eccentricity of 10cms with respect to the axis of radiation, corresponds to a maximum width of blut of 0.2mm. This, in most cases, is acceptable.

Another important reason for having a large distance between emission source and sample is related to the film. It is important the dose of radiation received should be as uniform as possible from one end of the sample to the other and between the different x-ray samples on the same film in order to speed up and facilitate the densitometric analysis. Xhe dose received varies inversely with the square of the distance between source and film, which may, even for a small size films, be translated into perceptible differences from one end of the negative to the other if distance from source is too small. With the adopted istance, however, a simple calculation shows that the maximum difference in the dose received between points on a film of 18 x 24cms is about one in a thousand, i.e. practically negligible.

Where, for any reason, radiation received on the film is not contained between two isodosic curves sufficiently close together, it would still be possible to carry out quantitative densitometric measurements, but it would be necessary to include on the recorded graph a plot of the optical density profile of the film taken at a point close to the image of the specimens (i.e., the background profile of the radiograph) alonside the density profile corresponding to the specimen itself. The density of the wood at a given point would then no longer be directly obtainable from the optic density of the corresponding point on the negative, but would be proportional to the difference between the latter and the background optic density of the nearest point.

While increasing source-film distance has the advantage of reducing blurring of the x-ray photographs and of rendering the radiation dose received by them more uniform, it requires rather long exposure times; e.g. 7 minutes for radiation of 20 mA and 23 kV.

5.4 ADVANTAGES OF THE METHOD

5.4.1 Speed

The average time needed for taking x-ray photographs, e.g. of a series of 15 samples, is about 15 minutes, including preparation. Developing the negative itself takes about 15 minutes also.

In densitometric analysis, it takes about 45 seconds to scan a sample 15 cms long. Total time for obtaining a density variation curve is less than 2½ minutes. The method is particularly fast and makes it possible to study a large number of samples. This, combined with the fact that it is non-destructive, is a valuable advantage in smapling.

5.4.2 Accuracy

Accuracy may be affected in three ways.

5.4.2-1 Blurring caused by several factors (e.g., sampling not perpendicular to wood grain, radiation not parallel to the boundaries of the growth rings):

5.4.2-2 Diffusion of radiation between zones of different density:

5.2.2-3 By the size of the slit used in the optical scanning.

One single wood characteristic makes it possible to integrate these causes of inaccuracy and to define the level of resolution of the method, namely the sharpness of transition of late wood to early wood for forest species of the temperate zone with clearly differentiated annual rings. In fact, no transition zones exist in these timbers between the last thick walled cells with small cavities of the latewood and the first thin-walled cells with large lumens of the early wood after this. The density of the wood decreases instantaneously from its maximum value to its minimum value, and an ideal method should supply density variation curves in which the transition of one yearly increment to the next appears on the graph as a straight line parallel to the density axis.

Densitometric analysis of x-ray negatives does not achieve this ideal accuracy, but is, nonetheless satisfactory. In current work on conifers the boundaries of growth rings appear as straight lines slightly inclined with respect to the density axis with a maximum difference between top and bottom of these straight lines for a density change from 0.8gms/cc at the end of the late wood to 0.3gms/cc at the beginning of the early wood, of about 2mm with a magnification of x5, corresponding to an accuracy of about 0.4mm.

5.4.3. Linearity

The method depends entirely on the linear relationship between optical density and the density of the wood.

The expected linearity of the relationship has been verified (with an error of plus or minus 5%) within a range of densities between 0.3gms/cc and 0.8 gms/cc which is suitable for the majority of trees in the temperate zone. These specimens were then exposed to parallel radiation in the radial direction in order to integrate density variations within the various growth rings as much as possible. The expected linearity of the relationship was again verified (with an error of plus or minus 5%) again within a range of densities between 0.3gms/cc and 0.8gms/cc.

ACKNOWLEDGEMENTS:

Much of the information in Section 5 has been derived from Monsieur H. Polge of the Centre National de Recherches Forestieres, Nancy, France, where this x-ray technique was pioneered and developed.